UNIVERSITÀ DI PARMA

UNIVERSITA’ DEGLI STUDI DI PARMA

DOTTORATO DI RICERCA IN INGEGNERIA INDUSTRIALE

CICLO XXXV

THE CONTRIBUTION OF NANOSTRUCTURES TO THE STRUCTURAL ADHESIVES FRACTURE TOUGHNESS

Coordinatore:

Chiar.mo Prof. Gianni Royer Carfagni

Tutore:

Chiar.mo Prof. Fabrizio Moroni

Chiar.mo Prof. Alessandro Pirondi

Dottorando: Stefania Minosi

Anni Accademici 2019/2020 – 2021/2022

TABLE OF CONTENT

LIST OF FIGURES

LIST OF TABLES

INTRODUCTION

Adhesive bonding technology has significantly evolved over the past century, with the development of synthetic polymers beginning in the 1940s. The ability to create different formulations not only of polymers but also hardeners, stabilizers, and additives in the laboratory has enabled the development of specific adhesive systems for each substrate and application. Bonded joints have many advantages compared to traditional joining techniques such as welding, bolting, and riveting. Adhesives allow the joining of dissimilar materials without adding extra weight, providing a more uniform stress distribution between bonded parts and eliminating the need to drill holes. Their polymeric nature provides corrosion resistance, thermal and electrical insulation, interesting damping properties, and high fatigue strength. These characteristics, coupled with low cost, have favored the entry of adhesives within various industries such as aerospace, automotive, marine, and rail, as well as electronics and biomedical.

Structural adhesives, which can withstand substantial loads and are responsible for the strength and stiffness of the structure, are of considerable importance. The most commonly used structural adhesives are epoxy resins. These resins belong to the thermosetting polymer family and exhibit high modulus and tensile strength, low creep, and good performance at high temperatures due to their highly cross-linked structure. Aerospace and automotive industries extensively use epoxy resins for composites production and repair, bonding aluminum skins to aircraft bodies, bonding structures, flange hems, and anti-flutter to car bodies. Thermosetting polymer structure, particularly epoxy resin structure, makes these materials brittle and barely resistant to crack initiation and propagation caused by defects or voids. The joint failure due to catastrophic crack propagation occurs without any indication of damage. Because of low toughness, the strength of adhesives and joints has extensive scattering, which is related to the size scattering of the defects. Currently, it is difficult to guarantee the reliability of adhesive joints throughout their service life, so there are still limitations in their use. Consequently, it has become crucial to study fracture toughness, which represents the ability of a material to resist defect propagation.

Fracture toughness can be improved by changing the chemical structure of the resin, altering its mechanical properties, or introducing organic (rubber-like), inorganic (metal, ceramic) particles or short fibers. The particles can be locally added while retaining the mechanical properties of the resin in other areas. Rubber addition is one of the most widely adopted methods to mitigate epoxy brittleness. Fracture toughness is enhanced by already cross-linked rubbery particles or core shells or by mixing liquid (i.e., non-cross-linked) rubber with resin precursors, promoting rubber precipitation during the resin cross-linking process. Similar to bonded joints, improving the fracture toughness of epoxy resins is also critical for composite materials. Several studies [1]–[11] demonstrate that polymer nanofibers between composite layers improve the mechanical properties of the laminate. These nanofibers promote bridging between layers, increasing the delamination resistance and fracture toughness. Logically, nanofiber integration into bonded joints could improve fracture toughness, as it happens for composite materials. Only a few works have investigated the effect of electrospun nanofibers on adhesive joints. These studies are focused mainly on epoxy resins with medium to low fracture toughness [12]–[15].

Nanoparticles can also improve the performance of bonded joints. The Engineered nanomaterials have a high surface-to-volume ratio and few structural defects. The volume, size, and nature of the nanomaterials are significant characteristics that determine the performance of the joint, as does their interfacial adhesion. Strong interfacial adhesion ensures proper load transfer from the polymer matrix to the nanocomposite. Carbon nanotubes (CNTs) and graphene nanopatterns (GNPs) can improve the stiffness, strength, fracture toughness, and electrical conductivity of adhesive. Conductive joints can be used for electrical measurements in quality and structural health monitoring (SHM) and other sensing applications [16]–[18]. One of the main drawbacks of adhesive joints is related to the difficulty of inspection and monitoring. Some non-destructive techniques are available, such as fiber Bragg grating sensors and ultrasonic acoustic waves. However, these techniques are often not easy to understand, as their analysis requires complex mathematical and statistical tools.

This work aims to expand knowledge on the effects of nanostructures on the fracture toughness of bonded joints and to evaluate their applicability at an industrial level. Despite the non-marginal scientific literature on the incorporation of nanostructures within epoxy resins, the application to adhesive bonding is still limited and in-house procedures are used for incorporation, for which the possibility of scaling up to an industrial level is impractical or unclear. This thesis work aspires to investigate the possibility of incorporating such nanostructures to techniques and materials already used in and automotive and aerospace industries. Fracture toughness was estimated by calculating the critical value of the Mode I strain energy release rate based on Double Cantilever Beam (DCB) test data. Three types of nanostructures were investigated: electrospun nanofibres, multiwalled carbon nanotubes, and graphene nanoplatelets.

The nanofibre structures were produced by electrospinning. The effect of the integration of nylon and NBR/PCL nanofibres, developed and produced at the University of Bologna, was studied. These nanofibres were impregnated with a structural epoxy resin to produce prepreg layers. The prepregs obtained were used to manufacture S235 steel joints. To correctly assess the effect of the nanofibres integrated into the epoxy system, it is crucial that during the tests, the crack propagates in the adhesive layer and not at the interface or within the adherends. The mechanical and chemical interaction between the surface of the adherends and the adhesive is the parameter that most influences the bonding. The surface roughness of the adherends plays a fundamental role in the mechanical interlocking between resin and supports. The surface treatment before an adhesive deposition can determine the success or failure of the bonding application. Therefore, an optimization of the sandblasting parameters was carried out by evaluating the shear strength and fracture surfaces on steel Single Lap Joints (SLJ). The optimized treatment is used for adherends preparation before bonding.

The effect of commercial XD 10 Polyamide nanofibers (XantuLayr) within composite joints bonded with the epoxy film was also studied. Materials and bonding techniques commonly employed in the automotive and aerospace sector were used for joint manufacturing. This choice is due to the desire to investigate solutions that are compatible with current industrial practices and can be easily implemented at an industrial level. The nanomat was used in two different ways. The first consists of applying the nanofibres to the adhesive/adherends interfaces, and the second consists of interleaving the nanofibres between two layers of adhesive. Finally, the toughening effects of multiwalled carbon nanotubes and graphene nanoplates integrated with different concentrations were investigated. Carbon-based nanofiller were integrated in an epoxy film used to bond composite substrate. The nanofillers were first dispersed in acetone and then sprayed on the bonding surface of composite adherends with an airbrush. After the solvent evaporation, the two substrates were bonded with the adhesive film and cured in autoclave. Composite DCB joints were manufactured to assess the Mode I fracture toughness of the different configurations. The electrical resistance between two points through the thickness of the joints was measured during mechanical testing to investigate the potential relationship between resistance variation and crack length.

The structure of the thesis is described below.

In Chapter 1, general concepts of adhesive bonding will be introduced. Different aspects will be discussed, including the main advantages of using adhesives, the main theories of adhesion, the types of adhesives with a focus on structural adhesives, the mechanisms of fracture, toughening, and structural monitoring of joints. Chapter 2 introduced the main characteristic of composite materials. The attention is focused on thermoset composites, their production, bonding and monitoring processes. Chapter 3 describes the materials, tools, and techniques used for sample production, mechanical characterization, and analysis of the results obtained. Chapter 4 reports the results obtained from the mechanical tests and subsequent morphological analysis of the fracture surfaces of steel joints toughened with electrospun nanofibers. Finally, Chapter 5 presents the results of mechanical tests and morphological analyses on fracture surfaces of composite joints reinforced with commercial XD 10 Polyamide nanofibers and carbon-based nanoparticles. The results of mechanical tests are compared with the electrical measurements carried out during crack propagation.

1 ADHESIVE BONDING

1.1 INTRODUCTION

‘Adhesive may be defined as material which when applied to surfaces of materials can join them together and resist separation [19]. This general definition proposed by Kinloch includes also materials not usually considered as adhesives such as mortar and solder. On the other hand, some substances which show the phenomenon of adhesion are outside from this definition, like paints and printing inks [20], [21].

Adhesive materials have been used for a long time, however bonding technology has significantly evolved over the past century, with the development of synthetic polymers beginning in the 1940s. The adhesives are formed after the chemical reaction of an organic polymers, or one or more compounds. The adhesion occurs in two main steps: the achievement of intimate interfacial contact between the adhesive and adherends followed by the hardening of the polymer system. The intimate interfacial contact between the adhesive and adherends occurs in some stage during the bonding operation when the adhesive is in a 'liquid' form and flows into the asperities of the substrate surface with which can generate molecular bonds [19], [20]. The adhesive liquid state can be obtained by heating the solid adhesive, dissolving the adhesive in a solvent, and using monomers in a yet liquid form which is subsequently polymerized. The liquid form can solidify by cooling, solvent evaporation, and chemical reaction. Adhesives can therefore be classified according to the hardening/solidification method. Pressure-sensitive adhesives are omitted from the classification; this class of adhesives does not harden but remains permanently tacky [21]. Adhesives can also be classified according to their chemical nature, although some of them are blends of different polymers and therefore hard to classify. Based on this classification, adhesives can be thermosetting, thermoplastic, elastomeric or a combination of these types of polymers. The ability to create different formulations not only of polymers but also hardeners, stabilizers, and additives in the laboratory has enabled the development of specific adhesive systems for each substrate and application. The development of synthetic polymers made possible the advent of modern structural adhesives [19], [21]. The structural adhesives can withstand significant loads and are responsible for the strength and stiffness of the structure. Structural adhesive are typically thermosetting polymers, but some thermoplastic polymers are also used in some structural applications [21]. Epoxy adhesives are the most important of the structural adhesives family.

In general, bonded joints have many advantages compared to traditional joining techniques such as welding, bolting, and riveting. Adhesives allow the joining of dissimilar materials, have good strength-to-weight ratios and ensure uniform load distribution between bonded parts while avoiding drilling holes. Their polymeric nature provides corrosion resistance, thermal and electrical insulation, interesting damping properties, and high fatigue strength. These characteristics, coupled with low cost, have favored the entry of adhesives within various industries such as aerospace, automotive, marine, and rail, as well as electronics and biomedical.

In this chapter general concepts of adhesive bonding will be introduced. Different aspects will be discussed, including the main advantages of using adhesives, the main theories of adhesion, the types of adhesives with a focus on structural adhesives, the mechanisms of fracture, toughening, and structural monitoring of joints.

1.2 ADVANTAGES AND DISADVANTAGES

Many advantages drive the interest in better-performing adhesives to replace traditional joining technologies such as welding, riveting, bolting, etc.

The advantages of polymer adhesives are listed below [19], [21]:

- Good strength-to-weight ratio
- Ability to join complex structures and dissimilar materials with different coefficients of thermal expansion because of the adhesive flexibility
- Greater flexibility in the design of bonded structures
- The efficient joining of thin sheets because, although adhesives have lower strength than metals, the strength of the adhesive is sufficient for structural applications when used to bond thin sheets with a large area,
- Reduction of the weight of the structure because adhesives are lightweight polymers while screws and bolts are usually metallic
- Uniform load distribution, guaranteed by a large contact area and absence of drilling impart very good fatigue resistance to the joint.
- Prevention or reduction of galvanic corrosion between dissimilar materials
- Thermal and electrical insulation of bonded structures
- Viscoelastic properties of adhesives promote sound absorption and vibration damping which also enable to have high fatigue strength.

- Reduction of joint permeability to gasses, water, and other solvents
- Reduced costs compared to other types of joints, especially when bonding large surfaces and when an automated joint manufacturing process is used
- Improved joint appearance as adhesives allows for very smooth surface finishing, avoiding rivet or bolt holes or weld marks.

Nevertheless, as with any technology, adhesive bonding presents some critical aspects, listed below [19], [21]:

- Low strength compared to mechanical joints
- Reduced resistance to extreme temperature and humidity conditions due to the polymeric nature of the adhesive
- Many adhesives require temperature and pressure to cure; this is an economic disadvantage.
- Need for careful surface preparation (solvent cleaning, chemical treatment, and mechanical abrasion) to ensure good interfacial strength and a durable joint
- Need to use masks and equipment to hold substrates in place during bonding care
- More difficulty in monitoring the quality of bonded joints than mechanical joints because it is not possible to disassemble an adhesive bonding without damaging the joint; recycling is also complex for the same reason
- A limited number of non-destructive testing methods compared to other joining methods.

1.3 THEORY OF ADHESION

The first aspect to consider to produce a resistant and stable adhesive joint is obtaining intimate molecular contact at the interface between adhesive and substrates. This step is followed by the generation of adhesive forces at the interface. These must be sufficiently strong and stable to ensure that the interface is not the weakest link in the joint, either at the time of manufacture or during its service life.

The chemical and physical adhesion mechanisms activated during bonding are numerous and complex.

Therefore, several theories have been proposed to explain the phenomenon of adhesion, the most important of which are listed below [19], [21], [22]:

- Adsorption theory
- Mechanical interlocking theory

- Diffusion theory
- Electrostatic theory
- Weak boundary layer theory

1.3.1 Adsorption Theory

The adsorption theory is the theory with the greatest applicability. According to the adsorption theory, intimate contact at the adhesive/substrate interface allows interatomic and intermolecular forces to be established between the atoms and molecules of the adhesive and substrate surfaces. The bonds that can be established between the adhesive and the substrate can be either primary or secondary.

Primary bonds tend to be quite strong and may be covalent, ionic or metallic in nature. The phenomenon that leads to the formation of primary bonds between adhesive and adherend is known as chemisorption. Secondary bonds, weaker than the previous ones, can be traced back to dipole-dipole interactions, induced dipoles, dispersion forces, and Van der Waals forces. The hydrogen bond can be considered as a particular case of secondary bonding since it results from electron-negative atoms sharing a proton, however, the force associated with this type of bond is of the same order as weak primary bonds. Donor-acceptor bonds are typically of intermediate strength between secondary and primary bonds. Table 1.1 reports the list of bonds type and the range of magnitude of their bond energies.

Table 1.1 – Bond types and typical bond energies [19]

Type	Bond Energy (kJ/mol)
Primary bond	
Ionic	600-1100
Covalent	60-700
Metallic	110-350
Donor-acceptor bonds	
Bronsted acid-base interaction	Up to 1000
Lewis acid-base interactions	Up to 80
Secondary bonds	
Hydrogen bonds	
Involving fluorine	Up to 40
Excluding fluorine	10-25
van der Waals bonds	
Permanent dipole-dipole interactions	4-20
Dipole-induced dipole interactions	Less than 2
Dispersion (London) forces	0.08 - 40

Some studies reveal the presence of covalent bonds between organo-silane adhesion promoters, used to bond epoxies or other adhesives to metal and glass surfaces. The evidence of silicon-oxygen-metal covalent bonds was produced by secondary ion mass spectroscopy (SIMS). The work [23] used infrared spectroscopy to demonstrate the presence of covalent primary bonds between a polyurethane adhesive and epoxy-based primers. The bond nature between poly(acrylic acid) and metal oxides was investigate in [6] and [7]. The studies reveal the presence of highly ionic interfacial primary bonds The presence of hydrogen bonding, ionic bonding, and ion-dipole interactions was assessed by [26]. The authors used X-ray photoelectron spectroscopy to study the interface of ultrathin films of poly - (methyl methacrylate) (PMMA) in various PMMA/metal substrate systems.

The relevance of secondary bonding, and in particular of van der Waals bonds, was assessed by many works [19], [27]–[31], in particular Huntsberger [30], [31] analyze the secondary force contribution to attractive interaction between two planar bulk phases. A distance of only one nanometer results in a joint strength in tension of approximately 100 MPa, higher compared to the strength measured for most adhesive joints. The calculation of the theoretical resistance does not take into account possible defects or voids acting as stress intensifiers. However, the value obtained is quite high and demonstrates that the secondary forces are more than sufficient to account for practical strengths of adhesive bonds [21]. These forces develop when the distance between the surfaces of the adhesive and the adherend does not exceed 5 Armstrong. Therefore, it is important that there is continuous intimate contact between the surfaces. That is, the adhesive must properly wet the surface of the support [32].

The adhesive suitably wets the substrate when it flows into the valleys and cracks in the surface of the adherend. On the contrary, poor wetting occurs when the adhesive bridges the valleys formed by these crevices. Poor wetting results in a smaller contact area between the adhesive and the adherend and increased stress in the air pockets along the interface. It causes a lower strength of the bonded joint. To better define the wettability property, the concept of surface free energy or interfacial tension must be introduced. The surface free energy is the energy associated to intermolecular forces at the interface between two substances. The wetting level can be determined by contact angle (between liquid adhesive and solid adherend) measurements (θ), that is related to interfacial tensions by means of Young equation:

1.1

$$\gamma_{SV} = \gamma_{SL} + \gamma_{LV} cos\theta$$

Where the terms γ_{SV}, γ_{SL}, and γ_{LV} are respectively the interfacial tension of the solid material in equilibrium with its vapor, the interfacial tension between solid and liquid materials, and the interfacial tension of the liquid material in equilibrium with its vapor. The three-phase equilibrium condition is represented in Figure 1-1.

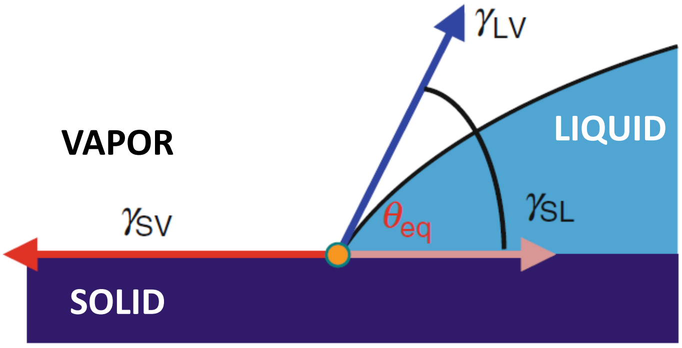

Figure 1-1 –Schematic representation of the equilibrium condition of interfacial forces, described by Young's equation.

Contact angles close to 0° occur when the adhesive, or in general a liquid substance, completely wets a solid surface. In the case of spontaneous wetting, the Young's equation can be written as follows:

1.2

$$\gamma_{SV} > \gamma_{SL} + \gamma_{LV}$$

Since γ_{SV} is the substrate surface energy ($\gamma_{substrate}$), γ_C is the substrate critical surface energy, and γ_{LV} the adhesive surface tension ($\gamma_{adhesive}$), wetting is favored when:

1.3

$$\gamma_{substrate} > \gamma_{adhesive}$$

1.4

$$\gamma_C > \gamma_{adhesive}$$

The term γ_C corresponds to the surface tension of a liquid that completely wets the solid surface ($\theta = 0°$). Polymeric adhesives, such as epoxies, have low energy and wet easily high-energy surfaces such as metals or ceramics. On the contrary, they show lower adhesion with polymeric substrates such as polyethylene, polypropylene, and the fluorocarbons [32].

1.3.2 Mechanical Interlocking Theory

The mechanical theory of adhesion states that successful bonding depends on the ability of the adhesive to penetrate the surface cavities, displace trapped air at the interface, and mechanically bond to the substrate. Although good adhesion can also be achieved with smooth surfaces, according to the mechanical theory of adhesion, rough surfaces increase the contact area between adhesive and substrate, where interfacial or intermolecular adhesion forces can develop.

Many studies report an improvement in joint strength as the surface roughness of the adhesion increases. The work [33] investigate the mechanical response of some aluminum and stainless-steel bonded joint as a function of surface roughness. The butt joint strength tends to increase with the surface roughness. This behavior can be attributed to the random macroscopic roughness obtained by surface treatments such as sandblasting that may prevent crack propagation along the weak interface where defects and small cracks may be aligned. The same phenomenon is less pronounced in ductile materials that show less difference in the strength of bonded joints with smooth or rough surfaces.

Another study also attributed the increased peel strength of the bonded joint realized with polyethylene and various metal substrates to the surface roughness that forms a barrier against the propagation of the crack, which is forced to cover a more tortuous path and dissipates more energy [34]. Figure 1-2 shows two joints with rough and smooth bonding surfaces, loaded with a wedge inserted into the edge of a narrow interface [32].

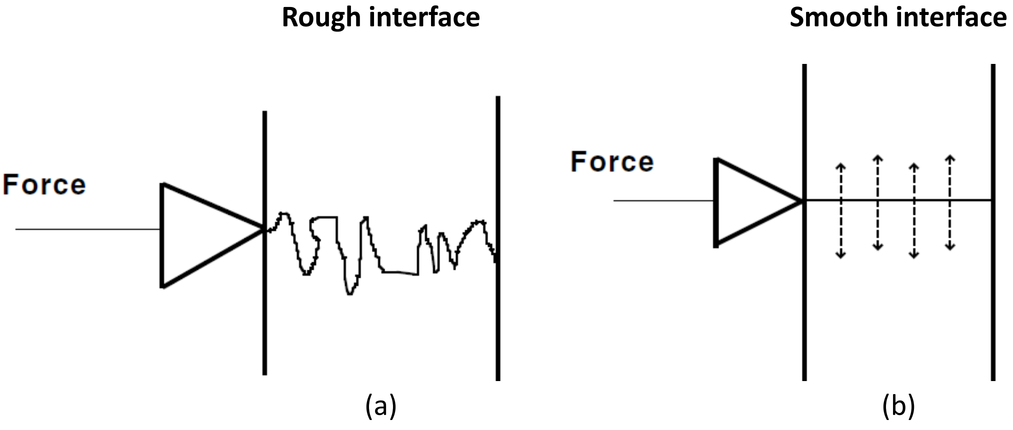

Figure 1-2 – Representation of adhesive bonded joint with rough (a) and smooth (b) surface [32]

The effect of the wedge is, however, a matter of debate. Other works show the increase in peel and cleavage strength, respectively, of bonded joints as a function of increasing surface roughness without finding any correlation with the chemical properties of the bond [35], [36]. On the contrary, some studies did not find a correlation between joint mechanical performances and surface roughness [37], [38].

Although abrasion or sandblasting increases interface roughness, improvements in joint performance may also result from physical-chemical changes in the surfaces of adherends. Joint strength, in many cases, depends on the combined contribution of adhesive forces and mechanical interlocking. However, only some phenomena can be explained by mechanical interlocking theory.

1.3.3 Diffusion Theory

The diffusion theory explains the adhesion phenomenon that occurs through the interdiffusion of molecules between adhesive and the adherend. The adhesion between similar polymers can be described with the diffusion theory because they possess macromolecules or chain segments with sufficient mobility and similar values of solubility parameter, therefore are mutually soluble [19], [32]. This theory well describes autohesion of elastomers, solvent or heat welding of thermoplastic substrates. The thickness of the diffuse interfacial layer (interphase) is in the range of 1-100 nm. This region is free from discontinuities and therefore no stress is present at the interface.

1.3.4 Electrostatic Theory

The electrostatic theory explains the contribution of electrostatic effects between the adhesive and the adherend to the bonded joint resistance. The adhesive/substrate interface can be considered as a double layer of electrical charge, and the resulting electrostatic forces contribute to the joint strength. The interface behavior can be compared to a capacitor. The failure at the interface increases the potential difference between the two layers and finally leads to an electrical discharge. Electrical discharges occur during joint peeling, proving the validity of this theory [19], [22], [39]. The electrostatic adhesion theory can explain some adhesion mechanisms between polymers and metals. The contribution of the electrostatic mechanism in non-metal systems to adhesion is small compared to that of chemical forces.

1.3.5 Weak Boundary Layer Theory

The weak boundary layer theory differs from the other theory because it does not describe an adhesion mechanism but the possible causes of the lack of adhesion in many cases. Based on this theory, the joint fails at the interface by the cohesive failure of the so-called weak boundary layer between adhesive and substrate without involving the adhesive layer [40]. Weak boundary layers may depend on the adhesive, the adherend, the environment, or the interaction between them. Weak boundary layers can form on the adhesive or substrate if some impurities concentrate near the bonding surface and inhibit adhesion mechanisms [32], [41].

Examples of substances that can originate a weak boundary layer are oxide layers, low molecular weight species, oils, and other contaminants. A weak boundary layer can form at any time during the life of a bonded joint, which can be roughly divided into three periods: adhesive application, setting, and service life. Common examples of weak boundary layers are air, oxides, and low molecular weight constituent. These layers can be removed before bonding by surface cleaning and pre-treatment. During the setting step (adhesive cross-linking or solidification), other weak boundary layers can originate from by-products of the chemical reaction between metal substrates and adhesive hardeners, from the adsorption of water or low molecular weight compounds contained in the adhesive, on the adherend surface. During joint service life, boundary layers can be generated by the moisture action. Moisture diffuses through the adhesive or the adherend, set at the interface, and promotes surface oxidation. Plasticizers and solvents can also migrate from the adherend or adhesive toward the interface forming a weak boundary layer. Other weak boundary layers are caused by adherend aging or reaction with the surrounding environment.

1.4 MECHANISMS OF BOND FAILURE

The failure of adhesive joints can be either adhesive or cohesive. Failure is defined as adhesive if it occurs at the adhesive/substrate interface. On the contrary, failure is defined cohesive when occurs within the adhesive layer and thus a layer of adhesive remains on both surfaces. If the substrate fails before the adhesive, it is known as cohesive failure of the substrate.

The joint failure modes are illustrated in Figure 1-3. However, it is common for joints to fail in a mixed adhesive/cohesive mode.

Cohesive failures are desirable because indicate that the maximum strength of the joint materials has been reached. The failure mode should not be considered as the only criterion for evaluating a bonded joint. Some joints that fail at the interface have greater strength than a bonded joint with a weaker adhesive that fails in a cohesive mode. Thus, the ultimate strength of a joint is a more relevant criterion for evaluating the joint quality. However, the failure mode analysis is useful in determining the root cause of adhesive failure and joint quality, as reported in Table 1.2.

Adhesive failures can be caused by many factors. They are usually the presence of a weak boundary layer, inadequate surface preparation, poor wetting of the substrate by the adhesive, the development of internal tensions due to differences between the coefficients of thermal expansion of adhesive and substrate, and joint loading modes and speeds.

Adhesive failure

Choesive failure in the adhesive

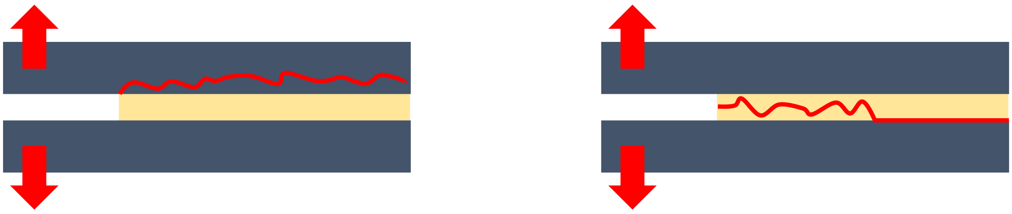

Choesive failure in the adherend

Mixed failure

Figure 1-3 – Scheme of cohesive, adhesive, and mixed failure

Table 1.2 – Failure mode as an indication of the bond quality [32]

Failure Mode	**Inference**
Adhesive failure (interfacial)	Cohesive strength > interfacial strength
Cohesive failure (bulk)	Interfacial strength > cohesive strength
Adhesives/ cohesive (mixed failure mode)	Interfacial strength ≈ cohesive strength

1.5 Adhesive Families

Adhesives are classified in many ways. The first general classification divides adhesives according to their origin, natural or synthetic. This classification is generic and impractical, so the industry has established other parameters for classifying adhesives, such as their chemical composition, function, mode of application or reaction, physical form, cost, and end-use.

Based on their physical/chemical nature, adhesives can be classified as thermosetting, thermoplastic, elastomeric, or hybrid modification.

Thermosetting adhesives are typically available in liquid, paste, and solid form. The liquid form is generally a one- or two-component system. The curing reaction is triggered by heat or chemical catalysts and allows the formation of a three-dimensional network with a high molecular weight.

This structure provides the adhesive with exceptional mechanical strength, resistance to temperatures moderately above the curing temperature, solvent resistance, and low creep. Thermosetting adhesives exist in the form of films of various thicknesses, which can be reinforced with synthetic fabrics, woven or non-woven nylon, polyesters, etc. Adhesive films are flexible, easy to handle, and fit readily to bonded surfaces. Adhesive films usually contain latent hardeners, which are activated at temperatures close to the cure temperature. Some widely used thermosetting adhesives are epoxies, unsaturated polyesters, vinyl esters, phenolic adhesives, cyanoacrylates, and acrylics.

Thermoplastic adhesives are based on thermoplastic polymers that melt when heated and return to solid form when cooled. Their molecular structure is linear or branched, so they are soluble in solvents. Thermoplastic adhesives are single-component systems, and are available in various ranges of molecular weight, melt viscosity, elastic modulus, and tensile and impact strength. Thermoplastic adhesives can be found in solid or liquid form. Thermoplastic adhesives have little creep resistance and are used for low-temperature applications below 90 °C, usually to bond non-metallic materials. Some widely used thermoplastic adhesives are polyvinyl acetate, polyurethane, polyamides, and aromatic polyamides.

Elastomeric adhesives are based on synthetic or natural elastomeric polymers with high toughness and elongation. They can be thermosetting or thermoplastic. These materials return to their initial size and shape after the applied load is removed. Elastomers have low elastic modulus but offer good resistance to joints subjected to irregular load and are suitable for bonding substrates with different coefficients of thermal expansion. Elastomeric adhesives are in the form of solutions, pressure-sensitive films, liquid or solid with one or more components. The hardening or the curing of adhesive varies depending on their formulation. Polyurethane, Butyl rubber, Polysulfide, Polyisobutylene, Silicone, Nitrile rubber, and Neoprene are some of the most commonly used elastomeric adhesives.

Adhesives families can also be classified by their function as structural and non-structural.

Structural adhesives are used for permanent applications and where high mechanical strength is required. Most structural adhesives are thermosets that crosslink at high temperatures and with a curing agent. Epoxy adhesives are the most important structural adhesives. Polyurethane, which is an elastomeric-thermosetting adhesive, is also classified as a structural adhesive

Non-structural adhesives have lower strength and creep resistance at medium to high temperatures compared to structural adhesives. These adhesives are employed in assembly line-fastening operations where environmental service conditions are not extreme. Non-structural adhesives are usually elastomers and thermoplastics. They are usually used in the form of pressure-sensitive adhesives, contact adhesives, mastics, hot melts, and thermoplastic emulsions. Some adhesives classified as non-structural can be used in structural applications if the substrate, environmental, and loading conditions permit. An example is polyvinyl acetate used in the furniture industry.

1.5.1 Epoxy Adhesive

Epoxy adhesives are commercially available since 1946 and employed in many industrial fields, such as the naval, railway, automotive, and aerospace industries. Epoxy adhesives are thermosetting polymers, their chemical structure before crosslinking is characterized by the presence of two or more epoxy groups, with the structure shown in the figure. There are more than two dozen epoxy systems and tens of curing agents, such as amines, primary and secondary amines, and anhydrides. Epoxy adhesives can be formulated or modified to achieve specific chemical, physical and mechanical properties curing kinetic, suitable for the final application.

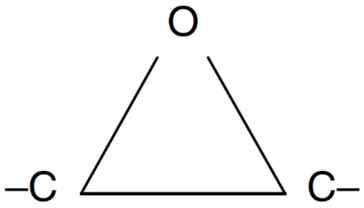

Figure 1-4 – Epoxy group [32]

Epoxy adhesives exhibit good adhesion to various materials, except for some low surface energy polymers.

Thanks to the high crosslinked structure, epoxies show excellent tensile-shear strength and good resistance to oil, moisture, and many solvents. High–quality epoxies show low shrinkage during curing and high resistance to creep. Epoxy-based adhesives are usually formed by an epoxy resin and a curing agent that can be integrated into the resin, defined as single component adhesive, or mixed with the resin just before application. As for most thermosetting adhesives, epoxy adhesives are available in the form of liquids, pastes, films, and solids. Most epoxy adhesives on the market are either single-component, heat-curing adhesives or multiple-component adhesives that cure at either room or elevated temperature.

Generally, epoxy systems that cure at elevated temperatures have a higher crosslinking density and glass transition temperature than systems that cure at room temperature. High-temperature curing resins have better shear strength, especially at elevated temperatures, and better environmental resistance. However, they usually have low toughness and peel strength. Secondary epoxy modifiers are the following elements: diluents to tune viscosity, mineral fillers that lower cost, adjust viscosity and coefficient of thermal expansion, fibrous fillers that improve thixotropic behavior and cohesive strength, and other resins to enhance specific properties, for example, elastomeric resins are used to improve toughness or peel strength.

Epoxy adhesives are used as coatings, due to their excellent adhesion, toughness, corrosion, and chemical resistance and as encapsulating materials for electrical and electronic devices. Epoxies are used to produce a high-strength fiber-reinforced polymers (FRP) with good electrical and thermal properties. Usually, fillers are used to improve physical and mechanical properties. Metal powder or silver-coated glass spheres improve electrical/thermal conductivity; alumina fillers provide thermal conductivity; mica enhances electrical resistance; silica and calcium carbonates provide cost reduction; and graphite guarantee provides low friction. In general, fillers increase the T_g, thermal conductivity, and thermal resistance and reduce the shrinkage of resin and the composite. The amount and the type of filler used influence the resin's rheological behavior.

The aerospace and defense industry employs epoxy adhesives for structural application, coatings, and composite production and repair

1.6 ADHESIVE FRACTURE MECHANICS

The primary cause of failure in adhesive joints is the initiation and propagation of defects. These phenomena are well described through the theory of continuous fracture mechanics.

Fracture mechanics study the adhesive toughness, failure mechanisms, and service life of structures 'damaged' by defects, environmental attacks, or particular loading conditions. Knowledge of stress distribution in bonded joints is useful in the initial design phase and for understanding the effects of joint geometric parameters.

Two approaches have been considered to describe fracture mechanics. The first is the energy criterion proposed by *Griffith* and *Orowan*, according to which fracture occurs when crack growth provides sufficient energy to create two new surfaces. This approach, therefore, provides a measure of the energy required to extend a crack over a unit area, referred to as the fracture energy or critical strain energy release rate, G_C.

The second approach proposed by Irwin assesses that the stress field around a net crack in a linear-elastic material can be defined by a parameter called the stress intensity factor, K, and that fracture occurs when the K-value exceeds a critical value, K_C. Therefore, K is a material-independent stress field parameter, while K_C, often referred to as fracture toughness, is a measure of material property.

Fracture mechanics aims to identify fracture criteria such as G_C and K_C that are independent of joint geometry and test conditions. Fracture mechanics is a useful tool to describe the fracture process and design of joints, particularly concerning life prediction studies.

1.6.1 Loading Modes for Cracked Body

A cracked body may be stressed in three different modes, reported in Figure 1-5 and listed below:

- Mode I, cleavage or tensile-opening mode, is caused by tensile stresses, resulting in the crack faces moving apart.
- Mode II, the sliding mode or in-plane shear mode, is caused by shear stress and the crack faces slide one over the other, in a direction normal to the leading edge of the crack.
- Mode III, the tearing mode or antiplane shear mode, involves relative sliding of the crack faces, along direction parallel to the leading edge.

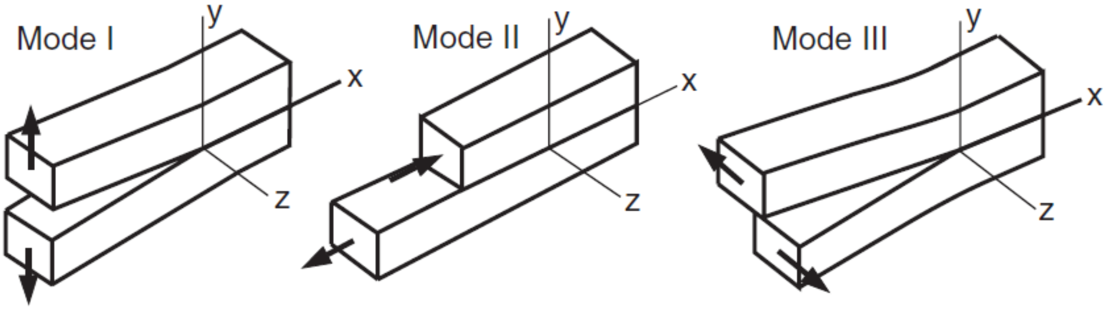

Figure 1-5 – Crack loading mode [42]

Mode I is the most important since is the cause of most cracking problems of engineering interest and the one which most often results in failure.

1.6.2 Energy Balance Approach

The approach proposed by Griffith and later Orowan assesses that the facture occurs when crack growth provides sufficient energy to create two new surfaces.

The crack propagation in the quasi-static condition is described by Griffith as the conversion of the work of external force, W_d, and available elastic energy stored in the bulk specimen, U, into the surface free energy, γ_m. It may be written as:

1.5

$$\frac{\partial(W_d - U)}{\partial a} \geq \frac{\partial A}{\partial a}$$

where ∂*A* is the increase in surface area related with crack growth ∂*a*.

For crack propagation inside a lamina of thickness, t, the relation can be written as follow:

1.6

$$\frac{1}{t}\frac{\partial(W_d - U)}{\partial a} \geq 2\gamma_m$$

The deformation energy of the system can be defined as the sum of potential energy, E_P, and work of the external forces:

1.7

$$U = E_P + W_d$$

it is then possible to write:

1.8

$$-\frac{1}{t}\frac{\partial(E_P)}{\partial a} \geq 2\gamma_m$$

Griffith stated that all the potential energy released was used to propagate the crack and create the new free surface. This is approximately true for brittle materials that do not deform plastically, such as the glass tested by Griffith.

Experimental evidence shows that the theory proposed by Giffith does not allow for a correct assessment of fracture stress values for less brittle materials. For example, Orowan verified that for metals and other materials, the energy required for crack propagation is more than twice the surface-free energy. The fracture of adhesives, involves localized viscoelastic and/or plastic energy dissipative phenomena when high strains are experienced, even for the most brittle of adhesives. These micro-mechanisms are the main source of energy absorption during adhesive failure. However, Griffith's model, can be applied if the behavior of the structure is predominantly linear and non-linear phenomena are confined to a zone not extended to the crack tip.

Irwin and Orowan, independently, introduced the concept of fracture energy, G_C, which also takes into account the phenomena of plastic material behavior.

It is possible to write the following equation:

1.9

$$G = -\frac{1}{t}\frac{\partial(E_P)}{\partial a}$$

where G is the variation of the available potential energy.

The fracture energy represents the critical value of G, whereby the change in the potential energy of the system is equal to the energy required for crack propagation, G_C. In other words, crack propagation occurs when G has values greater than or equal to G_C:

1.10

$$-\frac{1}{t}\frac{\partial(E_P)}{\partial a} \geq G_C$$

Gc is calculated as the contribution of two term:

1.11

$$G_C = G_0 + \psi$$

where G_0 is equal to $2\gamma_m$, and ψ takes into account dissipative effects. This equation has general validity, since it is not restricted to materials that exhibit a linear-elastic behavior and whose behavior can be modeled by linear-elastic fracture mechanism (LEFM) approach.

However, for materials with linear-elastic behavior, this equation is applicable:

1.12

$$G_C = \frac{P_C^2}{2t} \cdot \frac{\partial C}{\partial a}$$

Where P_C is the load at the onset of the crack propagation and C the compliance of the structure. This equation applies to a cracked body under constant load or fixed deformation conditions

1.6.3 Stress Intensity Factor Approach

The presence of defects weakens any component leading to failure at stresses below the characteristic material strength. Defects have indeed been proven to cause stress intensification at the crack tip.

Consider an elliptical hole in in a homogeneous, infinite and uniformly stressed (σ_o) plate and, assuming linear elastic behavior with infinitesimal deformations, the stress field for regions close to the crack tip can be defined as follows:

1.13

$$\sigma_{ij=}\sigma_0\sqrt{\frac{a}{2r}} \cdot f_{ij}(\theta)$$

where σ_{ij} are the components of the stress at a point, r and θ are the polar coordinates of the point, taking the crack tip as the origin, and 2a is the length of the crack.

Figure 1-6 shows the cracked plate scheme.

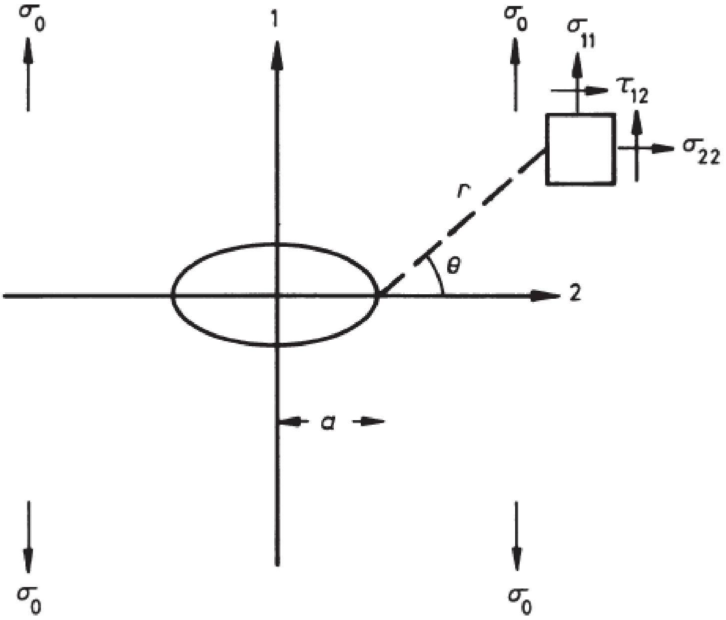

Figure 1-6 – Sharp crack in a uniformly stressed, infinite lamina [19]

Irwin modified the relation as follows:

1.14

$$\sigma_{ij} = \frac{K}{\sqrt{2\pi r}} f_{ij}(\theta)$$

The parameter K is representing the stress intensity factor that relates the magnitude of the stress at the crack tip to the applied stress and geometrical factor.

Considering the loading-mode I (tensile opening), the stress at the crack tips assumes the following values:

1.15

$$\begin{Bmatrix} \sigma_{11} \\ \tau_{12} \\ \sigma_{22} \end{Bmatrix} = \frac{K_I}{\sqrt{2\pi r}} \cos\left(\frac{\theta}{2}\right) \cdot \begin{Bmatrix} 1 + \sin\left(\frac{\theta}{2}\right) \sin\left(\frac{3\theta}{2}\right) \\ \sin\left(\frac{\theta}{2}\right) \cos\left(\frac{3\theta}{2}\right) \\ 1 - \sin\left(\frac{\theta}{2}\right) \sin\left(\frac{3\theta}{2}\right) \end{Bmatrix}$$

Similar expression may be developed for the other two modes.

It is evident from the equation that the stress σ_{ij} tends to infinite as r is close to zero, thus the stress alone could not be a local fracture criterion. The stress field close to the crack can be defined by K_I, and Irwin postulated that the fracture occurs when the K exceeds a critical value K_{IC}.

The fracture criterion is therefore:

1.16

$$K_I \geq K_{IC}$$

The critical value for the crack growth, K_{IC}, is defined as fracture toughness and is a material property.

The parameter K_I can be calculated as follows:

1.17

$$K_I = Q\sigma_0\sqrt{a}$$

and therefore, K_{IC} assumes the following value:

1.18

$$K_{IC} = Q\sigma_C\sqrt{a}$$

Where Q is a geometry factor that can be determines theoretically or by empirical test, σ_C is the stress applied at the crack tip.

1.6.4 Relationship Between G and K

In the context of LEFM, a relationship between G_C and K_c exists.

This relationship, for a homogenous body under plane strain condition, is given by

1.19

$$G_c = G_{Ic} + G_{IIc} + G_{IIIc} = \frac{(1-\nu^2)}{E}K_{Ic}^2 + \frac{(1-\nu^2)}{E}K_{IIc}^2 + \frac{(1+\nu)}{E}K_{IIIc}^2$$

Where E and ν are the tensile modulus and the Poisson coefficient of the material.

However, most practical applications involve Mode I, thus

1.20

$$G_c = G_{Ic}$$

In the case of plane stress, it is possible to write:

1.21

$$G_{Ic} = \frac{K_{Ic}^2}{E}$$

While, in the case of plane strain the equation becomes:

1.22

$$G_{Ic} = \frac{(1 - \nu^2)}{E} K_{Ic}^2$$

For a crack in the center of an adhesive layer the prior expressions are valid using the tensile modulus and the Poisson coefficient of the adhesive, thus, for plane strain:

1.23

$$G_{Ic} = \frac{(1 - {\nu_a}^2)}{E_a} K_{Ic}^2$$

1.6.5 Double Cantilever Beam (DCB) Test

The Mode I fracture resistance of adhesive joints is usually evaluated by Double Cantilever Beam (DCB) test, described in ASTM D3433 [43].

The joint test specimen is formed by two adherends (the double cantilevers) bonded together with a layer of adhesive. At one end of the joint, a crack is artificially induced during joint manufacturing, for example by positioning a piece of releasing film in the adhesive.

During the test, the joint adherends are pulled apart with a specific rate. The load is introduced via circular holes that can be drilled through the end of the substrates, or through metallic blocks bonded to the ends of each support, as in Figure 1-7.

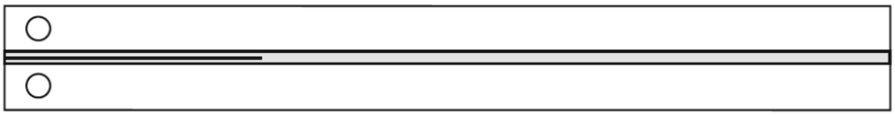

Figure 1-7 – DCB specimen [21]

The load increases as well as deflection of the adherend until critical value that that determine the crack propagation and the cohesive or adhesive failure of the joint. Crack growth results in the drop of joint stiffness. The following equation is proposed by the ASTM D3433 standard for the calculation of the fracture toughness associated to the opening mode:

1.24

$$G_C = \frac{4P_{MAX}^2(3a^2 + h^2)}{Eb^2h^3}$$

Where P_{MAX} is the critical load value, required to trigger the crack propagation, E is the Young's modulus of the adherends, b is the width of the specimen, h is the thickness of the adherent, and a is the length of the crack length measured as the distance from the load axis to the crack tip. This equation is based on elastic stress analysis and is valid for a sharp-crack condition. It is supposed that near the tip of a sharp defect the plastic region is small compared to the crack size and the condition of plane strain is assumed.

When the compliance of the adhesive can not be neglect the fracture toughness should be assessed trough compliance method, reported in the following equation:

1.25

$$G_C = \frac{P^2}{2b} \cdot \frac{\partial C}{\partial a}$$

where P is the applied load and C is the joint compliance.

The relation between compliance and crack length can be evaluated with different theories, the most used are the Euler-Bernoulli and Timoshenko beam theories. These two theories, however do not consider the adhesive flexibility and the rotation of the adherends at the crack tip. The contribute of the rotation of the crack tip and the flexibility of the adhesive can be included in the compliance calculation by adding a corrective factor which can be empirically determined.

In this work, the system compliance is determined using the Krenk's model [44] which automatically takes into account the flexibility of the adhesive and the rotation at the crack tip.

1.7 STRENGTHENING AND TOUGHENING STRATEGIES

The common methods used to improve the toughness of structural adhesive, in particular epoxy systems, and prevent catastrophic failure, are the addition of fillers, thermally expandable particles (TEPs) or the modification of chemical resin composition [45]–[47].

The rubber addition is one of the most adopted methods to improve adhesives fracture toughness [48]. The rubbery phase can be integrated into the adhesive layer in the form of already cross-linked [49], [50] or core-shell rubbery particles [51]. The not crosslinked liquid rubber could also be mixed with resin precursors, allowing the precipitation of rubbery particles during the resin cross-linking process [50], [52]. Toughening- effect for the epoxy systems is achieved by adding a rubbery fraction between 5 and 20 %wt. High amount, however, may reduce the glass transition temperature (T_g), the elastic modulus and the strength of the neat resin [53].

Another strategy to increase the fracture toughness of structural adhesive is the addition of organic and inorganic fillers, like particles or short fibers [45], [54]. Short glass fibers are broadly used as reinforcement and toughening agent [55], [56]. Nanoparticles not only increase fracture toughness but also strength and stiffness of bonded joints [45].

Engineered nanomaterials possess high surface area and limited number of structural defects, and could improve thermal, electrical, and mechanical properties of adhesives depending on their nature, quantity, size, and interfacial adhesion. It's important to develop a strong interfacial adhesion to transfer correctly the load from the polymeric matrix to the nano-reinforcement [45]. Alumina nanospheres and nanorods integration increase shear strength and mode I fracture toughness of adhesive joint [57]. The integration of polymeric nanofibers is an interesting solution for the toughening of epoxy matrix, even in composite materials. [58]. Carbon-based nanoparticles such as carbon nanotubes (CNTs) and graphene nanoplatelets (GNPs) can enhance stiffness, strength, fracture toughness and electrical conductivity of bonded joints [16], [59]–[67].

1.8 NANOFIBERS

Nanofibers have one characteristic dimension, the diameter, in the nanometer range that is approximately 100 nm. Electrospinning is widely used for the nanofibers production because ensure extremely high stretching rate and alignment of macromolecular chains along the nanofiber axes during the ejection pf polymeric solution. Nanofibers, showed in Figure 1-8 possess high aspect ratio and thus huge specific area that improve the interfacial bonding strength. Moreover, fiber mechanical strength tends to increase and the number of inner defects tends to decrease as the fiber diameter is reduced [35].

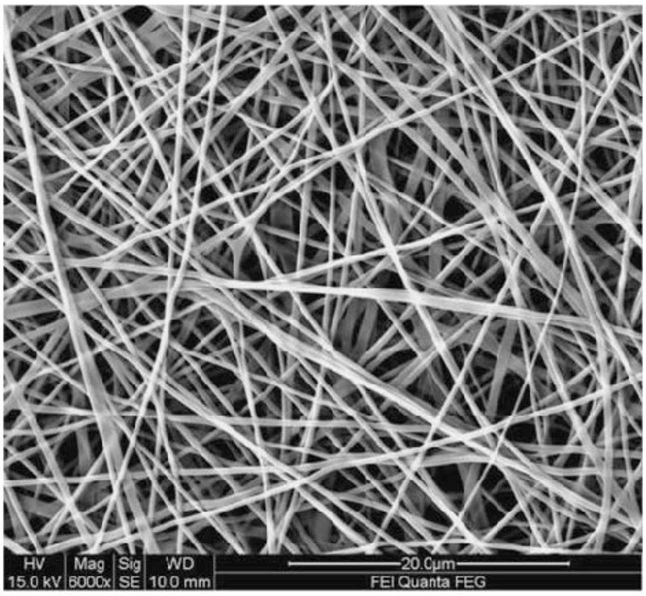

Figure 1-8 – Morphology of electrospun nanofibrous mat [68]

Gilbert et al [69] studied the toughening effect of nano-alumina fibers on mode I and mode II interlaminar fracture toughness of secondary bonded and co-cured carbon fiber/epoxy composite joints. The results reveal that the mode I fracture toughness of co-cured samples increases while it tends to decrease for secondary bonded joints. A contrary effect is noted for the mode II fracture toughness.

Carbon nanofibers are widely investigated in literature. Gude et al. analyzed the effect of CNF on mode-I adhesive fracture energy (G_{IC}) of DCB joints and found an increment of 10% when 0.25 wt% CNFs are added [61].

The tensile strength of aluminum and poly(methylmetacrilate) (PMMA) joints bonded with a commercial epoxy adhesive reinforced with carbon nanofibers was studied by Xu et al [70]. The mechanical properties are reduced for aluminum joint, while for PMMA adherend bonded with nano-reinforced adhesive 0.3 to 0.8 wt% they increase up to 30%.

Many studies prove that composite laminates reinforced with electrospun polymeric nanofibers exhibit enhanced mechanical properties [1]–[11]. The interposition of thermoplastic nanomat between composite layers promotes the ply-to-ply bridging effect resulting in Mode I and Mode II fracture toughness and fatigue delamination strength enhancement [4]–[11]. These results suggest that polymeric nanofibers could improve crack toughening also for bonded joints

Currently, only a few studies investigate the use of electrospun nanofibers in adhesives bonding and are mainly focused on medium-low fracture toughness epoxy resins [12]–[15]. Razavi et al. manufactured aluminum DCB joint bonded with 2k epoxy resin on which polyacrylonitrile (PAN) nanofibers were directly electrospun. The DCB tests reveal a two-fold increase in fracture toughness, although this value was quite low (G_C = 0.11 N/mm over 30 mm of crack propagation) for the neat resin [14]. Ekrem and Avci studie poly(vinyl alcohol) (PVA) nanofibrous mats placed into the adhesive layer of Single Lap Joints (SLJ) and DCB joints. The results proved that shear strength increased by 13.5%, while mode I fracture toughness was about twice the the one of the neat adhesive [15].

The works [71]–[74] have shown that electrospun nylon nanofibres act as reinforcement and support for the adhesive layer. Tests on DCB joints made with pre-impregnated nano-fibers showed that the nano-mat improves the fracture toughness of some low-toughness resins. The results obtained and the procedures developed in [71]–[74] represents the starting point of this work of thesis.

In [71], a nanomat with a thickness between 70 - 90 μm was integrated into a low-viscosity 2k epoxy resin for composite hand lay-up. This resin was preferred to a two-component epoxy adhesive because of its low viscosity and slow reactivity at room temperature. The room-temperature viscosity of most epoxy resins is lower than that of 2K epoxy adhesives, and this characteristic helps to minimize problems related to impregnation. The cross-linking reaction of epoxy resins is also very slow at room temperature, making them more suitable for controlling the impregnation process, at least in the first experimental phase. The impregnation was performed by placing resin on both sides of the nano-mat. The resulting prepreg was used to bond two 2024-T3 aluminum substrates, properly sandblasted and degreased. The specimens were bonded using a bonding template kept under a vacuum for the whole curing cycle. These first tests showed a diffuse presence of air microbubbles. In addition, the thickness of the nanomaterial was too low to fill the entire gap of the bond line. The crack also showed a tendency to propagate along the interface producing scattered results and making it impossible to assess the actual contribution of the nano reinforcements. However, it should be remarked that the hand lay-up resin in [71] has a lower adhesion and fracture toughness than epoxy adhesives: this may have favored adhesive-type failures.

Based on previous experiments, a new procedure was developed in [72], [73] to impregnate the Nylon 6.6 nanomat and manufacture a bonded joint to better asses the nanofibre contribution to the toughening of the adhesive. The nanomat thickness is in the range of 200-300 μm to fill the whole bondline gap. In [72], a two-component high-modulus resin for hand lay-up was used. The nanofibers were immersed into the resin until complete impregnation. The nanomat strip was partially cured before being used as an adhesive for the sandblasted 2024-T3 aluminum adherends. Again, the joints were manufactured in a bonding template and cured under a vacuum. Tests showed that the failure mode of the virgin and nanomodified samples was similar also in this case. However, the introduction of nanofibres improved the fracture toughness of the resin, which was very low. Although the joints exhibit adhesive-type failures, the fracture surfaces analyzed by SEM showed the presence of starched nanofibres attached to the surface of the adherends. Their presence may be associated with a crack-bridging mechanism that lead to the increase of fracture toughness, even if the crack has not passed through the adhesive layer.

In [73], a two-component unfilled epoxy adhesive was used to produce the prepreg. To achieve better interfacial adhesion, an epoxy adhesive was chosen rather than a resin for hand layering. The 2024-T3 aluminum adherend surfaces were treated by chemical etching to promote cohesive failure mode and correctly assess the effect of nanofibers. To this end, three ways of generating the initial DCB defect were evaluated, which led to similar results: fatigue pre-cracking, razor blade tapping, and nanomat exfoliation. In nanomodified specimens, the force during the propagation phase is higher, and the decrease is smoother. This behavior was reflected in fracture toughness which, starting from a similar value of the virgin joints, increased steadily, becoming twice of virgin specimens around 40 mm of crack growth. The highest fracture toughness was reached when the crack propagation mechanism switched from adhesive to cohesive.

In [74], the procedure for prepreg production was further refined using two calibrated and counter-rotating drums. A structural, multi-purpose, unfilled, low-toughness epoxy adhesive was used to bond 6082-T4 aluminum adherends chemically etched. The cross-linking process was carried out without vacuum application to avoid the suction of the not yet cured adhesive from virgin specimens. Specimens were subjected to a dead load during the curing cycle to enhance the adhesion between adherend and adhesive. The nanomat thickness is between 50 and 85 µm, lower than in [71]–[73], to facilitate the wetting of the nanomaterial by the adhesive, which has a higher viscosity than the resins used in previous work. Once again, nanofibres did not show any detrimental effect but, on the contrary, a tendency towards improved fracture toughness, although the adhesive fracture mode for both virgin and nanomodified joints.

Works [71]–[74] have shown that electrospun Nylon 6,6 nanofibres can be used to produce prepregs with a structural epoxy adhesive that acts as an alternative carrier to more conventional substrates. The definition of the impregnation procedure starts with low- and medium-viscosity epoxy resins for hand lay-up application to facilitate the wetting of the nanomaterial. A medium viscosity unfilled two-component epoxy adhesive was then used, before optimizing the process for a high viscosity, high strength two-component epoxy adhesive system. However, the bonds did not have proper interfacial adhesion since all the failures were adhesive. Interfacial failure shows that the presence of the nanomat does not influence the fracture mechanisms and that the interfacial adhesion was not optimal, neither for the sandblasted nor for the chemically etched joints. The improvement of interfacial adhesion is crucial for the evaluation of nanofibrous structures.

1.8.1 Polymeric Nanofibers Production

Nanofibers can be produced using different method [58]. The most common ones are described below:

- *The drawing* process requires highly viscoelastic material subjected to strong deformations. These materials must be cohesive enough to support the stresses developed during the pulling. The solidification follows the pulling step to consolidate the single fibers [75]. The basic setup of the fibre-drawing production method is reported in Figure 1-9.

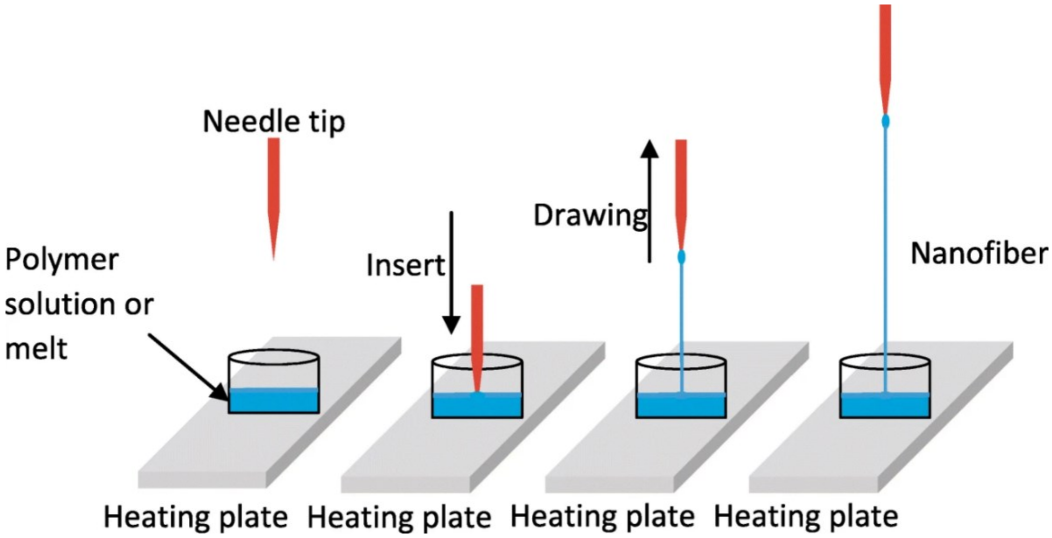

Figure 1-9 – Nano-fibres drawing process [76]

- *The template synthesis* process uses nano-porous membrane as template, as shown in Figure 1-10. The solution is extruded into the membrane through the nanometric-size holes to control the fiber diameter [77]. Fibrils and tubule can be manufactured, but one-by-one continuous nanofibers cannot.

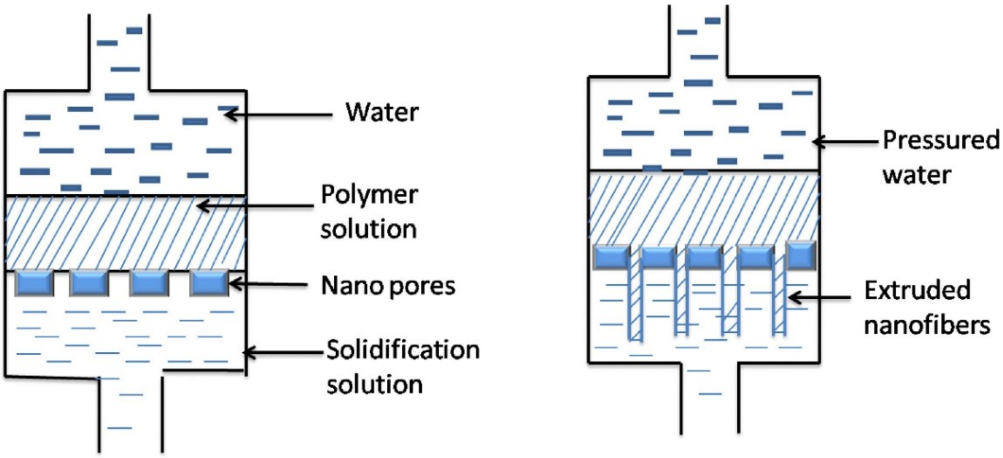

Figure 1-10 – Nanofibers template synthesis process [78]

- *Phase separation* consists in the dissolution, gelation, extraction using a different solvent, freezing and drying. Phase separation occurs during the gelation step. After gelation nanofibers can be extracted [79]. A simplification of the phase separation process is described in Figure 1-11.

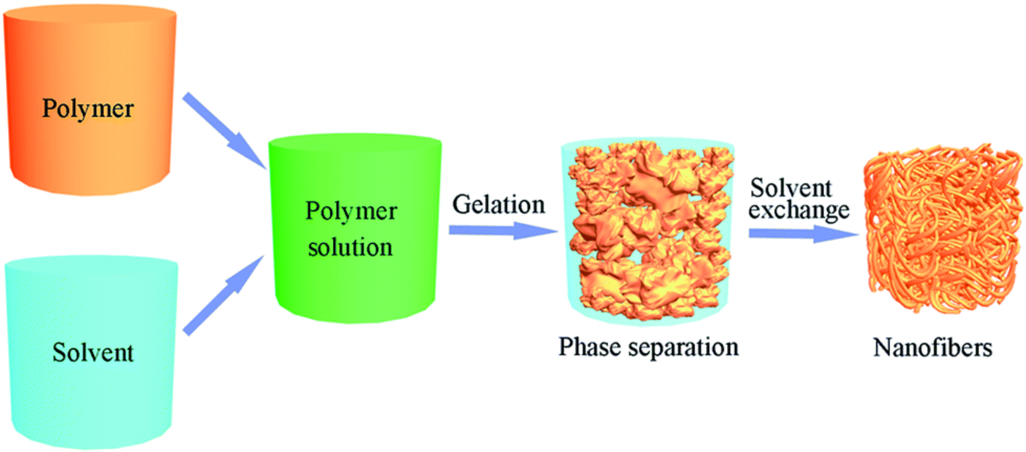

Figure 1-11 – Phase separation of nanofibers [80]

- *Self-assembly* allows that pre-existing components organize or arrange themselves into a desired pattern and function, resulting in the formation of nanofiber mesh [79] or structured filaments, as displayed in Figure 1-12, along a preferential direction. The assembly occurs by adding chemical reactants to the starting solution.

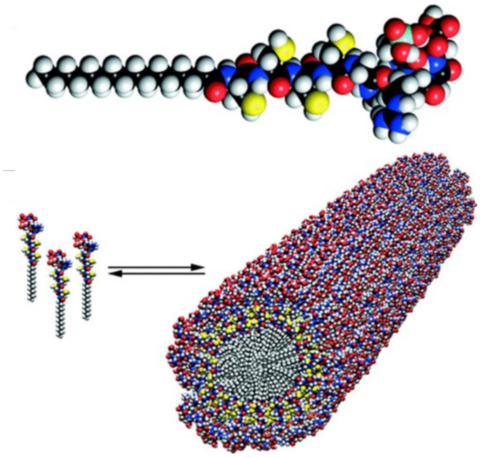

Figure 1-12 – Formation of nanofibers by self-assembly *[81]*

- *Electrospinning* is the most common method used for fabrication of nanofiber. The polymer solution passed through a high voltage of electrospinning machine [79]. More details about electrospinning process are in the following paragraph.

1.8.1.1 Electrospinning

This technique involves the use of an electric field to generate polymer fibres from a liquid solution. The process, therefore, consists of the ejection of an electrically charged fluid polymer onto a substrate, which is also charged but in an opposite manner.

This technique is widely used to engineer nanostructures that vary in:

- Fibre diameter
- Mesh size
- Porosity
- Structure

The apparatus for performing electrospinning consists mainly of the following components

- High voltage power generator
- Syringe and metal needl
- Syringe pump
- Collector

A syringe contains the solution that is pushed through a needle using a pump. An electric field is applied at the tip of the needle, due to a potential difference between the collector and the needle. A droplet of fluid at the tip of the metal needle is held by its own surface tension, until it is electrically charged. Jet ejection occurs when the applied potential difference exceeds a certain critical value drop t causing the electrostatic forces to exceed the surface tension of the polymer solution and the elongation of the drop, forcing the ejection of the liquid jet from the tip of what is defined as the Taylor cone. The solvents contained into the polymeric solution tends to evaporate during the ejection and the polymer is deposited on the collector in the form of mat of nanofibers. A schematization of electrospinning process is reported in Figure 1-13.

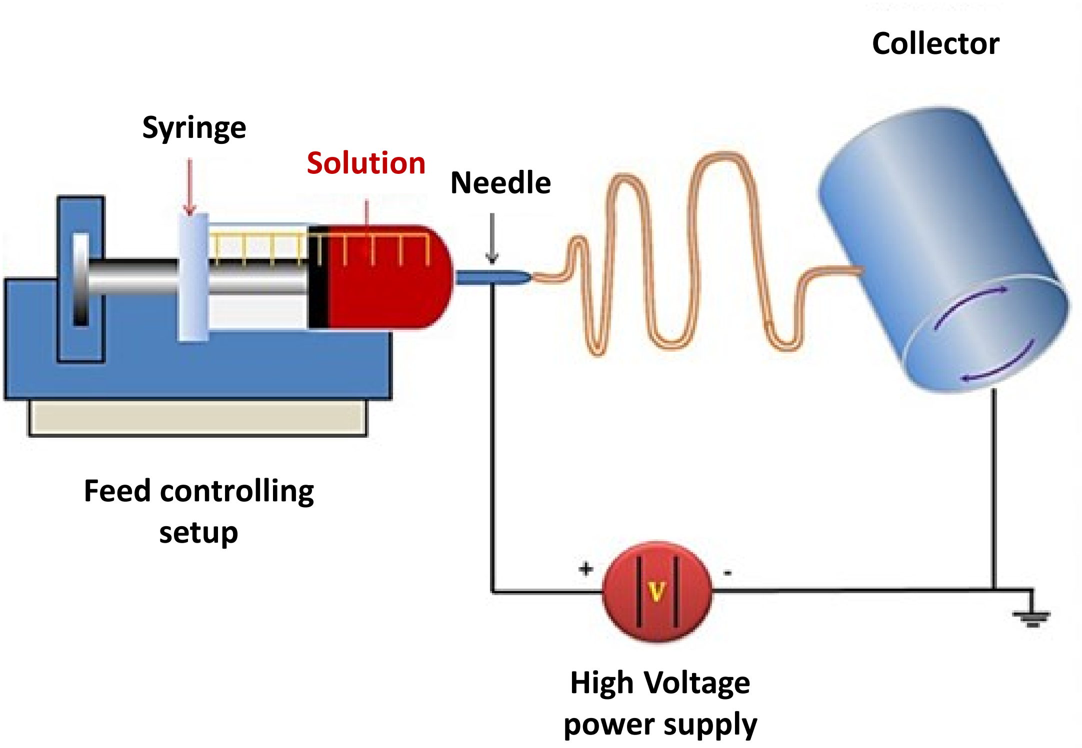

Figure 1-13 – Electrospinning working scheme[78]

The electrospinning apparatus I composed by the following components [82]:

- High voltage generator connected to the needles (electrode) that lead to polymeric solution charging
- Pumping system composed by one or more syringes filled with the polymer solution. Each syringe is provided with a needle connected the high voltage generator.
- Metal collector connected to ground. It may come in different shapes such as plate or rotating drum.

The nanofiber morphology can be influenced by different parameters concerning the solution, process and also environmental condition [82], [83].

The solution parameters that influenced the nanofiber manufacturing are the following:

- *The concentration of polymer* determines nanofiber morphology, diameter and mechanical properties. Low concentration facilitate electrospray instead of electrospinning, resulting in the formation of nano particles. Higher concentration generates a mixture of beads and fibres. Very high concentration promotes helix-shaped micro- ribbons with bigger diameters. In Figure 1-14 the four different nanofibers morphologies corresponding to the four different concentrations reported above are reported.

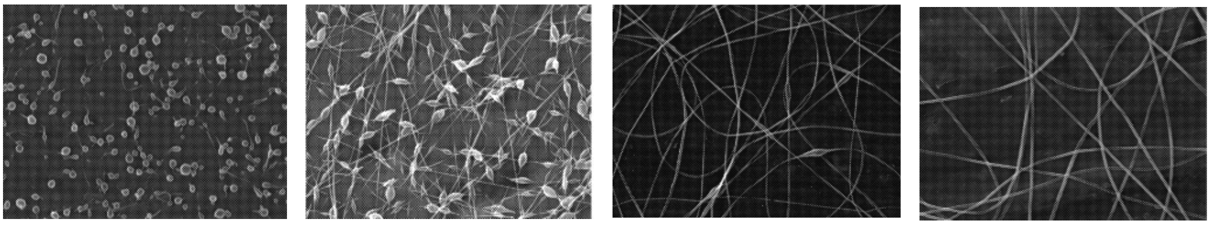

(a) (b) (c) (d)

Figure 1-14 – Nanofibers morphologies with different polymer concentration: (a) very low, (b) low, (c) right and (d) high *[84]*

Obviously, the higher is the polymer concentration, the higher will be the viscosity of the solution.

- *The viscosity* is a critical parameter: too high viscosity hinders the ejection of the solution, too low viscosity results in the formation of beads.
- *The molecular weight* directly influences the viscosity since higher molecular weight leads to higher viscosity. Keeping the concentration of the polymer fixed, a low molecular weight caused beads formation rather than smooth nanofibers.
- *The surface tension* is also an important factor. Keeping the concentration of the polymer fixed, lower surface tension promotes smooth fibres. A way to reduce surface tension is to use a solvent/solvent mixture with a lower surface tension or to use surfactants.
- *The electric conductivity* of the solution acts on the fibre diameter. It decreases with increasing of conductivity. The solution conductivity can be increased by adding ionic salts to the solution.
- *The vapor pressure* can cause problems with solvent evaporation before and during spinning. At the same time, a wrong value of surface tension may influence the formation of non-cylindrical morphologies.

The process parameters that influenced the nanofiber manufacturing are the following:

- *The voltage* applied influenced the final diameter of fibers. Higher values lead to smaller diameters.
- *The distance* between the collector and needle tip affects the solvent evaporation: if the distance is too small the evaporation does not fully occur; if it is too big, beads are produced.

- *The flow rate* determines the speed of the ejection of the solution. Lower flow rate promotes a better degree of polarization of the solution; too low rate results in non-constant jet and then a stop in the development of Taylor cone. When the flow rate is too high a pulsing jet is ejected and bead fibres are deposited.

The environmental parameters that influenced the nanofiber manufacturing are the following:

- *The temperature* affects the viscosity of the solution; higher temperature reduces the viscosity and smaller fibre diameters are obtained.
- *The humidity* must be always controlled. In principle, the degree of humidity must be kept low in order to facilitate solvent evaporation. Higher humidity level results in thicker diameter and causes problems to the solvent evaporation.

1.9 CARBON NANOTUBES

Carbon nanotubes (CNTs) are cylindrical particles that consist of rolled-up sheets of single-layer carbon atoms (i.e., graphene). They can be single walled (SWCNT) with a diameter of less than 1 nanometre (nm) or multiwalled (MWCNT), with several concentrically interlinked nanotubes, with diameters reaching more than 100 nm. Their length can reach several micrometres or even millimetres, therefore, they are also known as 1D-nanomaterials. CNTs are chemically bonded with sp^2 hybridisation and tend to rope together via van der Waals forces, resulting in ultra-high strength, low-weight materials with highly conductive electrical and thermal properties. All these characteristics makes CNTs very attractive for numerous applications, such as adhesive bonding.

Takeda et Narita investigated the Mode I fracture behavior of bonded Carbon Fiber Reinforced Polymer (CFRP) joints with MWCNT/ epoxy adhesive layer. They found that with a nanotube content of 0.32 wt%, the fracture toughness increased by 12%, and was comparable to the neat epoxy adhesive joints when 0.65 wt% MCWNT was added to the resin. However, the fracture toughness of the system decreased with a concentration of 1.3 wt% of MWCNTs. Furthermore, the electrical resistance behavior of the MCWNT/epoxy adhesive correlated well with the crack propagation, regardless of the fracture mechanisms (cohesive and interfacial fracture). The resin conductivity increased due to tunneling conductive networks in the adhesive layer [16].

Gude et al. analyzed the effect of CNTs on mode-I adhesive fracture energy (G_{IC}) of DCB joints and found an increment of 23.5% when 0.25 wt% CNTs are added. The toughening micro mechanisms observed in the fracture surfaces are fibrillation, pull-out and crack bridging [61].

Korayem et al. realized double strap joints with two steel plates joined by CFRP laminates using epoxy adhesive reinforced with 3 wt% of CNTs. The ultimate axial strain along the CFRP laminates was greater for the nano reinforced joints, indicating that CNT-epoxy could transfer more load than pure epoxy from the steel substrate to the CFRP laminates [62].

The work of Khoramishad and Zarifpour investigated the effect of adding aligned (in the thickness direction) and randomly dispersed MWCNTs on the mechanical behavior of adhesive joints under mode-I loading. The MWCTs became aligned when exposed to an external electric field. The addition of 0.3 wt% randomly dispersed MWCNTs improved the joint strength by about 55%. The same concentration of aligned MWCNTs caused a maximum improvement of 88%. The mode-I fracture energy of joints reinforced with randomly dispersed and aligned MWCNTs was improved by 135% and 160%, respectively. The SEM fractography revealed that the aligned MWCNTs could contribute more to the joint load bearing compared to the randomly dispersed MWCNTs because they promote the fracture mechanisms of nanotube pull-out and crack bridging [85].

Wernik and Meguid evaluated an improvement of 36% of the mode-I fracture toughness for epoxy reinforced with 1 wt%. However, increasing the amount of CNT decreased the fracture toughness due to poor deagglomeration [86].

Han et al. evaluated the CNT-bridging across Al/CFRP thin adhesive joints. They developed a resin precoating, sprayed on adherends, that filled all microcavities over both substrate surfaces, pulling inside it the CNTs. Two aluminum chemical treatments were also used to pre-treat the substrates, resulting in two different roughness profile. The effectiveness of CNT-bridging was related to the surface profiles of both Al and CFRP substrates. The CNT addition improved the bonding strength of 13% and 20% trough interfacial toughening [87].

Srivastava et al. investigated the fracture toughness in mode I, mode II and shear strength of single lap carbon fiber composites joint. The adhesive used was an epoxy system reinforced with 2 wt% of CNTs. The fracture toughness G_{IIC}, G_{IC} under DCB and ENF test was improved by the inclusion of CNT. The resistance to crack growth was higher for nano reinforced samples due to the interference of nanoparticles [88].

Other interesting work were presented by Sánchez-Romate et al. that developed an innovative CNT-doped adhesive film to detect crack propagation exploiting the electrical properties that carbon nanotubes provide to the adhesive. CNTs were dispersed in water in a weight fraction of 0.1 wt% with a surfactant at 0.25 wt. The solution was sprayed over the epoxy adhesive film surface with an airbrush. Mechanical tests assess that mode I and mode II fracture toughness that result slightly improved compared neat resin. The technology was also used to monitor artificial defects realized in skin-stringer sub-elements. Two types of joints were manufactured using co- bonding and secondary bonding. Co-bonding is the process of bonding an uncured part with a cured part, which may involve the use of an adhesive, and then curing them together using the same curing process. Secondary bonding is the process of bonding two already cured parts with an adhesive, which is then cured. Joints made by secondary bonding show a much sharper increase in electrical resistance in the early stages of the test. This is caused by sudden crack propagation along the joint edges. For each type of joint, a load drop corresponds to a sharp increase in electrical resistance, proving the good potential and applicability of this technology for the identification of different types of defects [17], [18], [89]–[92]

Carbon nanotubes were also useful to enhanced mechanical performance in particular, fracture toughness, of composites materials. For instance, Hanif *et al.,* reported that fracture toughness of Twaron Aramid fibers and epoxy composite panels was three times higher than the baseline with the addition of 1 wt% of MWCNTs [93]. The nanotubes could be functionalized to enhance their dispersion inside the polymer matrices and achieve better mechanical properties. For example, a significant increase of 95% in fracture toughness was detected by Cha *et al.* when melamine functionalized-CNTs were used at concentration of 2 wt%, as compared to the neat epoxy resin [94]. Whereas, the same concentration of no-functionalized CNTs produced lower improvement, approximately around 40%, in fracture toughness.

1.9.1 Production

Three main methods are currently available for the production of CNTs: arc discharge, laser ablation of graphite and chemical vapor deposition (CVD) [95]. All three methods require the use of metals (e.g. iron, cobalt and nickel) as catalysts. The first two processes involve graphite combusted electrically or by laser, the CNTs developed in the gas phase are then separated.

The CVD process allows the production of larger quantities of CNTs with easily controllable conditions and at lower cost. The process combines a metal catalyst, such as iron, with reaction gasses that contain carbon, such as hydrogen or carbon monoxide. Carbon nanotubes are formed on the catalyst inside a high-temperature furnace. The CVD process can be purely catalytic or plasma-supported. The catalytic process, in Figure 1-15 requires temperatures up to 1000 °C, while plasma-supported process requires slightly lower temperatures, in the range of 200-500 °C [96].

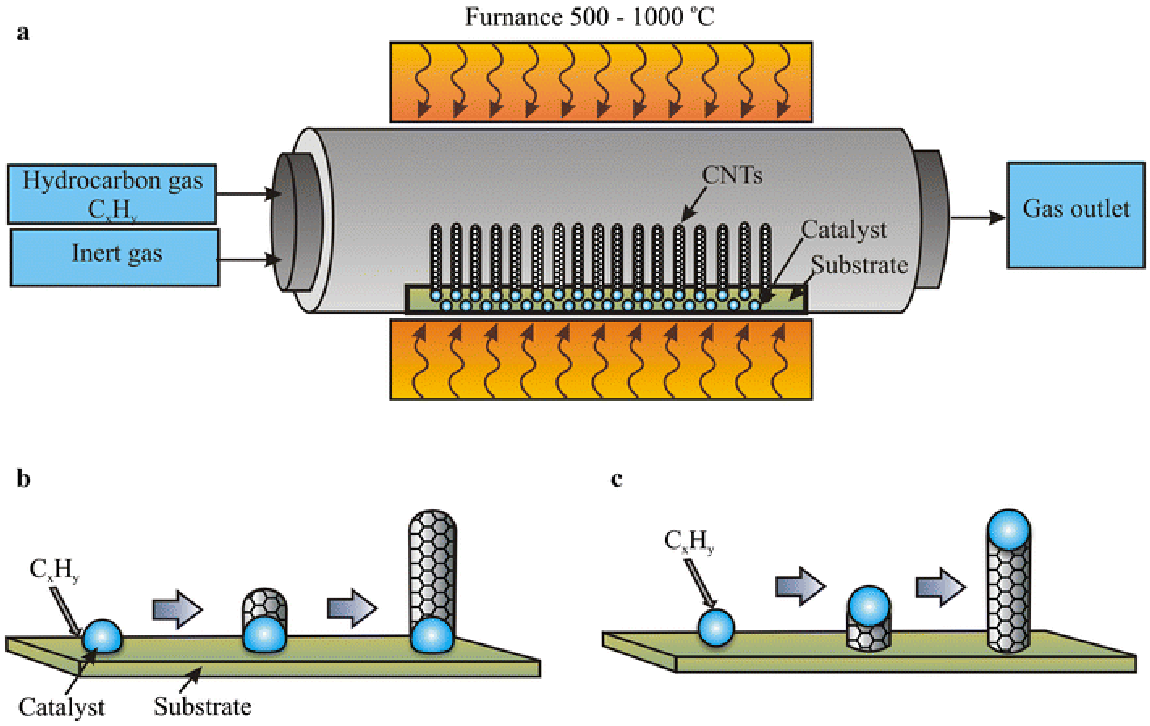

Figure 1-15 – Scheme of catalytic chemical vapor deposition (CVD) process: (a) CVD reactor, (b) base-growth model of CNT, c tip-growth model of CNT [97]

Although recent technological developments have improved the synthetic techniques to obtain carbon nanotubes of high purity, the formation of impurities such as metal encapsulated nanoparticles, metal particles in the tip of a carbon nanotube and amorphous carbon is inevitable, because the metal nanoparticles are essential for the nanotube growth [98].

These foreign nanoparticles and structural defects that occurred during synthesis modify the physical-chemical properties of the carbon nanotubes. Carbon nanotubes need to be purified and various methods can be used such as acid treatment or ultrasound, after the production process.

1.9.2 Properties

Carbon nanotubes have unique electrical, thermal and mechanical properties that can be exploited in the development of new materials.

Their Young's modulus is approximately 180 TPa, their tensile strength is 400 times that of steel, their aspect ratio is greater than 1000, their density is one-sixth that of steel, and their thermal conductivity is higher than diamond. At low temperatures, carbon nanotubes have exhibited a range of intriguing mesoscopic phenomena, such as single-electron charging, resonant tunneling through discrete energy levels, and proximity-induced superconductivity. At relatively high temperatures, tunneling conductance into the nanotubes displays power-law suppression as a function of temperature and bias voltage [99]. Carbon nanotube are highly chemically stable and can virtually resist any chemical impact unless they are simultaneously exposed to high temperatures and oxygen, resulting extremely resistant to corrosion. Their hollow structure can be filled with different nanomaterials, separating and shielding them from the surrounding environment. This property is extremely useful for nanomedicine applications like drug delivery.

The graphene layers rolling-up direction or chiral vector, reported in Figure 1-16 defines the electrical properties of the nanotubes. Different types of nanotubes can be defended, depending on their chiral vector: armchair, zigzag, and chiral nanotubes, reported in Figure 1-17. The chiral vector $\overrightarrow{C_h}$ is expressed by two-unit vectors $\overrightarrow{a_1}$ and $\overrightarrow{a_2}$ according to the equation:

1.26

$$\overrightarrow{C_h} = n\,\overrightarrow{a_1} + m\,\overrightarrow{a_2}$$

The vector $\overrightarrow{a_1}$ and $\overrightarrow{a_2}$ are the basis vectors of the honeycomb lattice. The angle θ is the one that $\overrightarrow{C_h}$ forms with respect to the direction of the zigzag unit vector of the honeycomb lattice (n,0). Chiral vector and angle are represented in Figure 1-16. For the armchair configuration, n and m have the same value; for m=0, a zigzag tube is formed; all other combinations are called chiral nanotubes. The higher the values of n and/or m are, the larger is the diameter of the nanotube. The height or length of the nanotube is defined by the quantity of unit cells stacked together, considering that a unit cell is the basic element of the structure [100].

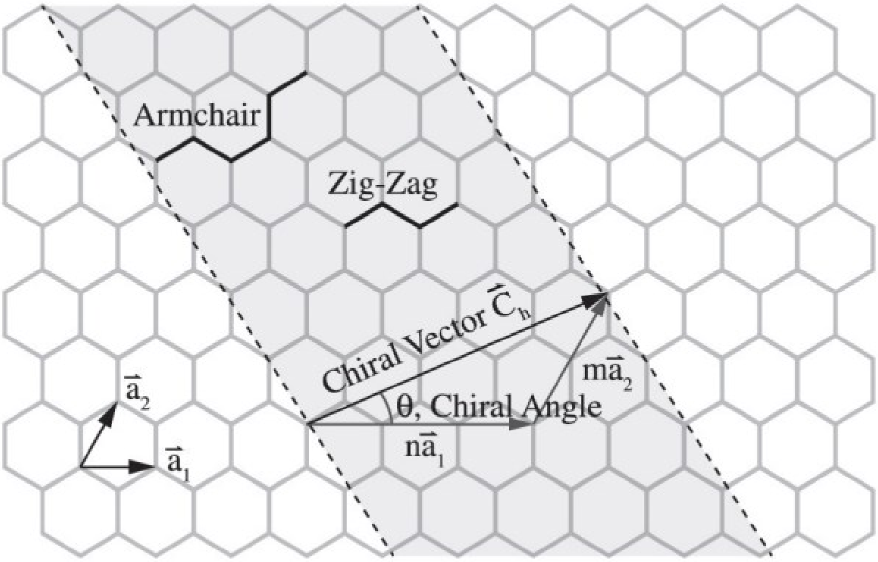

Figure 1-16 - Schematic representation of rolling graphene layer to create CNT [96]

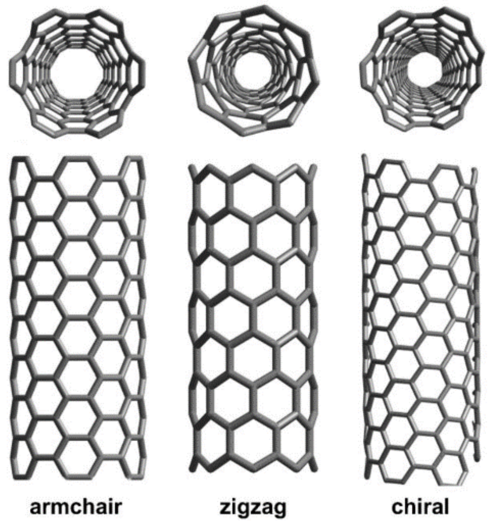

Figure 1-17 – Different type of CNT [102]

The conductivity of SWCNT is strictly related to their chiral vector and angle. Armchair having armchair-like shaped edges are highly desired for their conductivity, zigzag nanotubes behave like semiconductors. MWCNTs exhibit always high conductivity, similar to metals

Thanks to their characteristic, carbon nanotubes are ideal for several applications, like electronic devices, chemical/electrochemical and biosensors, transistors, electron field emitters, lithium-ion batteries, white light sources, hydrogen storage cells, cathode ray tubes (CRTs), electrostatic discharge (ESD) and electrical-shielding.

Actually, CNT powders are broadly used as additives. Powdered CNTs are in a highly entangled and agglomerated form. Therefore, to fully exploit the properties of nanotubes, they must be untangled and uniformly distributed in the matrix. Another important aspect is the coupling between nanotubes and matrix, which can be facilitated by custom functionalizing the nanotube surface. Carbon nanotubes can also be spun into fibers, which can be used to manufacture special fabrics.

1.10 GRAPHENE

Graphene consists of a single layer of sp^2 carbon atoms bonded the three neighbouring carbon atoms in a repeating hexagonal pattern. The unhybridized p^z orbitals overlap, forming π bonds in which free electrons are delocalized. This confers extraordinary electrical properties to graphene [103]. Monolayers of graphene stacked on top of each other form graphite. Graphite consists of multiple layers of graphene held together by van der Waals bonds, as shown in Figure 1-18, which can be broken during the exfoliation process. The structure of graphene dates back to the 19th century, however, only in 2004 Andre Geim and Konstantin Novoselov, two physicists from the

University of Manchester, were able to separate the graphene layers by using with a simple adhesive tape. For their discovery, the scientists received the Nobel Prize in 2010. Graphene is 0.34 nm thick and extends in the plane, so it is considered a two-dimensional material. Graphene oxide (GO, oxidized form of graphene), MXene, hexagonal boron nitride (h-BN) and molybdenum disulfide (MoS_2) are some common examples of 2D nanomaterials [104]. Carbon-based nanomaterials, such as graphene and graphene derivatives have been intensively explored to enhance the strength and fracture toughness of polymer and composites materials. due to their planer geometry.

Khoramishad et al. used graphene oxide nanoplatelets (GOPs), characterized by a thickness range of 4-7 nm and diameter range of 10-15 μm, to modify an epoxy adhesive with 0.1, 0.3, and 0.5 wt% of nonreinforcement. The modified adhesive was used to bond aluminium DCB specimens for the evaluation of mode I fracture energy. The fracture energy is improved of 69% with 0.3 wt% of GOPs, concentration of 0.5 wt% of GOPs caused a fracture energy reduction due to nano-fillers agglomerations. Two toughening mechanisms identified with SEM micrographs are crack deviation when it collides with GOPs and the debonding of GOPs from the adhesive, considered two toughening mechanisms [105].

Srivastava et al. investigated the fracture toughness in mode I, mode II and shear strength of single lap carbon fiber composites joint. The adhesive used was an epoxy system reinforced with 2 wt% of GNPs. The mode I and mode II fracture toughness, under DCB and ENF test, were improved by the inclusion of GNP. The resistance to crack growth was higher for nano reinforced samples due to the interference of nanoparticles [88].

The shear strength of TAST steel joints bonded with epoxy adhesive loaded with various amounts of graphene, increases as the nanoparticle content increases. The addition of 0.75 wt% graphene increased the shear strength of 102% compared with neat epoxy adhesive. In addition to shear strength, shear modulus, shear strain at failure and toughness also increased, which demonstrated the effectiveness of graphene on improving shear properties of epoxy adhesive [106].

Jojibabu et al. studied the effect of different carbon nanofillers on the lap shear strength of epoxy. They found an improvement of 49% in lap shear strength compared to neat epoxy adhesive joints, when 0.5 wt% GNP were added. SEM results showed that relatively low weight fractions nano-fillers lead to uniform dispersion without any agglomerates that results in cohesive failures. At higher fractions of carbon nano-fillers a mixed mode (cohesive and adhesive) failure was observed reducing the lap shear strength even below that of virgin joint [107].

Jia et al. produced nanomodified adhesives containing three different graphene contents: 0.25 wt%, 0.5 wt% and 0.75 wt%. All three nanocomposites showed higher peak load and maximum displacement than the neat epoxy adhesive, but this improvement is not linearly dependent on GNP content. The nanocomposites containing 0.25 wt% GNP has the highest peak load, maximum displacement, and mode I fracture toughness. The nanocomposite with graphene content of 0.25 wt% shows almost 5 times increase in mode I fracture toughness compared with the neat epoxy. However, increasing the graphene content decreased the mode I fracture toughness due to the aggregation of GNPs in the epoxy adhesive, especially in DCB specimens with a GNP content of 0.5 wt% [108].

Aradhana et al. used graphene oxide (GO) and reduced graphene oxide (rGO) synthesized from graphite powder as fillers for epoxy resin to prepare epoxy-based nanocomposite adhesives. The presence of oxygen functionalities in GO and removal of some functional groups in rGO was confirmed by FTIR and XRD. The mechanical properties of GO -modified adhesive are superior than rGO -modified systems due to the higher number of oxygen functional groups in GO that promote the reaction between epoxy and curing agent [109].

The influence of graphene on the fracture toughness of composite materials was investigated in several works. Lokasani et al., studied the mode-I fracture toughness of epoxy reinforce with carbon fiber and GO. An improvement of 53% was detected, compared to the neat samples [110].

The optimal compatibility between filler and matrix and suitable dispersion parameters lead to enhance the mode-I fracture toughness from 28 to 111% with the addition of 1 wt % of GO into epoxy matrix [111]. Bhasin et al. assessed that mode-I fracture toughness improved by 103% for composite modified with 0.5 wt.% of GNPs [112]. Galpaya et al. revealed that mode-I fracture toughness of carbon fiber reinforced composite was increased by approximately 50% with the addition of 0.1 wt. % GO to the epoxy [113]. Domun et al., founded that the fracture toughness of epoxy modified with 0.25 wt% of plasma functionalized graphene nanoplatelets is enhanced more than 50% compared to the neat epoxy [114].

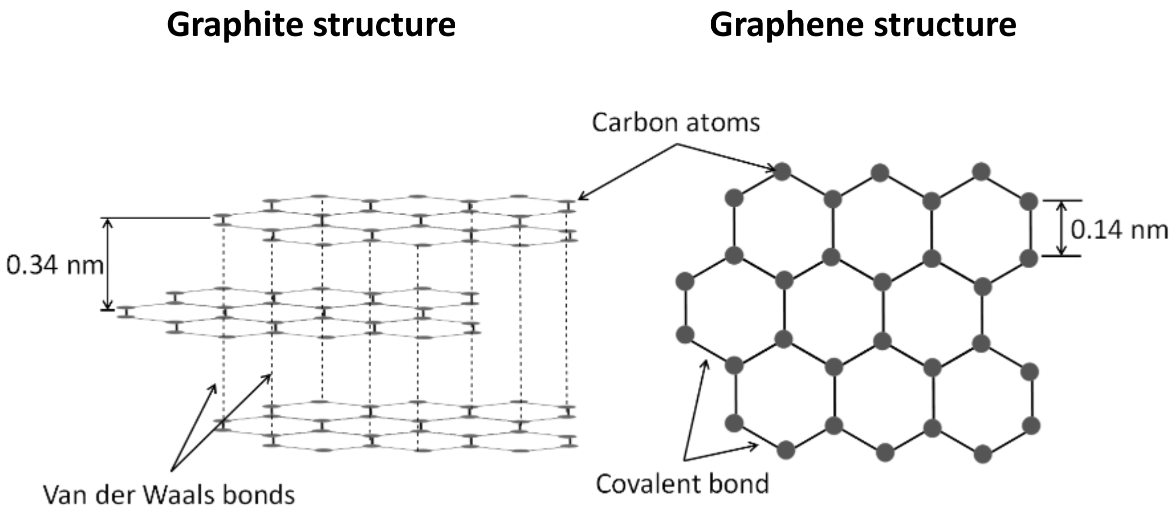

Graphite structure

Graphene structure

Figure 1-18 – Chemical structure of graphite and single layer graphene

1.10.1 Production

Several methods were developed for graphene production, such as epitaxial growth on SiC, chemical vapor deposition (CVD) on different metal substrates, and unzipping of carbon nanotube [103].

The CVD and epitaxial growth are bottom-up approach: each graphene sheet grows from carbon bearing precursors such as methane gas or SiC. These methods lead to the production of high-quality graphene; however, they work at elevated temperatures, are complicated and expensive process that need sophisticated setup and have moderate scalability.

Alternative methods can be applied to produce graphene with medium quality and lower electrical and thermal conductivities. These large-scale process leads to produce graphene with lower cost and suitable for polymer modification. Such methods adopt top-down approach starting from graphite.

The graphite is composed by graphene layers held together by weak van der Waals, that can be broken by mechanical, electrical and chemical actions [115]. The resulting final product contains individual graphene layers or graphite with reduced number of graphene layers (or multilayer graphene).

For example, liquid phase exfoliation and reduction of GO are two most prominent methods with scale up potential, that produce mixture of mono, bi, few and multi-layer graphene. International Organization for Standardization (ISO/TS 80004-13:2017) classifies graphene as follows [116]:

- Monolayer graphene or single layer graphene (SLG): single layer of carbon atoms
- Bilayer graphene (BLG): two well-defined stacked graphene layers

- Few-layer graphene (FLG): 3–10 well-defined stacked graphene layers
- Multilayer graphene (MLG) or graphene nanoplatelets (GNPs): graphene with thickness more than 3 nm (i.e., >10 layers)

Liquid phase exfoliation (LPE) used ultrasound to generate liquid cavitation and thus strong hydrodynamic shear-force that breaks basal structure of graphite. The separated graphene sheets form stable colloidal if the solvent surface energy is comparable to that of graphene. Expensive and often noxious solvent were initially used such as Dimethylformamide (DMF), N-methyl pyrrolidone (NMP), pyridine and other perfluorinated and o-dichlorobenzene [117]. Actually ethanol, iso-propanol, other simple alchools or water are successfully used together with stabilizing agent to prepare graphene [118], [119]. The final product of LPE process is quite heterogeneous and consist of a mixture of SLG, FLG and MLG where only 1-20% is pure SLG and the remaining proportion is largely MLG with more than 10 graphene layers. Further centrifugation helps to increase the production of SLG, but the process becomes less productive and more expensive. The LPE is used for MLG or GNPs production with defect free graphene layers. Prolonged sonication cycles can dissociate the solvent molecules and form peroxyl radicals that can attack the graphene carbon bonds and reduce lateral size of the separated sheets [120].

The reduction of GO is another technique used to produce graphene. Natural graphite is oxidized with strong acid and oxidant agent like epoxy, hydroxyl and carboxyl groups. The oxidation is followed by exfoliation in water and solvent under the action of ultrasound. The oxidized exfoliate graphene is reduced to remove the oxygenated functional group. Chemical oxidation of natural graphite was first introduced by Brodie in 1859 by adding potassium chlorate ($KClO_3$) to graphite slurry in fuming HNO_3. Staudenmaier later replaced two-thirds of fuming HNO3 with concentrated $H2SO_4$ and gradually introduced $KClO_3$ [121]. In the mid-20th century, Hummer and Offeman proposed an alternative method with $NaNO_3$, $KMnO_4$ and concentrated H_2SO_4 as oxidants, as shown in Figure 1-19. The oxidation reaction produces pale yellow GO products in contrast to black graphite. This method, while rapid, has a low yield, emits toxic gases (NO_2, $N2O_4$) and residual nitrate. Several approaches using Hummer's modified method have been published to produce oxidized graphite. The main purpose is to introduce nontoxic and more sustainable substances than $NaNO_3$ and $H2SO_4$. Depending on the chemicals used, the reaction conditions and the graphite precursor, a carbon-oxygen (C/O) ratio up to 2:1 can be achieved.

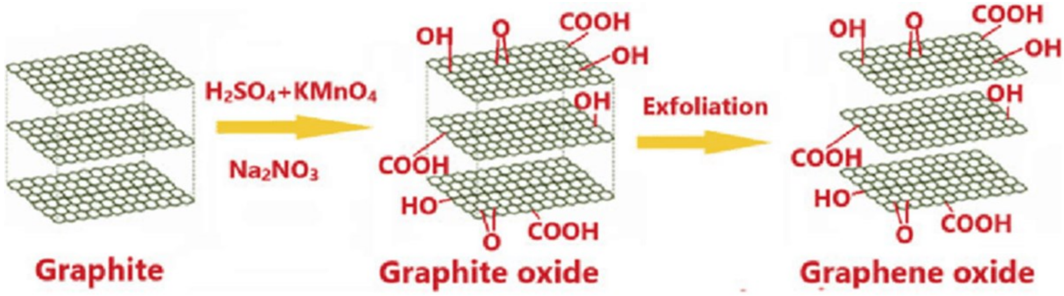

Figure 1-19 – Hummers' method representation for GO production and [122]

The oxidized graphite behaves as hydrophilic material because of oxygen moieties distributed all over the surface, therefore it can be dispersed in water and solvents, such as ethanol an iso-propanol. Ultrasound are used to promote the separation of GO in single layer, bi-layer and few-layer. Hydroxyl groups on the surface of oxidized graphene increase compatibility with polymer matrices, while electrical and thermal properties are reduced, probably because free electrons are engaged with oxygen functional groups [123]. The reduction process can be thermal, chemical, electrochemical and hydrothermal. Nanoparticles of rGO can reach a maximum C/O ratio between 25:1 and 29.9:1 indicating that some residues are present. Residues of oxygenated groups can be used to further functionalize rGOs. Initially, the GO production was considered as an intermediate step for the production of single and multilayer graphene films and bulk graphene structures. Over time, GO found several applications such as membranes, coatings, sensors, photo catalysis, and solar cells [123].

Flash Joule Heating is another process recently applied to produce graphene. The process employs an electrical charge to heat the feeding material at temperature higher than 3000 K. In 2020, it was used to synthesize gram-scale quantities of graphene from a carbon black, coal, petroleum coke, waste foods, and plastics. This method allows waste plastic to be directly transformed into graphene, without passing through intermediate steps and without using furnaces or inefficient heat transfers.

1.10.2 Properties

Graphene's electronic structure gives it unique properties such as electron mobility 100 times faster than silicon, high thermal conductivity twice that of diamond, and reduced electrical resistance 13 times lower than that of copper. The single layer of graphene is transparent and absorbs only 2.3% of reflective light, is impermeable to any gas or moisture, and has a surface area of 2,630 m^2/g. The surface of graphene can be functionalized with different chemical groups such as halogens, hydrogen, and groups containing oxygen, sulfur, nitrogen, phosphorus, boron, and several other elements [123]. Oxidized graphene has the carbon layers separated by functional groups, attached to each layer of carbon atoms. This material has significantly higher chemical activity and compatibility with polymer matrices, but the electrical and thermal conductivity are much lower than unoxidized graphene.

The high mechanical properties of graphene such as stiffness, strength and toughness are due to the stability of the sp^2 bonds that form the hexagonal lattice and resist a variety of in-plane deformations. Defect-free monolayer graphene is considered the strongest material ever tested, with an intrinsic strength of 130 GPa. Fracture toughness and was measured as a critical stress intensity factor of 4.0 ±0.6 MPa and critical strain energy release rate (G_C) of 15.9 J/m^2 [124].

2 COMPOSITE MATERIALS

Composite materials are created by combining two or more components with dissimilar molecular structures that can be physically separated. These components interact in bulk form, resulting in properties that are superior to those of the individual components. Generally, composite materials are formed by reinforcing fibers in a matrix. The reinforcements can be fibers, particulates, or whiskers made from polymers, ceramics, or metals, and can be continuous, long, or short. The matrix materials can be also metals, plastics, or ceramics. Polymer-based composites are now commonplace in many industries. The reinforcing fibers or fabrics give the composite strength and stiffness, while the matrix, thermoset or thermoplastic, provides rigidity and protection from the environment. Reinforcing fibers come in various forms, from long continuous fibers to woven fabric to short chopped fibers and mat. The properties of the composite depend on how the fibers are arranged. Long continuous fibers are best for structural applications, while short fibers are more suitable for nonstructural applications [125]–[127]. A classification of composites based on fiber type is presented in Figure 2-1 .

Depending on the application and manufacturing method, the fiber form is chosen. Injection and compression molding use short fibers, while filament winding, pultrusion, and roll wrapping use continuous fibers. The properties of the composite are significantly higher when long continuous fibers are used in the direction of the load. Chopped fibers, however, yield lower properties than continuous fibers [125]–[127].

Composite materials have become increasingly popular, moreover in the transportation industry, due to their high stiffness and strength-to-weight ratio, allowing for the design of lighter and more efficient vehicles. Advances in technology have created a need for new materials and associated manufacturing techniques, and composites have been able to provide specific solutions for each application. The cost of fiber has decreased, and automation and high-volume production methods have been developed, leading to a vast expansion in the use of composites across various industries, including aerospace, automotive, construction, marine, corrosion resistant equipment, consumer products, appliance/business equipment, and more [125]–[127].

The aerospace industry was one of the first to recognize the advantages of composite materials, which have enabled airplanes, rockets, and missiles to fly higher, faster, and farther. Carbon fiber composites are the most commonly used in the aerospace industry due to their superior performance characteristics. The prepreg lay-up, RTM, and filament winding are all used to manufacture aerospace parts. Composite materials are also favored in the automotive industry for their cost-effectiveness, attractive appearance, and excellent performance. From sports cars to passenger cars to trucks, composite body panels have proven to be successful in all categories. Additionally, carbon epoxy composite laminates can be designed to have a zero coefficient of thermal expansion, making them ideal for spacecraft applications [125]–[127].

2.1 COMPOSITE NOTATION

A concise way to represent the parameters of a laminate is through stacking-sequence terminology. This includes listing the layers and their orientations for regular laminates (equal-thickness layers), for example [0°/90°/45°], and adding layer thicknesses for irregular laminates, such as $[0^\circ_{t}/90^\circ_{2t}/45^\circ_{3t}]$ or [0°@t/90°@2t/45°@3t]. For symmetric laminates, a simple notation is used, e.g. [0°/90°/45°/45°/90°/0°] can be $[0^\circ/90^\circ/45^\circ]_{symmetric}$ or $[0^\circ/90^\circ/45^\circ]_{sym}$ or $[0^\circ/90^\circ/45^\circ]_{s}$. For multiple laminae of the same angle, subscripts are used, e.g. [0°/0°/0°/90°/90°] is equal to $[0^\circ_{3}/90^\circ_{2}]$. If sequences of laminae are repeated, these are grouped with a subscript to indicate the number of repetitions, e.g. [0°/90°/45°/0°/90°/45°] can be $[0^\circ/90^\circ/45^\circ]_{2}$. A bar is put over split layers, e.g. $[0^\circ/90^\circ/0^\circ] = [0^\circ/\overline{90}^\circ]_{s}$, and a subscript T is used to indicate complete specification and avoid ambiguity, e.g. $[0^\circ/90^\circ/45^\circ/-45^\circ/0^\circ/90^\circ]_{T}$. This notation is widely used in composite structures practice

2.2 THERMOSET COMPOSITE

Thermoset composites are widely used in commercial applications, accounting for over 75% of all composites. These materials are commonly found in the aerospace, automotive, marine, boat, sporting goods, and consumer industries. The most widely used fiber materials are glass, carbon, aramid, and boron. Carbon fibers range from low to high modulus and low to high strength. Thermoset composites offer a range of advantages, including easy processability, improved fiber impregnation, greater thermal and dimensional stability, higher rigidity, and enhanced electrical, chemical, and solvent resistance. Epoxy is the most commonly used resin material in thermoset composites, and it can be used for prepreg production and at room temperature for processes such as hand lay-up, filament winding, pultrusion, and RTM [125]–[127].

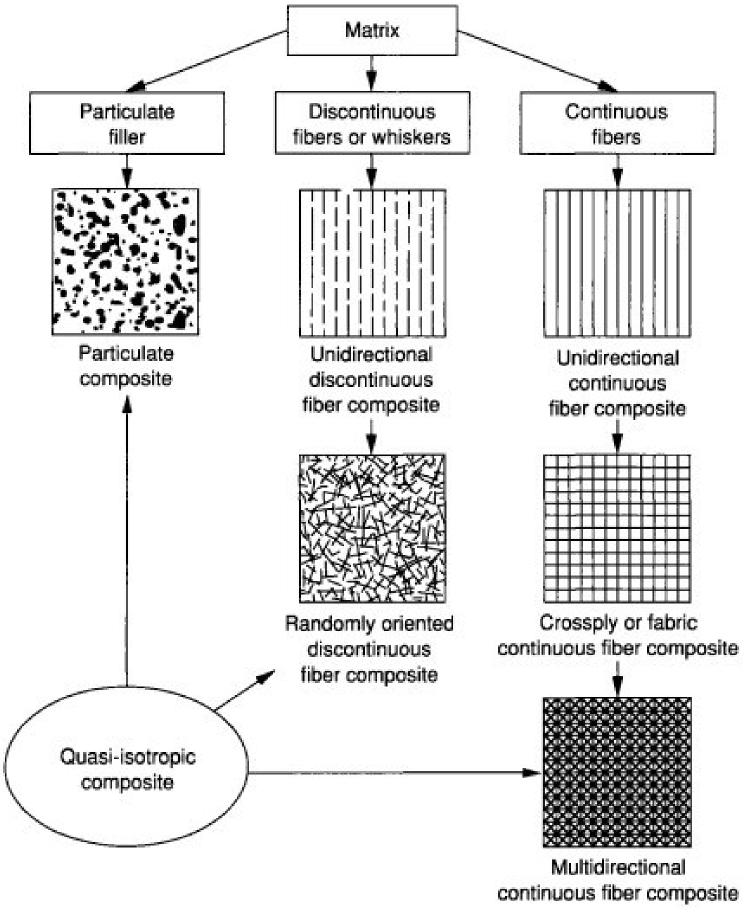

Figure 2-1 – Composites classification [126]

2.2.1 Prepreg

Preimpregnated fibers, fabrics, and mats are commonly referred to as prepregs. These materials are available in various forms, such as unidirectional tape, woven fabric tape, and rovings. Unidirectional tape is used to tailor the composite properties in the desired direction, while woven fabric prepregs are used to make highly contoured parts and sandwich panels. Preimpregnated rovings are primarily used in filament winding applications.

Prepregs offer consistent properties, fiber/resin mix, and complete wet-out, eliminating the need for weighing and mixing resin and catalyst. They also come with varying levels of drape and tack, allowing them to be used for a variety of applications. Drape is the ability of prepreg to conform to a contoured surface, while tack is the stickiness of uncured prepregs, which is necessary for easy laying and processing. Prepregs are used in a variety of applications because they provide faster manufacturing, higher fiber volume fraction than other composite products, as well as more controlled properties and higher stiffness and strength. The main disadvantage of prepregs is their higher cost [125], [127].

Epoxy-based prepregs are the most common type and come in flat sheet form with a thickness range of 0.127 mm to 0.254 mm. Fiber-reinforced epoxy prepregs are manufactured by passing uniformly spaced fibers through a bath of catalyzed epoxy resin dissolved in a solvent to control viscosity (Figure 2-2). The impregnated fibers are then heated in a controlled manner to partially cure the resin and create a tack-free state known as B-staging. The prepreg sheet is then backed up with a release film or waxed paper and wound around a take-up roll. Typically, a prepreg contains 42 wt% of resin. The backup material is removed just before the prepreg is placed in the mold. The shelf life of epoxy prepregs is typically 6-8 days at 23 °C, but can be extended up to 6 months or more if stored at -18 °C [125], [127].

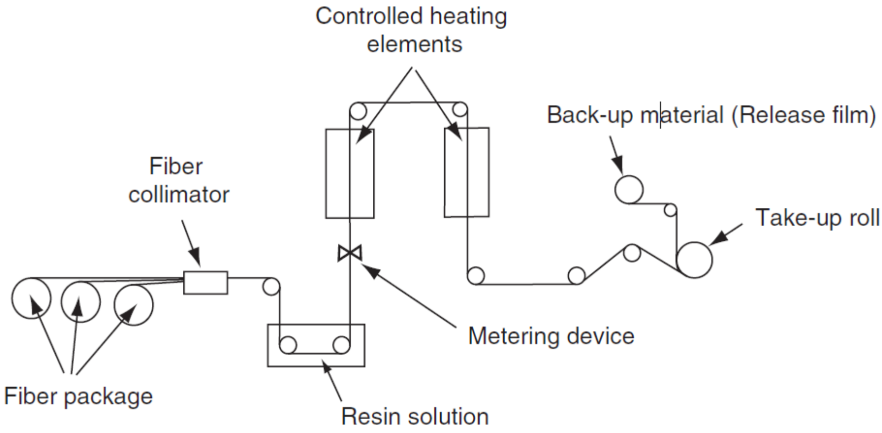

Figure 2-2 – Scheme of thermoset prepreg manufacturing [125]

2.2.2 Composite Production Processes

Composite part fabrication involves four distinct steps: wetting/impregnation, lay-up, consolidation, and solidification. These steps are common to all composite manufacturing processes, though they may be carried out in different ways [127].

1. *Impregnation* step involves mixing fibers and resins to form a lamina. This is done in different ways depending on the process, such as filament winding, hand lay-up, or wet lay-up. The purpose of this step is to ensure that the resin is evenly distributed around all fibers. The viscosity, surface tension, and capillary action of the resin are the main parameters that affect the impregnation process [127].
2. *Lay-up* phase involves forming laminates by placing fiber and resin mixtures or prepregs in the desired orientation and locations. This is done either manually or by machine, depending on the process. The lay-up is important for achieving the desired fiber architecture and performance of the composite structure, as dictated by the design [127].

3. *Consolidation* is a key step in the production of continuous fiber composites, as it ensures that all entrapped air is removed between layers and that the parts have no voids or dry spots. The process involves two components: resin flow through porous media and elastic fiber deformation. Pressure is applied to the component. Initially, it is carried solely by the resin, but as the pressure increases, the fibers go through elastic deformation and the resin flows out towards the boundary [127].
4. The *solidification* process of thermoset and thermoplastic composites requires different approaches. In thermosets, heat is applied to expedite the cure rate of the resin, while in thermoplastics, the temperature is lowered to achieve a rigid part. The rate of solidification depends on the resin formulation and cure kinetics for thermosets, and the cooling rate of the process for thermoplastics. Vacuum or pressure is maintained during this period, and the lower the solidification time, the higher the production rate achievable by the process [127].

The fabrication of thermoset matrix composites, such as epoxy matrix, is outlined below.

The wet lay-up process is a popular fabrication method for composite parts, particularly in the marine and prototype industries. This labor-intensive process involves the application of liquid resin to a mold, followed by the placement of reinforcement material on top. A roller is used to ensure the resin is evenly distributed. This process is repeated until the desired thickness is achieved. The manual placement of the reinforcement material makes this process also known as the hand lay-up process. The wet lay-up process has several advantages, including its flexibility, low capital investment, and ease of use. However, this method is not without its drawbacks, like the potential for styrene emission due to its open-mold nature.

The spray-up process is a more efficient and cost-effective alternative to the wet lay-up process, as it utilizes a spraygun to apply resin and reinforcements to the mold. This method is faster and more economical as it uses rovings and can deliver up to 800 kg of material per hour. The spraygun chops continuous fiber rovings into predetermined lengths of 10 to 40 mm and simultaneously impels it through a resin/catalyst spray onto the mold. This process is a great choice for those looking for a more efficient and cost-effective way to apply fiber and resin materials onto a mold.

Filament winding is a process in which resin-soaked fibers are wound at a specific angle around a rotating mandrel. This technique is used to make tubular parts, pressure vessels, and other specialized structures in a cost-effective and automated manner. Figures 6.29 and 6.30 illustrate the typical filament winding process, in which the carriage unit moves back and forth and the mandrel rotates at a predetermined speed to create the desired fiber angle.

The pultrusion process is a cost-effective, high-volume manufacturing technique that produces parts of a constant cross-section and continuous length. Unlike metal extrusion, which involves pushing material through a die, pultrusion involves pulling resin-impregnated fibers through a heated die. The process is simple, low-cost, continuous, and automated, and the parts produced require little or no post-processing.

The *resin transfer molding* (RTM) process, also known as liquid transfer molding, is a method of producing structural parts in medium-volume quantities using low-cost tooling. It is a closed mold operation in which a dry fiber preform is placed inside a mold and then a pre-catalyzed thermosetting resin is injected through an inlet port until the mold is filled. After curing, the part is then removed from the mold. This process offers near-net-shape complex parts with controlled fiber directions and good surface finish on both sides of the part. However, the main issues in the RTM process are resin flow, curing, and heat transfer in porous media.

Compression molding is an advantageous process for the automotive industry due to its ability to produce large volumes of parts and cost savings. Sheet molding compounds (SMCs) and bulk molding compounds (BMCs) are the most commonly utilized raw materials. SMC is a sheet product composed of a mixture of liquid resin, fillers, and fibers. Additionally, prepregs and core materials are used to make structural panels. This single-step process requires minimal equipment and molds. Compression molding of SMC offers numerous advantages, such as the ability to create complex geometries with ribs and bosses, increased stiffness due to short ribs, and the ability to incorporate up to 30% fiber content for improved strength. The process involves the placement of a predetermined quantity of SMC onto the bottom half of a preheated mold cavity, followed by the application of pressure and heat until the material flows and fills the cavity, expelling any entrapped air. The molding pressure and temperature are varied depending on the part complexity and fiber content, and the part is removed once the material has cured.

Another important process is the *prepreg lay-up*, described in the following section.

2.2.2.1 *Prepreg lay-up*

The prepreg lay-up process, also called autoclave processing or vacuum bagging process, is a popular method used in the aerospace industry to create complex shapes with high fiber volume fractions. It is an open molding process with low-volume capability, which involves cutting prepregs and laying them down in the desired fiber orientation on a tool, followed by vacuum bagging. The composite with the mold is then placed in an oven or autoclave and heated and pressurized to cure and consolidate the part. Carbon/epoxy prepregs are the most popular choice for the prepreg lay-up process due to their lightweight and strong properties, which provide greater mass savings in the component.

Tools for the prepreg lay-up process are typically made from machined metals, woods, plastics, and composite materials. Steel is also a common material for tooling. A wide variety of prepregs with room-temperature, intermediate-, and high-temperature cure are available for use in the mold.

To make a composite part, prepreg material must be removed from the refrigerator and brought to room temperature. The prepreg should be thawed in its original package to avoid condensation, then cut to the desired length and shape. For aerospace applications, this process must take place in a clean, dust-free environment with controlled humidity and temperature.

Automated cutting machines are used to cut prepregs into desired patterns for production parts of decent quantity. These machines are computer-controlled and use software to optimize ply cutting, minimize scrap, and ensure repeatability and consistency. They can cut multiple layers of prepregs at once, and predominantly unidirectional fiber prepregs are used for part fabrication. Prepregs made of fabrics may also be used. The plies are cut to provide the desired fiber orientation, and release agent is applied to the mold for easy removal of the part.

The backing film is first removed from the prepreg and then laid down according to the instructions of the manufacturing chart. Vacuum bagging preparations are then made in order to cure and consolidate the part. Once the layup is finished, a porous release cloth and several layers of bleeder papers are laid on top of the prepreg stack. These bleeder papers are used to absorb any excess resin that may flow out during the molding process. The layup is then covered with a Teflon-coated glass fabric separator, a caul plate, and a thin heat-resistant vacuum bag, which is sealed around its edges with a sealant.

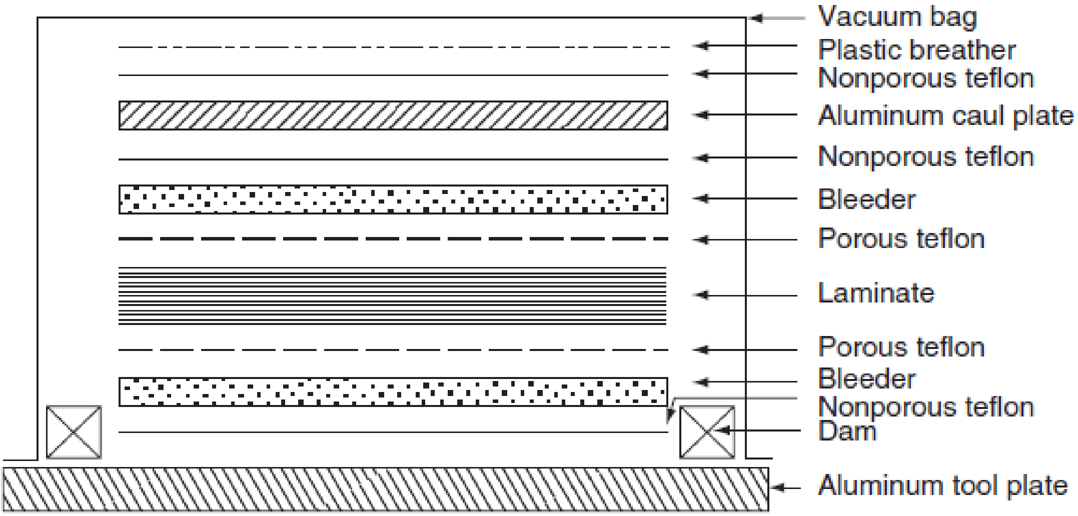

Figure 2-3 – Vacuum bag scheme [125]

The application of peel ply fabrics on top of prepreg layers is necessary when consolidated parts are to be adhesively bonded. This creates a bondable surface on the fabricated part, eliminating the need for extra processing steps. After the part is cured, the vacuum bag is removed and the peel ply taken off, leaving behind a clean bondable surface. The mold is placed in an autoclave to cure and consolidate the composite. This pressure vessel is able to maintain the desired temperature and pressure for the processing of the part. The cure cycle is dependent on the type of resin, the thickness, and the geometry of the component. To create the necessary pressure, the vacuum bag is connected to a vacuum pump and pressurized air or nitrogen is injected into the autoclave. This combination of external pressure and vacuum inside the bag creates sufficient pressure to compact the laminate against the mold and ensure intimate contact between each layer.

The curing process of composites is achieved by heating the air or nitrogen supplied to the autoclave and using cartridge heaters inside the chamber. A computer-controlled system outside the autoclave is used to regulate the temperature and pressure according to the pre-set cure profile.

The cure cycle for a carbon fiber-epoxy prepreg begins with a controlled increase in temperature to 130 °C. At this point, the resin viscosity reaches its minimum. The cycle is then completed by dwelling at this temperature for approximately 60 minutes, during which time the curing reaction proceeds to completion. Figure 2-4 illustrates this process.

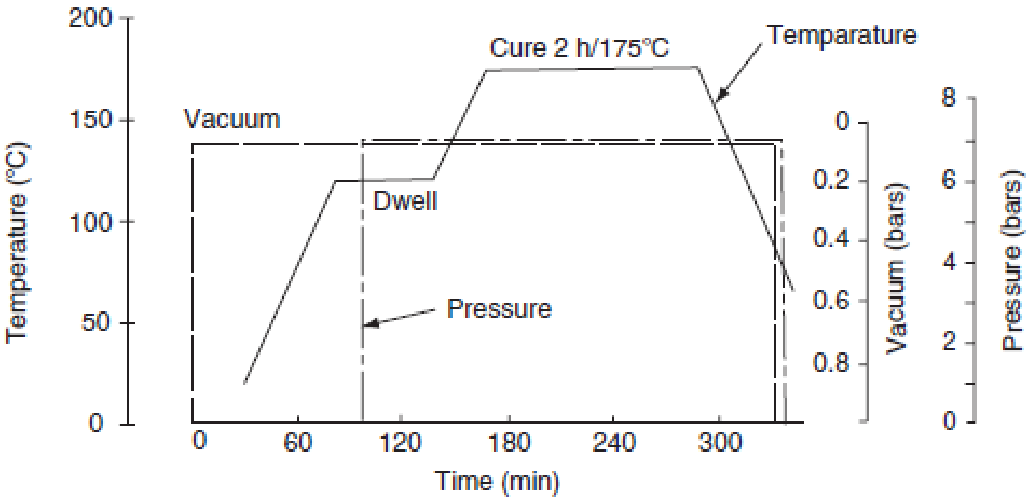

Figure 2-4 – Example of two-stage cure cycle for a carbon fiber–epoxy prepreg [125]

During this period of elevated temperature, an external pressure is applied to the prepreg stack, causing the excess resin to flow out into the bleeder papers. This resin flow is essential for the removal of entrapped air and volatiles from the prepreg, thus reducing the void content in the cured laminate. After the temperature dwell, the autoclave temperature is increased to the curing temperature for the resin and maintained for two hours or more until the desired level of cure is achieved. The temperature is then slowly decreased while the laminate is still under pressure. Once the laminate is removed from the vacuum bag, it may be post-cured in an air-circulating oven at an elevated temperature, if necessary.

The importance of resin flow in reducing void content in cured laminates produced through bag-molding is significant. Face bleeding, as opposed to edge bleeding allows for a shorter resin-flow path in the thickness direction. This shorter path makes it easier to remove entrapped air and volatiles from the center of the laminate.

2.2.3 Composite Bonding

Advanced composite materials are used in even more structural applications and, in particular, for the transportation industry because their high stiffens and strength-to-weight ratio enable the design of light to add more efficient vehicles. The development of composite materials triggers the improvement of structural adhesive to join complex and multi-material structures, providing high joint strength and uniform stress distribution [21]. This technique has begun to enhance or replace the more traditional mechanical fastening, also because the adhesive bonding allows joint reparability without further damage to the structures [128]–[130]. However, composite adhesive bonding subjected to high peel loads tends to fail by delamination because the stress act along composite transverse and unreinforced direction [131]. Therefore, new adhesive materials and bonding techniques are strategic to reduce delamination risk and improve the reliability of adhesive structures. In general, the methods to prevent or delay delamination are focused on joint geometrical parameters to reduce undesirable stress, joining materials selection and modification, obtaining suitable mechanical properties, and integration of additional materials on the composite adherends. Adhesive stiffness is an important parameter that could influence composite joint delamination. Several studies demonstrate that ductile adhesives are useful for manufacturing stronger joints [131]–[133]. Flexible and ductile adhesives have low strength but can distribute stress uniformly, compared to stiffer polymers. Ductile adhesives have higher toughness, deform plastically, and are more resistant to crack propagation than brittle adhesives [21]. The ideal adhesive should be strong, ductile, and flexible but is difficult to achieve although the properties are independent. An interesting way to enhance the mechanical properties of adhesive is the addition of micro and nano-sized fillers. Nanofillers with different material and geometrical characteristics have different effects on the material properties [45].

The process of bonding composite structures, such as those used in aerospace, is distinct from that of bonding metal structures. Rather than relying on mechanical or physical bonding, the matrix polymer, such as epoxy, bismaleimide, or polyimide, can be used as the adhesive. This provides excellent chemical compatibility and adhesion between the substrate and the adhesive. Furthermore, the adhesive and the adherends can be cured simultaneously, which reduces the cost of multiple curing cycles and encourages extensive chemical bonding and interdiffusion of polymeric chains during the curing process. This occurs when the chains are mobile and the interface is under compressive forces.

The use of co-bonding and secondary bonding is common in the fabrication of complex or large structures. To ensure a successful bond, the composite surface must be prepared prior to bonding. This preparation includes the removal of any mold-release agents that may have been applied to the mold or tool surface. Peel plies are typically used to achieve the desired surface. This sacrificial layer of fabric is applied to the composite's surface during part fabrication and is designed to form a weakened bond. Before the secondary bonding operation, the peel ply can be removed to reveal a clean, active surface for bonding. An alternative approach is to use surface abrasion or grit blasting to remove the outermost layer of matrix resin. This can be a labor-intensive process for large structures and raises two issues: nonuniformity and the risk of damaging the fibers in the composite. Additionally, abrasion may simply spread contamination from one area to another.

Secondary bonding is also used to repair existing structures. To ensure a successful bond, the surface area must be clean and activation is necessary. Silane coupling agents are a common method to form interfacial chemical bonds. Additionally, composite resins can be treated with the same processes used for plastics, such as wet chemical or plasma treatments, to ensure compatibility with the adhesive.

To ensure quality assurance, industrial adhesives and tooling assemblies for bonding and inspection devices have been developed. Automated surface preparation methods such as low pressure plasma, laser and blasting have been implemented as they are more reliable than manual sanding and grinding, and can be used in the manufacture of increasingly large and complex components. The utilization of automated infrared spectroscopy probes for surface analysis is being studied in the laboratory, but has yet to be offered to the industry. Currently, the surface inspection of adhesiveness through the surface energy displayed by chemical-mechanical activation is checked using the qualitative water break test or water drop test. This test requires visual analysis and relies on the memory of the inspector. To improve this method, EADS has developed a robust and reliable surface monitoring method within the framework of a European research program. This method involves spraying water droplets of a range of 0.1-0.3 mm onto the surface of the composite, characterizing the wetting by the mean droplet size and their distribution, recording the image with a camera, analyzing the image with software, and drying the surface of the composite with a hot air gun if needed.

Nondestructive inspection (NDI) techniques, such as ultrasonic and infrared imaging, can be used to identify structural bonding defects, such as lack of adhesive, bubbles, and discontinuities between the adhesive and adherends. These techniques can detect issues such as air blade at the interface between skins and honeycomb core or composite and composite or composite and metal, and bubbles in the join, which can reduce the working loading surface and lead to premature failure.

Although NDI methods are useful for assessing the condition of large-scale structures, they are labor-intensive and time-consuming. Furthermore, disassembly of the structures may be necessary in order to make the inspection area accessible, resulting in increased maintenance costs [134].

Structural health monitoring (SHM), an emerging technique derived from NDT, utilizes advanced sensor technology and intelligent algorithms to assess the structural integrity [8]. In contrast to NDT, SHM enables real-time and online damage detection through in-situ sensors. The demand for SHM in composite materials is increasing, with potential benefits including enhanced reliability and safety, reduced lifecycle costs, and aiding in the design of composite materials [134], [135].

2.2.4 Structural Health Monitoring

SHM is a process that acquires and analyzes data from on-board sensors to assess the structural integrity of a given entity. SHM systems are composed by a network of permanently-installed sensors, together with on-board data handling and computing facilities, are used to develop algorithms that compare stored data from the originally pristine structure to recently-acquired data in order to calculate a damage index, and to assess the existence, localization, and type of damage [136].

Broadly speaking, SHM technologies can be subcategorized as local and global. Local techniques, such as comparative vacuum monitoring (CVM) and electro-mechanical impedance (EMI), are limited to the area in the immediate vicinity of the sensor. Global methods, on the other hand, are capable of detecting damage anywhere in the structure by using a network of sensors distributed across the entire area under surveillance. Technologies can be categorized according to the physical principle on which they are based, as reported in Table 2.1, similar to the manner in which Non-Destructive Testing (NDT) procedures are classified. Different types of sensors (e.g. piezoelectric wafers PZT, fiber optic sensors, accelerometers, and MEMS) may be utilized for multiple techniques [136].

Table 2.1 – Classification of SHM technologies, based on physical principles [136]

Physical Principle	**Techniques**	**Main Sensor Type**	**Range**	**Reference**
Continuous Mechanics	Vibration methods	Accelerometers	Global local	[137], [138]
	Strain-based methods	Fiber optic sensors	Mid-range	[139], [140]
Elastic waves	Guided waves	PZT	Mid-range	[141], [142]
	Acoustic emission	PZT, Acoustic emission probes	Mid-range	[143], [143]
	Phased arrays	PZT	Mid-range	[144], [145]
Fluid dynamics	Comparative vacuum monitoring (CVM)	Patch with microchannels	Local	[146]
Electricity and magnetism	Electromechanical impedance (EMI)	PZT	Local	[147], [148]
	Electrical impedance tomography	CNT-doped resins	Local	[149], [150]
	Eddy currents	Eddy probes	Local	[151], [152]

SHM involves the integration of various sensors into target structures to measure various structural properties, including temperature, strain, stress, and vibration. Commonly used SHM sensors include resistance strain gages, fibre optic sensors, piezoelectric sensors, eddy current sensors, microelectromechanical systems (MEMS) and also carbon based-nanofiller[134], [136], [153].

The incorporation of carbon-based nanofillers into resins has been met with varied success in terms of improving interlaminar properties. Additionally, the materials have proven useful in the fabrication of strain and damage sensors, as they possess high sensitivity and can be easily adapted to any structural shape [17], [135], [136], [149], [153]–[161]. Different production processes are available, such as mixing a dispersion with the uncured resin, in situ deposition or growing, and preparing an ink to be applied onto prepreg or adhesive films. The quality and percentage of nanofillers used in the manufacturing process have a significant effect on sensor properties, yet reproducibility remains a significant challenge. Cyclic load testing conducted in a pressure vessel has revealed inconsistent strain measurements, with damage initiation often identifiable by a large change in resistance, but the magnitude of damage cannot be accurately determined [136], [154].

A technique of real-time Structural Health Monitoring (SHM) utilizing electric potential measurements has been demonstrated for the purpose of detecting, locating and quantifying damage (such as impacts and drilled holes) in large composite structures with electrically conductive epoxy matrices, including those incorporating Carbon Nanotube (CNT) elements [156]. Studies of Carbon Fiber Reinforced Polymer (CFRP) composite specimens with carbon black-filled thermoplastic matrices that were submitted to incremental tensile cycles, revealed a strong correlation between the mechanical behavior and the electrical resistance variation, thus indicating potential as an indicator of volume damage [157]. Researchers have also embarked on the development of a CNT film sensor embedded within a cross-ply CFRP laminate, with the aim of using it for SHM applications during uniaxial tension–tension fatigue loading, and found that it had high strain sensing capabilities and piezoresistivity which could be used as a damage indicator [160]. Additionally, in-situ SHM of Glass Fiber Reinforced Polymer (GFRP) composites embedded with CNT fibers which were subjected to incremental cyclic tensile and three-point bending tests, revealed direct correlation between the mechanical loading and electrical resistance (ER) change, with damage accumulation being also correlated with ER [159]. Furthermore, the use of glass fibers with electrically conductive CNT or graphene coatings embedded in an epoxy matrix, in order to manufacture piezoresistive GFRP composites, was explored through tensile tests, which revealed that both coatings were sensitive to strain, though the graphene coating seemed to provide more SHM capabilities than the CNT coating [158].

3 MATERIALS AND METHODS

This chapter outlines the materials and processes used to produce and characterize the bonded joints studied. Steel joints were bonded with a two-component epoxy resin modified with nylon and rubbery nanofibers, both of which were produced in the laboratory. Composite joints were modified with commercial nanofibers and carbon-based nanofillers, such as carbon nanotubes and graphene nanoplatelets, in various concentrations. Characterization of the joints was conducted using a variety of techniques, including DCB test and scanning electron microscopy (SEM).

3.1 METAL JOINTS

Metal joints are manufactured to investigate the effects of laboratory electrospun polymer nanofiber on the mode I fracture toughness. The metal adherends were sandblasted using parameters optimized by evaluating the shear strength and fracture surfaces of SLJs.

3.1.1 Surface Treatment Optimization for Steel Adherends

Sandblasting is a simple and effective method to increase the surface roughness of the substrate in a controlled way and improve the interfacial strength [162]–[166]. The literature [167]–[169] has identified the parameters that most significantly affect the sandblasting process, which include the nozzle distance from the substrate, blasting time, pressure and angle. Two values were considered for each parameter, as reported in Table 3.1, resulting in 16 sandblasting treatments.

Table 3.1 – Sandblasting Parameters for SLJs

Sandblasting Parameters	Values	
Distance (cm)	8	13
Pressure (bar)	2	6
Angle (deg)	75	90
Time (s)	10	60

For each sandblasting treatment, a S235 steel specimens, with an area of 25 mm x 25 mm was produced and sandblasted to evaluate the surface roughness (S_a) according to ISO 25178-2 [170].

The surface roughness can be evaluated as:

3.1

$$S_a = \frac{1}{A} \iint |z(x, y)| dx dy$$

where A is the area, whose roughness must be calculated, z is the coordinate in the normal-to-the-surface direction while the x-y plane is the one on which the surface lies.

For each specimen, five S_a values were measured using over a 4 x 4 mm^2 zone, using the CCI Taylor-Hobson 3D optical profilometer. The profilometer has resolution of 340 nm on the longitudinal x-y plane and 1 nm on the vertical z-axis. Analysis of variance was used to assess the effect of sandblasting parameters on the final S_a.

The optimal sandblasting treatment for the preparation of DCB joint was determined through a series of SLJs manufactured and tested according to ASTM D1002 standard [171]. The adhesive used was the same as that used for DCB joints, Elan-tech® AS90/AW91, cured with the standard cycle suggested by the supplier (70 °C for 5 hours). The characteristic dimensions of the SLJ are reported in Figure 3-1. The adherends are composed by 3 mm thick steel substrate. The sample was tested using an Instron 440 electro-mechanical machine equipped with a 30 kN load cell (Instron, Torino, Italy).

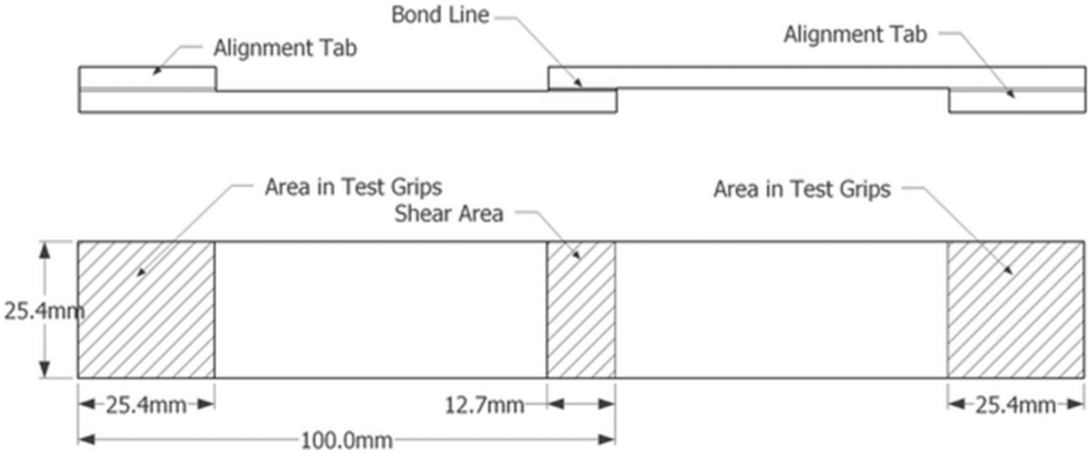

Figure 3-1 – SLJ dimensions [172]

The samples are subjected to a tensile force. The test aims to compare the effectiveness of the different sandblasting treatment throughout the evaluation of the shear strength, calculated using the average shear stress model:

3.2

$$\tau = \frac{P}{wb}$$

where P is the applied load, b is the overlap length and w the sample with.

The shear strengths of the joints were recorded and analyzed using the Analysis of Variance. The results obtained whit SLJs were also compared to the measurements of surface roughness (S_a).

For the S235 steel DCB joint, the parameters used to treat the bonding surface were 6 bar of pressure, 8 cm of nozzle distance, 90° nozzle angle relative to the sample surface and a total sandblasting time of 6 minutes for each adherend surface.

Further details and results of the optimization campaign can be found in the paragraph 4.1.1

3.1.2 Adherends

A cold-drawn S235 steel bar was machined to obtain 150 x 25 x 10 mm^3 DCB adherends for the realization of virgin and nanomodified DCB joints, the latter with nanofibrous mat integrated into the adhesive layer. The elastic modulus of the steel was assumed to be 210 GPa, with a yield strength of 235 MPa. To connect the specimens to the testing machine, one perforated steel block was bonded to each adherend. The geometry of the DCB adherends is shown in Figure 3-2Figure 3-2 – DCB adherend geometry, with dimensions that were reduced compared to ASTM D3433 [43] standards in order to simplify the manipulation of the nanomat after impregnation with epoxy resin. The steel surfaces were pre-treated using the following procedure:

1. degreasing using acetone;
2. sandblasting;
3. sonication for 60 seconds in acetone.

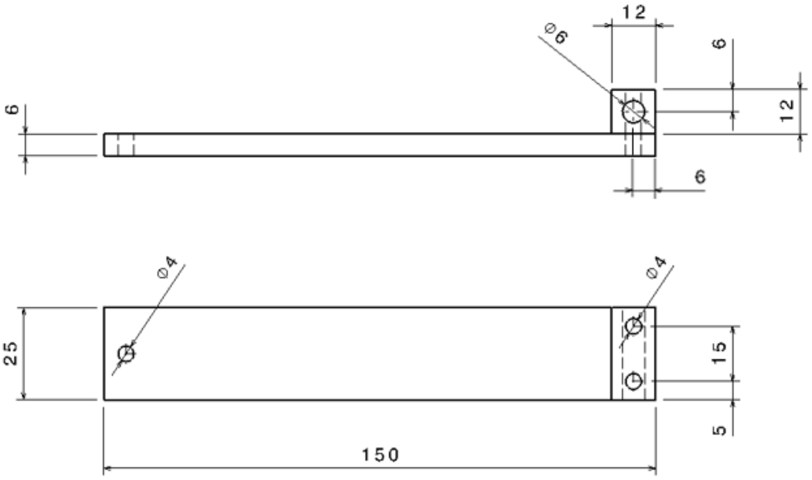

Figure 3-2 – DCB adherend geometry

3.1.3 Adhesive System Elan-tech® AS90/AW91

The Elan-tech® AS90/AW91 epoxy system from ELANTAS Europe SRL (Collecchio (PR), Italy) was used to manufacture DCB joints. This epoxy system was depleted from thixotropic agents by the supplier to reduce viscosity and improve wettability of nanofibers, while maintaining mechanical properties. The resin was provided in cartridges to reduce air entrapment during manual mixing. Table 3.2 provides details of the adhesive bulk properties.

Table 3.2 – Elan-tech® AS90/AW91, (ELANTAS Europe srl, Italy) Bulk properties at room temperature

Property	**Units**	**Value**
Viscosity	mPa·s	5000
Gel Time	h	5-6
Cure cycle suggested by the supplier	h	5
	°C	70
Glass transition temperature (ASTM D 3418) after 24 h at RT	°C	40-47
Flexural strength (ASTM D 790)	MPa	70-80
Strain at break (ASTM D 790)	%	4.5-7.5
Flexural modulus (ASTM D 790)	MPa	2000-2500
Tensile strength (ASTM D 638)	MPa	45-55
Elongation at break (ASTM D 638)	%	4.5-6.5
Shear strength (ASTM D 1002) on AISI316, cured 5h at 70°C	MPa	24.5-29.5
Peel strength (ASTM D 1876) on Aluminum, cured 5h at 70°C	N/cm	35-43

In this work of thesis, the resin was cured using two different curing cycles: cycle A, the standard, at 70°C for 5 hours, and cycle B at 50°C for 80 hours. Cycle B is employed to preserve the nanofibrous structure of the NBR/PCL blend, as the crystalline phase of PCL melts in the temperature range between 55 and 65°C [173]. The comparison of the two different curing cycles enables the evaluation of the toughening effect of the rubber blend (cycle A) and the nanostructure (cycle B). Elantas also provided the flexural modulus (E_{bend}) data which was evaluated with a three-point bending test according to the ASTM D790 standards for both curing cycles. The epoxy resin cured with cycle A showed a flexural modulus of 2447 ± 30 MPa, while the adhesive cured with cycle B showed a slightly lower flexural modulus of 2330 ± 23 MPa. The reasons for using these two curing cycles are discussed in section below 3.1.6.

3.1.4 Nylon Nanofibers

The EM252 electrospun nanomat was produced following a procedure developed in previous works [174]–[176]. A 13 wt. % solution of 6,6 Zytel E53 NC010 (DuPont de Nemours Italiana S.r.l., Cernusco Sul Naviglio (MI), Italy) nylon pellets was prepared in a 10:60:30 by volume trifluoracetic acid/formic acid/chloroform solution (Sigma Aldrich - Italy, Milan). The nylon pellets are dissolved in formic and trifluoracetic acid and then chloroform is added. The electrospinning parameters for the solution were optimized by the Research Group on Electrospinning (RGE) team of the University of Bologna in a previous work [177], and are summarized in Table 3.3. A multi-needle configuration (two or four) was selected, and the collector was a rotating drum kept at zero potential, on which a sheet of Polyethylene-coated paper was placed to collect the randomly-deposited nanofibers. The electrospinning system is showed Figure 3-3. The nylon nanomat webs were collected in the form of a 400 × 300 mm^2 foil. The nanomat thickness was measured along the nanomat strip by a digital indicator (ALPA, Pontoglio (BS), Italy) with a preload of 0.65 N, resolution of 1 µm, the maximum error of 4 µm, and repeatability of 2 µm. Its value lies in the range between 120 to 160 µm. The diameter of nanofibers was determined to be 150 ± 20 nm after manually measuring more than 100 individual fiber diameters on SEM images comparable to the one in Figure 3-4.

Figure 3-3 – Electrospinning setup [178], [179]

Table 3.3 – Electrospinning parameters [178], [179]

Production parameters	Values
Flow rate	0.70 mL/h
Electric Potential	25 kV
Needle-collector distance	6.50 cm
Needle inner diameter	0.51 mm
Temperature	24 °C
Relative Humidity	40 %
Tangential speed of drum	400 mm/s

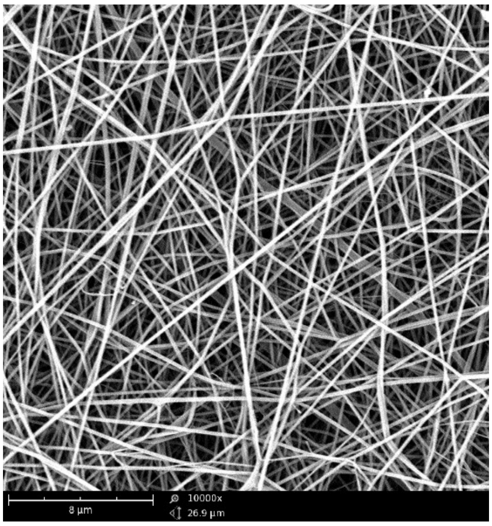

Figure 3-4 – SEM image of the electrospun nylon 6,6 nanofibers *[178]*

3.1.5 Rubbery Nanofibers

The production of a Nitrile Butadiene Rubber/poly(ε-caprolactone) (NBR/PCL) rubbery nanomat was accomplished using an electrospinning technique, as reported in [173]. The electrospinning technique enabled the production of nanofibers from the NBR/PCL blend, which mimicked the behaviour of a thermoplastic elastomer (TPE) without the need for a crosslinking step. Carboxylated nitrile butadiene rubber (NBR) NIPOL 1072CGX and poly(ε-caprolactone) (PCL) were purchased from Zeon Chemicals (Lousville, USA) and Sigma-Aldrich (Milan, Italy), respectively, and used without any preliminary treatment. N,N-dimethylacetamide (DMAc), N,N-dimethylformamide (DMF) and chloroform (CHCl3) were obtained from Sigma-Aldrich and used as solvents without further purification.

PCL is a semi-crystalline polymer with a Tg of -58 °C and a melting temperature of approximately 60 °C. On the other hand, the amorphous NBR does not exhibit melting, but rather two Tgs centered at -14 and -42 °C. To prepare a blend of the two polymers, a 10 wt.% solution of NBR in DMAc was prepared under magnetic stirring at room temperature to form a homogeneous solution, named S-NBR. Similarly, a 10 wt.% solution of PCL in a DMF/CHCl3 1:1 wt solvent system was prepared under magnetic stirring at room temperature to form a homogeneous solution, named S-PCL. Finally, a blend of the two polymers was created by mixing S-NBR and S-PCL in a 60:40 weight ratio to obtain NBR/PCL blend with a 60 wt.% of NBR content, named N-60/40.The blend must be stirred for a minimum of two hours to ensure homogenization.

An electrospinning machine with a 5 mL syringe connected to a 0.84 mm inner diameter, 55 mm long needle via a teflon tube was employed. The nanofibers were collected on a grounded drum collector with a tangential speed of 0.40 m/s. A nanomat strip was electrospun on the central part of the drum, which was covered with polyethylene-coated paper, while grease was added on the sides, as shown in Figure 3-5.

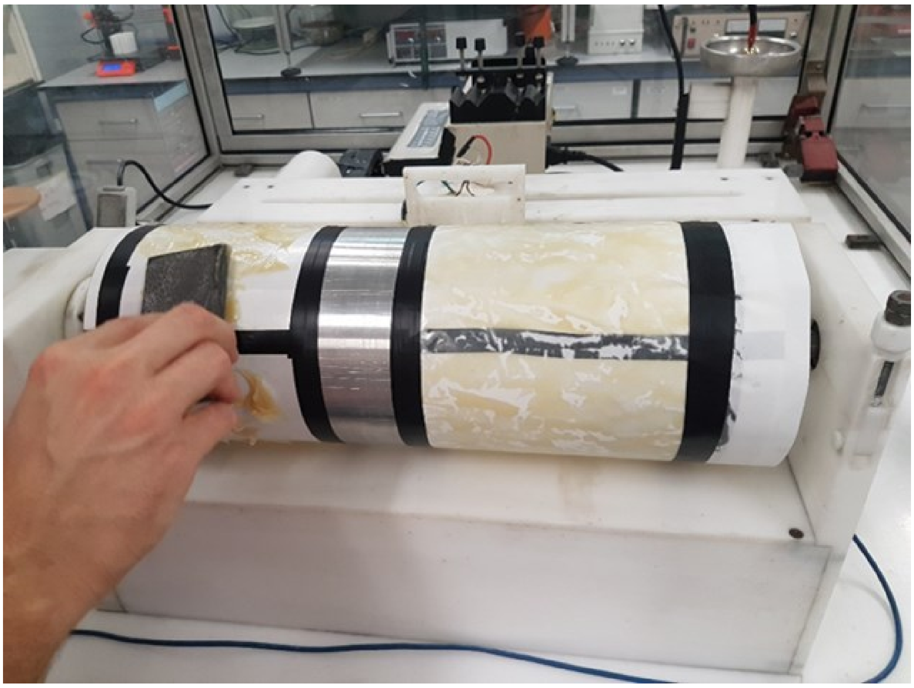

Figure 3-5 – Preparation of the collector drum

The process and environmental parameters used are shown in Table 3.4. A 450 x 50 mm^2 rubber nanomat foil was collected to fabricate the patches necessary for the DCB joints.

The initial crack of the DCB joint must be created during the electrospinning process. This is necessary due to the difficulty of introducing a defect in the middle of the nanomat after electrospinning. A two-step approach is utilized, beginning with electrospinning the first half of the nanomat. Three equidistant strips of Teflon were placed on the membrane, to form a predetermined length of 30 mm for the DCB joint defect, as reported in Figure 3-6. The second half of the nanomat is then electrospun. Prior to integration into the epoxy resin, the DCB patches were cut to the final dimensions of 150 x 25 mm^2. The thickness of the nanomat was measured to be within the range of 80-110 µm using a digital indicator (ALPA Megarod, Pontoglio (BS), Italy) with a measuring pressure of 100 g/cm^2. The morphology of the N-60/40 nanofibrous mat was analysed by SEM (Phenom ProX, ThermoFisher Scientific, Waltham, USA). Figure 3-7 shows SEM images of the N-60/40 nanomat at different magnifications. The average fiber diameter was determined to be 268 ± 62 nm, with values derived from manual measurement of over 100 single fiber diameters.

Table 3.4 - Electrospinning parameters [179]

Electrospinning parameter	**N-60/40 nanomat**
Flow rate	0.55 mL/h
Electric potential	18.3 kV
Distance	13 cm
Electric field	1.4 kV/cm
Temperature	22-26 °C
Relative Humidity (RH)	23-25 %

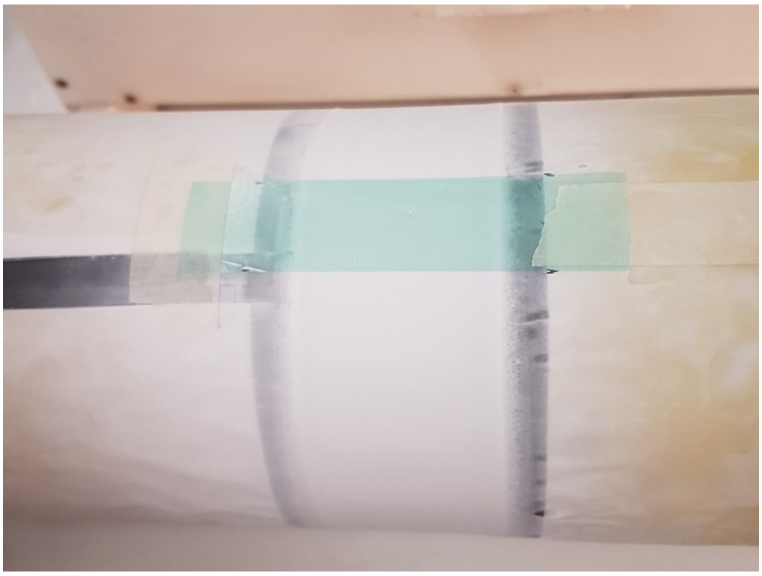

Figure 3-6 – Initial defect realization with Teflon strip

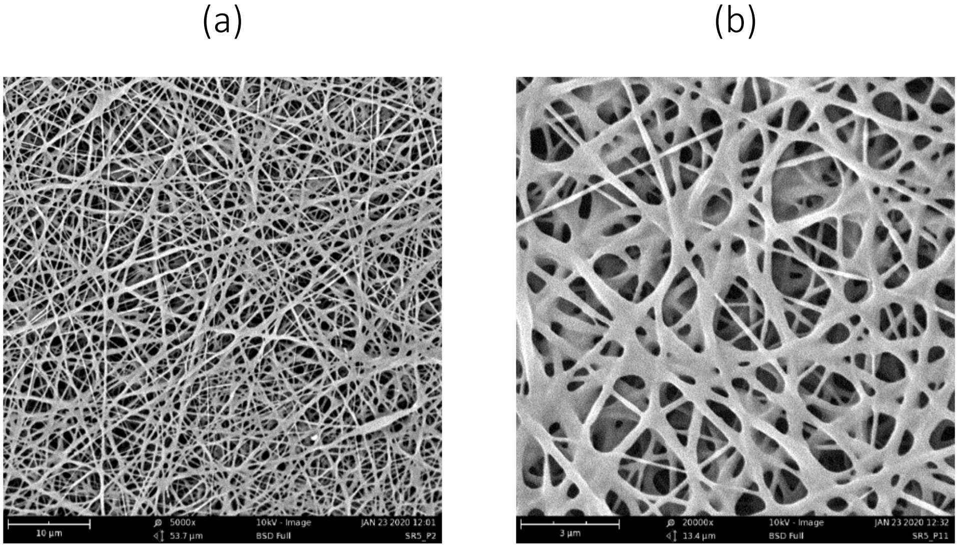

Figure 3-7 – SEM images of NBR/PCL nanofibrous mat N-60/40 at (a) 5000X and (b) 20000X [179]

3.1.6 Double Cantilever Beam Fabrication

Five classes of DCB joints were produced to evaluate the fracture toughness of the adhesive system with and without the integration of nanomat.

The different configurations are reported in Table 3.5 – Metal DCB joints configurationsTable 3.5.

Table 3.5 – Metal DCB joints configurations

Series ID	Adhesive layer	Curing Cycle	Number of Samples
V 70	AS90/AW91	A - 70 °C for 5 h	3
Ny 70	AS90/AW91 + EM252	A - 70 °C for 5 h	3
V 50	AS90/AW91	B - 50 °C for 80 h	3
NBR/PCL 70	AS90/AW91+N/6040	A - 70 °C for 5 h	3
NBR/PCL 50	EAS90/AW91+N6040	B - 50 °C for 80 h	3

Curing Cycle A, consisting of a temperature of 70°C for 5 hours with slow heating and cooling phases, is applied to manufacture virgin samples V70, nylon-modified samples Ny 70 and NBR/PCL-modified NBR/PCL 70 samples. Curing Cycle B, consisting of a temperature of 50°C for 80 hours, is used for virgin samples V50 and NBR/PCL-modified NBR/PCL 50 samples. This cycle is employed to preserve the nanofibrous structure of the NBR/PCL blend, as the crystalline phase of PCL melts in the temperature range between 55 and 65°C [173]. Nylon has a higher melting temperature, so with curing cycle A the nanofiber structure is preserved. There is no need to use a cure cycle at lower temperatures. Curing temperatures below the melting temperature of the crystalline fraction of the PCL maintain the nanofiber structure, which affect the fracture toughness of the system with their structure. Conversely, when the curing temperature is above the PCL melting range, the nanofiber structure is partially destroyed, allowing the rubber to spread in the adhesive, thus acting as a carrier for toughening agents, as explain in Figure 4-2. The complete crosslinking of the matrix was assessed by DCS analysis reported in paragraph 4.1.2.1

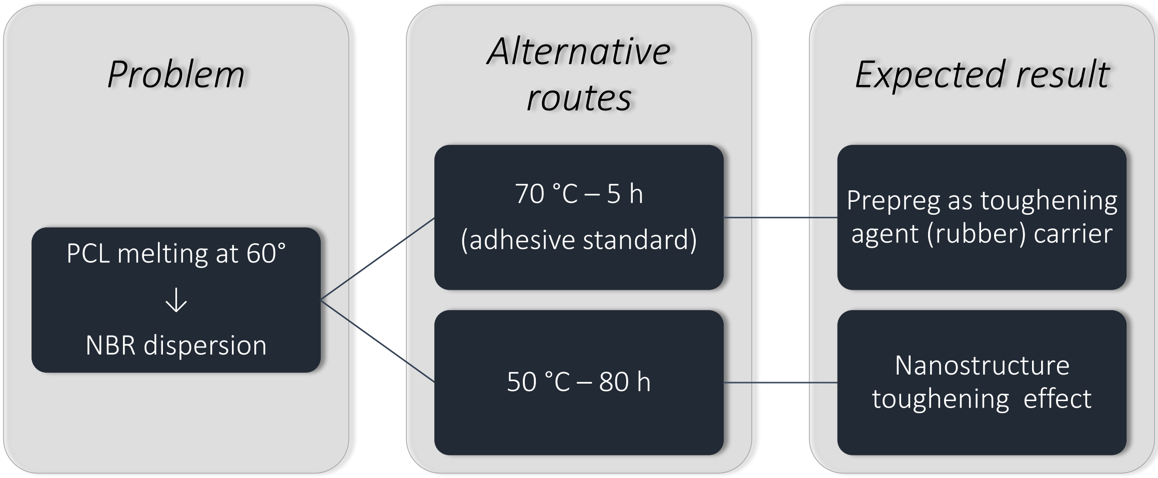

Figure 3-8 – Curing cycle selection for NBR/PCL nanorinforced joints

The steel bonded surfaces were sandblasted, as previously defined. Each adherend was sonicated in acetone for 60 s before bonding.

3.1.6.1 Vingin joint

The virgin DCBs of the series V 70 and V 50 were fabricated by inserting metal spacers of 150 μm thickness at the ends of one adherend of the junction, in order to achieve the same thickness as the nano-reinforced joints. Additionally, a 30 mm long defect was introduced by applying a PTFE strip on the same adherend. The adhesive was applied to the surfaces to be joined using a spatula. The mixture of the resin and the hardener in the cartridge prevents the formation of air bubbles, eliminating the need for needles to break them. The adherends were then overlapped and joined together with bolts and nuts at the joint extremities. Following this, each series of DCBs was exposed to its respective curing cycle. Finally, the bolts and nuts were removed after polymerization.

3.1.6.2 Nylon-modified joint

Prior to joining DCB specimens, an impregnaion test was conducted on two nylon nanoreinforced samples. This test was conducted to verify that the impregnation technique is suitable for obtaining a uniform bonded section free of defects that could cause failure of the joint.The test involved placing a strip of nylon nanomat onto an epoxy resin layer (Figure 3-9 a) and then rolling it between two calibrated and counter-rotating drums (Figure 3-9 b) to remove excess adhesive. The prepreg was then embedded within two S235 steel supports and cured (Figure 3-9 c). Following dissolution of the nylon nanofibers in formic acid and surface polishing, the cross-section of the bonded Ny 70 joint was analyzed under SEM. The results of this test are discussed in detail in 4.1.4.2

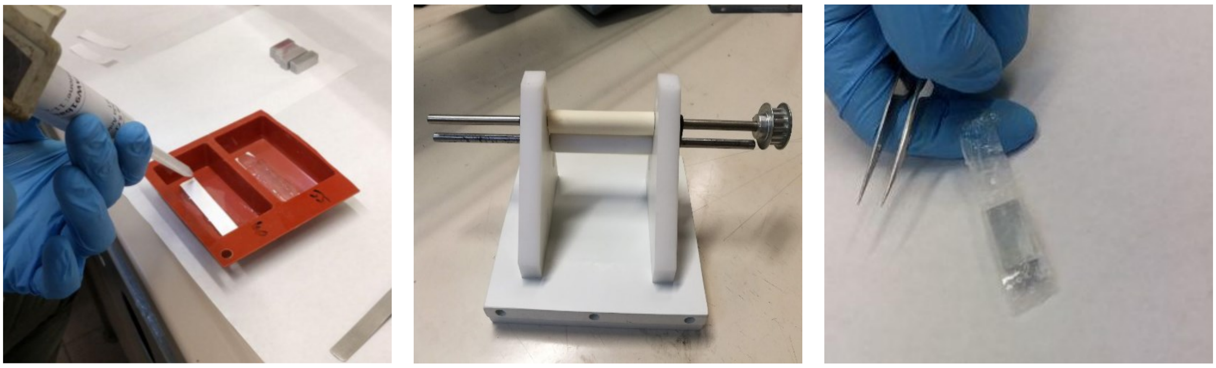

(a) (b) (c)

Figure 3-9 – Manufacturing of samples for impregnation test: resin soak up (a), calibrate the wet nanomat through counter-rotating drums (b), and place the nanomat between two metal supports (c)

In order to produce the nylon nano-reinforced DCB, the pre-cracked nylon nanomat was initially exfoliated to a length of 30 mm to insert the Teflon sheet defect, as showed inFigure 3-10. The nanomat was then impregnated with epoxy resin with the help of a spatula (Figure 3-11 a and b) and squeezed between two counter-rotating drums to remove any adhesive excess (Figure 3-11 c). The adherend surfaces were prepared according to the specifications in 3.1.2. The nanofibrous prepreg was then placed on the bonding surface of one steel support, followed by the overlapping and bolting of the second adherend.

It is important that the screws exert the same force, so the procedure below has been followed to tighten the screws:

- Insert the screws and nuts until they reach the adherend

- Tighten the screw by performing a quarter turn, starting from the screw C then A and B, as reported in Figure 3-13.
- Repeat until they are tightened at the same way

The bond line thickness was determined by the nanomat thickness. After the curing cycle, the bolts were removed.

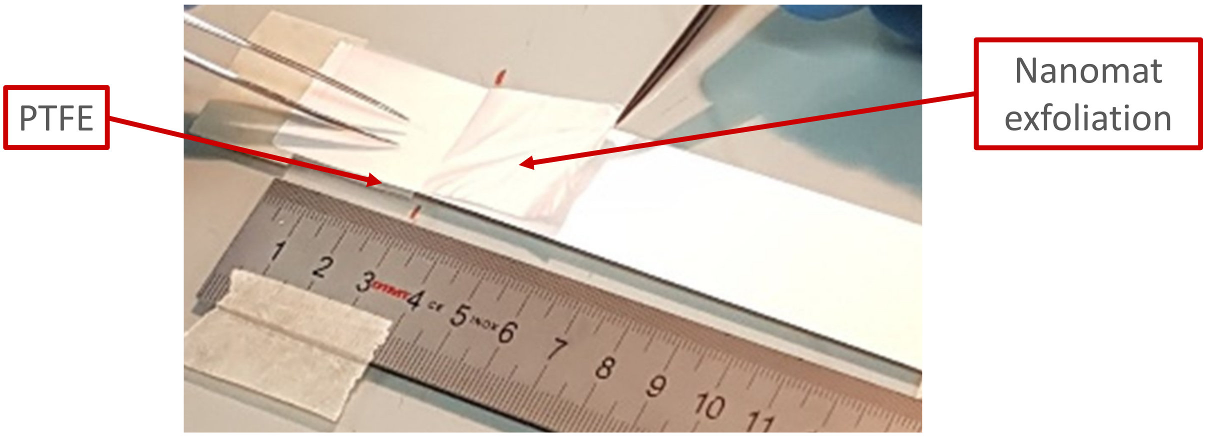

Figure 3-10 – Nylon nanomat exfoliation

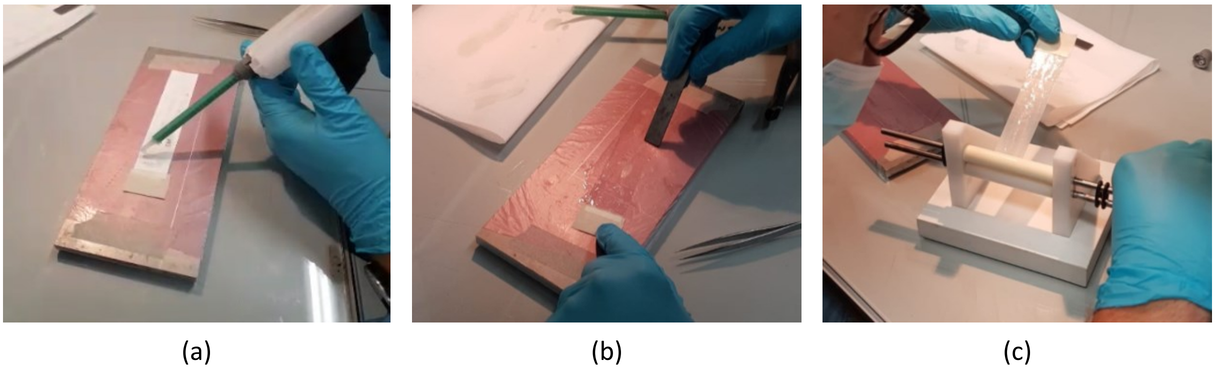

Figure 3-11 – Manufacturing of nylon-nanomat prepreg: resin deposition (a), spreading (b), and squeezing of nanomat resin excess through counter-rotating drums (c)

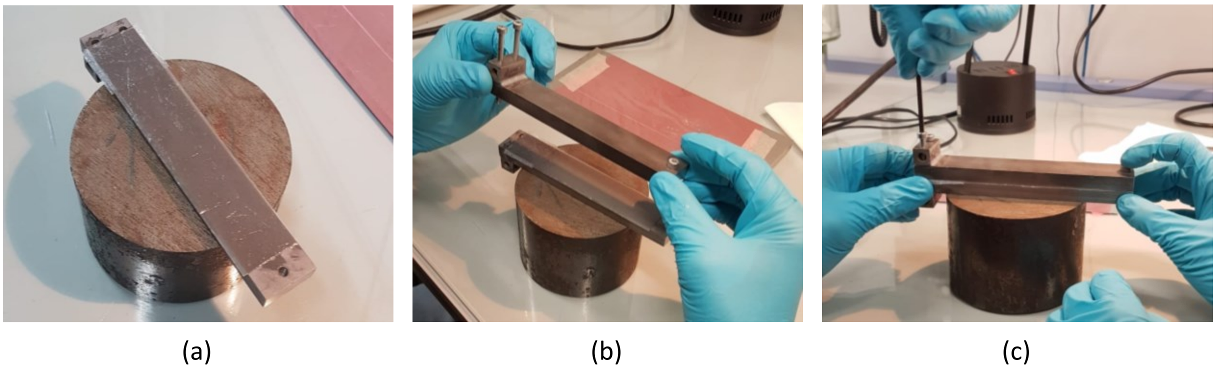
(a) (b) (c)

Figure 3-12 – Manufacturing of nylon-modified joint: placement of pre-cracked nanomat prepreg (a) overlapping adherends (b), and securing the joint with bolts and nuts (c)

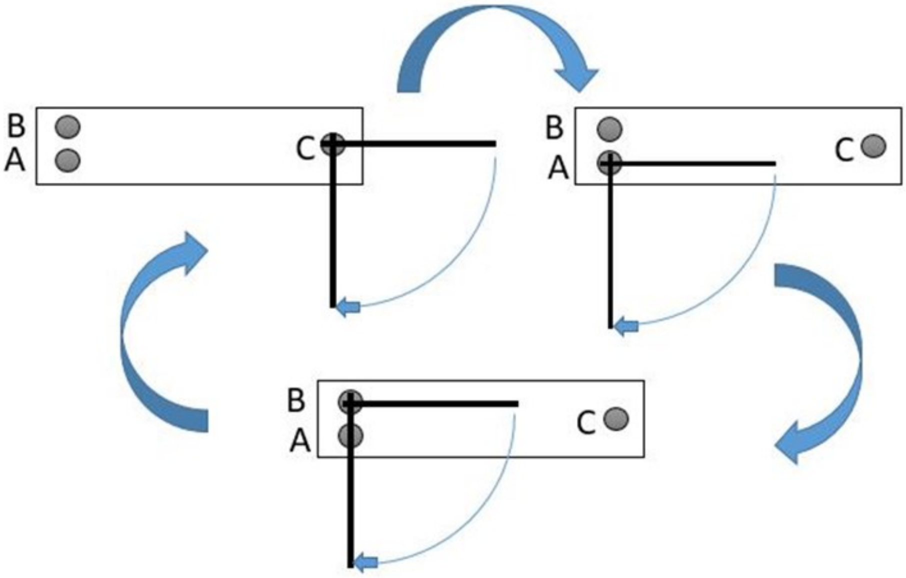

Figure 3-13 – Representation of the procedure to tighten the joints

3.1.6.3 NBR/PCL-modified joints

A test of impregnation was conducted prior to manufacturing the NBR/PCL-modified joint, even though the prepreg had been produced according to the laboratory route developed in previous works [72]–[74], which ensured good impregnation of the nanomaterial. Although the same impregnation procedure was used as for the nylon nanotmats, the materials used and the dimensions of the NBR/PCL nanotmat are different. For this reason, further proof of a successful impregnation process is important. The effectiveness of the impregnation was evaluated through a SEM analysis on the cross section of the nano-reinforced S235 steel joints after undergoing two different curing cycles (A and B). The cross sections of the joints were polished and examined with the SEM, and the results were reported in 4.1.4.2. The same procedure used for DCB joint was used to prepare the prepreg for the impregnation test, as described below.

The manufacturing process of the NBR/PCL nanomodified joints of the series NBR/PCL 70 and NBR/PCL 50 starts by spreading a layer of epoxy resin on a Teflon-cover plate and placing a nanomat strip on top. After adding additional resin to facilitate impregnation, the nanomat is fully wet and the excess resin is removed with a spatula. The prepreg, previously pre-cracked with a 30 mm long defect, is then positioned on the sandblasted surface of one metal adherend with the help of a spatula. To remove any air bubbles, a needle is used. The second adherend is then overlapped and bolted to the first one at the joint extremities. The bondline thickness is determined by the nanomat thickness, and after curing the bolts are removed.

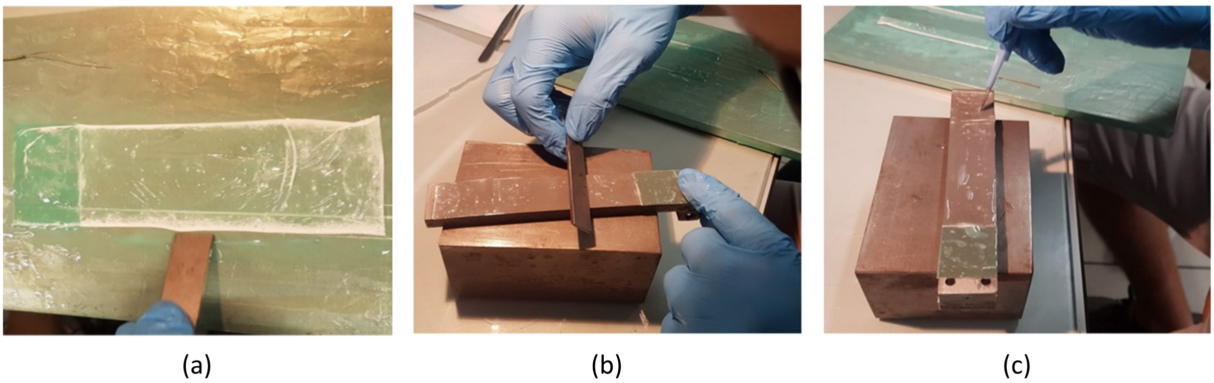
(a) (b) (c)

Figure 3-14 – Manufacturing of NBR/PCL-modified joint: (a) nanomat impregnation, (b) nanomat placemen on sandblasted adherends and (c) air bubble removal with a needle [179].

3.2 COMPOSITE JOINTS

Composite joints are manufactured to investigate the effects of commercially electrospun nylon nanofibers and carbon-based nanoparticles on the mode I fracture toughness.

3.2.1 Adherends

Commercially available prepregs CYCOM® 977-2, supplied by Solvay, were used to manufacture composite adherends. This prepreg is formulated for autoclave or press molding and has an epoxy matrix with a glass transition temperature (Tg) of 126-138°C in dry condition and 104°C in wet form. The unidirectional tape used had a nominal thickness of 0.186 mm and a resin content of 34 wt.%. These properties make it suitable for primary and secondary structure applications in aircraft and aerospace, or any application requiring impact resistance and light weight. Composite panels of 150 x 190 mm2 were produced by lay-up of 32 layers of prepreg, slightly larger than the final panel size, to form a quasi-isotropic laminate with lamination sequence [45/0/-45/90]4s. The panel was then vacuum bagged and cured in an autoclave using the cycle specified by the prepreg technical datasheet (Figure 3-15). The panel was placed on a composite flat tool and the vacuum bag was prepared as reported in Figure 3-16 with a vacuum valve and peel ply layer in contact with the surface for bonding. The peel ply method has been employed in the assembly of composite components for commercial aircraft. This technique involves the application of a sacrificial layer of fabric to the surface of the composite part prior to bonding, which is then peeled away after the adhesive has cured. This method has proven to be an effective means of ensuring a strong bond between the composite parts. After curing, the part was debagged and cut to size. The Peel ply is removed from the panel surface prior to bonding.

The Elastic Modulus of the Laminate was calculated on three samples subjected to Tensile Testing, in accordance with ASTM D3039 Standard [180]. The samples measured 150 mm in length, 25 mm in width, and had a thickness of 6 mm, matching that of the adherends. The servo-hydraulic universal testing machine MTS 370.25 Landmark Load frame, equipped with a 250 kN load cell, was used to perform the tests. The test speed was set to 2 mm/min, and the sample deformation was calculated using an extensometer, which was removed once the force reached 60 kN. The purpose of the test was to determine the elastic modulus, and the specimens were not loaded until failure. The Figure 3-17 illustrates a graph of a tested sample, and the results indicate that the average elastic modulus of the laminate was 58 GPa.

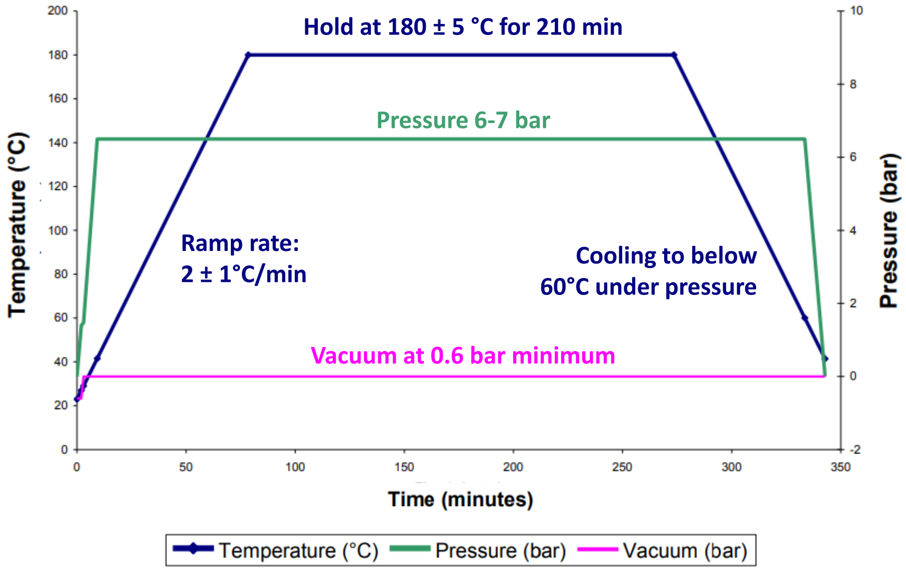

Figure 3-15 – CYCOM ® 977-2 curing cycle

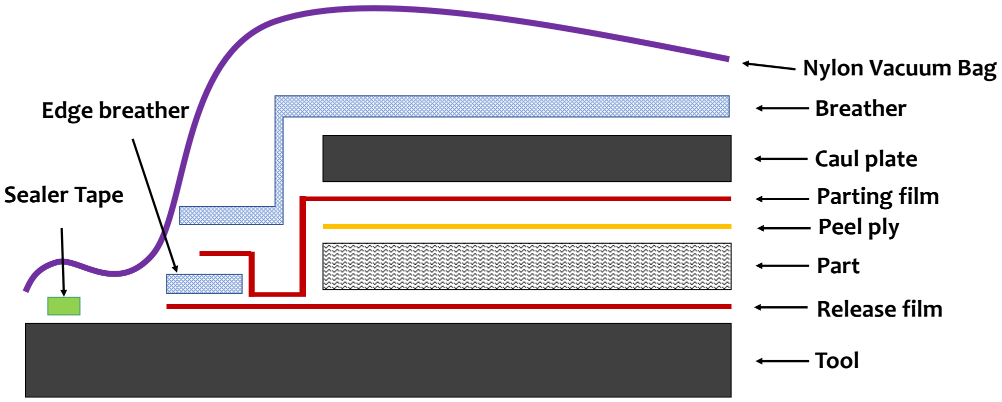

Figure 3-16 – Vacuum bag scheme

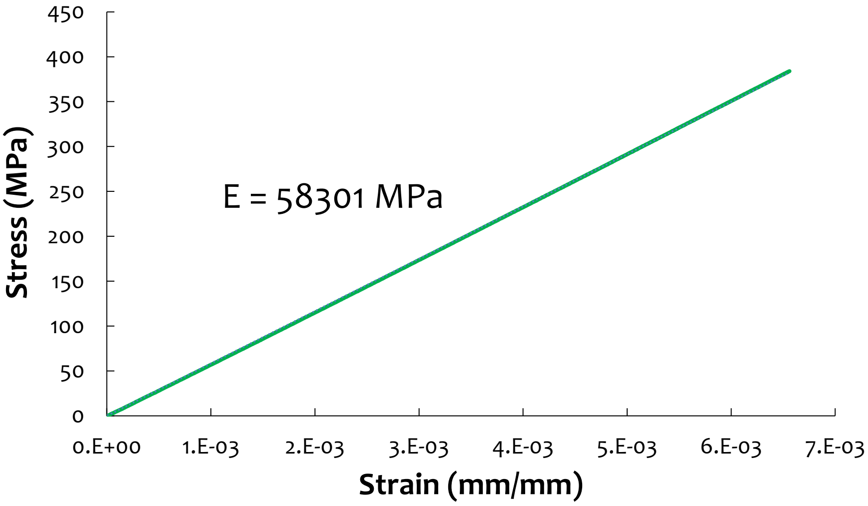

Figure 3-17 – Tensile test of composite adherend

3.2.2 Adhesive System METLBOND® 1515-4M

The METLBOND® 1515-4M adhesive is a 177° C curing epoxy system designed for composite and metal bonding applications, and can be cured at lower temperatures. It has excellent adhesion to a variety of substrates, including metals, composites, and other materials. It has excellent shear and tensile strength, as well as good resistance to water, solvents, and chemicals. The adhesive film selected for this study has a nominal weight of 242 g/m^2, with a nylon carrier constituting 7.5% of the total weight. The presence of the nylon cloth inside the adhesive layer ensures joints with a constant adhesive cross-section. The nylon cloth weight was determined by weighing the material after dissolution of the resin in acetone and comparing it to the initial weight of the film. The elastic modulus of adhesive film is strictly related to the curing pressure and temperature. The Elastic modulus of METLBOND® 1515-4M was determined to be 3.5 GPa based on supplier recommendations as well as findings from various studies in the literature [181]–[183].

Table 3.6 report the composite bonding mechanical properties from technical datasheet supplied by Solvay.

The substrate properties for each test are reported below:

- Double Lap Shear – 8 and 16 ply panels of procured CYCOM® 934/PW T300 3K.
- Honeycomb Flatwise Tensile – Face sheets: 3 plies of co-cured CYCOM® 934/PW T300 3K.
- Core: HRP, 0.1875 in (0.476 cm), 8pcf (0.128 g/cc), 0.50 in (1.27 cm) thick.
- Sandwich Beam Shear – Face sheets: 3 plies of co-cured CYCOM® 934/PW T300 3K.
- Core: HRP, 0.1875 in (0.476 cm), 8pcf (0.128 g/cc), 0.50 in (1.27 cm) thick.
- Double Cantilever Beam – Precured 10 ply laminate CYCOM® 934/PW T300 3K.

Table 3.6 – METLBOND® 1515-4M Composite Bonding: Mechanical Properties

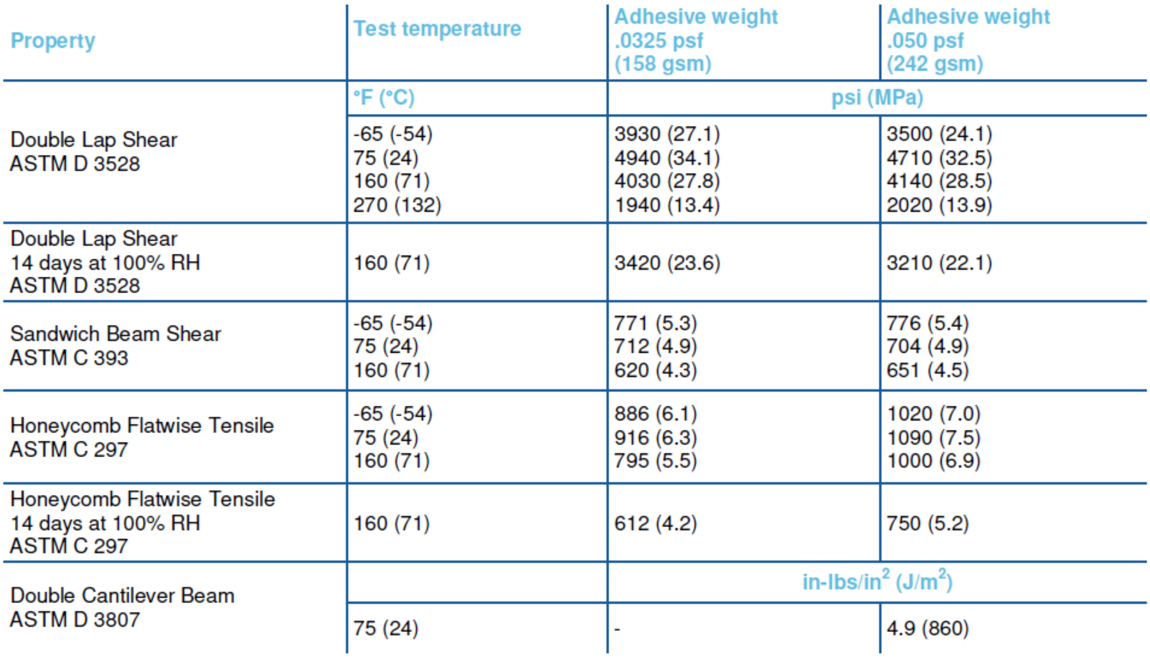

Property	Test temperature	Adhesive weight .0325 psf (158 gsm)	Adhesive weight .050 psf (242 gsm)
	°F (°C)	psi (MPa)	
Double Lap Shear ASTM D 3528	-65 (-54)	3930 (27.1)	3500 (24.1)
	75 (24)	4940 (34.1)	4710 (32.5)
	160 (71)	4030 (27.8)	4140 (28.5)
	270 (132)	1940 (13.4)	2020 (13.9)
Double Lap Shear 14 days at 100% RH ASTM D 3528	160 (71)	3420 (23.6)	3210 (22.1)
Sandwich Beam Shear ASTM C 393	-65 (-54)	771 (5.3)	776 (5.4)
	75 (24)	712 (4.9)	704 (4.9)
	160 (71)	620 (4.3)	651 (4.5)
Honeycomb Flatwise Tensile ASTM C 297	-65 (-54)	886 (6.1)	1020 (7.0)
	75 (24)	916 (6.3)	1090 (7.5)
	160 (71)	795 (5.5)	1000 (6.9)
Honeycomb Flatwise Tensile 14 days at 100% RH ASTM C 297	160 (71)	612 (4.2)	750 (5.2)
Double Cantilever Beam ASTM D 3807		in-lbs/in^2 (J/m^2)	
	75 (24)	-	4.9 (860)

Table 3.7 – Recommended curing cycle for METLBOND® 1515-4M

Adhesive Cure Cycle	**Apply full vacuum, 0.081 MPa minimum.** **Apply 0.21 - 0.31 MPa pressure, vent vacuum at 0.14 MPa.** **Heat from 24 °C to 177 °C at 1-3 °C/minute.** **Hold at 177 °C for 120 minutes.** **Cool under pressure below 60 °C at 1-3 °C/minute**
Composite prepreg	Apply full vacuum, 0.081 MPa minimum. Apply 0.55 MPa pressure, vent vacuum 0.14 MPa. Heat from 24 °C to 177 °C at 1-3 °C/minute. Hold at 177 °C for 120 minutes. Cool under pressure below 60 °C at 1-3 °C/minute
Peel Ply	Cure prepreg panels using polyester peel ply on all surfaces to be bonded.

The application of the cure cycle to the joints bonded with the adhesive was identical to the process used to manufacture the adherends and reported in Figure 3-15.

This cure cycle was selected for its industrial relevance, as it is typically used for composite manufacturing. Additionally, this cycle was chosen for two main reasons:

- It allows for the consolidation and cure of prepreg and secondary bonding simultaneously, thus reducing time and energy expenditure.

- It is suitable for use in the case of co-bonding joints.

3.2.3 Nanofibers XantuLayr®

XantuLayr® is a thermoplastic nanofibre veil designed to enhance the performance of fibre reinforced thermoset polymer composite materials. Produced using Sonic Electrospinning Technology, XantuLayr® is an ultra-thin non-woven web consisting of kilometre long XD10 polyamide nanofibres. When placed in-between the plies of reinforcing fibres in a composite laminate, XantuLayr® nanofibre veils are able to improve fracture toughness, compression after impact strength and fatigue resistance, while adding minimal thickness and weight. The XantuLayr® nanomat selected for this study has an areal density of 3 g/m^2.

The nanomat was supplied in a roll form and its properties are listed in Table 3.8.

Table 3.8 – XantuLayr® characteristic

Product name	**XANTU.LAYRTM XLB SERIES**
Fibre	Nanifber
Fibre format	Non-woven Mat
Colour	White
Product format	Rolled goods
Length	100 m
With	1 m
Substrate	Release paper
Base materia	XD10 Polyamide
Porosity	80% by colume
Typical fiber length	230 nm
Maximum operating temperature	Continuous
Average fiber diameter	190 °C
Manufacturing method	Electrospun
XANTU.LAYR XLB 1.5 gsm	1.5 g/m^2
XANTU.LAYR XLB 3 gsm	3.0 g/m^2
XANTU.LAYR XLB 4.5 gsm	4.5 g/m^2

The thickness of the nanomat was measured using a digital indicator (ALPA, Pontoglio (BS), Italy) with a preload of 0.65 N, a resolution of 1 µm, a maximum error of 4 µm, and a repeatability of 2 µm. The thickness was found to lie in the range of 120 to 160 µm.

3.2.4 Multiwalled Carbon Nanotubes

MWCNTs used in this work of thesis are supplied by Cheaptubes. Their properties are listed below:

- Outer Diameter: <8nm
- Inside Diameter: 2-5nm
- Ash: <1.5 wt%
- Purity: >95 wt%
- Length: 10-30 µm
- Specific Surface Area: 500 m2/g
- Electrical Conductivity: >100 S/cm
- Bulk density: 0.27 g/cm3
- True density: ~2.1 g/cm3

A 0.1 wt.% solution of MWCNTs was prepared in acetone by mechanical stirring. The solution was then sonicated for 90 minutes at a low temperature, maintained by an ice bat, using a Hielscher UP200S-24 kHz high power ultrasonic probe, as illustrated in Figure 3-18. The quantity of acetone and duration of sonication were optimized to obtain a homogeneous solution free from agglomerates and stable over time.

Figure 3-18 – MWCNs sonication with Hielscher UP200S-24 kHz high power ultrasonic probe

3.2.5 Graphene Nanoplatelets

In this work, the GNPs used are functionalised with carboxylic groups, making them suitable for a variety of advanced applications. These carboxylate GNPs are used as nanoscale additives for advanced composites, components in advanced batteries and ultra/super capacitors, conductive components in specialty coatings and adhesives, and components of e-inks and printable electronic circuits. Moreover, they can be used to create exceptionally strong and impermeable packaging, better lubricants, and highly sensitive biosensors. The GNPs consist of several layers of graphene with an overall thickness of 3-10 nanometers.

Product spcifications are listed below:

- Process Gas: Proprietary Oxygen Based
- Primary Functionality: COOH – Carboxylate
- Other Functionalities: COH, C=O, Other Oxygen
- Source Material: Natural Graphite
- Form Supplied: Dry Powder

The properties of GNPs are as follows:

- Purity: 97%
- X & Y Dimensions: >2um
- Average thickness: 3-10 µm
- Specific Surface Area: 500 – 700 m2/g

A 0.5 wt.% solution of GNPs was prepared in acetone by mechanical stirring. The solution was then sonicated for 90 minutes at a low temperature, maintained by an ice bat, using a Hielscher UP200S-24 kHz high power ultrasonic probe, as illustrated in Figure 3-19. The quantity of acetone and duration of sonication were optimized to obtain a homogeneous solution free from agglomerates and stable over time.

Figure 3-19 – GNPs sonication with Hielscher UP200S-24 kHz high power ultrasonic probe

3.2.6 Double Cantilever Beam Fabrication

Nine classes of DCB joints were produced to evaluate the fracture toughness of the adhesive system with and without the integration of commercial nanofibers and carbon-based nanofiller.

The different configurations are reported in Table 3.9 and Figure 3-20.

Table 3.9 – Composite DCB joints configurations

Series ID	Adhesive layer	Number of Samples
1S	METLBOND® 1515-4M	7
2S	2 METLBOND® 1515-4M	8
1S-2NF	XantuLayr® + METLBOND® 1515-4M + XantuLayr®	5
2S -1NF	METLBOND® 1515-4M + XantuLayr® + METLBOND® 1515-4M	5
C1%	METLBOND® 1515-4M + 1 wt.% MWCTs	5
C0.5%	METLBOND® 1515-4M + 0.5 wt.% MWCTs	4
C0.25%	METLBOND® 1515-4M + 0.25 wt.% MWCTs	3
G1%	METLBOND® 1515-4M + 1 wt.% GNPs	5
G0.5%	METLBOND® 1515-4M+ 0.5 wt.% GNPs	5

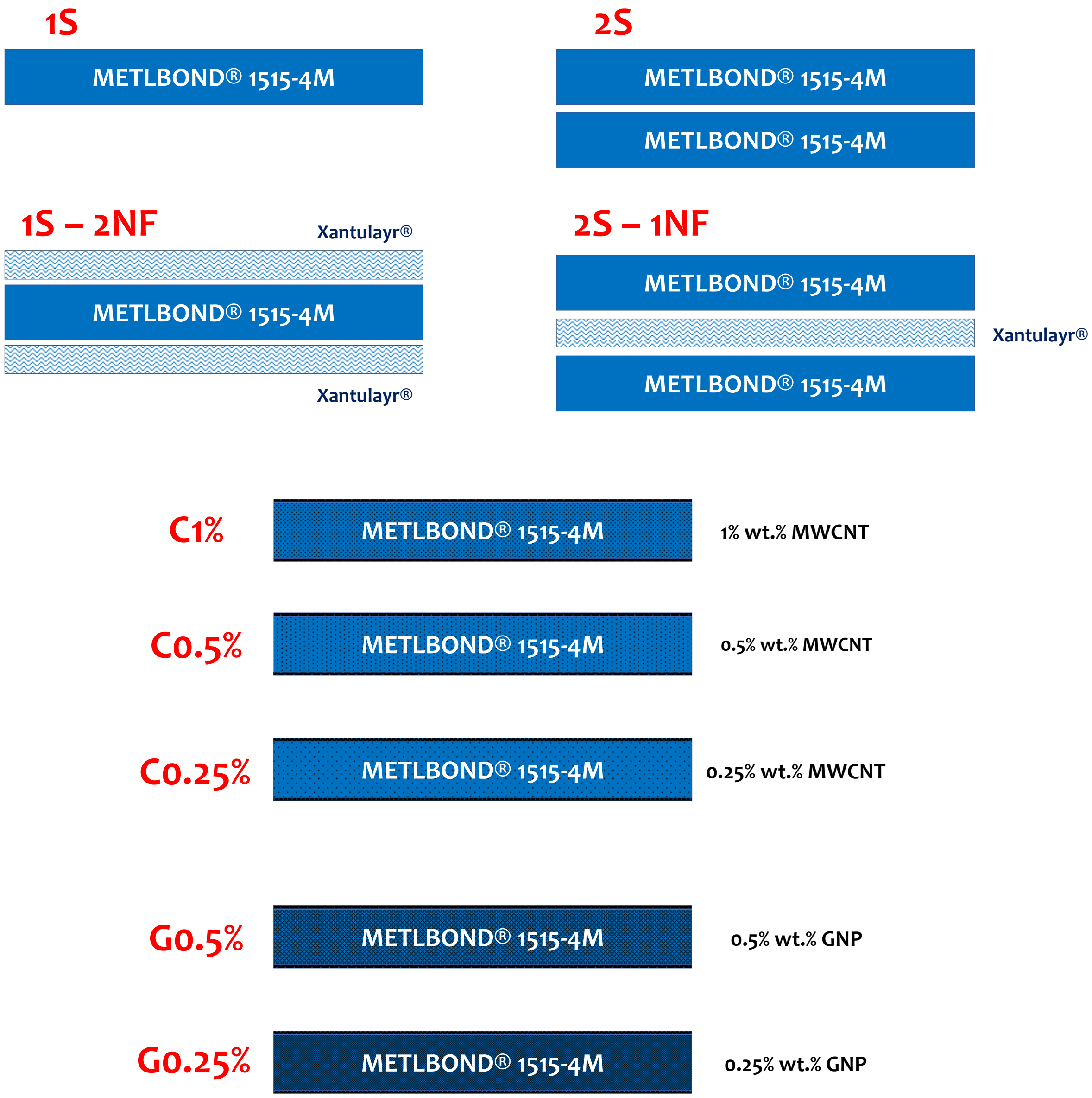

Figure 3-20 – Composite joints configurations

The specimens were manufactured by bonding two composite panels (190 x 150 mm^2) together. The samples are then placed in a vacuum bag (Figure 3-21) and subjected to a curing cycle in an autoclave at a pressure of 6 bar and a temperature of 180 °C for 210 minutes, as illustrated in Figure 3-15. During the bonding stage, a 25-mm initial defect was created by placing a patch of Teflon on one end of the joint. After the curing process, the panels were cut to 150 mm in length and 25 mm in width to form DCB joints. Subsequently, holes were machined in each joint to facilitate the attachment of steel blocks, which were used to secure the specimen in the testing apparatus. The geometry of the DCB is depicted in Figure 3-22.

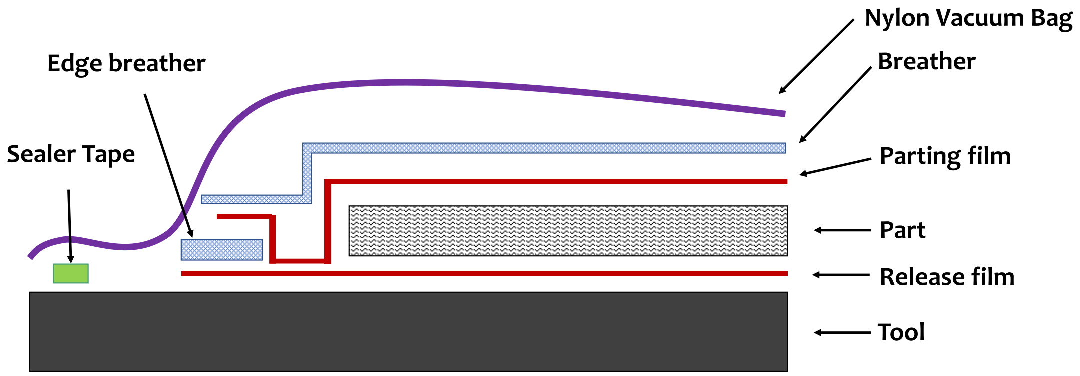

Figure 3-21 – Vacuum bag scheme for composite joints

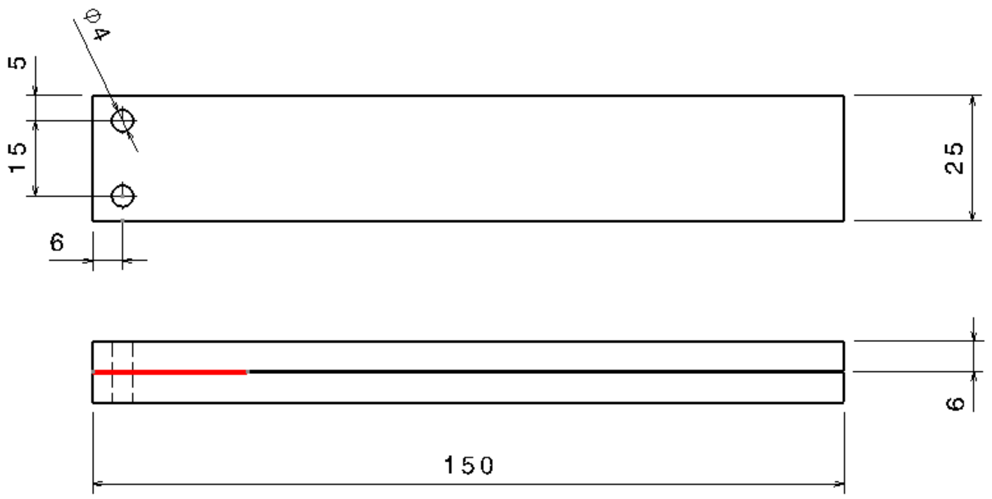

Figure 3-22 - Composite DCB geometry, the red line represents the initial defect

3.2.6.1 *Virgin Joints*

Virgin DCB joints preparation involves the following step:

1. Preparation of materials for a vacuum bag
2. Cutting adhesive film and Teflon sheet to adequate sizes
3. Preparation of the lamination tool
4. Removal of peel ply from the bonding surfaces
5. Positioning of adhesive film (191 x 119 mm2) on one bonding surface, one layer for 1S and 2layer for 2S
6. Positioning of Teflon on the adhesive free end of the same adherend to create a no-bonding zone of 31 mm (Teflon in the middle of the two adhesive layers for the configuration 25)
7. Overlapping of the second adherend (Figure 3-24)
8. Creation of the vacuum bag (Figure 3-25), and curing in an autoclave at 180 °C for 3 hours.

Two pairs of bonded panels were manufactured for each configuration (1S and 2S)

At the end of the curing process, the bonded panels are cut and a maximum of 5 DCBs are extracted from the central area. Steel blocks are then glued to the DCBs using Loctite Hysol 9466 adhesive. To ensure the correct positioning of the blocks, they are fastened to the adherends with screws and bolts. Once the adhesive is polymerized after 24 hours at room temperature, screws and nuts can be removed and the DCB is ready to be tested.

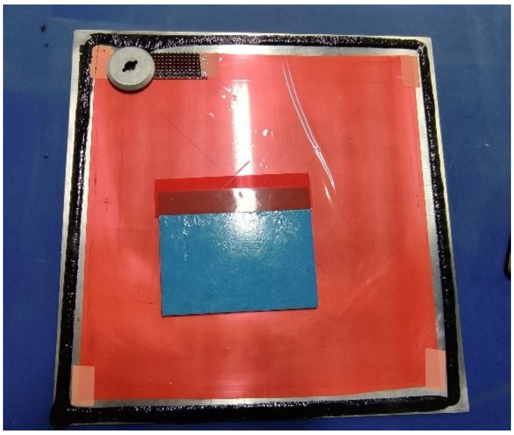

Figure 3-23 -Positioning of Teflon and adhesive film on bonding surface

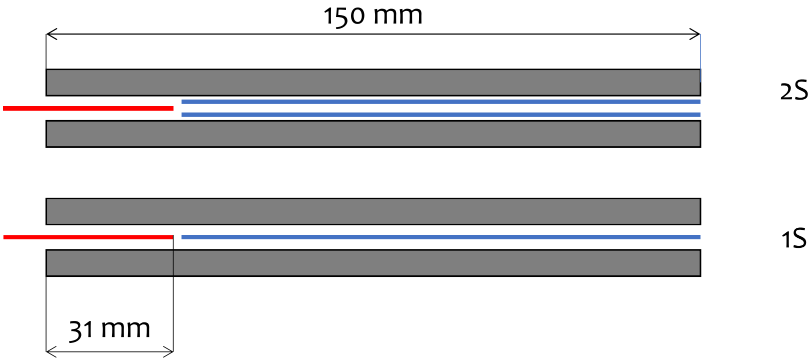

Figure 3-24 – Virgin composite bonding

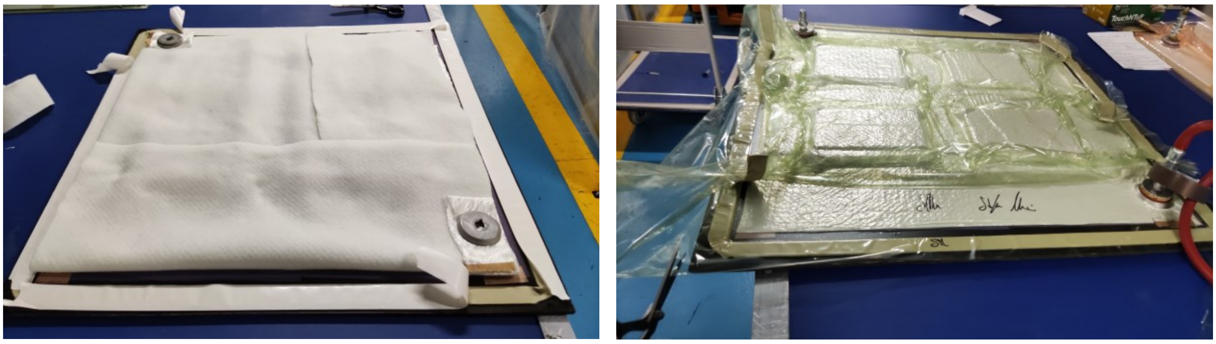

(a)

(b)

Figure 3-25 - Vacuum bag realization: (a) breather positioning, and (b) vacuum test

3.2.6.2 *Polyamide-modified Joints*

Nanofiber modified DCB joints preparation involves the following step:

1. Preparation of materials for a vacuum bag
2. Cutting adhesive film, nanofibers layers and Teflon sheet to adequate sizes
3. Preparation of the lamination tool
4. Removal of peel ply from the bonding surfaces
5. Positioning of nanofibers layer and adhesive film (with same dimensions of 191 x 119 mm2) on one bonding surface following the scheme of each configuration: nanofibers + adhesive film + nanofibers for the configuration 1S (Figure 3-27), adhesive film + nanofibers + Adhesive film for the configuration 2S (Figure 3-26)
6. Positioning of Teflon on the adhesive free end of the same adherend to create a no-bonding zone of 31 mm (Teflon in the middle of the two adhesive layers for the configuration 25)
7. Overlapping of the second adherend
8. Creation of the vacuum bag and curing in an autoclave at 180 °C for 3 hours.

One pair of bonded panels were manufactured for each configuration (1S – 2NF and 2S – 1NF)

At the end of the curing process, the bonded panels are cut and 5 DCBs are extracted from the central area. Steel blocks are then glued to the DCBs using Loctite Hysol 9466 adhesive. To ensure the correct positioning of the blocks, they are fastened to the adherends with screws and bolts. Once the adhesive is polymerized after 24 hours at room temperature, screws and nuts can be removed and the DCB is ready to be tested.

The verification of the good quality impregnation was conducted by manufacturing smaller test samples and applying the same bonding technique used to realize the DCB joint. The samples cross section was polished and analyzed with optical microscope and SEM. The results of this integration process are reported in 5.1.2.1.

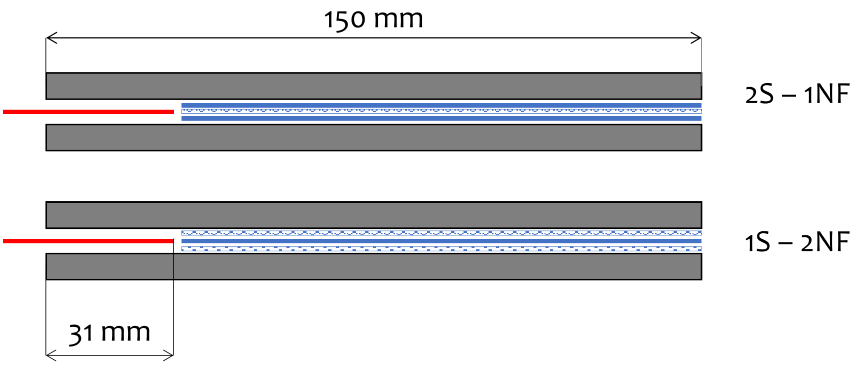

Figure 3-26 – Nanofibers modified composite joints

Figure 3-27 – 1S-2NF panel before curing

3.2.6.3 MWCNT-modified and GNP-modified Joint

The preparation of carbon-based nanoparticle-modified joints involves 2 phases: adherends preparation and bonding. The adherends preparation involves the following steps:

1. Assessing the necessary amount of solution for each configuration (as given in Table 1)
2. Preparing a solution containing the nano-additive according to the directions outlined in paragraph 3
3. Removing the peel ply on the surfaces to be bonded
4. Inserting the solution into an airbrush that work with compressed air (1 bar)
5. Spraying the prescribed amount of nanofiller onto the surfaces to be bonded in uniform way
6. Waiting for complete evaporation of the solvent (airbrush providing for much of it to evaporate)

The bonding phase follows these steps:

1. Preparation of materials for a vacuum bag
2. Cutting adhesive film and Teflon sheet to adequate sizes
3. Preparation of the lamination tool
4. Positioning of adhesive film (191 x 119 mm^2) on one bonding surface)
5. Positioning of Teflon on the adhesive free end of the same adherend to create a no-bonding zone of 31 mm
6. Overlapping of the second adherend

7. Creation of the vacuum bag and curing in an autoclave at 180 °C for 3 hours.

One pair of bonded panels were manufactured for each configuration

At the end of the curing process, the bonded panels are cut and a maximum of 5 joint are extracted from the central area. Steel blocks are then glued to the DCBs using Loctite Hysol 9466 adhesive. To ensure the correct positioning of the blocks, they are fastened to the adherends with screws and bolts. Once the adhesive is polymerized after 24 hours at room temperature, screws and nuts can be removed and the DCB is ready to be tested.

Integration quality was assessed by manufacturing smaller test samples and applying the same bonding technique used to realize the DCB joint. The two composite bonding surfaces were covered with Teflon foils and sprayed with the nanoparticles solution. Teflon foil prevents the CFRPs and epoxy bonding and allows the cured adhesive extraction. The results of this integration process are reported in 5.1.3.1

3.3 MECHANICAL CHARACTERIZATION

This section describes the geometry and testing procedures of metal and composite DCB joints.

3.3.1 Joint geometry

Metal and composite bonded DCB joints have similar geometry that are reported in Figure 3-28.

The metal joint dimensions were reduced if compared with ASTM D3433 standards [43]. This non-standard size has been selected to simplify the manipulation of the laboratory electrospun nanomat, after the impregnation with epoxy resin. Consequently, the same geometry was adopted for composite joints. The transmission of load during the test is allowed by two drilled blocks which are bonded on each substrate. Table 3.10 shows the characteristic dimensions of each joint family, which were used for the calculation of fracture toughness.

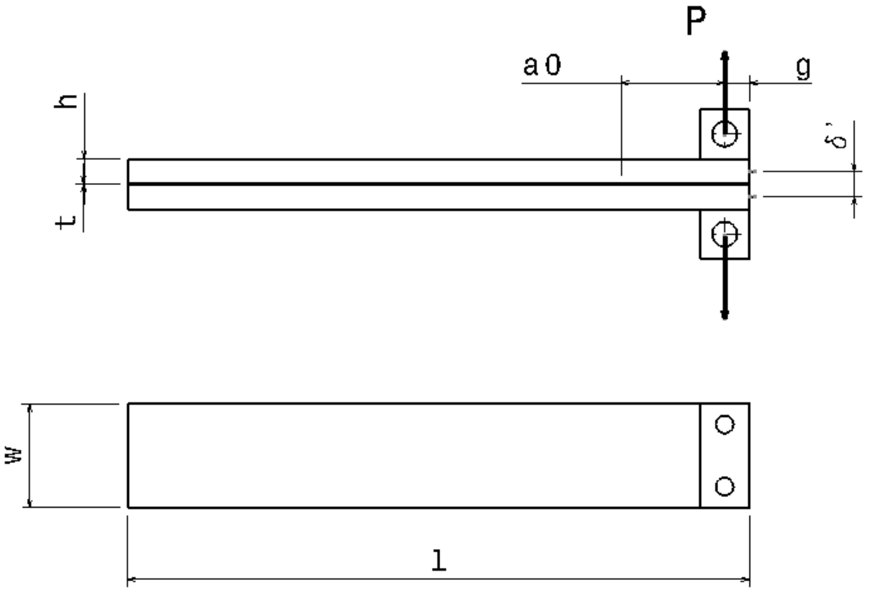

Figure 3-28 – DCB geometry [178], [179]

Table 3.10 – DCB Dimensions considered for fracture toughness evaluation

Sample ID	w (mm)	l (mm)	h (mm)	t (mm)
V 70	25	150	10	0.15
Ny 70	25	150	10	0.15
V 50	25	150	10	0.15
NBR/PCL 70	25	150	10	0.10
NBR/PCL 50	25	150	10	0.10
1S	25	150	6	0.17
2S	25	150	6	0.48
1S – 2NF	25	150	6	0.18
2S -1NF	25	150	6	0.52
C1%	25	150	6	0.17
C0.5%	25	150	6	0.14
C0.25%	25	150	6	0.15
G1%	25	150	6	0.18
G0.5%	25	150	6	0.18

3.3.2 Double Cantilever Beam Test

The DCB test is performed under displacement control at a constant crosshead speed on a servo-hydraulic MTS 810 testing machine equipped with a 3 kN load cell. The displacement follows a load-unload law at constant rate, in particular the loading rate is 2 mm/min, unloading rate is 5 mm/min. The partial un-loadings are needed to evaluate the specimen compliance and therefore the actual crack length, calculated through the Krenk's model reported in [44]. Each adherend is modelled as a beam on an elastic foundation and considers the out of plane deformation of the adhesive layer and the rotation at the crack tip. The model, represented by the equation 3.3:

3.3

$$C=\frac{\delta'}{P}=2\left[\frac{2\lambda_{\sigma}}{k}(1+\lambda_{\sigma}a)+(a+g)\frac{(2\lambda_{\sigma}^{2})}{k}(1+2\lambda_{\sigma}a)+\frac{a^{3}}{3EJ}+g\frac{a^{2}}{2EJ}\right]$$

Where C is the compliance of the joint, δ' is the Crack Mouth Opening Displacement (CMOD) measured at the front of the specimen, P is the load, a is the actual crack length, E is the Young's modulus od the adherends, J is the area moment of inertia of the adherend. During the test, the CMOD is evaluated using a clip gage. The model presented in 3.3 has been modified compared the one proposed by Krenk in order to take into account the distance g of measurement point from the load axis and the effect of shear.

The parameters λ_{σ} and k are reported in equation 3.4 and 3.5:

3.4

$$\lambda_{\sigma}=\sqrt[4]{\frac{6}{h^{3}t}\frac{E_{a}}{E(1-\upsilon_{a}^{2})}}$$

3.5

$$k=\frac{2E_{a}t}{t\,(1-\upsilon_{a}^{2})}$$

The Mode I strain energy release rate G is:

3.6

$$G_{I}=\frac{(Pa)^{2}}{tEJ}\left(1+\frac{1}{\lambda_{\sigma}a}\right)^{2}$$

Where E_a and υ_a are the Young's modulus and Poisson's ration of the adhesive layer, respectively.

The fracture toughness G_{IC} is calculate at crack initiation and during steady state crack propagation. The mean propagation value of G_{IC} can be deduced from an average of the propagation points. The G_{IC} values recorded as a function of crack length defining the resistance curve (R-curve). A typical R-curve is reported in Figure 3-29.

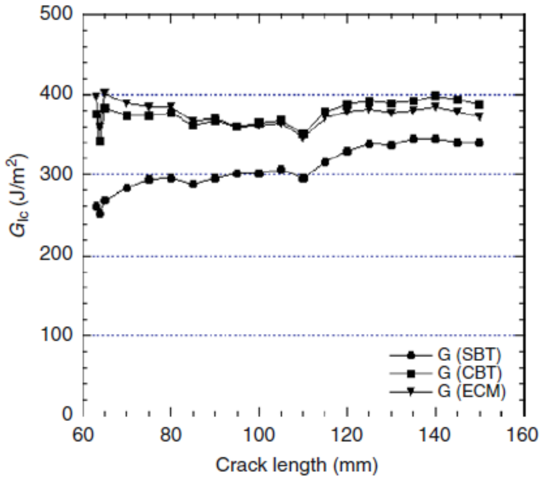

Figure 3-29 – Typical resistance curve (R-curve) for a DCB bonded with an epoxy adhesive [21].

For Metal Joints, Young's modulus of the adhesive, E_a, was considered equal to the experimental flexural modulus (E_{bend} =2447 MPa) and $\nu_a = 0.4$ as common in epoxies. Since the elastic modulus of Nylon 6,6 is approximatively the same of the epoxy resin, also the Young's modulus of the nanomat prepreg can be considered approximately the same of the neat adhesive.

For the adhesive modified with NBR/PCL nanomat, the Young's modulus was calculated with the rule of mixture, considering the Elastic Modulus and the volume fraction of each component:

- E_{PCL} =500 MPa, V_{PCL} = 0,4
- E_{NBR}=3,5 MPa, V_{NBR} = 0,6

The Elastic modulus of nanofibers was calculated as follows:

3.7

$$E_{fiber} = V_{PCL}E_{PCL} + V_{NBR}E_{NBR} = 202\ MPa$$

Considering that volume fraction of the nanofibers (V_F) is equal to 12%, the elastic modulus of the nanomodified adhesive layer was as follows:

3.8

$$E_a = V_F E_{fiber} + (1 - V_F)E_{Epoxy} = 2200\ MPa$$

For Composite Joints the adhesive Young's modulus, E_a, was considered equal 3500 MPa and ν_a = 0.4 as common in epoxies.

3.4 ELECTRICAL MEASUREMENTS

The electrical resistance of the composite samples modified with MWCNT and GNP was measured before and during the test between two points through the thickness, as shown in Figure 3-30. The electrodes were made of adhesive copper tape (conductive on both surfaces) attached to the CFRP external surface. The surface was manually abraded with sandpaper to remove the external resin thin layer and cleaned before affixing the electrodes. Copper tape was 5 mm wide and was placed along the joint width, avoiding contact with the sample edges. One terminal part of the electrode was formed by an extended section of copper adhesive tape which was folded back onto itself to create a flap, enabling the securement of an alligator clip connected to the B&K Precision 5491B multimeter (Figure 3-31) with a measurement rate of 25 readings/second. The connection between the electrode and the alligator clamp is showed in Figure 3-32. The multimeter was connected to a computer and controlled with the dedicated software. The final set -up is reported in Figure 3-33.

The electrical conductivity of the CFRP laminates was very high compared to that of the MWNT/epoxy or GNP/epoxy adhesives. Therefore, the contribution of the CFRP substrates to the bonded joint specimen resistance is negligible and the specimen resistance can be represented by the resistance of the nanomodified adhesive layer [16], [92]. Before starting the mechanical test, the sample was loaded with 20 N and the initial resistance R_0 was measured. The synchronization between the mechanical and electrical responses was done manually.

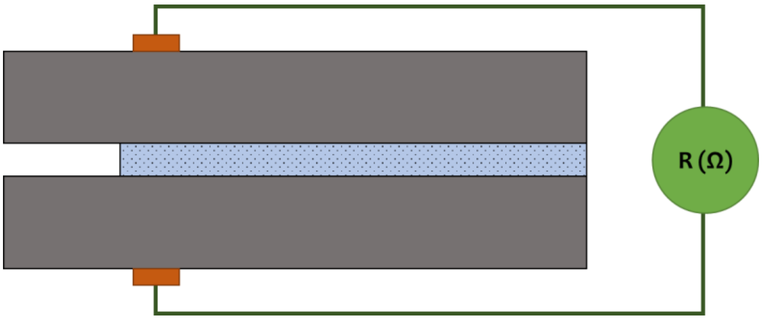

Figure 3-30 – Scheme of electrodes position

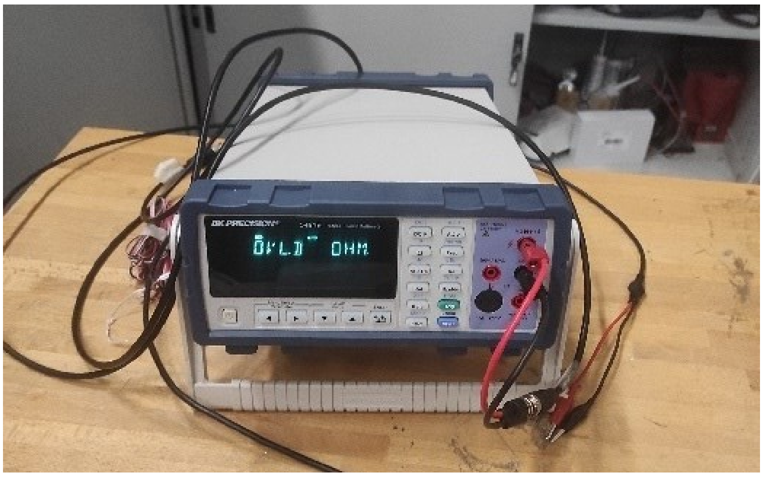

Figure 3-31 – B&K Precision 5491B multimeter

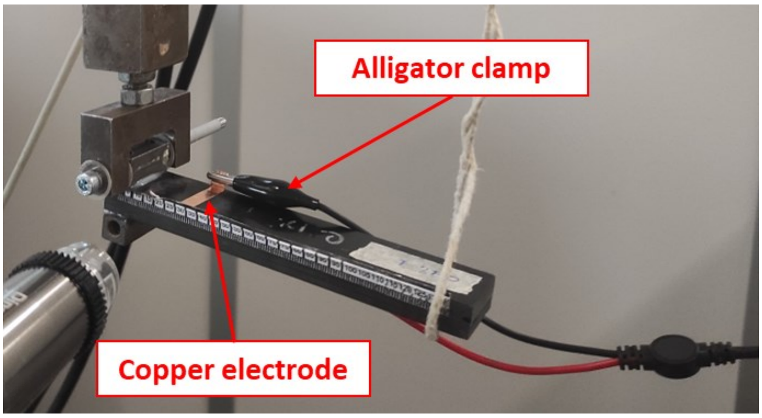

Figure 3-32 – Electrode and alligator clamp

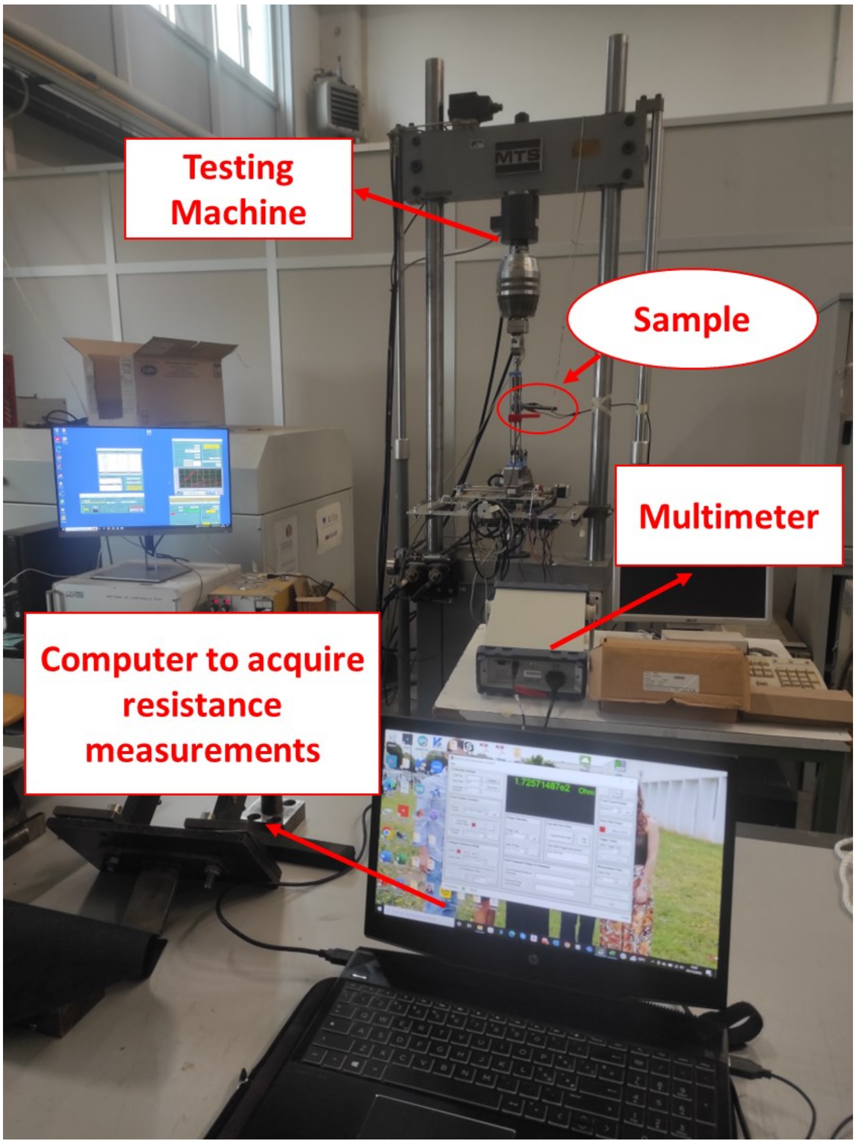

Figure 3-33 – Set-up for electrical measurements

3.5 FRACTURE SURFACE ANALYSIS

The fracture surface of the joint was analyzed using visual inspection and Scanning Electron Microscopy. Visual inspection is effective in determining whether the fracture is cohesive, adhesive, or mixed. SEM provides a more detailed analysis to identify the mechanism and site of failure.

The Scanning Electron Microscope (SEM) utilizes an electron beam of high energy in a vacuum, focused by a lens system and deflected to scan a sample area. A tungsten filament is usually excited by an electric current of the order of pA, which produces the electron beam. The beam-sample interaction leads to the generation of signals (X-rays, backscattered electrons, and secondary electrons), which are then received by the detectors and further processed to generate a high-resolution image.

The microscope consists of:

- Electron column with an electron gun for generating and emitting the electron beam.
- Condenser lenses that cause the beam to converge and pass through a focal point.
- Apertures that reduce and exclude extraneous electrons .
- A scanning system providing rastering of the electron beam across the specimen using deflection coils in the objective lens, a stigmator or astigmatism corrector located in the objective lens to reduce aberrations of the electron beam.
- A specimen chamber.
- Electron detectors to collect the signal generated from the interaction of the beam with the specimen.
- A vacuum system to maintain the vacuum inside the microscope.

The microscope used in this work as the Field-Emission SUPRA40 Zeiss SEM equipped with a GEMINI FESEM detection column.

3.6 DIFFERENTIAL SCAN CALORIMETRY (DSC)

Differential Scan Calorimetry (DSC) is a widely-utilized technique for determining the reaction degree of a material, its glass transition temperature, melting range for crystalline polymers, crystallization temperature, and other characteristics. This method is based on the calculation of the heat exchanged between a sample and a reference at specific temperatures and times. To ensure a constant coefficient of thermal exchange, the sample and reference are placed in special crucibles and subjected to a constant flux of inert gas. The instrument records a signal related to the evolution of the heat flow of the sample with respect to temperature or time. The sample mass should be of a few milligrams to minimize thermal inertia, especially when high heating or cooling rates are used. An example of a DSC thermogram is shown in Figure 3-34, which displays one exothermic and two endothermic peaks.

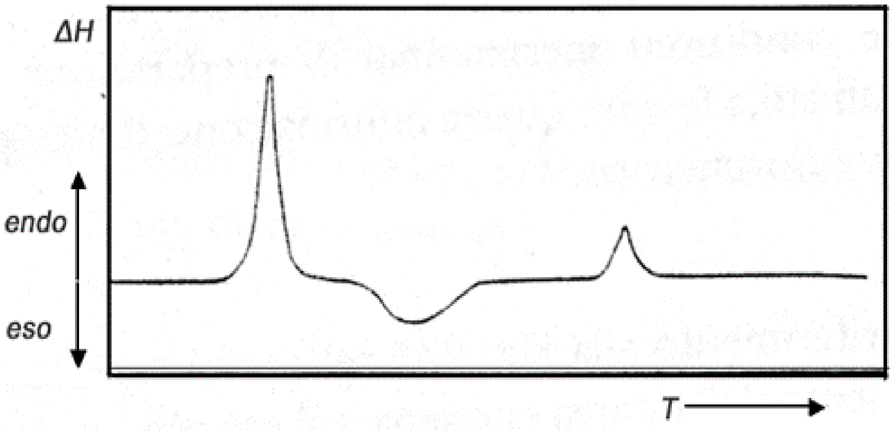

Figure 3-34 – Example of a DSC thermogram

The crystallization is an exothermic phenomenon that is detected as a deviation of the output signal of DSC from the baseline. The baseline is defined as the line which joins the two points at the beginning and at the end of the peak; it is determined by the thermal characteristics of the sample, and is not affected by the testing conditions. The area under a peak provides the heat flow ΔH related to that transformation. As a consequence, the heat exchanged by the sample in a time t is given by the integration of the peak once subtracted the baseline (BL):

3.9

$$H(t) = \int_{t_0}^{t} \left(\frac{dH}{dt} - BL \right) dt$$

Considering β a constant heating or cooling rate, the relation between time and temperature is:

3.10

$$T = T_0 + \beta(\mathrm{t} - \mathrm{t}_0)$$

3.11

$$dT = \beta dt$$

The final integration can be obtained changing the variable:

3.12

$$H(t) = \frac{1}{\beta} \int_{T_0}^{T} \left(\frac{dH}{dT} - BL \right) dT$$

There are two types of DSC systems: power compensation DSC and heat flux DSC.

In both cases, the thermograms report heat flow difference between the sample and reference as a function of temperature in a dynamic DSC or as a function of time if there are isothermal conditions.

In this work the DSC analyses are performed to evaluate if the curing cycle B (50°C for 80h) for Elantech® AS90/AW91 lead to a complete crosslinking. Moreover, the analysis is carried out on NBR/PCL nanomodified adhesive, cured at 70 °C and 50 °C to assess the influence of the nanofibers on the glass transition temperature of the adhesive system.

The DSC use the TA Instruments Q2000 Modulated DSC, connected to a RSC cooling system.

The method used is reported below:

- Equilibrate at 0°C
- Data storage on
- Heating Ramp 20°C/min up to 200°C.
- Mark end cycle 1
- Cooling ramp 20°C/min up to 0°C.
- Mark end of cycle 2
- Ramp 20°C/min up to 200°C.
- End of the procedure

3.7 STATISTICAL TOOLS

Different types of statistical tools are used in this study: analysis of variance (ANOVA) on a 2^4 factorial experiment is used to found the better surface treatment for the preparation of metal adherends. For this work of thesis, the software Minitab 19 was used for the ANOVA computation.

3.7.1 Analysis of Variance

Analysis of variance (ANOVA) was used to evaluate the statistical significance of different parameters. To this purpose, the F value, which is defined as the ratio of the variation between sample means over the variation within the samples, was calculated from the measured data. The critical F value, $F_{(a-1,\ a(n-1),\alpha)}$, can be estimate considering “a” the number of levels of the variance factor and “n” repetition for each level. It represents the F distribution value with degrees of freedom (a-1) and a(n-1), with at a confidence level α. The confidence level corresponds to the null hypothesis (equal means). When F is lower than the critical value, the population means are equivalent. On the contrary, when F value is higher than critical F, the population means are significantly different. The results of test hypothesis can be reported with the P-value that is the probability of the test statistic to be at least as extreme as the one observed, given that the null hypothesis is true. Usually, the P-value (and α) required to reject the test is defined before start the analysis. Usually, the null hypothesis is rejected if the test statistic exceeds the critical value α=0.05 or, if the P-value is smaller than 0.05.

ANOVA is a useful tool for the evaluation of the statistical significance of the factor or parameters that affect the final response of a process that can be modelled with 2^k factorial design.

A 2^k factorial design is characterized by k factor that can assume two level: high level (+) and low level (-). The statistical model of the experimental design includes the main effect, but also two-factor interactions, three-factor interactions, and one k-factor interaction. The different treatment may be written in standard order by introducing the factors one at a time. For example, a 2^4 design can be ordered in this way: (1), a, b, ab, c, ac, bc, abc, d, ad, bd, abd, cd, acd, bcd, and abcd. ANOVA is used to formally test for the significance of main effects and interaction. Table 3.11 report the analysis of variance for a 2^k factorial design with n replicates.

Table 3.11 – Analysis of variance for a 2^k factorial design with n replicates

Source of variation	Sum of square	Degree Of Freedom (DOF)
main effect		
A	SS_A	1
B	SS_B	1
…	…	…
K	SS_K	1
Two-factor interaction		
AB	SS_{AB}	1
AC	SS_{AC}	1
…	…	…
JK	SS_{JK}	1
K – factor interaction		
AB … K	$SS_{AB\dots K}$	1
Error	SS_E	$2^k(n-1)$
Total	SS_T	$N2^k-1$

SS_T is the Total Sum of Square. The Error Sum of Square can be calculated from this equation:

3.13

$$\mathrm{SS}_E = \mathrm{SS}_T - \mathrm{SS}_{FACTOR}$$

The sum of squares for an effect are determined from the contrast associated with that effect, using the following equation:

3.14

$$Contrast_{AB\ldots\ K} = (a \pm 1)(b \pm 1) \ldots (k \pm 1)$$

The sign in each set of parentheses is negative if the factor is included in the effect and positive if the factor is not included.

The effects value and the sums of squares can be calculated as:

3.15

$$AB \ldots K = \frac{2}{n2^k}(Contrast_{AB\ldots.\ K})$$

3.16

$$SS_{AB\ldots.\ K} = \frac{1}{n2^k}(Contrast_{AB\ldots.\ K})^2$$

The F values for each treatment can be calculated as ratio between factor and error mean square:

3.17

$$F_0 = \frac{MS_{FACTOR}}{MS_E}$$

where the mean square are calculated as follows:

3.18

$$MS_{FACTOR} = \frac{SS_{FACTOR}}{DOF_{FACTOR}}$$

3.19

$$MS_E = \frac{SS_E}{DOF_E}$$

MS_E estimates the variance of the experimental error.

4 NANOMODIFIED METAL JOINTS - RESULTS

This chapter investigates the effects of electrospun polymer nanofibre mats on the mode I fracture toughness of joints bonded with structural epoxies. Previous work [71]–[74] has shown that electrospun nylon nanofibres act as reinforcement and support for the adhesive layer. A laboratory procedure was developed to produce high-quality nano-fibres pre-impregnated with two-component, multi-purpose, low-toughness epoxy resin. Tests on DCB joints made with pre-impregnated nano-fibers showed that the nano-mat improves the fracture toughness of some low-toughness resins. With the same procedure, pre-pregs of nylon 6.6 and rubbery nano-fibers were realized using a two-component structural epoxy adhesive. Both types of nanomats were developed and produced at the University of Bologna. DCB joints were manufactured with pre-impregnated nanomats and s235 steel adherends. Since the improvement of interfacial adhesion is crucial for the evaluation of nanofibrous structures, metal substates were sandblasted using parameters optimized by evaluating the shear strength and fracture surfaces of SLJs. The most common methods for steel surface treatment include cleaning with solvents and mechanical abrasion by blasting [21], [169]. Mechanical abrasion on ductile surfaces, such as aluminum, can hinder the formation of a strong bond between adhesive and adherend. Chemical treatments are the most effective with aluminum alloys [162]. However, the execution of this type of treatment on a laboratory scale is very complex and has not ensured successful results. For this reason, steel has been preferred in this work.

Finally, DCB tests were performed to compare the mode I fracture toughness with and without the electrospun nanomats. Part of the results of this test campaign has been reported in [178], [179].The materials and methods used are described in the Chapter 4 .

4.1.1 Surface Treatment Optimization for Steel Adherends

Sandblasting is the simplest and most effective method to increase the surface roughness of the substrate to bond [162]–[166]. Roughness influences chemical bonds and mechanical interlocking between adhesive and adherends. Increasing the roughness also increases the contact area between adhesive and substrate and, therefore, chemical and mechanical interaction improves. The parameters that most influence the sandblasting process have been identified in the literature [167]–[169], which are the distance of the gun nozzle from the adherend surface, sandblasting time, pressure, and angle. For each parameter, two values were considered, as reported in Table 4.1.

Table 4.1 – Sandblasting parameters

Sandblasting parameters	Values	
Pressure (bar)	2	6
Distance (cm)	8	13
Angle (deg)	75	90
Time (s)	10	60

S235 steel specimens, with an area of 25 mm x 25 mm designed for treatment, were produced and sandblasted with one of the 16 combinations in Table 4.2. Five surface roughness values were measured for each specimen. The Figure 4-1 reports the morphology maps obtained with the profilometer, used to calculated the S_a of a sandblasted surface. Analysis of variance was used to assess the significance of the main effects and interactions. A significance level of 0.05 was selected for a two- side confidence interval. The results of the analysis are shown in Table 4.3 and Table 4.4.

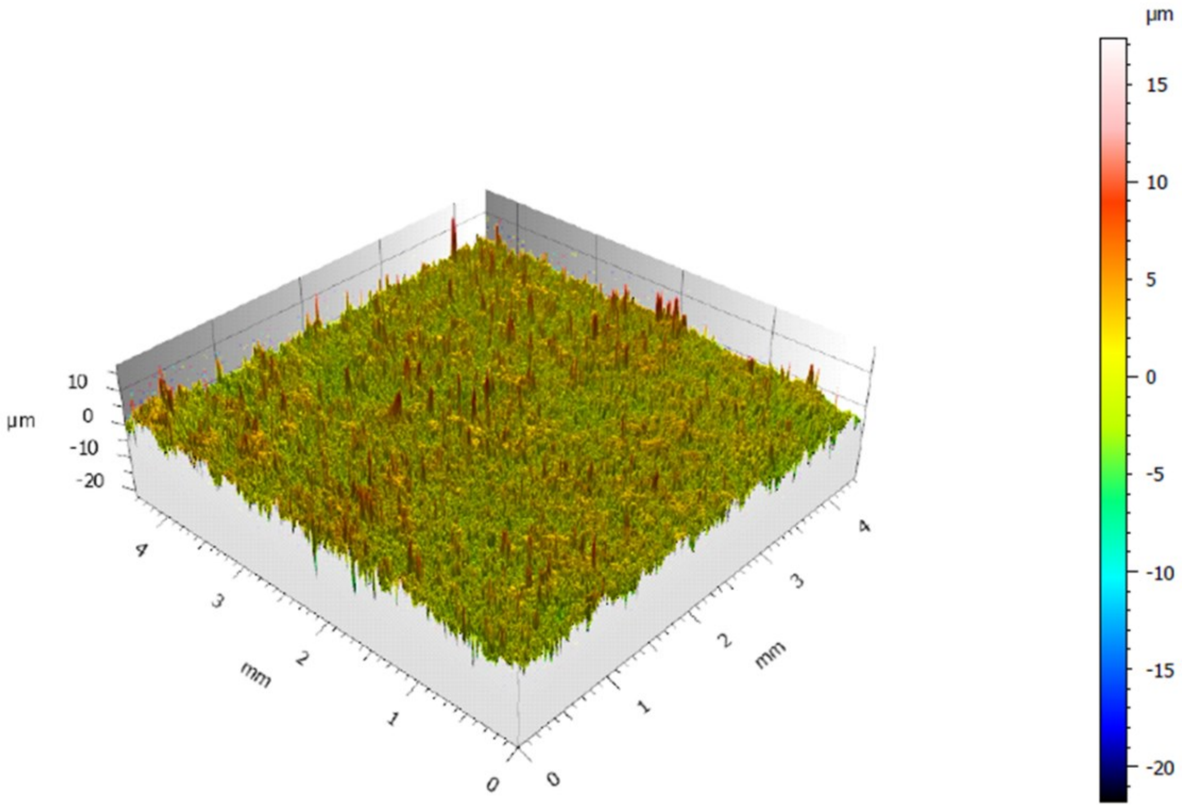

Figure 4-1 – Morphology Map, T1

Table 4.2 – Sandblasting treatment list

Treatment ID	Pressure (bar)	Distance (cm)	Angle (deg)	Time (s)
T1	2	8	75	10
T2	6	8	75	10
T3	2	13	75	10
T4	6	13	75	10
T5	2	8	90	10
T6	6	8	90	10
T7	2	13	90	10
T8	6	13	90	10
T9	2	8	75	60
T10	6	8	75	60
T11	2	13	75	60
T12	6	13	75	60
T13	2	8	90	60
T14	6	8	90	60
T15	2	13	90	60
T16	6	13	90	60

Table 4.3 – Coefficients table

Term	**Effect**	**Coef**	**SE Coef**	**T-Value**	**P-Value**
Constant		2.4255	0.0214	113.49	0.000
Pressure	0.9145	0.4573	0.0214	21.39	0.000
Distance	-0.1205	-0.0602	0.0214	-2.82	0.006
Angle	0.3595	0.1797	0.0214	8.41	0.000
Time	0.1535	0.0767	0.0214	3.59	0.001
Pressure*Distance	-0.0290	-0.0145	0.0214	-0.68	0.500
Pressure*Angle	-0.0690	-0.0345	0.0214	-1.61	0.111
Pressure*Time	-0.0810	-0.0405	0.0214	-1.89	0.062
Distance*Angle	0.2040	0.1020	0.0214	4.77	0.000
Distance*Time	0.1940	0.0970	0.0214	4.54	0.000
Angle*Time	-0.0430	-0.0215	0.0214	-1.01	0.318

Table 4.4 – Analysis of Variance – Sandblasting parameters

Source	DF	Seq SS	Contribution	Adj SS	Adj MS	F-Value
Model	10	21,9379	89,69%	21,9379	2,1938	60,03
Linear	4	20,0727	82,07%	20,0727	5,0182	137,32
Pressure	1	16,7262	68,38%	16,7262	16,7262	457,72
Distance	1	0,2904	1,19%	0,2904	0,2904	7,95
Angle	1	2,5848	10,57%	2,5848	2,5848	70,73
Time	1	0,4712	1,93%	0,4712	0,4712	12,90
2-Way Interactions	6	1,8653	7,63%	1,8653	0,3109	8,51
Pressure*Distance	1	0,0168	0,07%	0,0168	0,0168	0,46
Pressure*Angle	1	0,0952	0,39%	0,0952	0,0952	2,61
Pressure*Time	1	0,1312	0,54%	0,1312	0,1312	3,59
Distance*Angle	1	0,8323	3,40%	0,8323	0,8323	22,78
Distance*Time	1	0,7527	3,08%	0,7527	0,7527	20,60
Angle*Time	1	0,0370	0,15%	0,0370	0,0370	1,01
Error	69	2,5214	10,31%	2,5214	0,0365	
Lack-of-Fit	5	0.6821	2.79%	0.6821	0.1364	4.75
Pure Error	64	1.8394	7.52%	1.8397	0.0287	
Total	79	24,4594	100,00%			

The Pareto diagram in Figure 4-2 shows the absolute values of standardized effects with a reference line that indicates which are statistically significant. The position of the line depends on the significance level initially defined.

The Normal Probability plot in Figure 4-3 shows the standardized effects against the theoretical normal distribution. The non-significant effects are normally distributed with zero mean and tend to lie along a straight line, while significant effects have non-zero means and do not lie along a straight line. Positive effects increase the response when settings go from low to high value, while the contrary happens for negative ones. The distance the points must be from the straight line to be statistically significant depends on the level of significance initially defined.

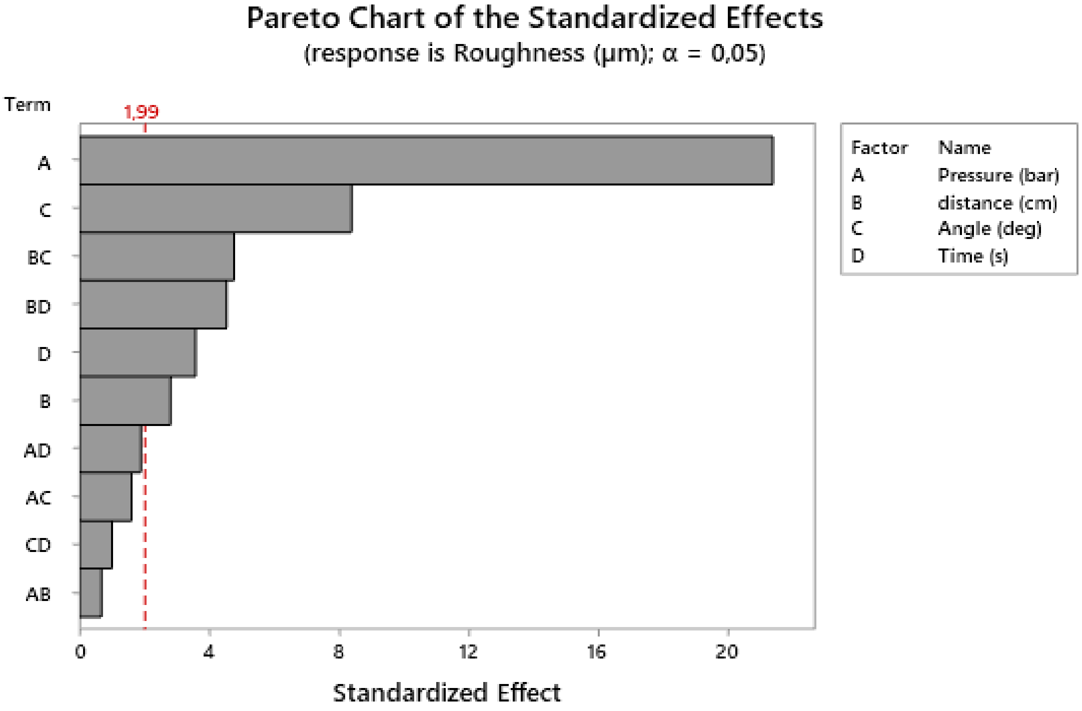

Figure 4-2 – Pareto Chart of sandblasting parameters standardized effects

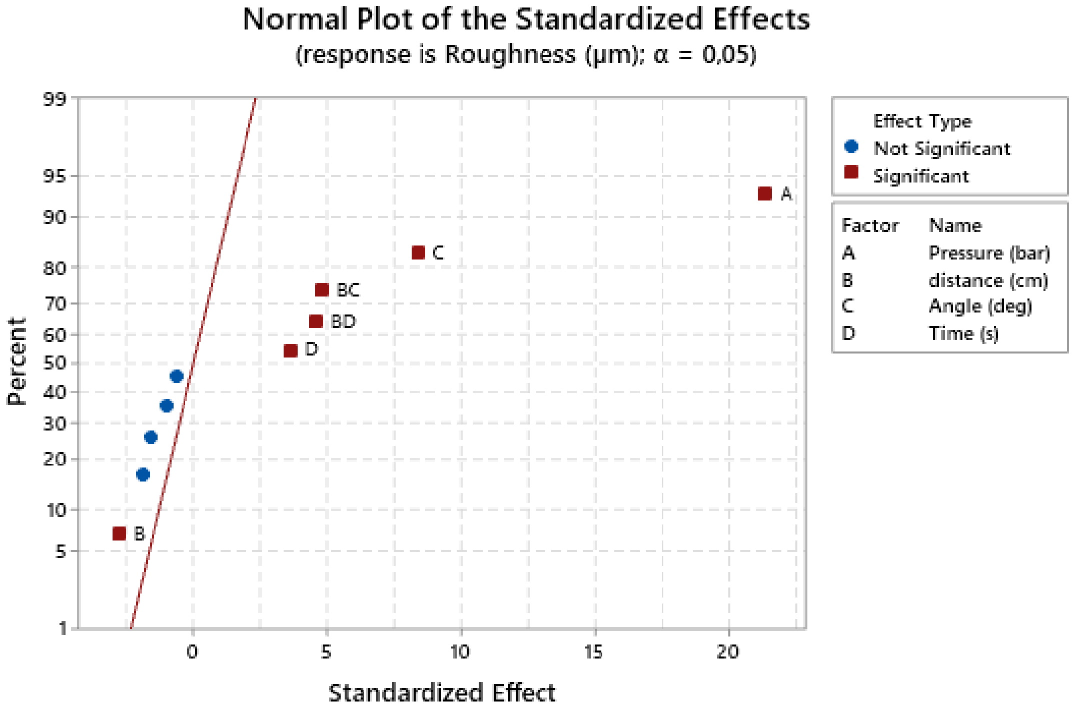

Figure 4-3 – Normal Plot standardize effects of sandblasting parameters

Figure 4-4 shows the graphs of the main effects to compare the changes in the means and identify the factors that most influence roughness. Pressure is the parameter that most influences roughness. In Figure 4-5 are the interaction diagrams Distance-Angle (BC) and Distance-Time (BD) showing more significant contributions. Non-parallel lines show that an interaction between the two effects occurs. It can be seen from the graph that, at the low-value distance, the roughness does not change much despite the variation in sandblasting angle and time. The response diverges, moving towards the high distance value.

Sandblasting processes performed at 90 deg for 60 s result in similar roughness values at both sandblasting distances.

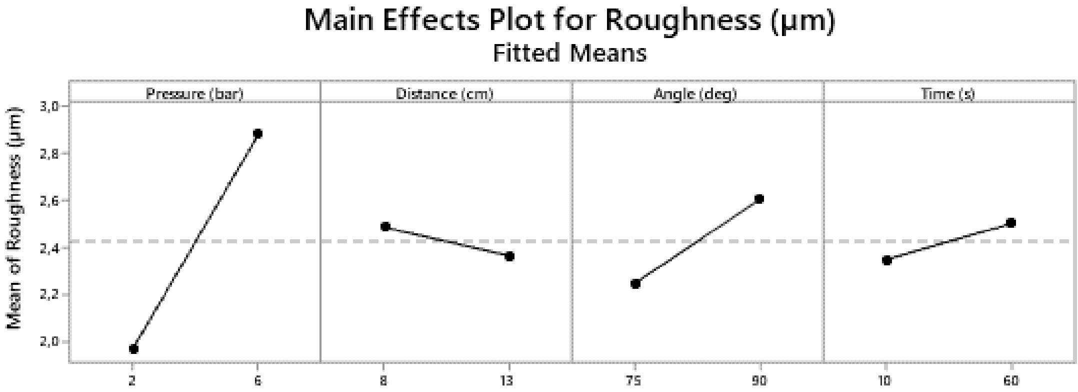

Figure 4-4 – Plots of Main Effect of sandblasting parameters

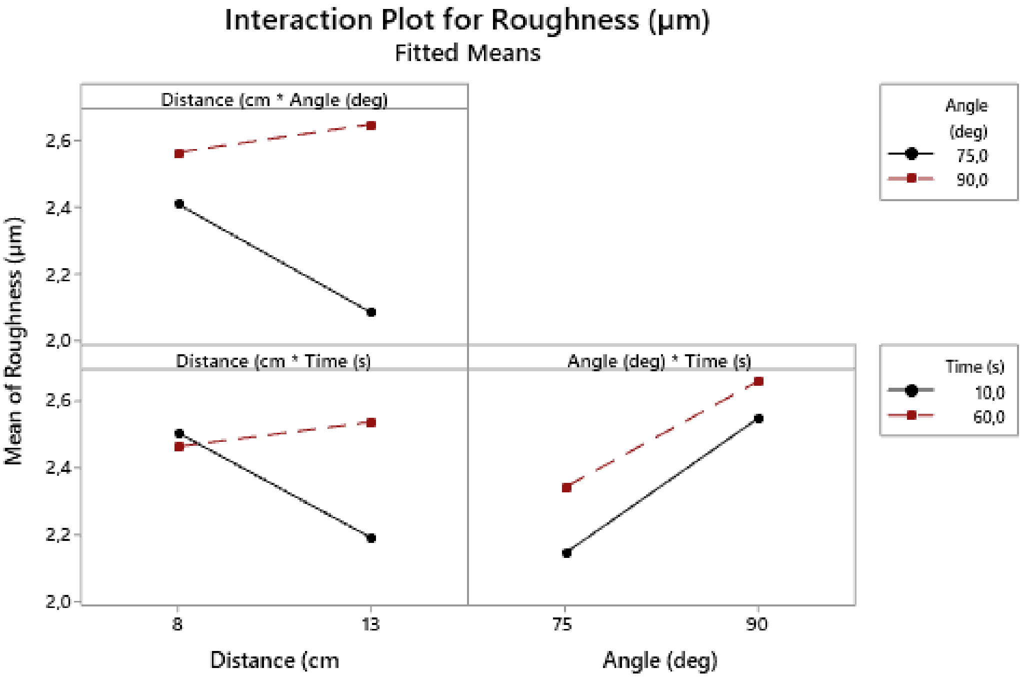

Figure 4-5 – Interaction Plots of sandblasting parameters

The equation describing the trend in roughness as the most significant effects change is as follows:

4.1

$$y = 2.43 + 0.46x_1 - 0.06x_2 + 0.18x_3 + 0.08x_4 + 0.10x_2x_3 + 0.10x_2x_4$$

The terms in

Table 4.5 are in the fitted equation that models the relationship between Y and the X variables:

Table 4.5 – Variables in model equation of sandblasting parameters

Sandblasting parameters	X variable	Low values	High value
Pressure (bar)	x_1	-1	1
Distance (cm)	x_2	-1	1
Angle (deg)	x_3	-1	1
Time (s)	x_4	-1	1

A normal probability plot of the residuals is shown in Figure 4-6. The points on this plot lie reasonably close to a straight line, lending support to our conclusion that x_1, x_2, x_3, x_4, x_2x_3, and x_2x_4 are the only significant effects and that the underlying assumptions of the analysis are satisfied.

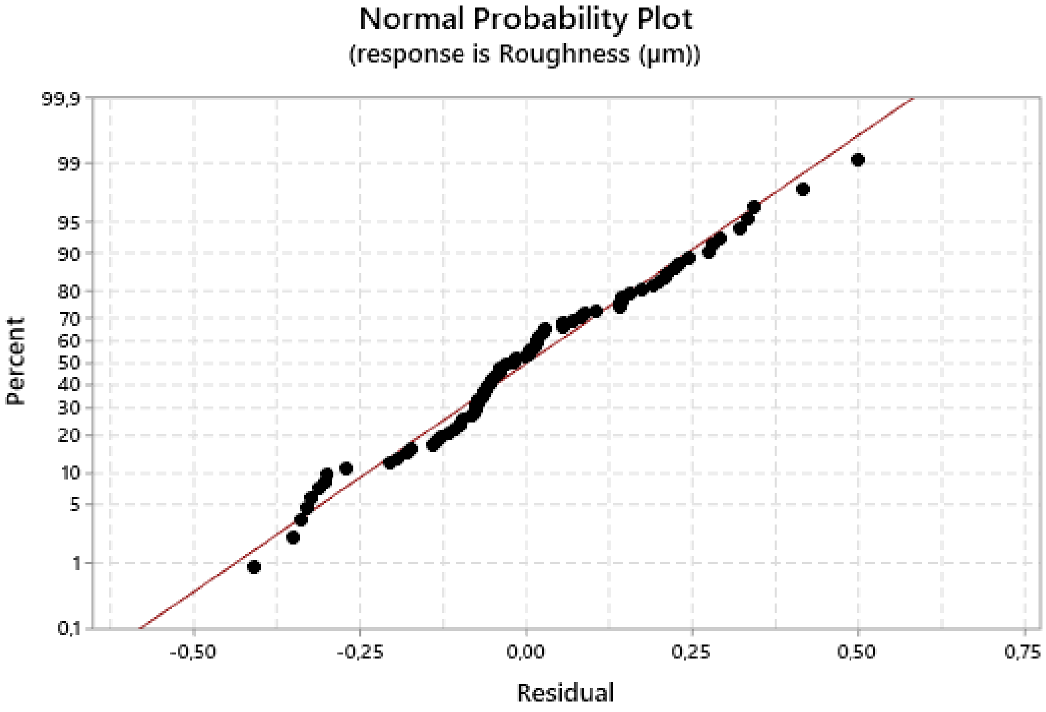

Figure 4-6 – Normal probability plot of residuals for roughness

Following the analysis performed, the five optimal solutions are in Table 4.6.

Table 4.6 – Best sandblasting treatments

Treatment ID	Pressure (bar)	Distance (cm)	Angle (deg)	Time (s)	Predict Roughness (μm)	Average Roughness (μm)
T16	6	13	90	60	3.27	3.32
T6	6	8	90	10	3.04	3.02
T14	6	8	90	60	3.00	2.91
T8	6	13	90	10	2.93	2.86
T2	6	8	75	10	2.88	3.22

In order to achieve good roughness, it is important to use high pressures, specifically 6 bar. Angles of 90 deg result in good blasting. The distance, in the range 8- 13 cm, does not seem to influence the result very much. The influence of time also does not seem to be significant.

For each combination, three SLJs were realized. The Table 4.7 shows for each treatment the average roughness, the average shear strength with its standard deviation, and the type of failure obtained. Parameter optimization was performed on SLJ joints to facilitate test execution. DCB tests require more time for both specimen preparation and the pre-cracking phase. Although the loading mode differs from DCB, SLJ is a valid mean to evaluate the effectiveness of surface treatment and epoxy adhesion on sandblasted steel substrates. The adhesive used for the SLJs is Elan- tech®AS90/AW91. The supplier's suggested standard curing cycle is 70 °C for 5 hours.

In Figure 4-7 it is shown a SLJ that fails with type of fracture clearly cohesive.

Table 4.7 – SLJs tests results

Treatment ID	Pressure (bar)	Average Roughness (µm)	Average Shear strength (MPa)	Standard deviation (MPa)	Failure mode
T1	2	1.68	20.56	0.49	Adhesive
T2	6	3.22	23.05	0.24	Adhesive
T3	2	1.40	23.52	1.19	Adhesive
T4	6	2.44	22.35	0.58	Adhesive
T5	2	2.25	19.63	2.45	Adhesive
T6	6	3.02	21.24	1.20	Cohesive
T7	2	2.07	20.05	2.03	Cohesive
T8	6	2.86	20.53	0.74	Cohesive
T9	2	2.04	22.67	1.60	Adhesive
T10	6	2.83	24.18	2.05	Cohesive
T11	2	1.89	21.75	0.25	Adhesive
T12	6	2.61	23.86	1.34	Cohesive
T13	2	2.07	25.41	1.28	Cohesive
T14	6	2.91	25.14	2.32	Cohesive
T15	2	2,33	21,34	0.55	Cohesive
T16	6	3,32	20,35	0.40	Cohesive

In general, the shear strength is ranged from 19 to 24 MPa. It can be seen from Figure 4-8 that, as shown above, higher pressure values lead to higher roughness values. Cohesive failure also seems to occur more frequently at higher roughness values. Shear strength values also seem to be higher for medium-high roughness levels.

Figure 4-7 – SLJ exhibiting a cohesive type of fracture [179].

The strength of joints sandblasted with T10, T12, T13, and T14 treatments is relatively high. In particular, the treatment T10, T12, and T14 are realized at 6 bar for 60s, suggesting that this parameters combination is useful to obtain cohesive failure and high strength, although with higher standard deviations.

For this reasons T14 was selected as the final sandblasting process.

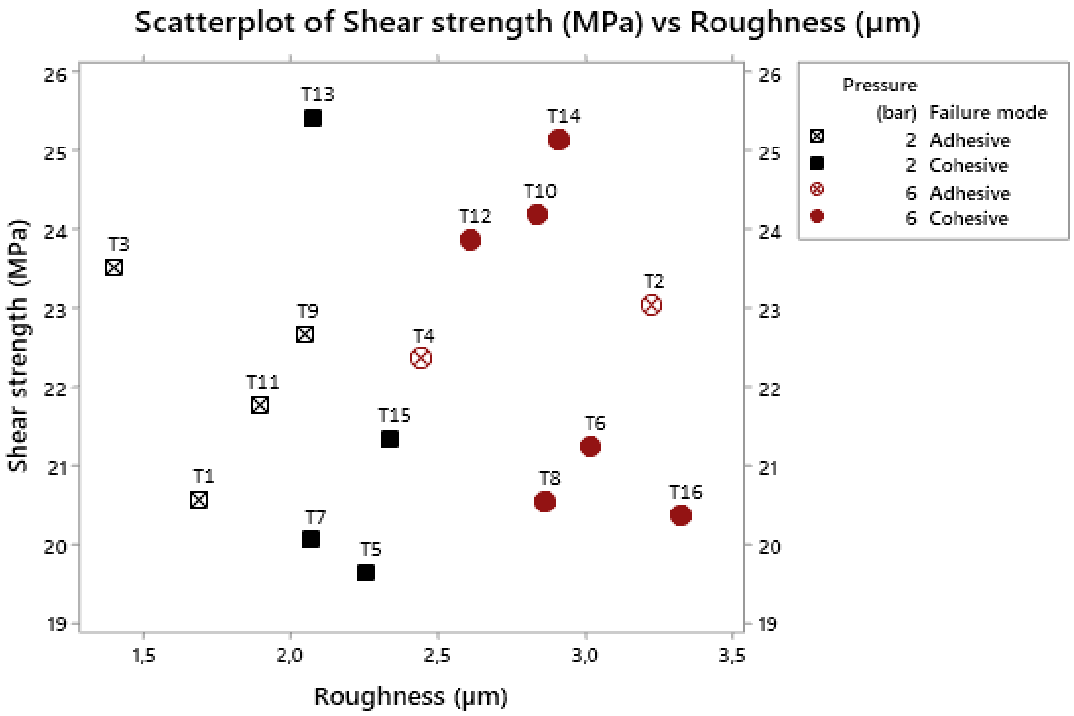

Figure 4-8 – Scatter plot Shear Strength vs Roughness

4.1.2 Virgin Adhesive

This section reports the results of mechanical characterization and fracture surface analysis of the virgin DCB joints. DSC analysis were also carried out on some resin samples subjected to the two curing cycles employed in the experimental work.

4.1.2.1 DSC Analysis

DSC analyses were performed on the adhesive cured with cycles A and B before performing the mechanical tests on the DCB joints, to assess the possible differences in the thermal response of the adhesive cured with both curing cycles. The cycles description is reported in Chapter 3 and Table 4.8.

Table 4.8 – Curing cycle for metal DCB joints

Cycle ID	Temperature	Time	Pressure
A (standard)	70 °C	5 h	Atmospheric
B	50 °C	80 h	Atmospheric

The DSC analyses in Figure 4-9 show that the lower-temperature curing cycle, cycle B, allows for achieving a good cross-linking degree. The T_g is around 68 °C, already from the first scan. The signal is followed by an enthalpic relaxation peak, which may be due to the slow cross-linking process that sets the polymer chains in a well-ordered arrangement.

The T_g of the adhesive cured at 50 ° is slightly lower but comparable with the T_g of the resin cured at 70 °C, which reaches 74 °C. This difference is reflected by the flexural modulus, reported in Chapter 2. The epoxy resin cured with cycle A shows E_{bend} equal to 2447 ± 30 MPa, while the adhesive cured with cycle B shows a slightly lower E_{bend} (2330 ± 23 MPa). However, the slow curing cycle leads to a complete crosslinking, as confirmed by no presence of exothermic signals, and T_g is comparable with the one of the curing cycle A, suggested by Elantas. Maybe a curing cycle of 80 hours is even too long.

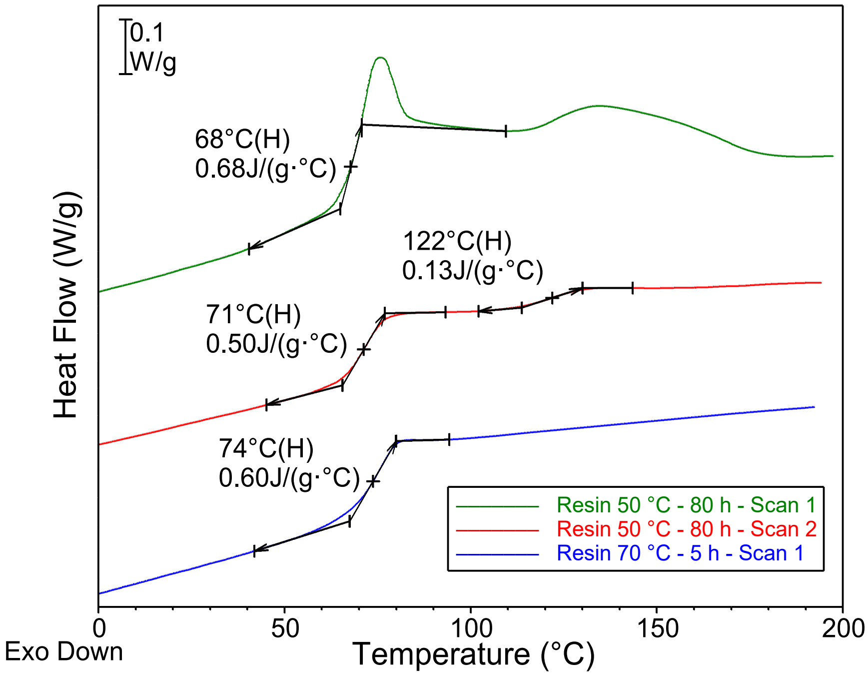

Figure 4-9 – DSC analysis on Elan- tech® AS90/AW91 cured with cycles A and B [179]

4.1.2.2 *Mechanical Characterization*

This paragraph reports the results of the mechanical test campaign conducted on virgin joints cured according to cycles A and B. The purpose of the tests is to provide a data set on unmodified joints to compare the results obtained on nanomodified samples. The virgin joints investigated in this paragraph were manufactured with the same adhesive but subjected to two different curing cycles, called A and B. Samples cured with curing cycle A are named V70, while V50 joints are cured with cycle B.

Figure 4-10 and Figure 4-11 show the load against CMOD for V 70 and V 50 samples, respectively. The specimens V 70 reach maximum load peaks around 1900 N, corresponding to a CMOD value of 0.5 mm. Specimen V 70 - 1 exhibits similar behavior to the other V 70, although the first load peaks are not shown due to a data storage error. In the V 50 samples, the rapid crack propagation causes the complete joint failure at CMOD values of about 1,5 mm, before the end of the test. On the contrary, the virgin specimens cured at 70 °C do not reach a complete failure during the DCB test. The load peaks of V 50 samples are roughly under 800 N, except for V 50-3, which reaches 1300 N. However, they exhibit a common trend after CMOD values of around 0,5 mm, as the curves show comparable values. In any case, V 50 specimens withstand lower loads than V 70 joints.

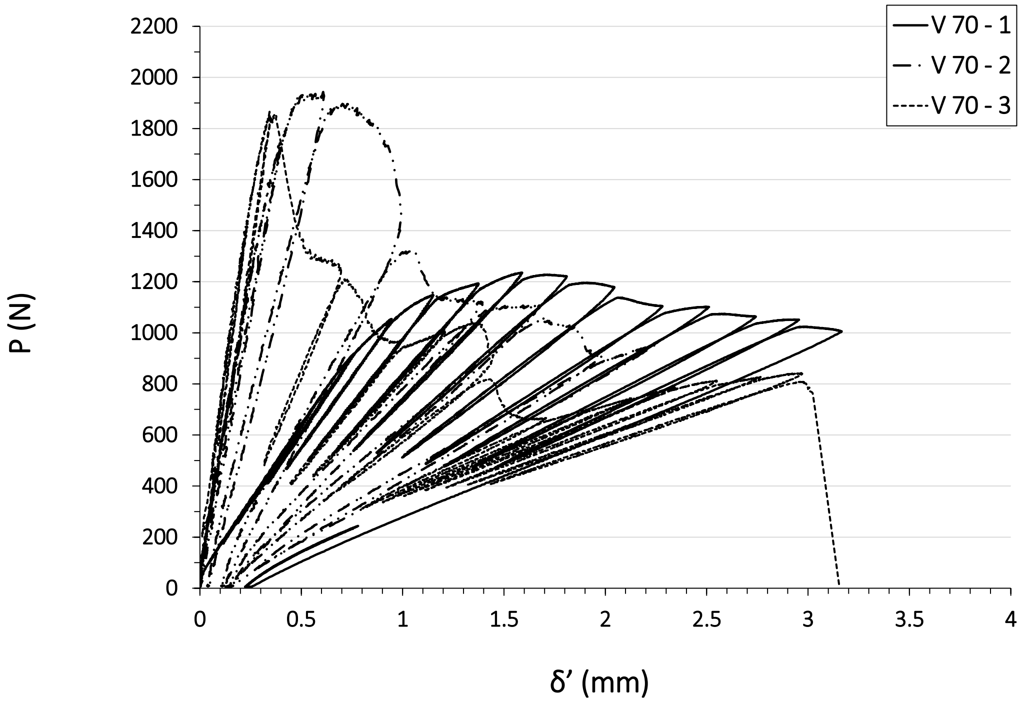

Figure 4-10 – Load against CMOD (δ') for virgin specimens V 70, cured with cycle A

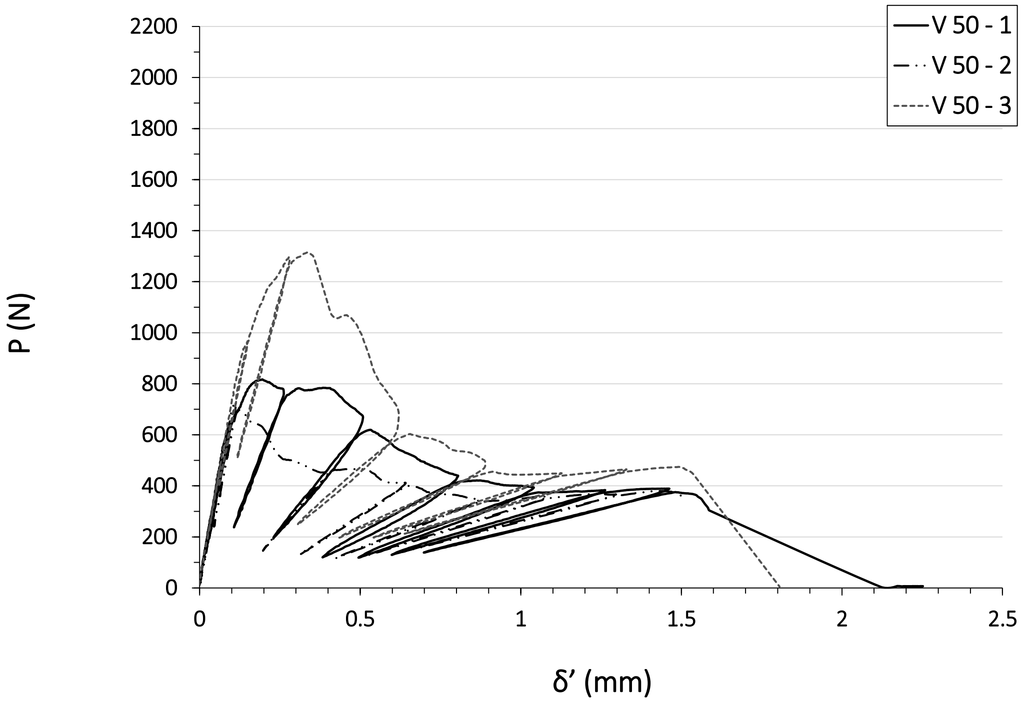

Figure 4-11 – Load against CMOD (δ') for virgin specimens V 50, cured with cycle B

Figure 4-12 shows the R-curves of V 70 and V 50 joints, respectively represented with dashed and solid curves. respectively. The black markers indicate the G_{IC} values considered for the average fracture toughness calculation, during the steady-state crack propagation phase after the maximum peak load, for each series of DCBs. The grey markers represent the values not included in this calculation.

The analysis of the results shows that the V 70 samples exhibit scattered but higher G_{IC} values, while the V 50 joints exhibit the lowest values, although the R curves have an increasing trend after the interval Δa 40÷50 mm. The average G_{IC} value of the virgin joints cured at 70 °C is 1.05 ± 0.28 N/mm, and the average G_{IC} value of the specimens cured at 50 °C is 0.22 ± 0.07 N/mm, resulting in an 84% reduction in fracture toughness compared to the V 70 specimens. The curves of V 50 are flat, with Δa between 40 and 50 mm. Only V 50-3 specimen reaches higher values at the beginning of crack propagation, but still below 0.4 N/mm.

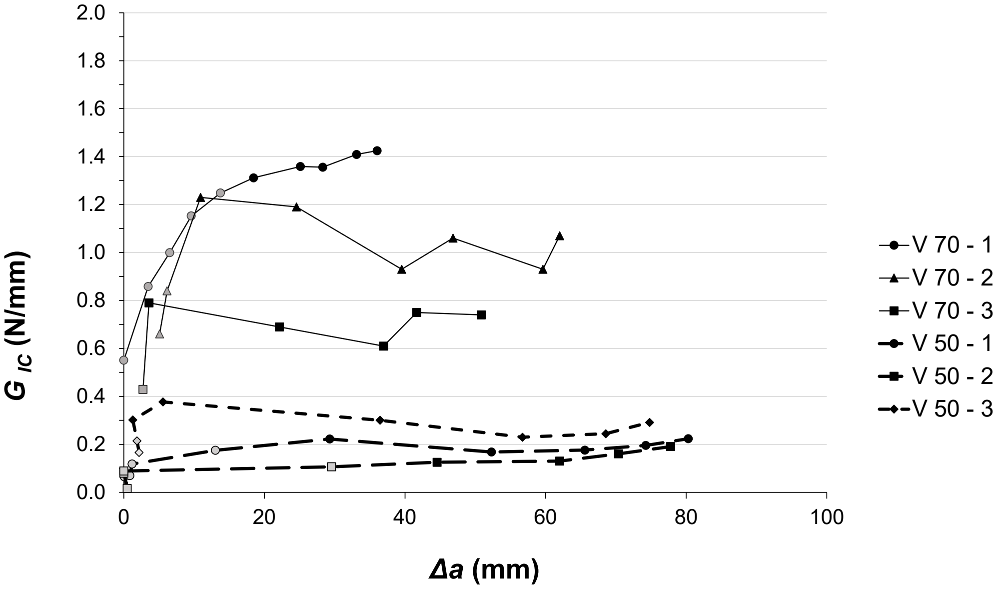

Figure 4-12 – R-Curves for virgin samples cured at 70 °C (V 70) and 50 °C (Ny 50).

4.1.2.3 Fracture Surface Analysis

This paragraph reports the morphological analysis on virgin joints cured according to cycles A and B. The results of the morphological analysis are related to the results obtained from the mechanical characterization presented in the previous paragraph.

Figure 4-13 and Figure 4-14 show the fracture surfaces of V 70 and V 70 samples, respectively. The failure modes of the V 70 specimens are mainly cohesive, which indicates that the surface treatments applied result in good interfacial adhesion for the joints subjected to standard curing cycle. Cohesive failure is evident in specimens in which a layer of adhesive is present on both bonded surfaces. In the case of V 50 specimens, regions of adhesive failure are evident because the adhesive is not uniformly present on both bonded surfaces. The fracture surfaces of the V 50 joints show adhesive failure, although the surface preparation of the adherends is the same for the V 70 samples and the DSC analysis suggests complete adhesive cross-linking. The V 50 samples show weak interfacial adhesion and exhibit adhesive failure and low fracture toughness values compared to V 70 ones, as a consequence. In sample V 50-1, the crack initially deflects from one adherend to another before propagating along the interface of a single adherend. In sample V 50 - 2, crack propagation occurs mainly along the same interface, with little deviation. Finally, the last specimen exhibits the most irregular fracture surface, with several crack deviations from one substrate to the other. The corresponding fracture toughness is slightly higher than the one of the other two specimens.

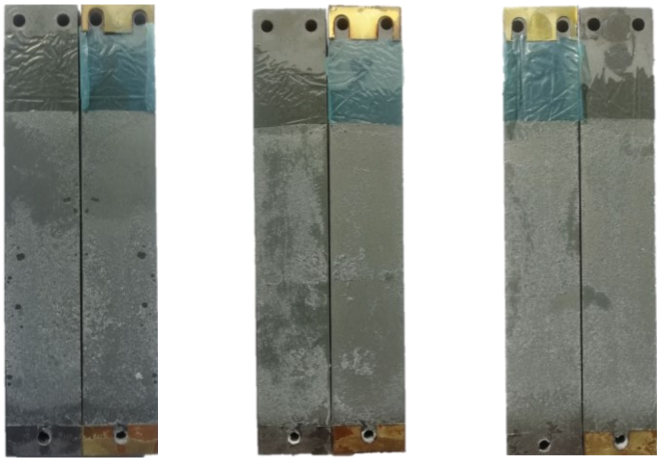

V 70 - 1 *V 70 - 2* *V 70 - 3*

Figure 4-13 – Fracture surface of V 70 samples

V 50 - 1 *V 50 - 2* *V 50 - 3*

Figure 4-14 – Fracture surface of V 50 samples

Figure 4-15 shows SEM images of the V 70 -2 fracture surface, the central area of the joint. The analyzed area is characterized by numerous micro-dimples in the adhesive layer caused by ductile failure mechanisms that result in high fracture toughness values. The fracture surface of sample V 50 - 3, shown in Figure 4-16, appears less rough and has fewer micro-dimples. No ductile failure mechanisms occur even because the crack propagates at the metal/adhesive interface.

Since DSC analyses demonstrate that the curing cycle B also provides high epoxy cross-linking, the possible different rheological profile of the adhesive could justify the poor interfacial adhesion. In particular, the resin viscosity should reach lower values during curing cycle A before gelling. Therefore, the wettability of the metal surfaces could be better than for cycle B. However, in addition to evaluating viscosity profiles at 70° and 50 °C, a specific surface treatment may be required for non-standard cure conditions.

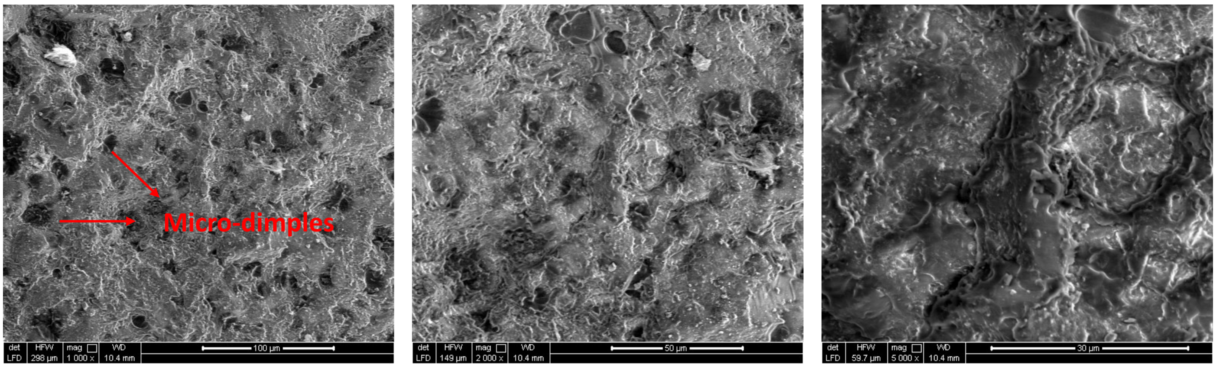

(a) (b) (c)

Figure 4-15 – SEM images of fracture surface of V 70 -2 at different magnification: 1000X (a), 2000 (b), and 5000X (c)

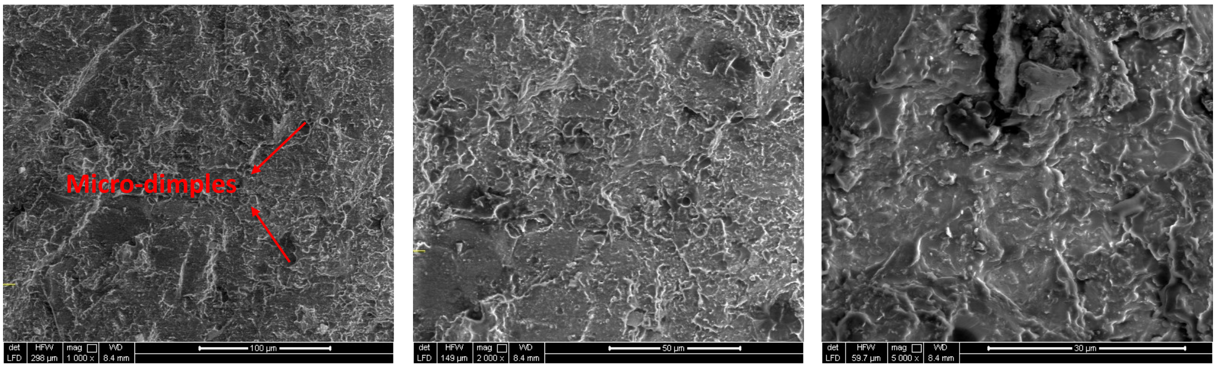

(a) (b) (c)

Figure 4-16 – SEM images of fracture surface of V 50 - 3 at different magnification: 1000X (a), 2000 (b), and 5000X (c)

4.1.3 Nylon Nanofibers

This section reports the results of the quality assessment of the integration of the Nylon 6.6 nanomat within the adhesive layer, the mechanical and morphological characterization of the bonded joints to investigate the effect of the nanofibers on the fracture toughness of the system.

4.1.3.1 Impregnation Test

An impregnation test was carried out to evaluate if the epoxy system impregnates properly the Nylon 6,6 nanomat, following procedure in Chapter 2.

Two Nylon 6.6 nanomats that differ in thickness were evaluated. The aim is to understand if the thickness of the nanomat may influence the quality of the final prepreg. The average thicknesses of the nanomats are 50 µm and 140 µm as shown in Figure 4-17 and Figure 4-18. This test was performed before the manufacture of virgin DCBs because it is intended to define the final thickness of the adhesive layer of the nanomodified joints to replicate this thickness on virgin joints.

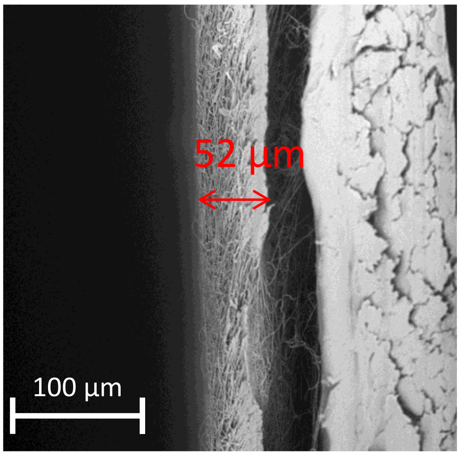

Figure 4-17 – Nylon 6.6 nanomat , on release paper, with thickness of 52 µm. The thickness measured at the specified point is 52 µm

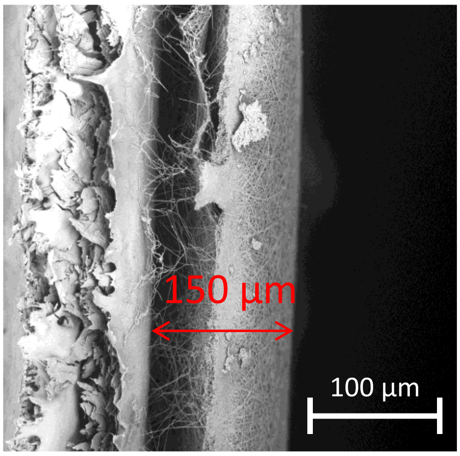

Figure 4-18 – Nylon 6.6 nanomat, on release paper, with average thickness of 140 µm. The thickness measured at the specified point is 150 µm

The applied curing cycle is the cycle A.

The S235 steel bonded joints were treated with formic acid to dissolve the nylon nano-fibres. The cross-sections of the joints were then subjected to SEM analysis after polishing.

The final thickness of the nano modified joints is similar to the neat nanomats, as shown in Figure 4-19. It is evident that in both cases, the nano-fibres fill the entire bondline thickness and reach both sides of the adherends. Figure 4-20 and Figure 4-21 show more in detail the adherend/adhesive interface of the joints modified with 50 µm and 140 µm nanomats, respectively.

The fibers appear uniformly distributed throughout the bondline. In addition, no air bubbles that could cause crack initiation were noted. This preliminary test confirms that the resin used is appropriate for nanometric impregnation and enables the production of high-quality prepregs, at least for both thicknesses analyzed.

Nanomat with an average thickness of 140 µm was preferred for the bonded joints because it allows easier removal of exceeding resin and is easier to handle during impregnation.

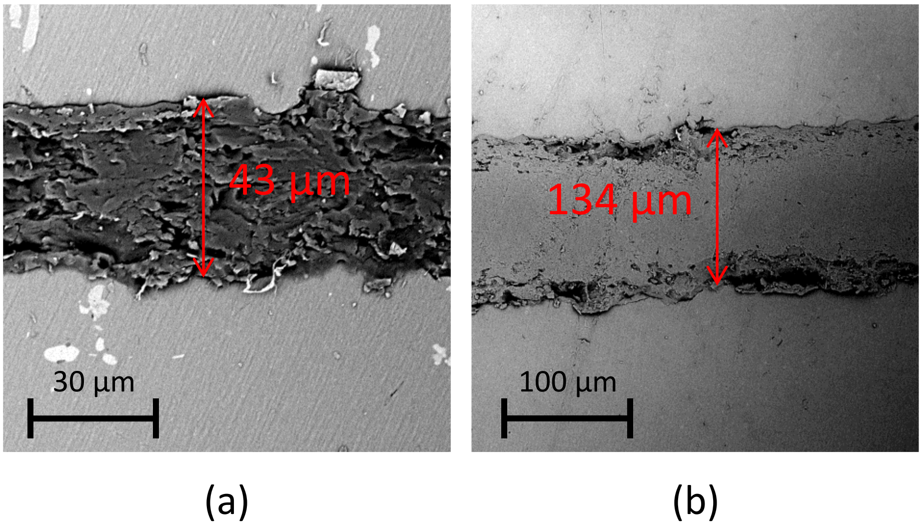

Figure 4-19 – Adhesive layer sections of samples modified with nylon nanomat of (a) 50 µm and (b) 140 µm

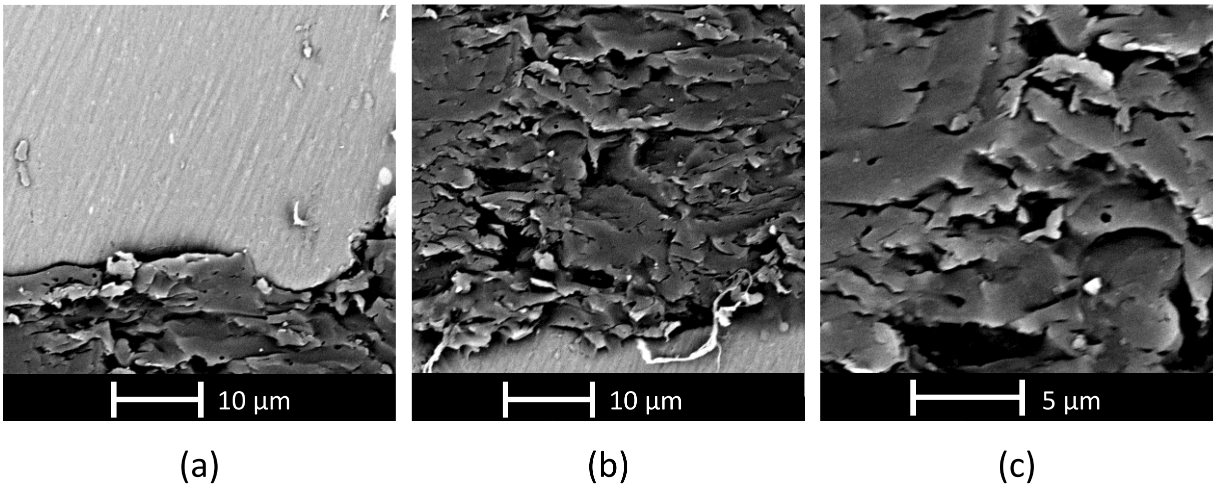

Figure 4-20 – SEM images of cross-section of adhesive layer modified with 50 µm Nylon 6.6 nanomat

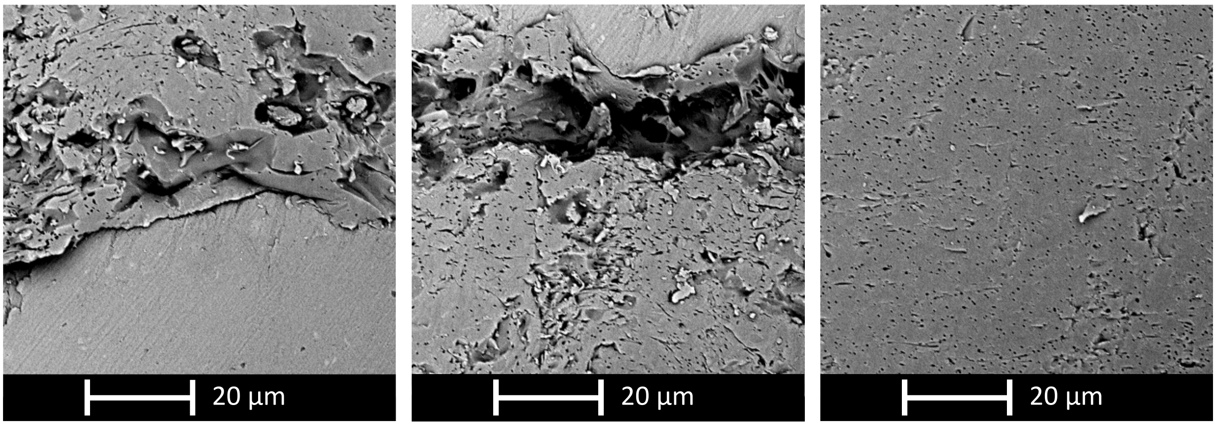

(a) (b) (c)

Figure 4-21 – SEM images of cross-section of adhesive layer modified with 140 µm Nylon 6.6 nanomat [178]

4.1.3.2 Mechanical Characterization

The experimental campaign aimed to evaluate the influence of the nylon 6.6 nanofibres embedded in the adhesive layer over the mechanical response of the bonded joints during quasi-static tests. The results of the DCB tests will be related to the results of the surface morphological analysis. The nanomodified joints are compared with virgin joints subjected to the same curing cycle.

Figure 4-22 shows the load against CMOD for Nylon 6.6 nanofibre-modified specimens, identified as Ny 70. Nanomodified specimens withstand lower loads than virgin ones cured with the same cycle (V 70). The maximum load peaks are below 1200 N, and all the samples broke completely at CMOD values of about 2 mm. This behavior suggests that the crack propagates rapidly within the specimens, and the nanostructure does not enhance the fracture toughness, on the contrary, it tends to decrease the joint strength. The negative effect of the nanofibres, which reduce the load peak by 42% compared to virgin joints with the same initial defect length, is evident.

Figure 4-23 shows the R-Curves of Virgin and Nylon 6.6 nanomodified joints. The dashed curves refer to the joints bonded with the pre-impregnated nanofibres, while the solid curves refer to the virgin ones. The black markers indicate the G_{IC} values considered for the average fracture toughness calculation, during the steady-state crack propagation phase after the maximum peak load, for each series of DCBs. The grey markers represent the values not included in this calculation. The virgin joints exhibit an average G_{IC} value of 1.05 ± 0.28 N/mm, while this value is 0.38 ± 0.07 N/mm for the nanomodified joints. The R-Curves confirm the negative contribution of the Nylon 6.6 nanomat on the fracture toughness of a high-strength, high-tenacity structural adhesive. The R-Curves of the nanomodified DCB show low initial G_{IC} values that increase before stabilizing during crack propagation. The R-Curves become flat after crack propagation in the range of 10-20 mm for almost all Ny 70 samples. This behavior is typical of DCB that undergo brittle fracture.

Virgin DCB samples reveal higher but more scattered. Nevertheless, the nanomodified samples showed a 64% reduction in fracture toughness compared to the virgin ones.

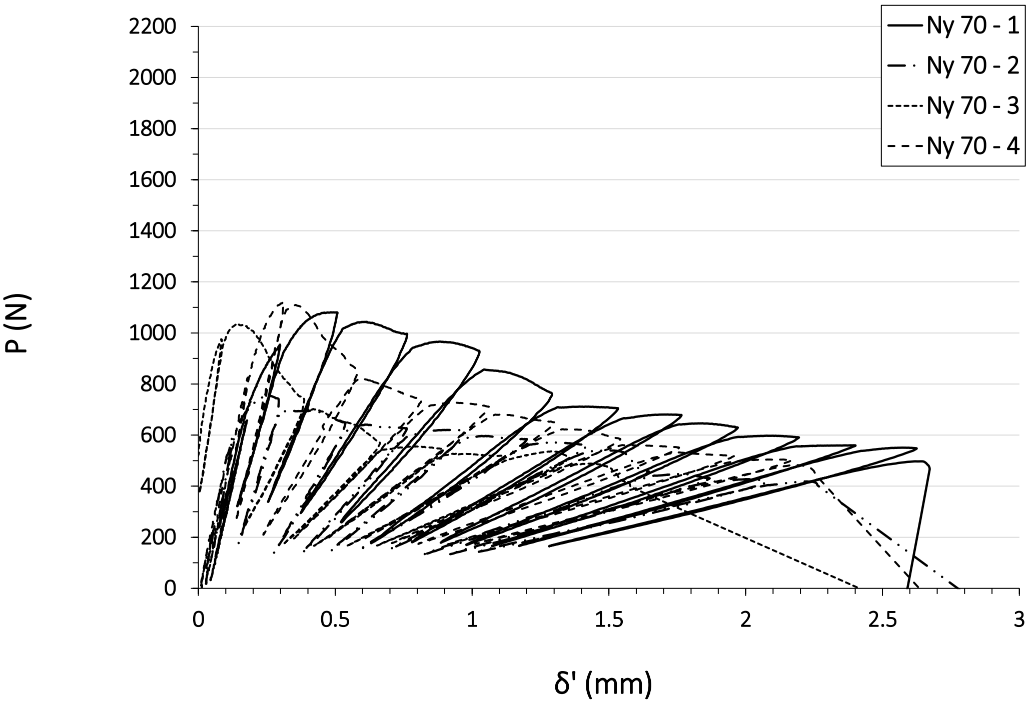

Figure 4-22 – Load against CMOD (δ') for Nylon 6.6 nanomodified specimens

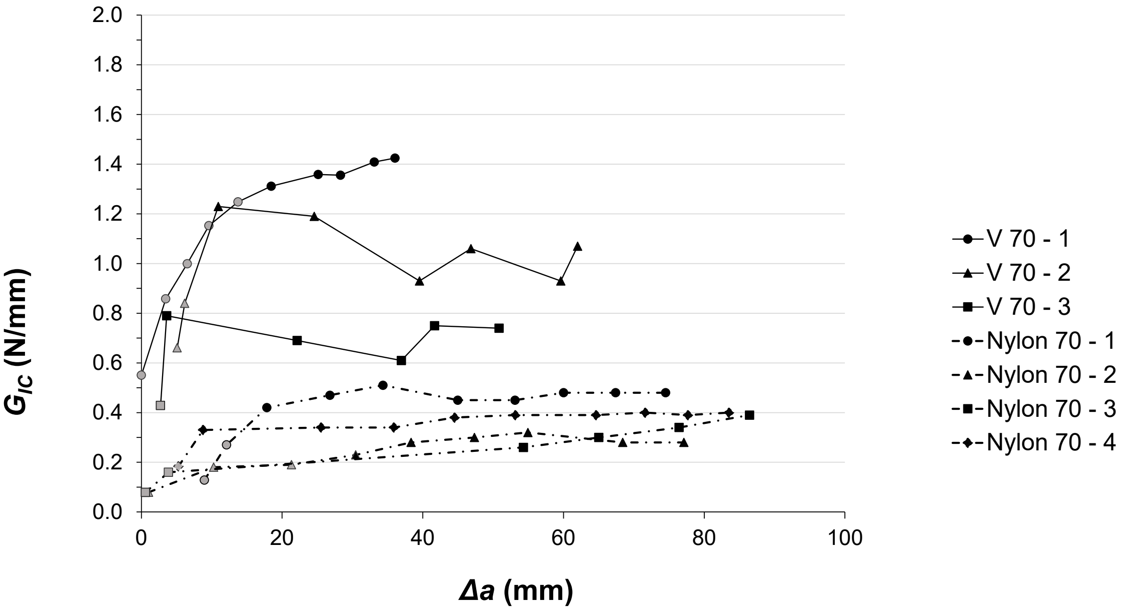

Figure 4-23 – R-Curves for Virgin (V 70) and Nylon 6.6 nanomodified (Ny 70) specimens [178].

4.1.3.3 Fracture Surface Analysis

This paragraph reports the comparison of morphological analysis on virgin and Nylon 6.6 nanomodified bonded joints to understand the phenomena that act in the adhesive layers.

Figure 4-24 show the fracture surfaces of Ny 70 samples. The failure modes of virgin joints are mainly cohesive, while they appear mixed and with some crack deflections to the adhesive-adherends interface for the nanomodified ones. This phenomenon is evident in the Ny 70 - 1 and Ny 70 - 4 samples, which have slightly higher G_{IC} values, close to 0.5 N/mm, but still low compared to virgin ones.

The fracture surface of the V 70-2 reveals the presence of micro-dimples in the adhesive layer, which proves that a ductile fracture mechanism occurred in the neat resin. In Figure 4-25 are reported the fracture surface of nylon nanomodified samples that look different from the surfaces of virgin sample. From these images it appears that exfoliation of the nanomaterial occurs without any pull-out or fiber bridging.

Furthermore, the absence of micro-dimples suggests that the adhesive does not undergo plastic deformation, resulting in lower fracture toughness compared to virgin samples.

The fracture surface of Ny 70 – 4 sample, in Figure 4-26, is similar to that of Ny 70 – 1. The two samples present comparable G_{IC} values in the analyzed area, at Δa values between 40 and 50 mm, considering the same initial crack.

This behavior was contrary to the trend detected in previous works, which focused on medium to low-toughness epoxies. Unlike previous studies where the joints exhibit adhesive failure mode, a good interfacial adhesion is achieved here. For this reason, the failure mechanism could be attributed to the nanofiber/epoxy interaction.

The nylon nanofiber integration has a detrimental effect on the mechanical performance of the joint because introduces defects and reduces plastic deformation around the crack tip.

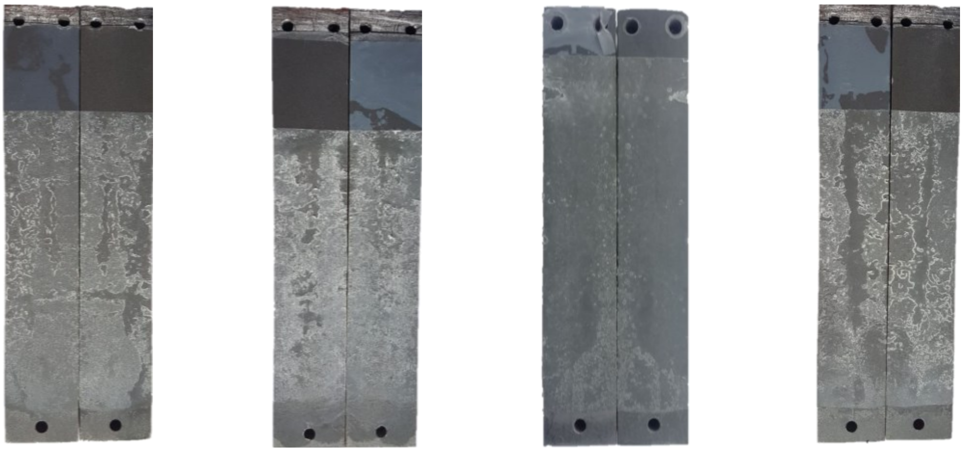

Ny 70 - 1 *Ny 70 - 2* *Ny 70 - 3* *Ny 70 - 4*

Figure 4-24 – Fracture surface of Ny 70 samples

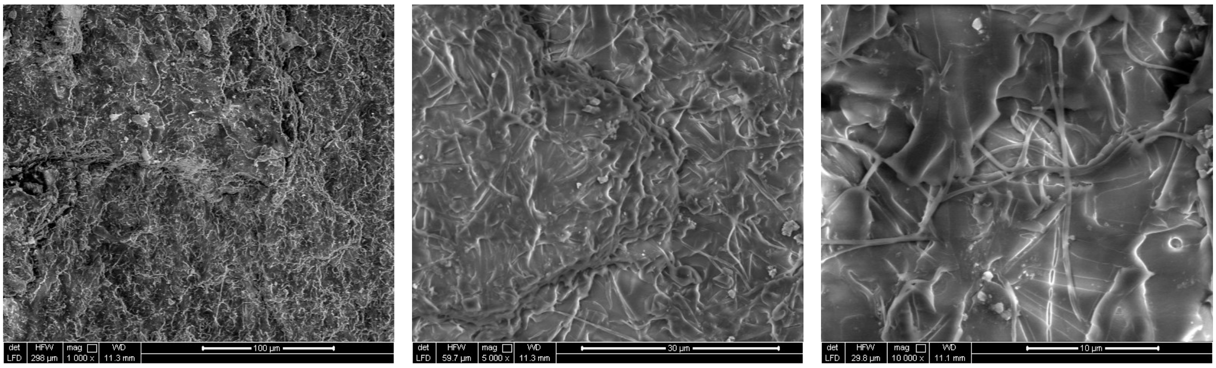

(a) (b) (c)

Figure 4-25 – SEM images of fracture surface of Ny 70 -1 at different magnification: 1000X (a), 5000 (b), and 10000X (c) [178]

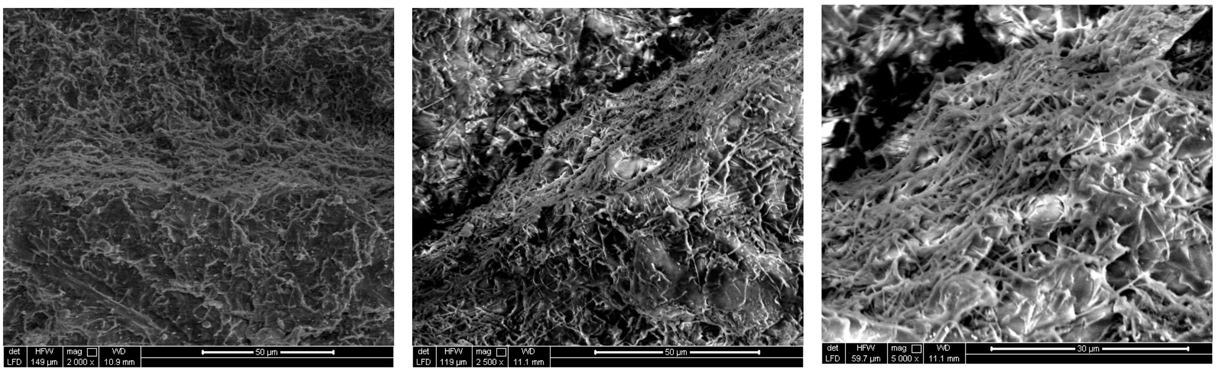

(a) (b) (c)

Figure 4-26 – SEM images of fracture surface of Ny 70 -4 at different magnification: 1000X (a), 5000 (b), and 10000X (c)

4.1.4 Rubbery Nanofibers

This section reports the results of the quality assessment of the addition of the NBR/PCL nanomat to the epoxy adhesive and the mechanical characterization of the bonded joints to investigate the effect of the rubbery nanofibers on the fracture toughness of the system.

4.1.4.1 DSC Analysis

DSC analyses were performed on the adhesive modified with NBR/PCL nanomat and cured with both cycle A and B to assess possible differences in the thermal response of the nanomat cured with cycle B compared to cycle A. Samples modified with rubbery nanofibers and cured with curing cycle A are named NBR/PCL 70, while NBR/PCL 50 joints are cured with cycle B.

The DSC analysis in Figure 4-27 shows the comparison between the two resin samples. In both cases, an endothermic peak in the temperature range typical of PCL melting [173] is present. The peak is expected for the sample cured at 50 °C, while it is unexpected for the sample cured at 70 °C. The step transition that follows the endotherm signal refers to the resin glass transition temperature and must be analysed.

In general, the crystalline fraction of PCL melts at temperatures at which the resin cured at 70 °C is already in an almost glassy state, and is unable to blend with the neighbour epoxy matrix, even when brought above its melting.

On the other hand, the rubbery phase can mix with the thermoset matrix because of its higher mobility. Specimen cured at 70 °C shows, in fact, a lower T_g due to a higher degree of mixing of the rubber with the epoxy matrix. NBR/PCL 50 exhibits a similar T_g to the virgin sample subjected to the same treatment, as the nanofibre structure is preserved because of the lack of melting of the PCL.

It was not possible to correctly determine the T_g of the nanomodified samples due to overlapping signals.

In conclusion, cure cycle A does lead to the partial melting of the nanofibrous structure and allows the rubbery phase to blend with the epoxy matrix. Cure cycle B, on the other hand, allows the nanofibre structure to be preserved as it is conducted at temperatures below the PCL melting range. Both curing temperatures are not able to promote full PCL miscibility with the epoxy resin, resulting in phase-separated PCL fraction within the epoxy matrix after curing.

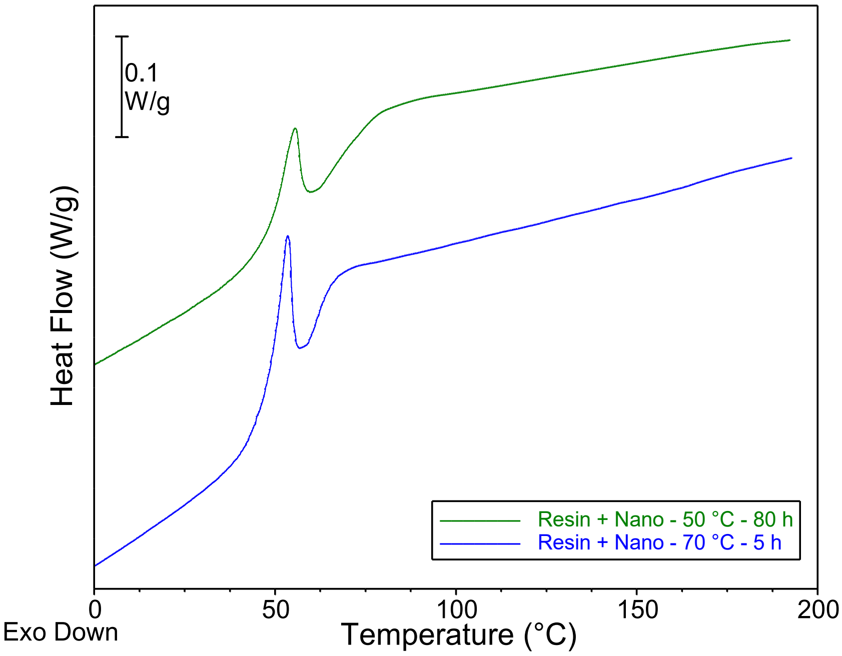

Figure 4-27 – DSC NBR/PCL 70 and NBR/PCL 50 [179]

4.1.4.2 *Impregnation Test*

An impregnation test was carried out to evaluate the capability of the epoxy system to impregnate properly the rubbery NBR/PCL nanomat, using both curing cycle A and B.

The effectiveness of the impregnation of two rubbery nanofibre prepregs, placed between two S235 steel substrates and subjected to the cure cycles A and B was evaluated by SEM analysis on bonded joints section.

Figure 4-28 shows the cross-sections of joints cured at 70 °C for 5 hours. The curing cycle A causes the NBR/PCL blend to mix with the epoxy resin and subsequent matrix toughening. This phenomenon could explain the more irregular surface of the specimen. Figure 4-29 shows the cross-section of the sample cured at 50 °C for 80 h, which exhibits smother surfaces. In both cases, there are no air bubbles trapped in the adhesive, the interface shows good adhesion between prepreg and adherends, and the adhesive layer thicknesses is similar to that of the neat nanomats.

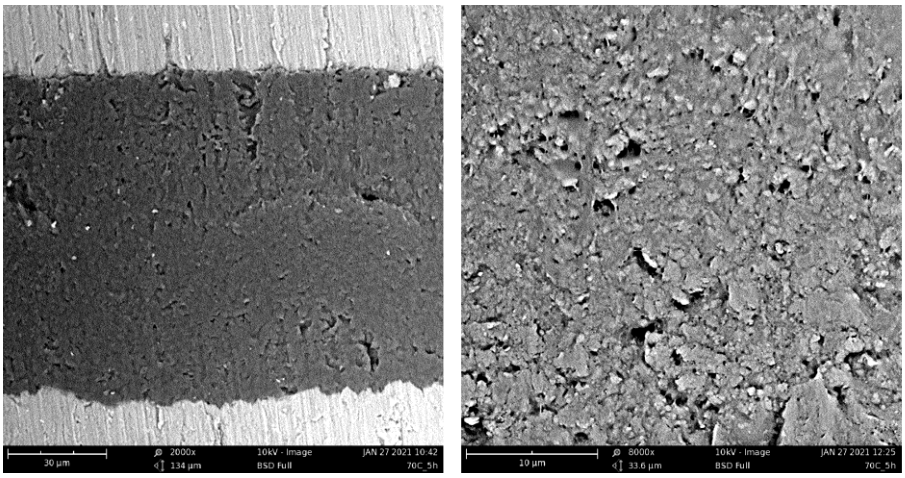

(a) (b)

Figure 4-28 - SEM images of cross-section of adhesive layer modified with NBR/PCL cured at 70 °C for 5h [179]

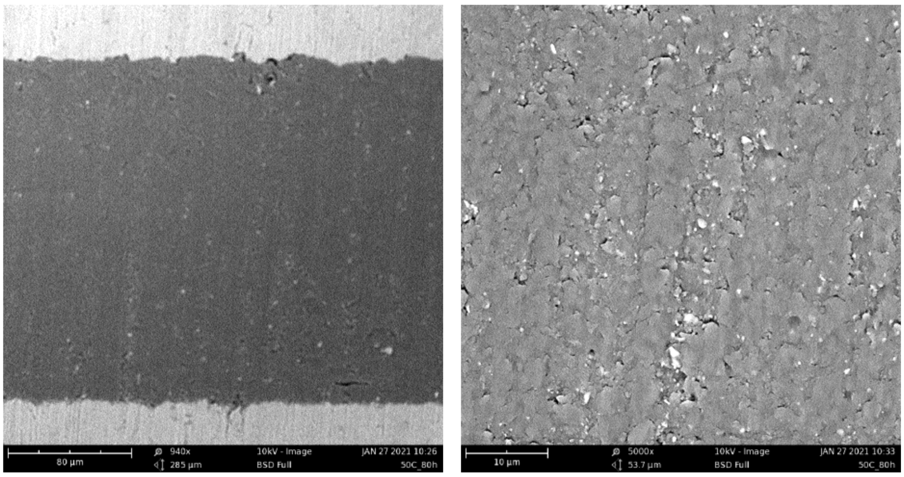

(a) (b)

Figure 4-29 - SEM images of cross-section of adhesive layer modified with NBR/PCL cured at 50 °C for 80h [179]

4.1.4.3 Mechanical Characterization

The experimental campaign is aimed to evaluate the influence of the NBR/PCL nanofiber embedded in the adhesive layer. The mechanical response of the bonded joints during quasi-static tests is analyzed and later compared with resulting fracture surface.

The nanomodified joints are compared with virgin joints subjected to the same curing cycles: **Errore. L'origine riferimento non è stata trovata.** and **Errore. L'origine riferimento non è stata**

trovata. show the load against CMOD for NBR/PCL nanofibre-modified specimens cured at 70 °C and 50 °C, respectively.

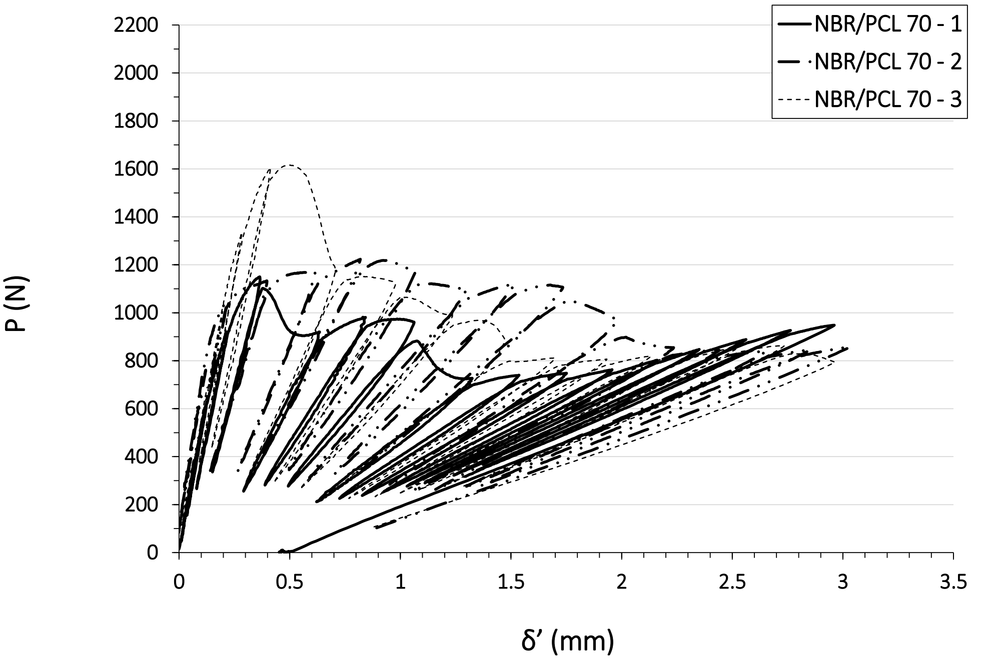

Figure 4-30 – Load against CMOD (δ') of nanomodified NBR/PCL 70 specimens

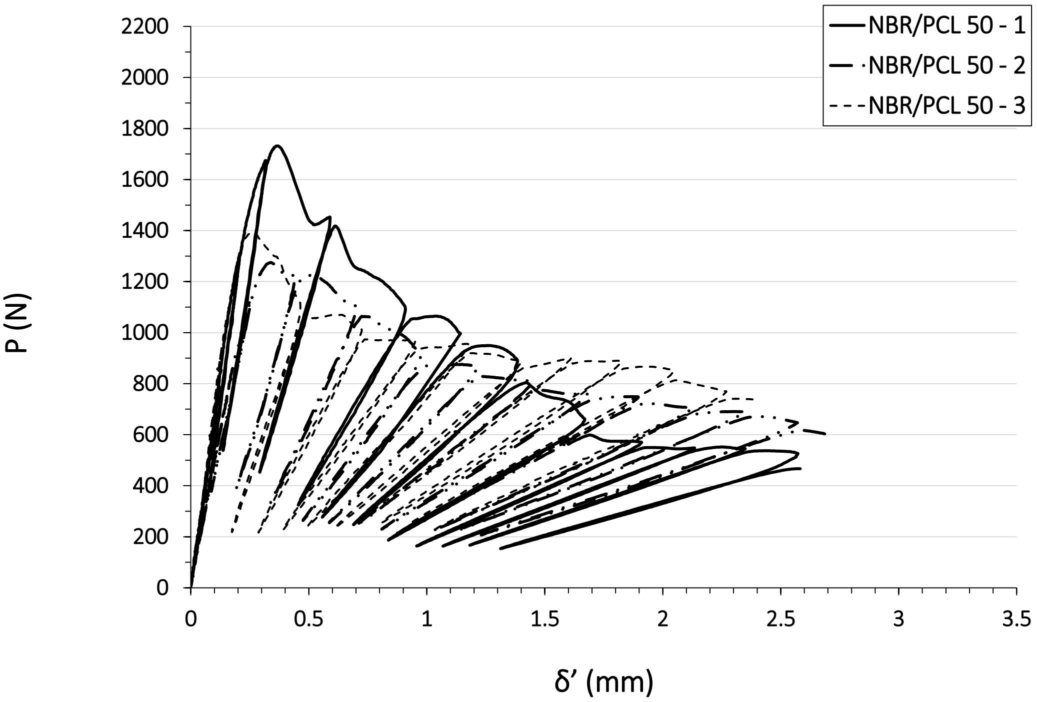

Figure 4-31 – Load against CMOD (δ') of nanomodified NBR/PCL 50

The NBR/PCL 70 samples show lower loads than the V 70. The NBR/PCL 70 and NBR/PCL 50 samples show similar peak values, but the load tends to decrease more steadily for the joints cured at 50°C. The NBR/PCL 50 samples fail completely when the clip-gage reached approximately 2.5 mm, near the end of the test, suggesting lower resistance to crack propagation than the virgin and nanorinforced samples cured at 70 °C. In contrast, the NBR/PCL 50 joints appear better to resist crack propagation than the virgin V 50 joints, which fail at CMOD values of only 1.5 mm.

The graphs show the detrimental effect of the rubbery nanofibers on fracture resistance of the joints cured under standard conditions., while the nanomat seems to enhance the mechanical performance of joints cured at 50 °C, under non-standard conditions.

Figure 4-32 and **Errore. L'origine riferimento non è stata trovata.** report R-curve that compare fracture toughness of virgin and nanomodified sample. The black markers identify the G_{IC} values considered for the calculation of the average fracture while the grey markers represent the excluded ones. The two set of nano modified joints exhibit almost the same fracture toughness value (G_{IC} = 0.63 ± 0.12 N/mm for N 70 and G_{IC} = 0.58 ± 0.07 N/mm for N 50). The R-curve of virgin DCB joints cured at 70 °C has a more scattered behavior compared the R-curve of the nanomodified samples that exhibit a rising trend. However, the average fracture toughness of the adhesive is negatively affected by the nanomat integration: the G_{IC} value is reduced by 45% compared with the V 70 joints. If compared with V 50 samples, NBR/PCL 50 shows a performance improvement.

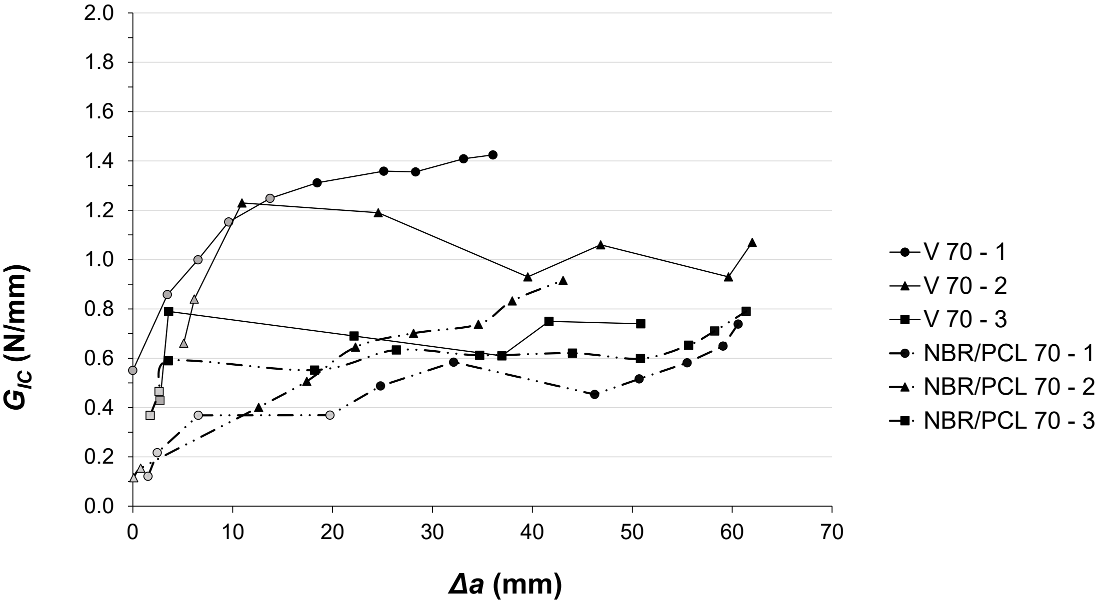

Figure 4-32 – R-Curves for Virgin (V 70) and NBR/PCL nanomodified (NBR/PCL 70) specimens cured at 70° C (Cycle A) [179]

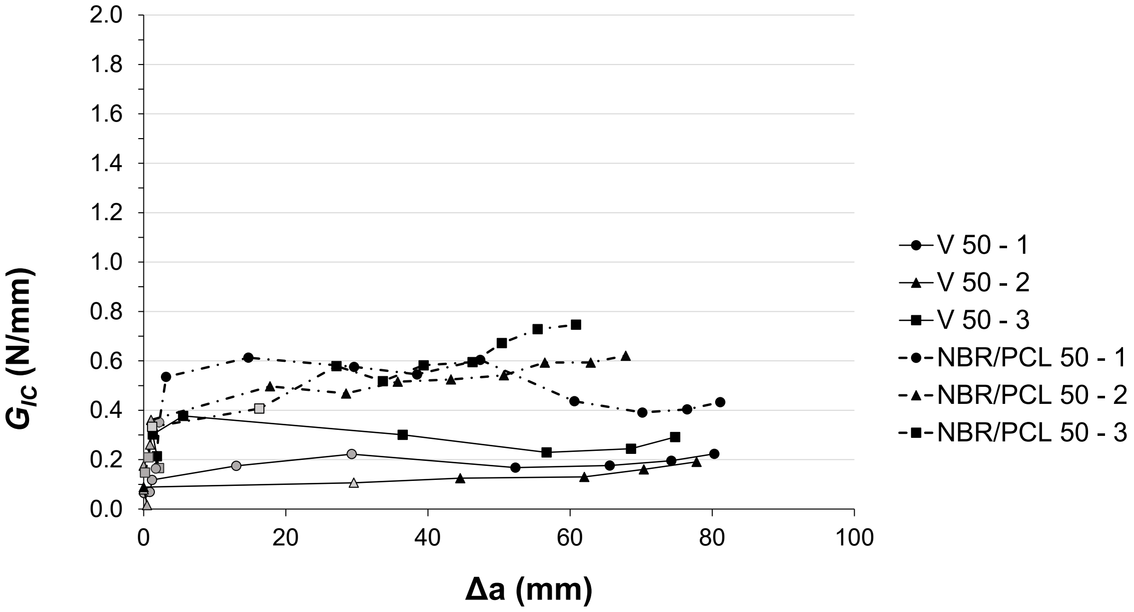

Figure 4-33 – R-Curves for Virgin (V 50) and NBR/PCL nanomodified (NBR/PCL 50) specimens cured at 50° C (Cycle B)

It is interesting to note that nanomodified joints show a constant fracture toughness trend as the crack propagates. It seems that nanofibers allow for a more reproducible result, regardless of the curing cycle adopted. Although performance may be reduced, a guaranteed minimum G_{IC} fracture toughness value seems to be achieved. The G_{IC} mean value of NBR/PCL specimens is nearly the same, independently from the curing cycle used. Therefore, it is likely that mechanisms such as fiber bridging, fibers pull-out, and crack deflection, have little or even no effect on fracture toughening compared with the presence of the rubbery phase. In the NBR/PCL 70 samples, an increasing trend of the R-curve is evident and could be due to the presence of the rubbery phase partially mixed with the epoxy matrix. Rising crack resistance behavior is typically observed when the size of the plastic zone increases following crack initiation. The dissipative mechanisms of cavitation and micro-cracking lead to the formation of a cohesive zone composed of yielded material and distributed micro-cracks. As loading is continued, the micro-cracks coalesce to form macro-cracks, which propagate and create additional micro-cracks and a plastic zone in the adhesive layer. This plastic zone enlarges as energy is dissipated by plastic deformation, resulting in a progressive toughening of the joint. However, nanomodified joints have lower fracture toughness, which may be attributed to the fibers that lead to early crack initiation [184], [185].

4.1.4.4 *Fracture Surface Analysis*

The nanomodified joints exhibit similar fracture mechanisms and the same fracture toughness value, independently from the polymerization cycle used.

Figure 4-34 and Figure 4-35 show that the fracture surfaces of NBR/PCL 70 and NBR/PCL 50 sample are cohesive, since the adhesive and nanomat are present on both bonded surfaces. The integration of the nanofibres promotes crack propagation within the adhesive layer, even at 50 °C. The presence of the nano-material enables good adhesion between the adhesive layer and the steel substrate, also at 50 °C, and limits the risk of uncontrollable adhesive fractures.

SEM images of NBR/PCL 70 - 1, in Figure 4-36, and NBR/PCL 50 – 1, in Figure 4-37, show comparable fracture surfaces. These appear poorly rough, and there is not a clear presence of micro dimples, characteristic of the V 70 samples with higher fracture toughness. In the NBR/PCL 50, the fiber structure is visible with no evidence of fiber-bridging or pull-out.

In NBR/PCL 50, the rubbery nanofibres partially retain their structure due to the inability of the PCL to complete fusion during the curing cycle. In fact, at 70 °C the PCL can melt, but this phenomenon probably occurs after the gel point of the adhesive during curing, hindering thermoplastic mixing with the epoxy resin. However, the highly mobile rubber phase can melt with the surrounding epoxy. Figure 4-36 shows the modification of the nanofibres structure that tends to form a sort of film. Morphological analysis confirms that the difference in the nanofiller structure do not affect the final fracture toughness, since no fiber bridging or pull-out was notice. Therefore, the presence of rubbery phase lead samples cured at 50 °C to reach higher fracture toughness values, comparable to NBR/PCL 70.

NBR/PCL 70 - 1 *NBR/PCL 70 - 2* *NBR/PCL 70 - 3*

Figure 4-34 – Fracture surface of NBR/PCL 70 samples

Figure 4-35 – Fracture surface of NBR/PCL 5 samples

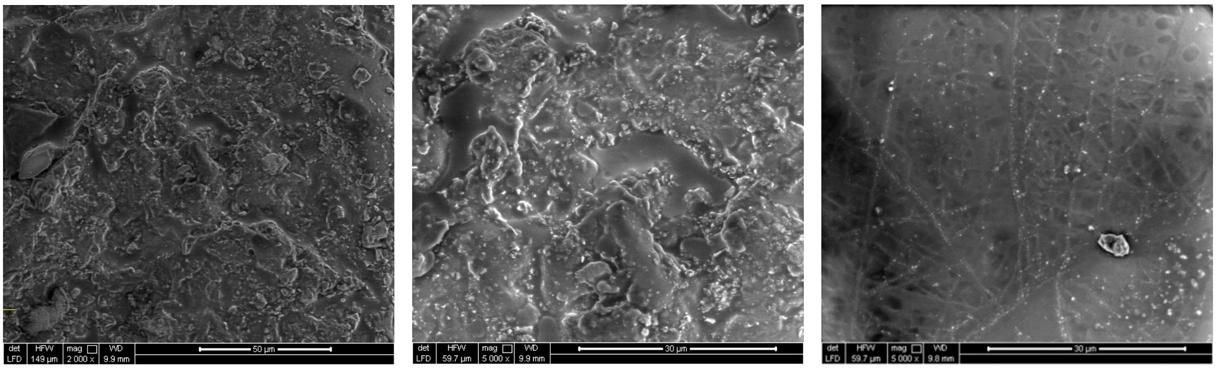

(a) (b) (c)

Figure 4-36 – SEM images of fracture surface of NBR/PCL 70 – 1 at different magnification: 2000X (a), and 5000X (b,c) [179]

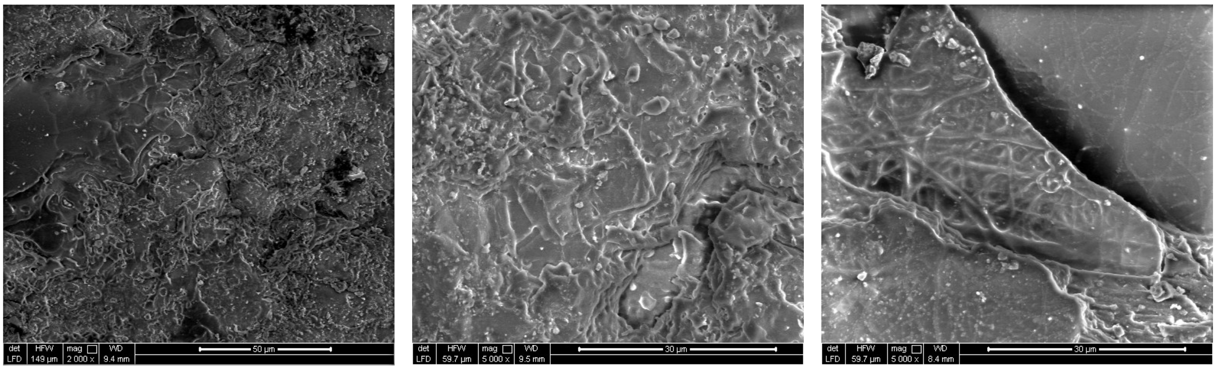

(a) (b) (c)

Figure 4-37 – SEM images of fracture surface of NBR/PCL 50 – 1 at different magnification: 2000X (a), and 5000X (b,c) [179]

4.1.5 Results Comparison

Figure 4-38 reports the R-Curves of representative samples of the series V 70, V 50, Ny 70, NBR/PCL 70 and NBR/PCL 70. Both nanostructure typology has lower fracture toughness than neat resin, however rubbery nanaofibers exhibit better performance than Nylon ones, as the mean G_{IC} value of NBR/PCL reinforced adhesive is 0.58 N/mm while the joints modified with Nylon 6.6 nanofiber has mean G_{IC} value of 0.38 N/mm. Anyway, the behavior of nanomodified joint is less scattered compared virgin sample. The result is confirmed by SEM analyses on fracture surfaces of nylon nanomodified specimens that show no presence of micro dimples, as occurs in virgin samples, and no evidence of fiber bridging or pull-out mechanisms. The rubber modified specimens, exhibit no phenomena of fiber bridging and pull-out, just like nylon specimens. Therefore, the differences in G_{IC} values is mainly due to the presence of rubbery phase, which absorbs more energy than nylon nanofibers. In any case, the fibers nanostructures do not contribute to improve adhesive fracture toughness but represent a preference pathway for the crack propagation that exfoliate the nanomat integrated into the epoxy matrix. In conclusion, the production of nanomat prepregs using structural 2K epoxy adhesive is possible, and the nanomat can act as an adhesive carrier. Both nanomats seems to have a detrimental effect on the fracture toughness of the adhesive, which has in this case already a high fracture toughness values, contrary to what experienced in previous work for which epoxy resins with a medium-low toughness have been employed [71]–[74]. As Reported in the paragraph 1.8, the works [71]–[74] have shown that joints bonded with medium-low toughness resins did not have proper interfacial adhesion since all the failures were adhesive. Interfacial failure shows that the presence of the nanomat does not influence the fracture mechanisms and that the interfacial adhesion was not optimal. For these kind of joints, nanofibres did not show any detrimental effect but, on the contrary, a tendency towards improved fracture toughness, although the adhesive fracture mode for both virgin and nanomodified joints.

The adhesive modified with nanofibers allow to obtain a more reproducible result, cohesive fracture and constant G_{IC} values. Considering NBR/PCL nanomodified joint, although performance may be reduced, a guaranteed minimum G_{IC} fracture toughness value seems to be achieved, regardless of the curing cycle adopted.

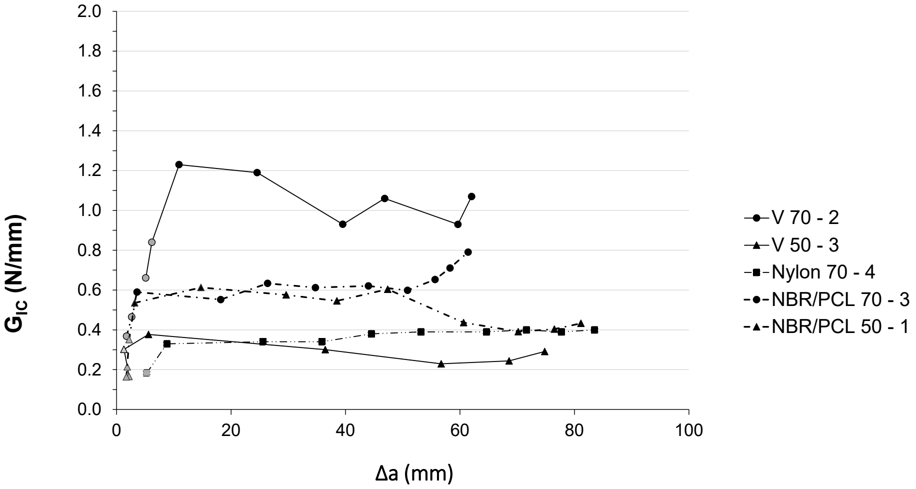

Figure 4-38 – Comparison of R-Curves of Virgin and NBR/PCL nanomodified specimens.

5 NANOMODIFIED COMPOSITE JOINTS - RESULTS

In this work, three different nano-sized additives were used to investigate their effect on the fracture toughness of composite joints bonded with epoxy film. The first nano-scale additive examined in this chapter is the nanomat of XD10 Polyamide electrospun (XD10 PA) nanofibers. The nanomat used is the XanturLayr (https://www.nanolayr.com/product/xantulayr/) with an aerial weight ok 3 g/m^2. This material is commercially available and used for enhancing mode I and mode II interlaminar fracture toughness in composite laminates, resulting in higher delamination resistance and damage tolerance[7], [186]. The works [7], [186] assessed that, since Polyamide can withstand higher strain before failure compared to epoxy, the plastic deformation of the nanofibers leads to dimmish crack energy and, therefore, increases the Mode I fracture toughness of the joint.

The second and third nano additive considered in this work are carbon-based materials: multiwalled carbon nanotubes (MWCNTs) and Graphene nanoplatelets (GNPs). Their addition inside the adhesive layer may enhance the adhesive mechanical properties and joint fracture toughness. For CNTs, several mechanisms, such as particle pull-out, debonding, and plastic void growth, can dissipate energy and increase joint fracture resistance [45], [59], [187], [188]. For graphene-reinforced polymers, crack deflection is the prominent toughening mechanism. This is attributed to the planar structure of graphene and its strong interfacial bonding [45], [187], [189].

Besides impressive mechanical performance, CNTs and GNPs exhibit exceptional electrical properties and can improve conductivity of polymers. Conductive polymers are receiving attention because they can be used as a sensor for Structural Health Monitoring (SHM) using electrical conductivity measurements [161], [190]–[193] and can be employed as an alternative system for non-destructive inspection for composite and adhesives.

This chapter reports the results of the experimental campaign on composite joints reinforced with XanturLayr nanofibers, MWCNTs and GNPs. Since the adhesive is in the film form, XanturLayr integration can be approached in two ways. The first is to apply the nanofiber at the adherends/adhesive interface. The second is to interleave the nanomat between two layers of adhesive. Both methodologies are investigated in the following paragraphs. The solid adhesive precludes carbon-based nanofillers from mixing before bonding the composite plates. For this reason, a filler solution was prepared and sprayed with an airbrush on the composite bonding surface.

The evaluation of mechanical test results on the composite joint is accompanied by morphological analysis to deeply understand the phenomena that occur inside the reinforced joint during crack propagation. The comparison with virgin samples is reported to assess the quality of the final result.

For the joints reinforced with carbon-based additives, a first evaluation of the electrical response is also reported. The materials and manufacturing techniques selected for these tests are employed in the aerospace and automotive industry. The work presented in this chapter aimed to evaluate the applicability of nanostructures at an industrial level, developing techniques that can improve the mechanical and electrical property of the joints, and can be easily implemented.

5.1.1 Virgin Adhesive

This section reports the results of the mechanical characterization and fracture surface analysis of the virgin bonded joints to assess the fracture toughness and the failure mode of virgin samples. The results will be used as comparison means for the nanomodified bonded joints investigated in the following paragraph.

5.1.1.1 Mechanical Characterization

This paragraph reports the results of the mechanical test on virgin joints 1S and 2S with single and double layer of adhesive, respectively.

Figure 5-2 reports the load against CMOD of two virgin specimens 1S and 2S, taken as representative. The load peak of both samples, and more generally of the two samples series, are slightly lower of 600 N. The behavior is similar for both joints families, so the employment of 2 layers instead of one do not cause any significant difference in adhesive performance.

Figure 5-3 and Figure 5-4 report the R-curve of 1S and 2S, respectively. The black markers identify the GIC values considered for the calculation of the average fracture toughness, while the grey markers represent the excluded ones. In this case, the excluded values refer to crack propagation inside composite laminas. Since the study aims to evaluate the fracture toughness of the adhesive layer, the average G_{IC} values must be calculated considering the points at which cracks propagate into the adhesive (Figure 5-1). As reported in able 5.1, the average fracture toughness of 1S series is 0.42 ± 0.07 N/mm, as for 2S samples which average G_{IC} value is 0.42 ± 0.10 N/mm.

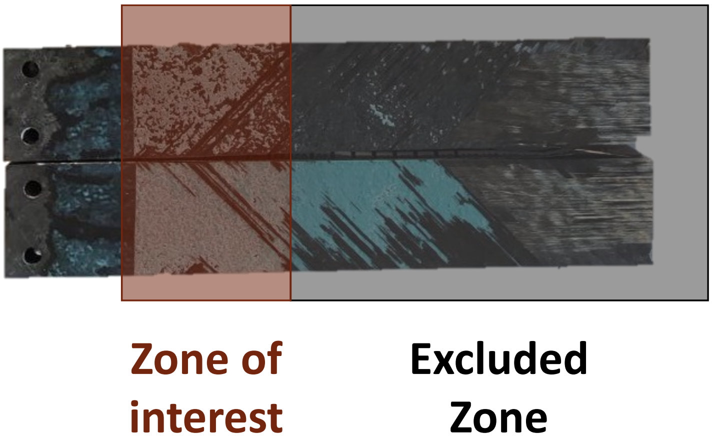

Figure 5-1 – Example of zone of interest and for the calculation of the fracture toughness. The zone of interest is characterized by cohesive failure

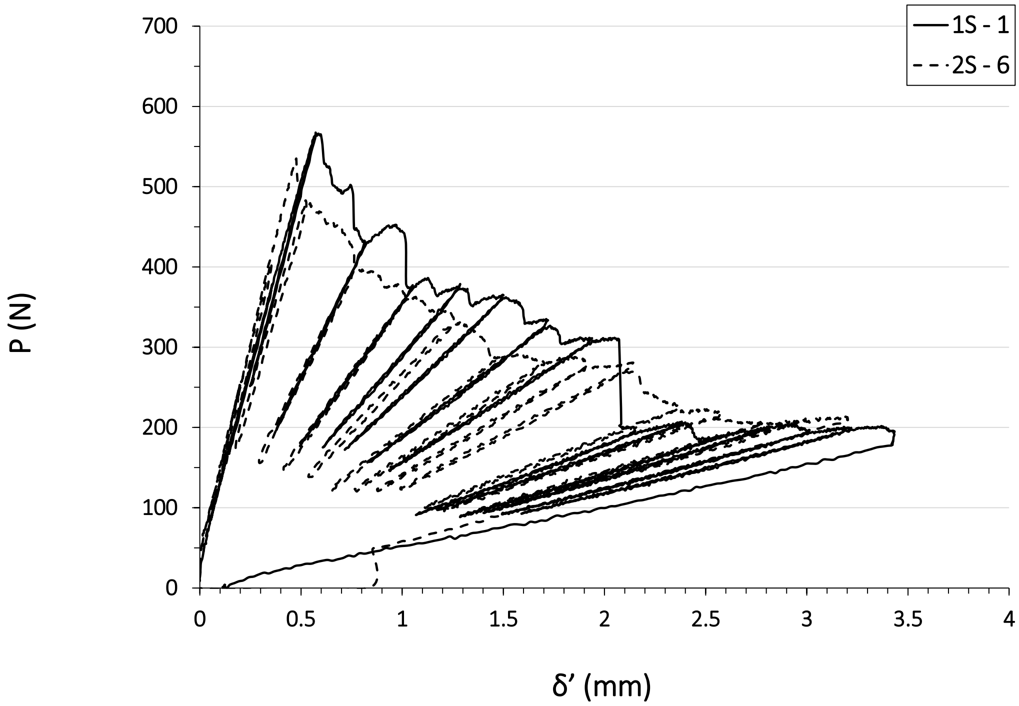

Figure 5-2 – Load against CMOD (δ') for virgin specimens 1S - 1 and 2S – 6, taken as representative

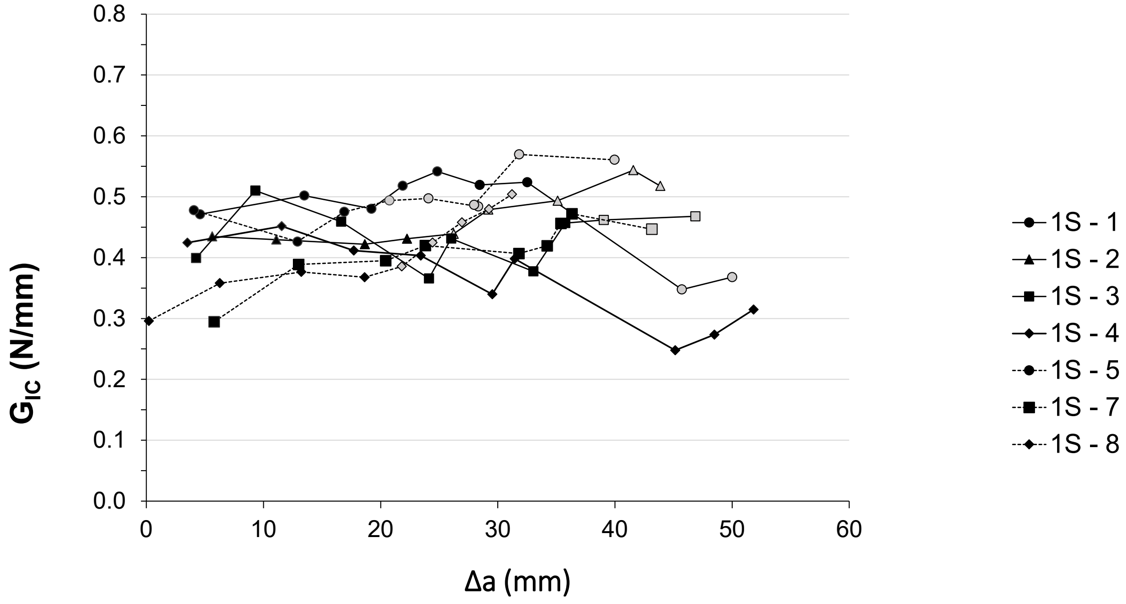

Figure 5-3 – R-Curves for virgin samples 1S, with single adhesive layer.

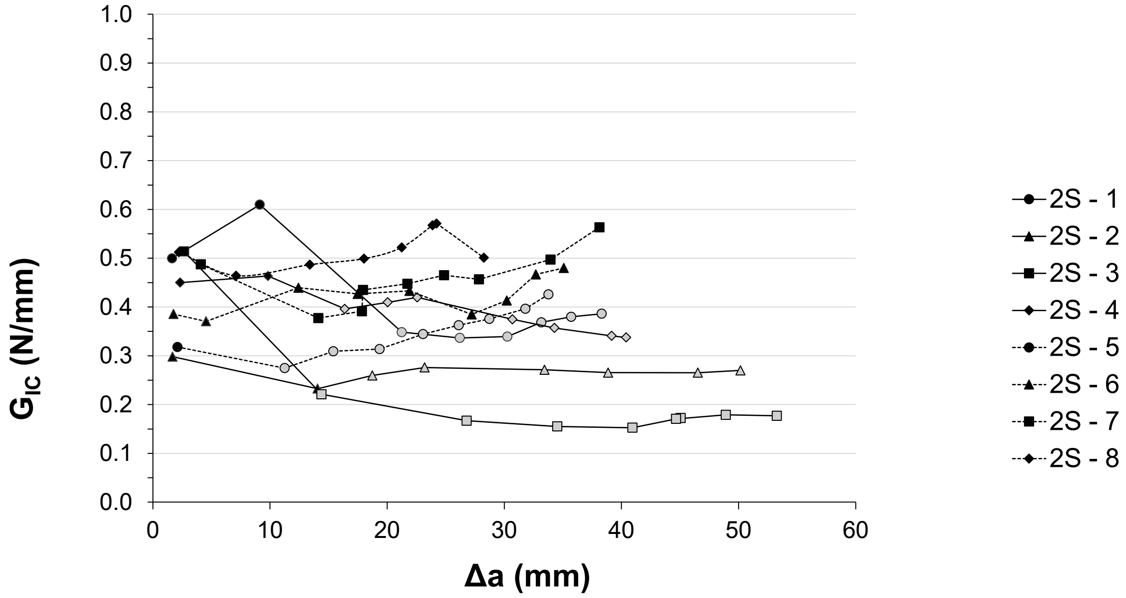

Figure 5-4 – R-Curves for virgin samples 2S, with double adhesive layer.

able 5.1 – Statistic of samples 1S and 2S

Sample ID	G_{IC} Mean (N/mm)	Standard Deviation (N/mm)

1S	0.42	0,07
2S	0.42	0,10

5.1.1.2 *Fracture Surface Analysis*

This paragraph reports the morphological analysis of virgin joints 1S and 2S. The results of the morphological analysis are related to the results obtained from the mechanical characterization presented in the previous paragraph.

Figure 5-5 and Figure 5-6 show the fracture surfaces of 1S and 2S samples, respectively. Figure 5-7 provides a description of the main failure mechanisms that can occur in joints.

The failure modes of the 1S specimens are mainly cohesive, but the crack tends to deviate inside the composite support after 30 mm of propagation inside the adhesive. The failure mode of 2S samples appears more scattered than the 1S sample. The joints 2S – 1, 2S – 4, and 2S - 5 exhibit cohesive failure of the adhesive in the initial stage of crack propagation, 2S - 2 and 2S - 3 exhibit interfacial fracture and consequently lower G_{IC}, and samples 2S – 6, 2S – 7 and 2S – 8 present mainly cohesive fracture surface and higher fracture toughness. These observations can explain the more scattered G_{IC} values of 2S samples, which have higher standard deviations compared to 1S.

Figure 5-8 shows SEM images of the 1S - 1 fracture surface at 30 -40 mm of crack propagation. The analyzed area is characterized by numerous micro-dimples in the adhesive layer caused by ductile failure mechanisms. In the images, the broken fibers of the nylon cloth are evident, confirming that the crack propagates in the adhesive layer. As already explained in section 3.2.2, the epoxy film is supported by a nylon carrier that ensures the handling of the film and the manufacture of joints with a constant cross-section of adhesive. Sample 2S – 6 exhibits a similar fracture surface, as presented in Figure 5-9 where micro dimples and broken nylon fiber are evident. The two samples have comparable fracture toughness in the investigated area, i.e. at Δa values of 30-40 mm.

On the contrary, sample 2S – 2 in Figure 5-10 shows a flat fracture surface, typical of adhesive failure.

There is no evidence of the presence of the nylon cloth, since the joint fails at the adherend interface, as a consequence the fracture toughness of sample 2S -2 is lower than the ones previously analyzed.

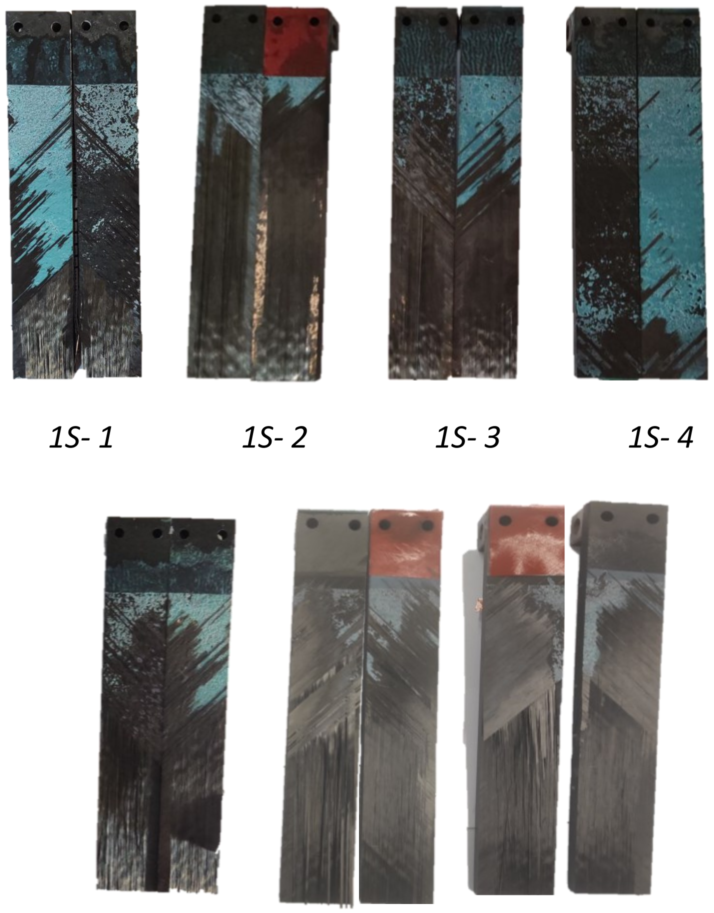

1S- 1 1S- 2 1S- 3 1S- 4

1S- 5 1S- 7 1S- 8

Figure 5-5 – Fracture surface of 1S samples

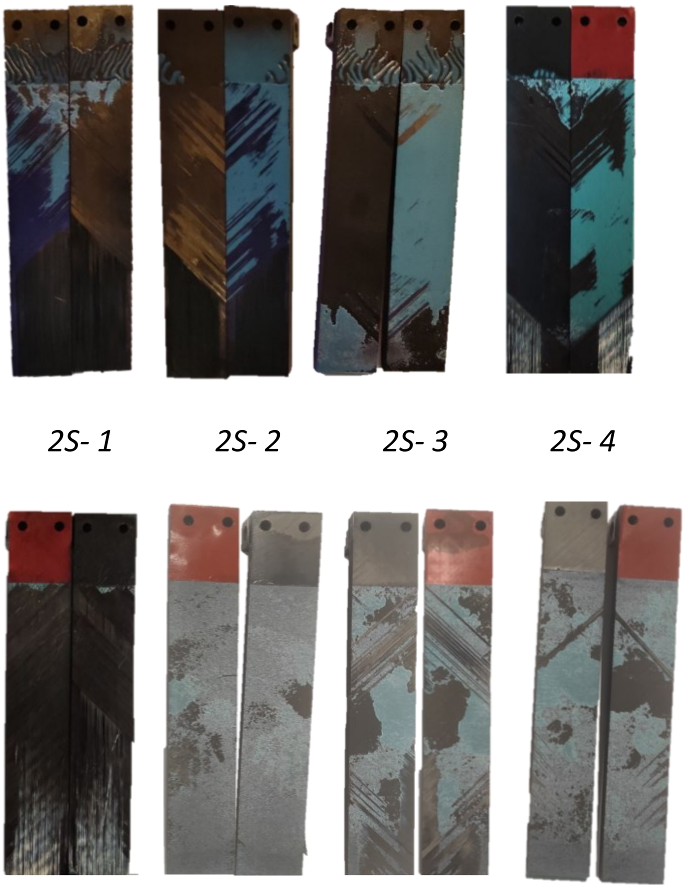

2S- 1 *2S- 2* *2S- 3* *2S- 4*

2S- 5 *2S- 6* *2S- 7* *2S- 8*

Figure 5-6 – Fracture surface of 2S samples

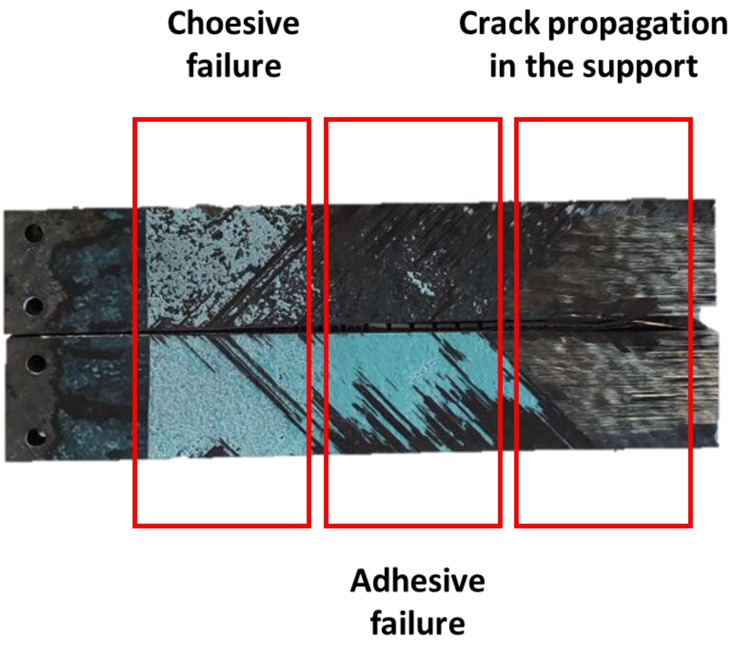

Figure 5-7 – Failure mechanism in the bonded joints. Cohesive failure zones are those considered in the calculation of the G_{IC}

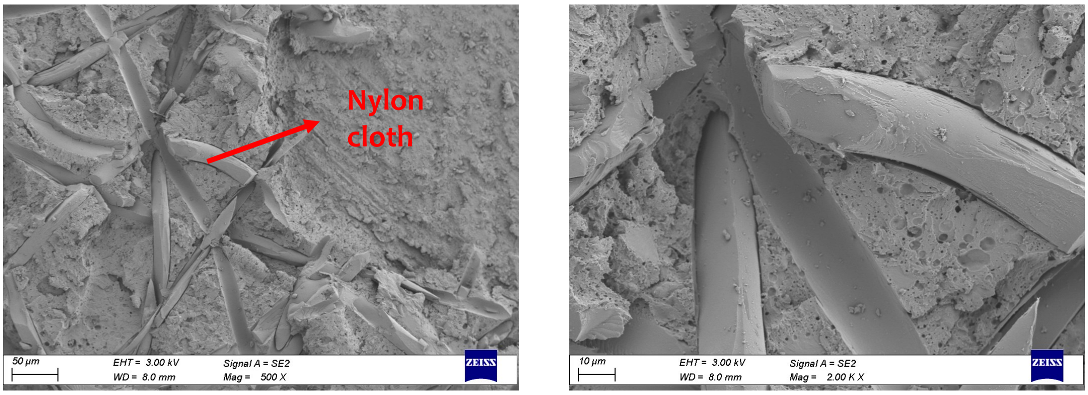

(a) (b)

Figure 5-8 – SEM images of fracture surface of 1S -1 at different magnification: 500X (a), and 2000X (b)

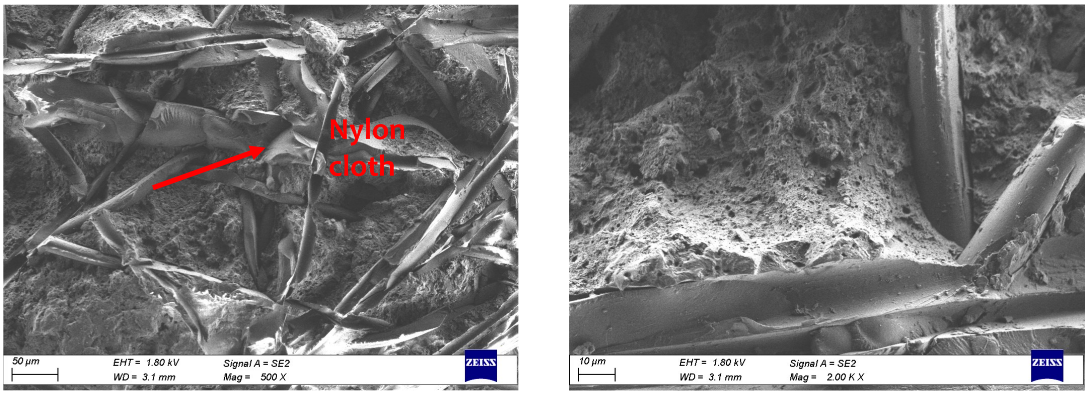

(a) (b)

Figure 5-9 – SEM images of fracture surface of 2S -6 at different magnification: 500X (a) and 2000X (b)

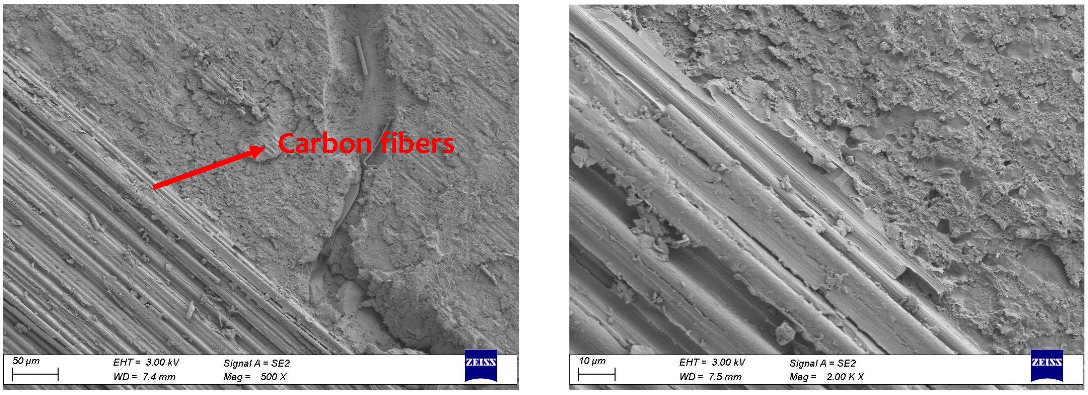

(a) (b)

Figure 5-10 – SEM images of fracture surface of 2S -2 at different magnification: 500X (a) and 2000X (b)

5.1.2 XantuLayr® Nanofibers

This section reports the results of the quality assessment of the addition of the commercial XD10 PA nanomat within the adhesive, the mechanical and morphological characterization on the bonded joints to assess the effect of nanofibers on the fracture toughness of the system. Two bonding configurations are analyzed, named 1S-2NF and 2S-1NF.

5.1.2.1 Impregnation Test

An impregnation test is carried out to evaluate if the epoxy film properly impregnates the XD10 PA nanomat, following the procedure in Chapter 3.

Figure 5-11 shows the cross-sections of two composite 1S-2NF and 2S-1NF. The optical microscope analysis shows constant adhesive layers, and no evidence of porosities or discontinuities at the interface adhesive/adherends and in the adhesive layer. At the adhesive/substrate interfaces in

Figure 5-11 (a), the presence of the nanofiber can be noted, as they appear as a zone with a slightly different color compared to the bulk adhesive. This darker zone is not very evident in the center of the adhesive layer of Figure 5-11 (b) but is still present. The 1S-2NF sample is thinner than the 2S-1NF manufactured with two layers of epoxy film. However, the thickness of both specimens is lower than the final thickness of adhesive joints. The samples used for the integration test are smaller than the panels used for DCB manufacturing, and consequently, more resin squeezes out, resulting in a thinner bond line. Further SEM analyses confirmed good-quality nanofibers integration for both configurations. In particular, Figure 5-12 shows the cross-section of the 1S-2NF joint with the details of the adhesive/ adherend interface, while Figure 5-13 shows the 2S-1NF cross-section and the details of the central zone where the nanomat is located. In both joints, no porosities are present, demonstrating that the integration of the nanofibers does not provoke discontinuities in the bondline and at the interfaces.

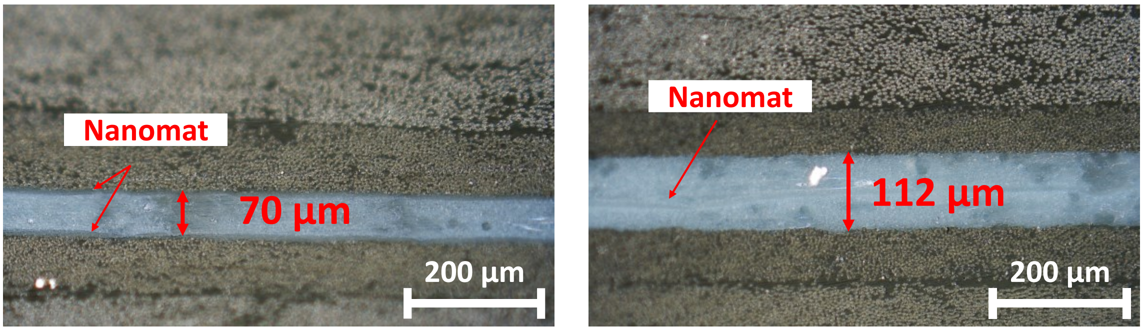

(a) (b)

Figure 5-11 – Optical microscope analysis of samples (a) 1S-2NF and (b) 2S-1NF cross-sections

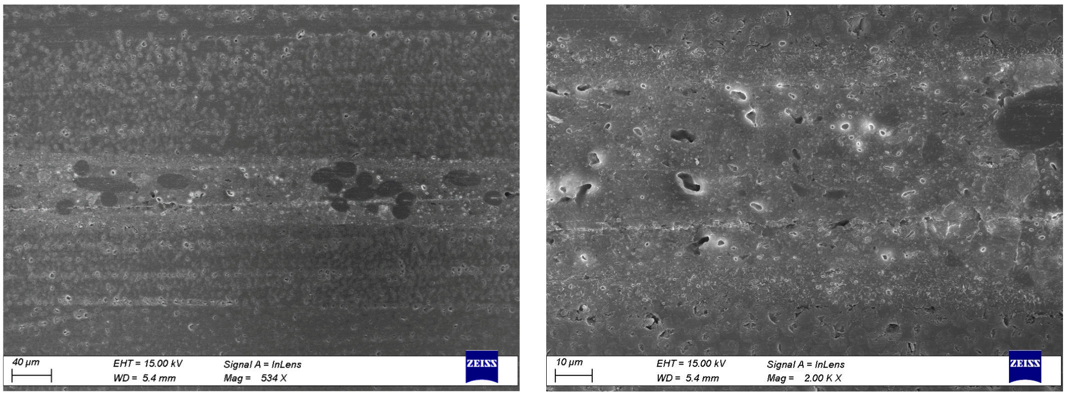

(a) (b)

Figure 5-12 – Adhesive joint cross- sections of sample 1S-2NF at different magnification: (a) 534X, and (b) 2000X

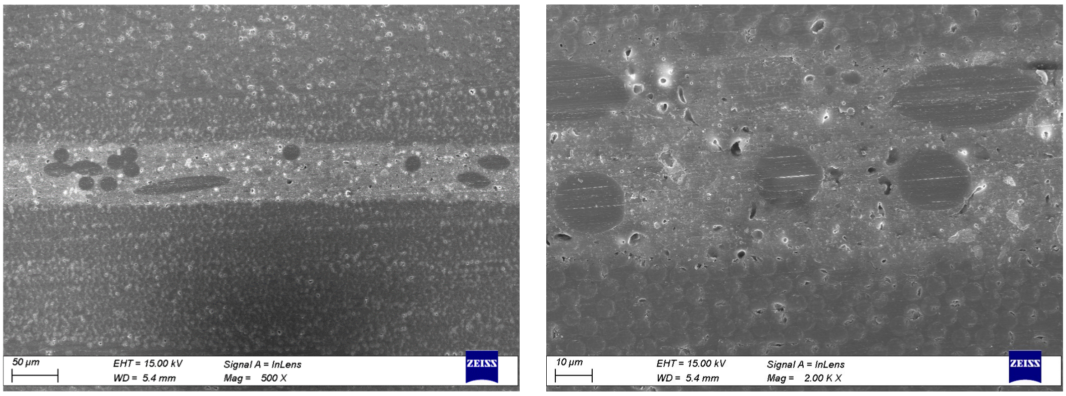

(a) (b)

Figure 5-13 – Adhesive joint cross- sections of sample 2S-1NF at different magnification: (a) 500X, and (b) 2000X

5.1.2.2 Mechanical Characterization

The experimental campaign on DCB joints aims to evaluate the influence of the XD10 PA nanofiber embedded in the adhesive layer of two different configurations, 1S-2NF and 2S-1NF. The mechanical response of the bonded joints during quasi-static tests is analyzed and later compared with the resulting fracture surface. The results of nanomodified and virgin samples are compared.

Figure 5-14 reports the load against CMOD for samples 1S - 2NF. The load peak of the nanomodified sample has slightly higher values of 600 N. During the crack propagation, the 1S-2NF joints withstand a higher load than the neat joint. The curves that represent the load against CMOD for the samples 2s – 1NF are reported in Figure 5-15. The peak load of the nano-reinforced specimen is slightly higher than the virgin sample but still comparable. The same consideration is valid for the other lo peak load in the graph. In general, the behavior of the 2S-1NF joint can be considered similar to virgin samples. Figure 5-16 and Figure 5-17report the R curve of 1S - 2NF and 2S- 1NF, respectively. The black markers identify the G_{IC} values considered for the average fracture toughness calculation, while the grey markers represent the excluded ones. In this case, the excluded values refer to crack propagation inside composite laminas. Since the study aims to evaluate the fracture toughness of the adhesive layer, th e average G_{IC} values must be calculated at the points at which cracks propagate into the adhesive. As reported in Table 5.2, the average fracture toughness of the 1S – 2NF series is 0.55 ± 0.16 N/mm, while for 2S – 1NF samples is about 0.44 ± 0.8 N/mm. The samples 1S-2NF present more spread values compared to 2S – 1N, even if the average G_{IC} is higher. The behavior of 2S-1NF is comparable with virgin samples 1S and 2S. Figure 5-18reports the comparison of the representative samples R-Curves of the series 1S, 2S, and 1S-2NF. The configuration 1S-2NF exhibits an improvement of 32% compared to 1S samples.

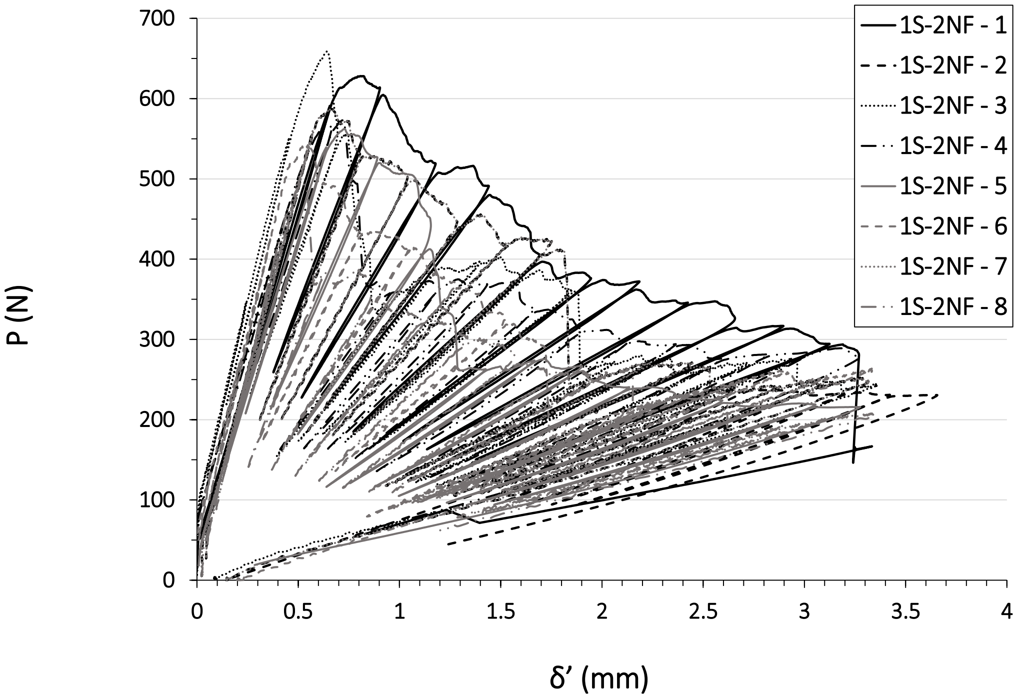

Figure 5-14 – Load against CMOD (δ') for 1S-2NF

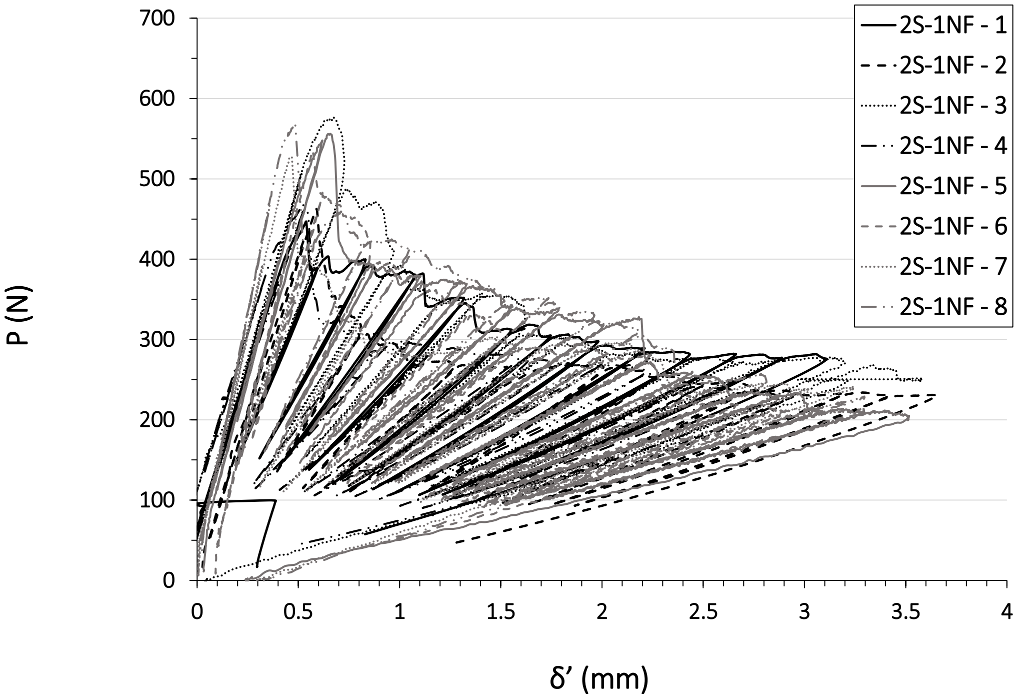

Figure 5-15 - Load against CMOD (δ') for 2S-1NF

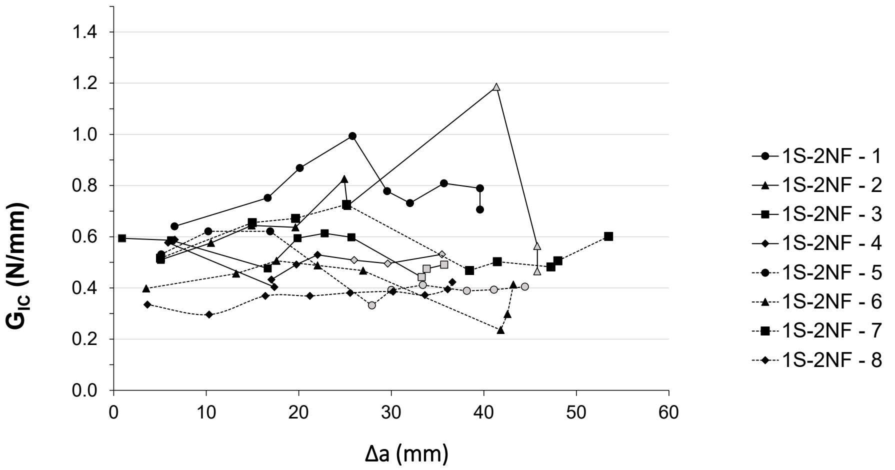

Figure 5-16 – R-Curves for nanomodified samples 1S-2NF, bonded with single adhesive layer and two nanomat layers at adherend/adhesive interface. The black markers of the R-Curves graph indicate the G_{IC} *values considered for the steady-state fracture toughness average value calculation, while the gray ones the excluded values*

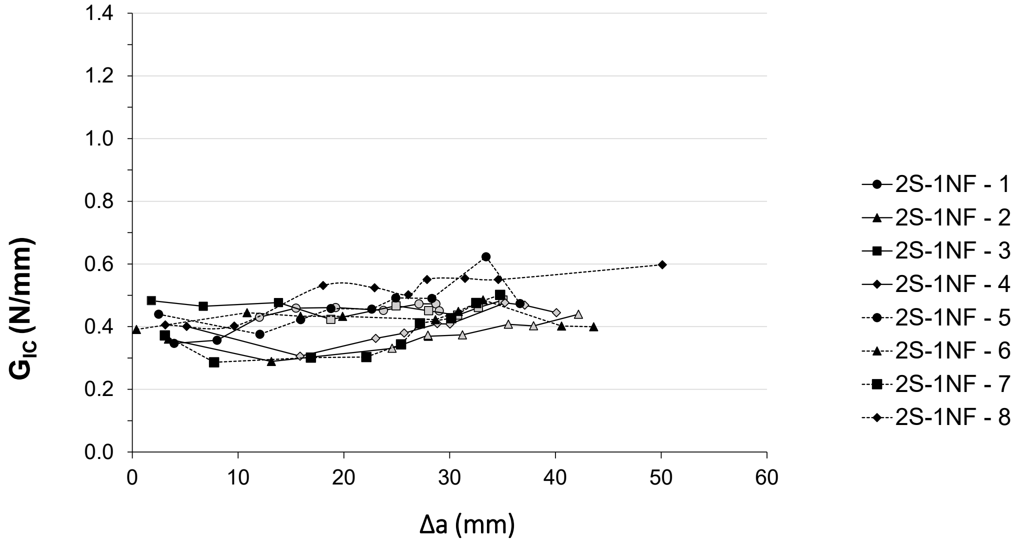

Figure 5-17 – R-Curves for nanomodified samples 2S-1NF, bonded with double adhesive layer and one nanomat layer in the middle.

Table 5.2 – Statistics of samples 1S, 2S, 1S-2NF, and 2S-1NF

Sample ID	G_{IC} Mean (N/mm)	Standard Deviation (N/mm)
1S	0.42	0,07
2S	0.42	0,10
1S – 2NF	0.55	0.16
2S – 1NF	0.44	0.08

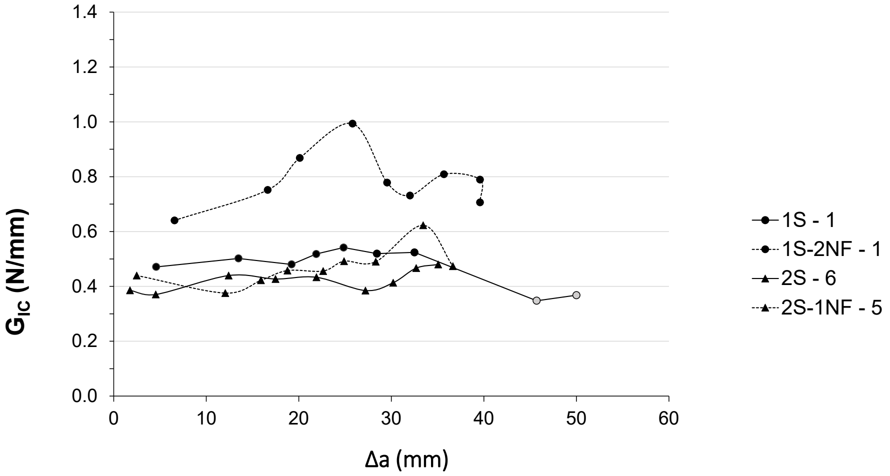

Figure 5-18 – Comparison of R-Curves of virgin (1S and 2S) and nanomodified (1S-2NF and 2S-1NF) specimens. The black markers of the R-curves indicate the G_{IC} values considered for the steady-state fracture toughness average value calculation, while the gray ones the excluded values

5.1.2.3 Fracture Surface Analysis

This paragraph reports the morphological analysis of joints 1S-2NF and 2S – 1NF. They are related to the results obtained from the mechanical characterization presented in the previous paragraph. The Nano-modifies samples are compared with virgin ones to understand the phenomena that act in the modified adhesive layers

Figure 5-19 and Figure 5-20 show the fracture surfaces of 1S-2NF and 2S-1NF samples, respectively. The failure modes of the 1S-2NF specimens are mainly cohesive but the crack tends to deviate inside the composite supports after 30 mm of propagation inside the adhesive. Samples 2S-1NF present cohesive failure, but the results are not very reproducible since half of the samples are subjected to crack propagation inside the composite layer at Δa values of 10-20 mm.

Figure 5-21 shows SEM images of the 1S - 2NF - 1 fracture surface at 10 -20 mm of crack propagation. As for the virgin samples, numerous micro-dimples are present, and the nylon carrier is also visible, confirming that the crack propagates into the center of the adhesive layer. The nanofibers are present in some zones of the analyzed areas, in particular near the interface. Figure 5-21 (c) and Figure 5-22 show the details of nanofiber-rich zones. The nanofibers appear stretched and pulled out. These mechanisms contribute to dissipating energy, increasing the system fracture toughness [15], [45]. Figure 5-23 shows the surface of sample 2S-1NF – 5, which appears rough and riches in micro dimples, as for virgin samples. Also, in this case, the area with nylon cloth and areas reach of nanofibers can be appreciated.

The nanofibers in Figure 5-23 appear less stretched and are broken inside the matrix without evident pull-out, justifying fracture toughness values lower than 1S-2NF samples and comparable with virgin ones. In these specimens, the presence of micro cavities is reduced, indicating that slightly lower adhesive strengths are reached during propagation [194].

1S-2NF- 1 *1S-2NF- 2* *1S-2NF- 3* *1S-2NF- 4*

1S-2NF- 5 *1S-2NF - 6* *1S-2NF- 7* *1S-2NF- 8*

Figure 5-19 – Fracture surface of 1S-2NF samples

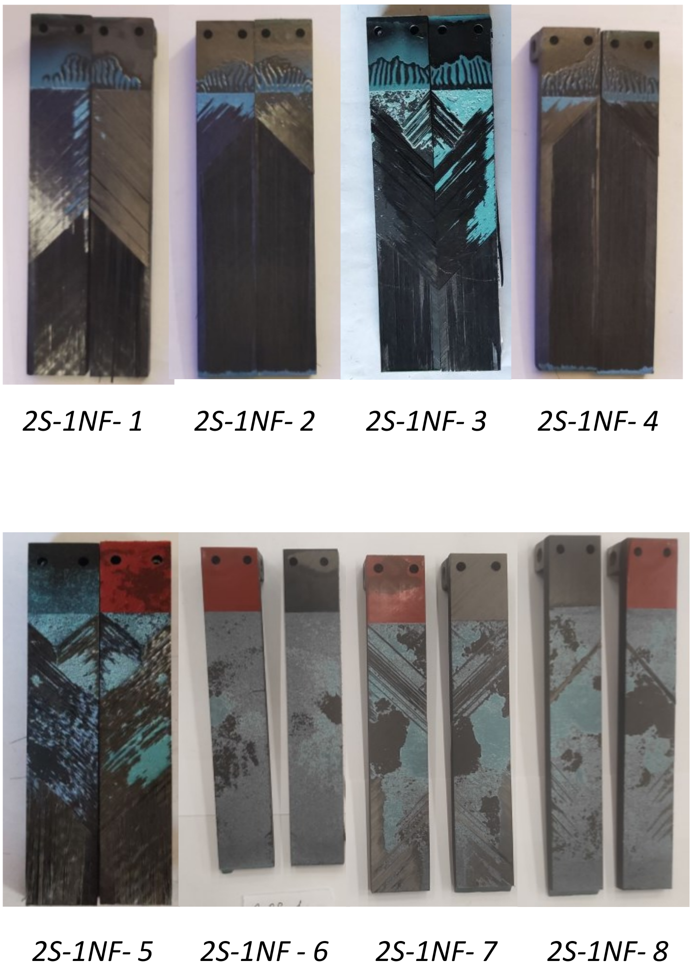

Figure 5-20 – Fracture surface of 2S-1NF samples

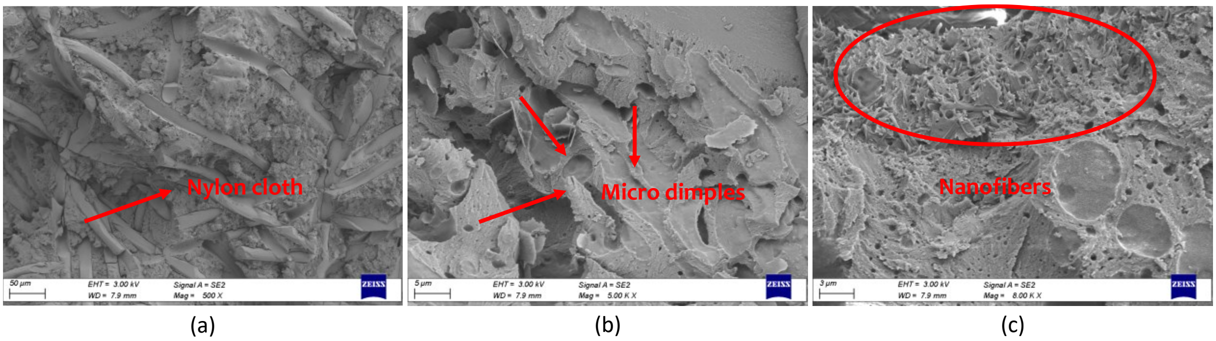

Figure 5-21 – SEM images of fracture surface of 1S-2NF – 1 at different magnification: 500X (a), 5000X (b) and 8000X (c)

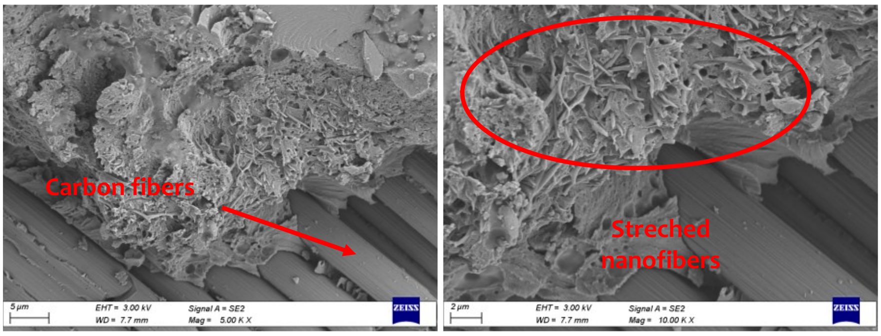

(a) (b)

Figure 5-22 – SEM images of fracture surface of 1S-2NF – 1 at different magnification: 5000X (a) and 10000X (b). The figures show the presence of nanofibers

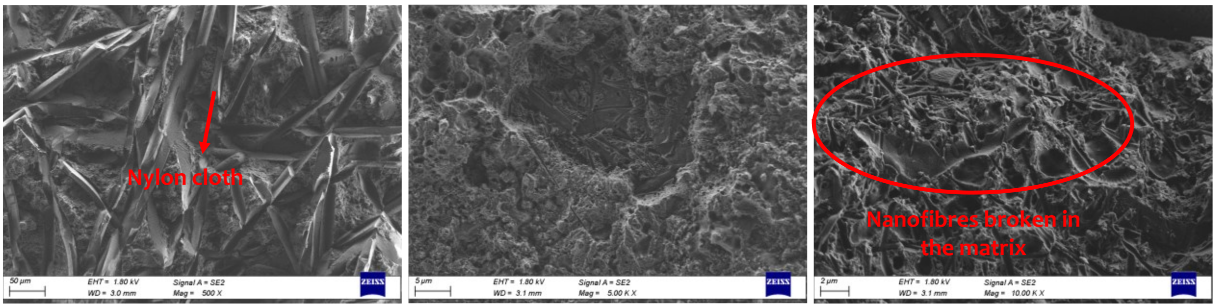

(a) (b) (c)

Figure 5-23 – SEM images of fracture surface of 2S-1NF – 5 at different magnification: 5000X (a) 5000X (b), and 10000X (c)

5.1.3 Multiwalled Carbon Nanotubes

This section reports the results of the quality assessment of the application of MWCNTs at the adhesive/ substrate interface, the mechanical characterization and the fracture surface analysis on bonded joints aimed to investigate the effect of the nanofillers on the fracture toughness of the system. The resistance variation of the system is evaluated during the DCB test, to evaluate these materials as a candidate for SHM of bonded joints. Three bonding configurations are analyzed, named C1%, C0.5%, and C0.25%. The samples differ in MWCNTs content is 1%, 0.5%, and 0.25% compared to the weight of epoxy fraction.

5.1.3.1 *Integration Test*

An integration test was carried out to evaluate how the MWCNTs are integrated inside the epoxy layer after the curing cycle, following the procedure in Chapter 3.

Figure 5-24 shows the nanomodified cross-linked adhesive layers compared with the virgin epoxy film. The three nanomodified samples simulate the configuration C0.25%, C0.5%, and C1%. The presence of the nanotubes is evident from the adhesive uniform darker color.

Cross-linked adhesive layers are analyzed with SEM. Figure 5-25, Figure 5-26, and Figure 5-27 show the presence of MWCNTs, especially on the surface. The nanotubes appear well dispersed in all samples, without entanglement.

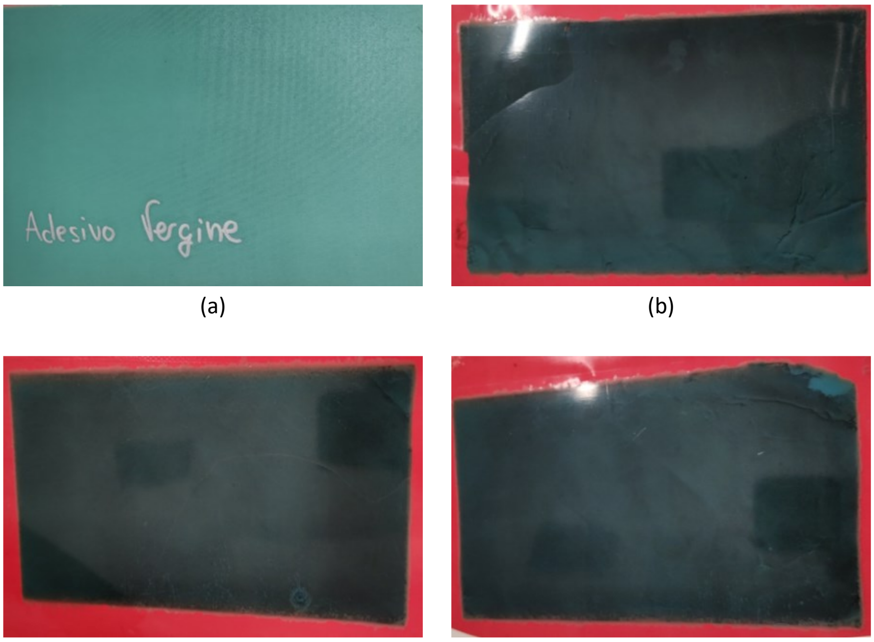

(a) (b)

(c) (d)

Figure 5-24 – Cured virgin (a) adhesive layers and nanomodified ones with 0.25wt% (b) , 0.5 wt% (c), and 1 wt% (d) of MWCNTs

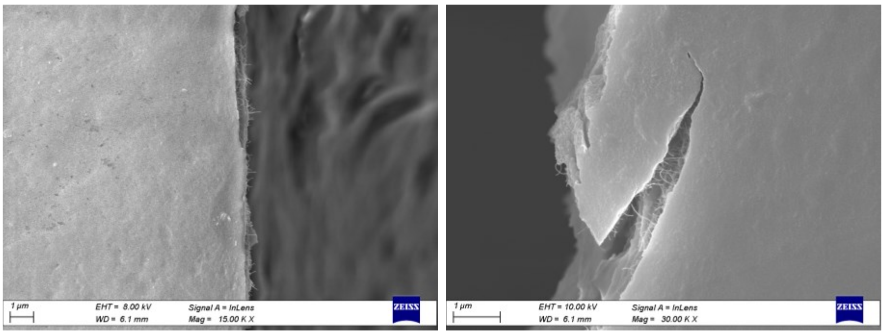

(a) (b)

Figure 5-25 – SEM images of cured adhesive modified with 0.25wt% of MWCNTs

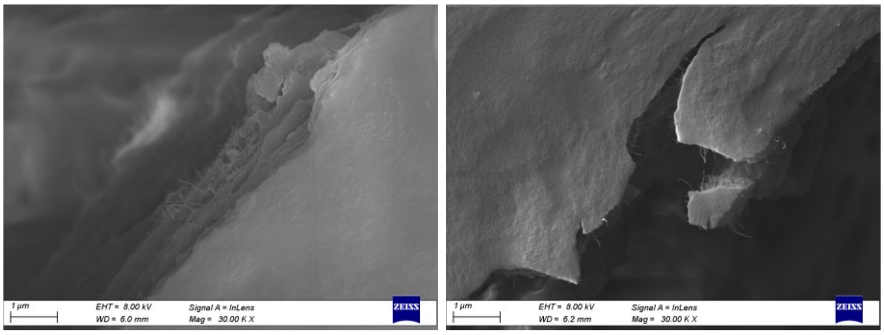

(a) (b)

Figure 5-26 – SEM images of cured adhesive modified with 0.5wt% of MWCNTs

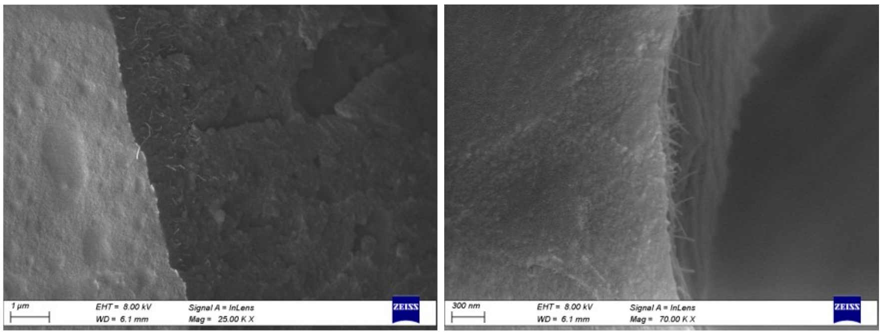

(a) (b)

Figure 5-27 – SEM images of cured adhesive modified with 1 wt% of MWCNTs

5.1.3.2 *Mechanical Characterization*

The experimental campaign in DCB joints is aimed to evaluate the influence of the MWCNTs embedded in the adhesive layer. Three different additive concentrations are considered, i.e. 1%, 0.5%, and 0.25% of the weight of epoxy fraction. The mechanical response of the DCBs is analyzed and later compared with the resulting fracture surface. The results of nanomodified and virgin samples are compared.

The Figure 5-28, Figure 5-29, and Figure 5-30 show the load against CMOD of the samples, C1%, C0.5% and C0.25%, respectively. Figure 5-31 reports the load against CMOD of samples 1S – 1, C1% - 2, C0.5% - 3, and C0.25% - 4, taken as representatives for each joint family. The load peak of nanomodified samples is around 550 N, except for the C0.5% sample that exhibits the first load peak at 400N. During the crack propagation, the C1% - 2 sample withstands to higher load compared to the neat joint, while C0.25% - 4 has lower values. The sample C0.5% - 3 has the lowest load value.

Figure 5-32, Figure 5-33, and Figure 5-34 report R-Curves of C1%, C0.5%, and C0.25%, respectively.

The average fracture toughness is reported in Table 5.3 for each joint series. Joints C1% have average fracture toughness of 0.52 ± 0.15 N/mm, joints C0.5% present the lowest of 0.26 ± 0.4 N/mm, while joints C0.25% have mean value of 0.38 ± 0.4 N/mm. Samples C1% have more spread values than the other samples with constant values and flat R-Curves. Figure 5-35 reports the R-Curve of the representative samples of 1S, C1%, C0.5%, and C0.25%.

The configuration C1% exhibits an improvement of 20% compared to 1S samples. C0.5% and C0.25% exhibit an average fracture toughness reduction of 39% and 8%, respectively. Figure 5-36 reports the variation of G_{IC} values as a function of MWCNTs content.

The presence of CNT reduces joint performance with CNTs concentration up to 0.5%. Higher concentrations of MWCNTs contribute to improving the mechanical performance of composite joints.

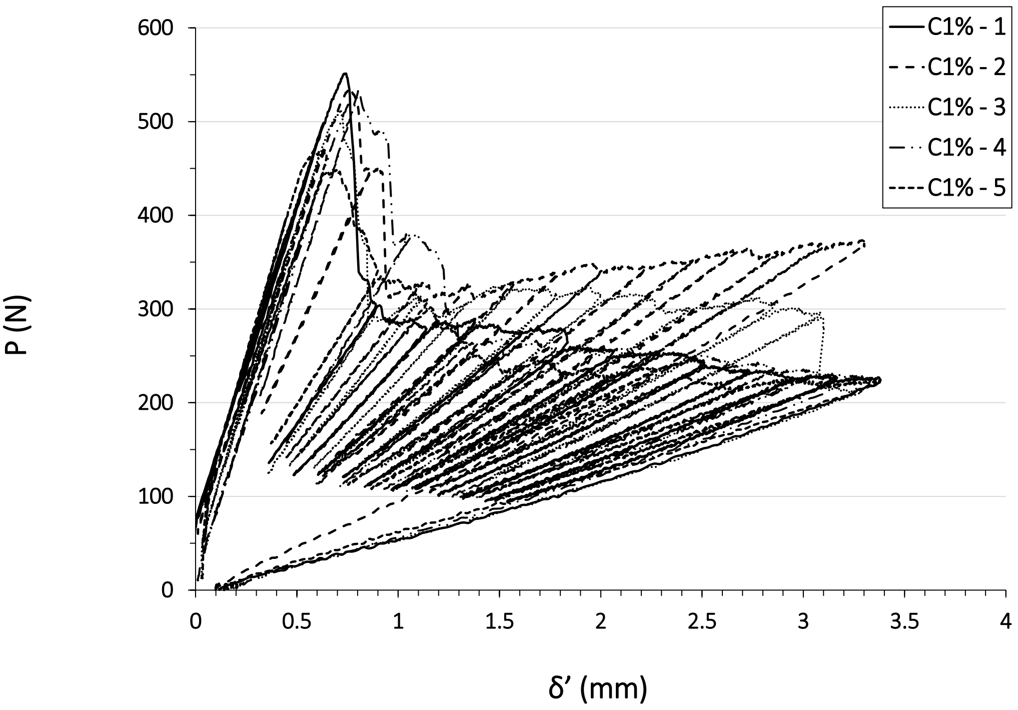

Figure 5-28 – Load against CMOD (δ') for C1% samples

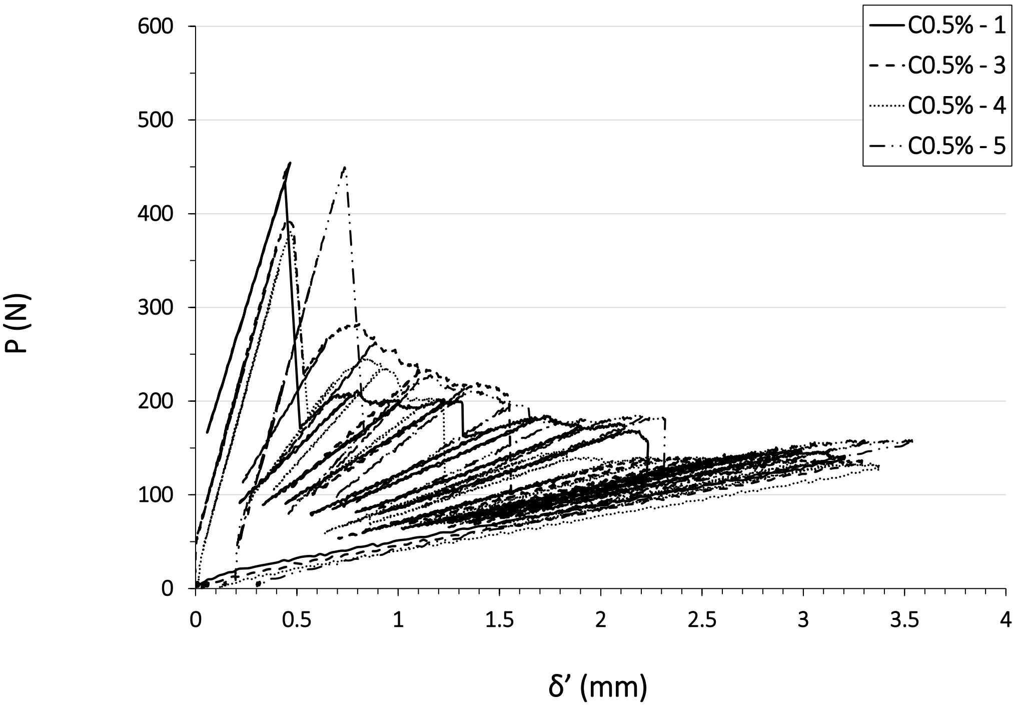

Figure 5-29 – Load against CMOD (δ') for C0.5% samples

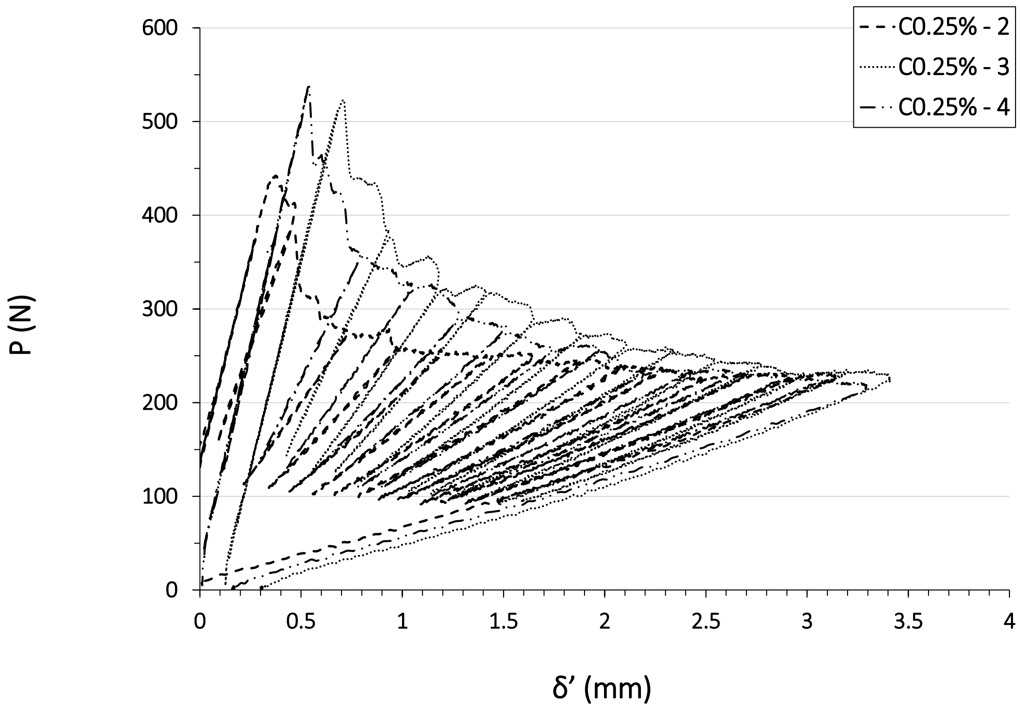

Figure 5-30 – Load against CMOD (δ') for C0.25% samples

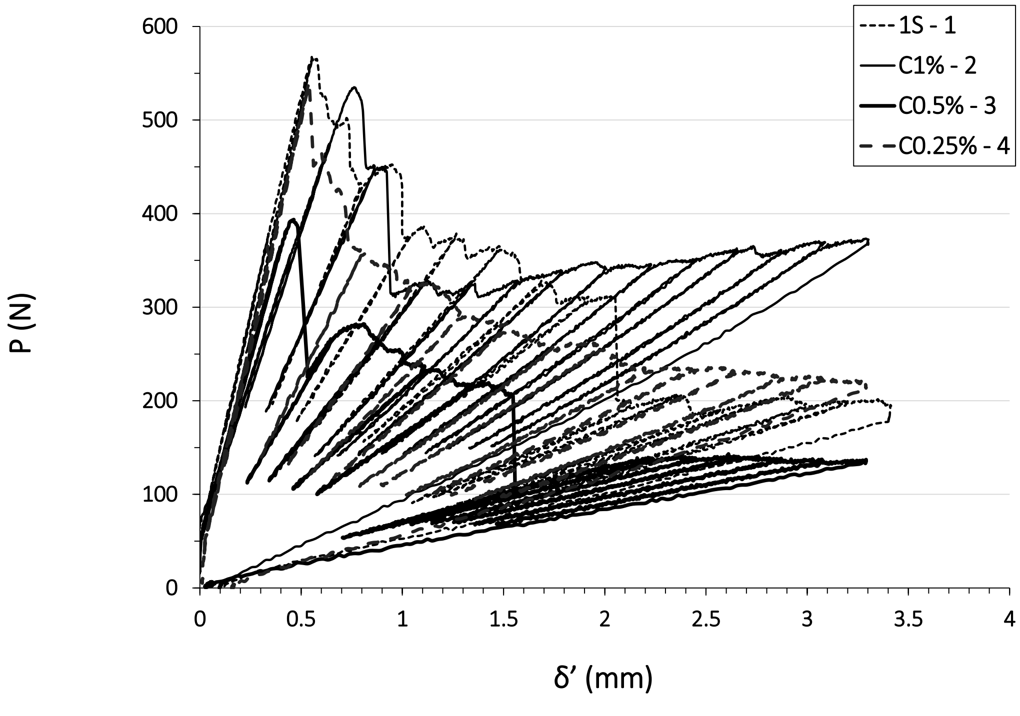

Figure 5-31 – Load against CMOD (δ') for both a virgin (1S 1 - 1) and MWCNTs nanomodified specimens (C1% - 2, C0.5% - 3, and C0.25% - 4) taken as representative

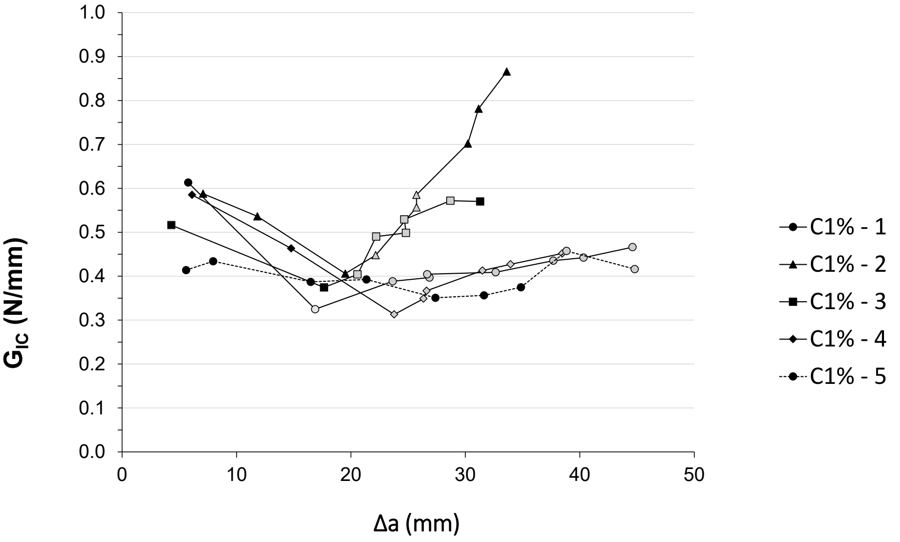

Figure 5-32 – R-Curves for nanomodified samples C1%.

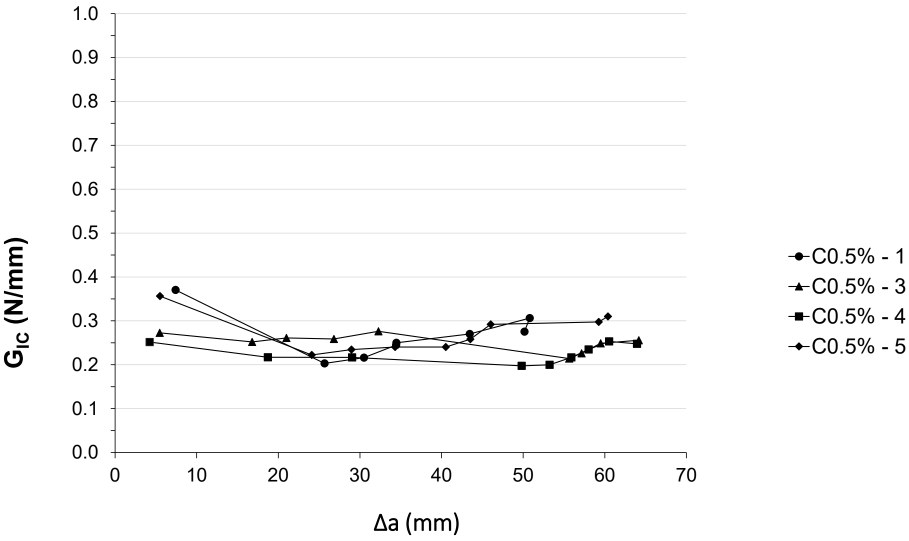

Figure 5-33 – R-Curves for nanomodified samples C0.5%.

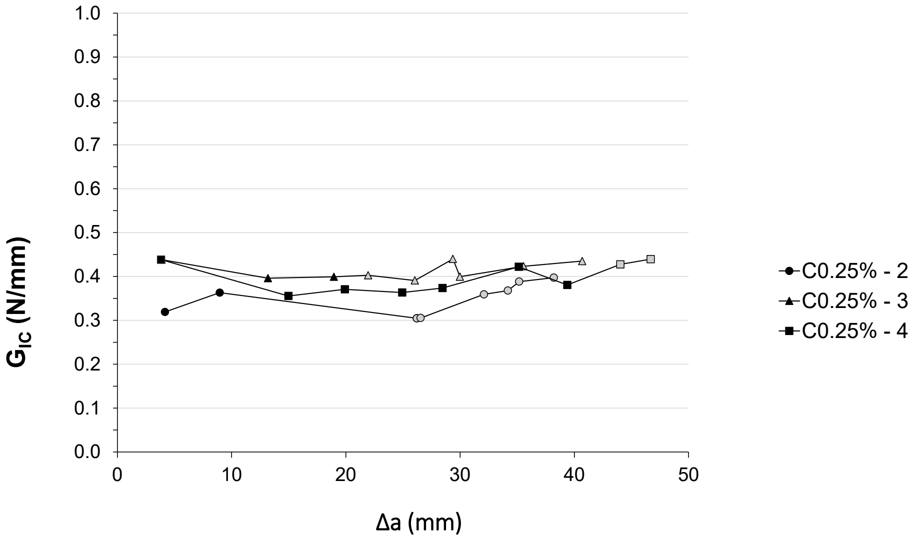

Figure 5-34 – R-Curves for nanomodified samples C0.25%.

Table 5.3 – Statistics of samples 1S, C1%, C0.5%, and C0.25%

Sample ID	G_{IC} Mean (N/mm)	Standard Deviation (N/mm)
1S	0.42	0,07
C1%	0.52	0.15
C0.5%	0.26	0.04
C0.25%	0.38	0.04

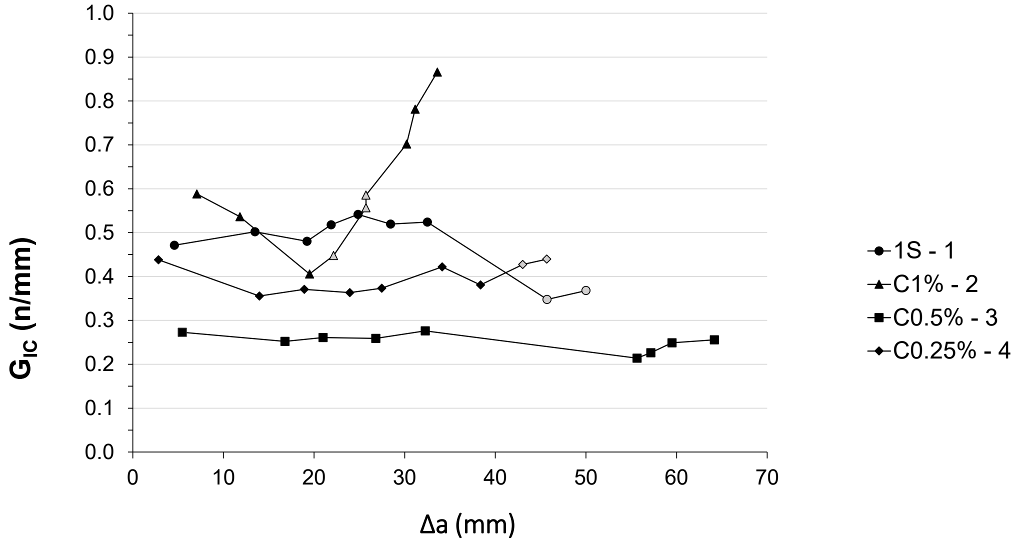

Figure 5-35 – Comparison of R-Curves of virgin (1S) and nanomodified (C1%, C0.5%, and C0.25%) specimens.

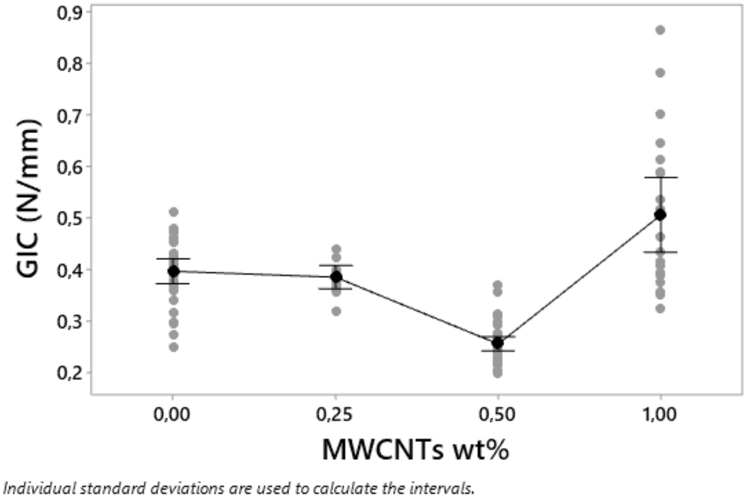

Figure 5-36 – Average G_{IC} variation as a function of MWCNTs content

5.1.3.3 Fracture Surface Analysis

This paragraph reports the morphological analysis of joints modified with different concentrations of MWCNTs. The results are related to the mechanical characterization previously presented. The Nano-modifies samples are compared with virgin ones to understand the phenomena that act in the modified adhesive layers.

Figure 5-37, Figure 5-38, and Figure 5-39 show the fracture surfaces of C1%, C0.5%, and C0.25% samples, respectively.

Samples C1% present cohesive failure in the Δa range of 10-20 mm. After 20 mm the crack tends to deviate inside the composite. Some C1% specimens have a crack that proceeds first in the adhesive, then in the composite, and afterwards tends to deflect back into the adhesive layer. This second deviation corresponds to increasing R-curve behavior. In this case, it is possible that the interactions between crack and CNT, mainly resent at the interface, increase. The interaction between the crack and nanoparticles can generate dissipative phenomena such as crack path deviation and debonding of particles followed by plastic void growth that increase the joint fracture toughness. Shear band are also present in the samples C0.5% -2 and C0.5% -4 [45].

Samples C0.5% have cohesive failure since the crack propagates inside the adhesive layer for the whole joint length. The fracture surface is comparable for all joints, and the behavior is similar for all samples, which show flat R-Curves with constant G_{IC} values.

The C0.5% specimens exhibit shear bands that are clearly visible. Shear bands in a polymer matrix are the result of local stress concentrations due to the presence of reinforcements, such as particles, fibers, or plates. Debonding at the particle-matrix interface leads to a decrease in triaxial stresses in the matrix, which allows the shear band to grow. Shear yielding begins at the point of maximum stress concentration. In this case the plastic zone of the matrix. the CNTs presence should reduce the size of the plastic zone for these samples that corresponds to low measurement of fracture energy. This phenomenon may be attributed to the reduced ability of the modified adhesive to undergo large deformations at relatively low stress values. The reduced deformations in the matrix can lead to a rapid crack propagation process, resulting in premature fracture of the specimen due to the propagation of cracks between neighboring particles.

Samples C0.25% exhibit cohesive failure only for the initial 10 mm of the propagation of the crack, which tends to go inside composite adherend after 10 mm. At low concentrations (0.25%), the fracture is not adhesive but proceeds in the adherend, indicating that the surface preparation is adequate and that the use of solvent as a dispersion medium does not generate a weak layer. Increasing the fraction of CNTs to 0.5% promotes crack propagation in the adhesive, but the adhesive is less prone to plastic deformation mechanisms. Further addition of CNTs with concentrations of 1% promotes crack deflection mechanisms, mainly in the vicinity of CNT-rich zones near the interface.

The fracture surfaces when Δa is in the range 10-20 mm of the representative samples are analyzed with SEM. Figure 5-40 shows SEM images of the C1% sample. The fracture surface appears rough, as in sample 1S, with the diffuse presence of micro dimples. The analyzed area exhibits cohesive failure and the presence of nylon cloth is evident. The fracture surface of Sample C0.5% is reported in Figure 5-41. It appears similar to C1% and 1S, but the fracture toughness is lower compared to other samples.

Sample C0.25% (Figure 5-42) presents a less rough surface and flat zone, especially near the interface zone, where the crack deviates from adhesive towards CFRP supports.

The three surfaces are investigated at different magnifications, but it is not possible to note the presence of CNT since they are located at the adhesive/adherend interface. In the specific case of C0.5%, the presence of the nanotubes promotes the adhesion between adhesive and adherends, leading to cohesive and reliable failure, even if the G_{IC} values are lower compared to the other samples.

Trends differ from the results of other work on MWCNTs, which suggest that polymer properties improve with increasing nanofiller concentrations up to a certain threshold, after which the trend reverses. For example in the works [16], [105]

the threshold value is an amount of MWCNT of 0.3%. In other works [195], [196] it has been shown that the highest toughness values are achieved at MWCNT concentrations of 1%

Figure 5-37 – Fracture surface of C1% samples

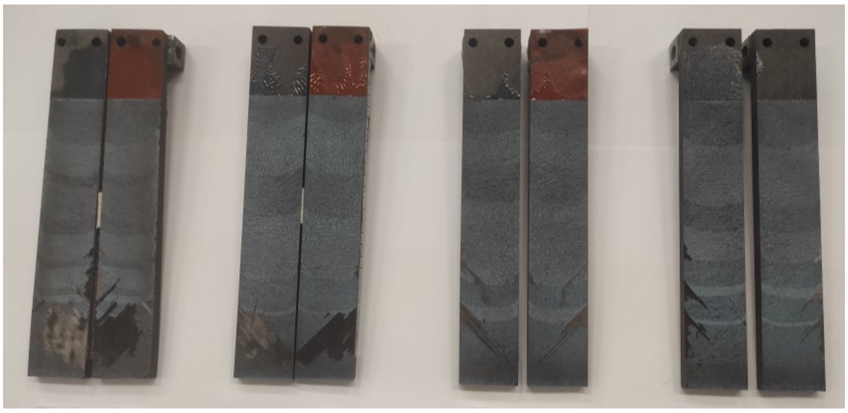

C0.5%- 1   C0.5%- 3   C0.5%- 4   C0.5%- 5

Figure 5-38 – Fracture surface of C0.5% samples

C0.25%- 2   C0.25%- 3   C0.25%- 4

Figure 5-39 – Fracture surface of C0.25% samples

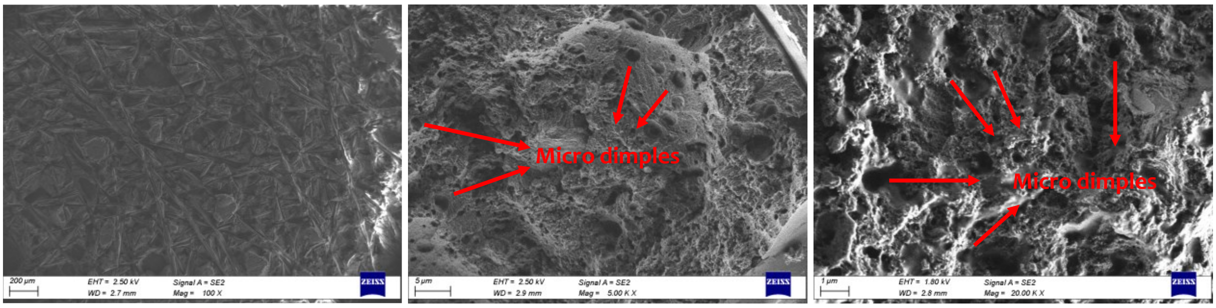

(a) (b) (c)

Figure 5-40 – SEM images of fracture surface of C1% - 2 at different magnification: 500X (a), 5000X (b) and 20000X (c)

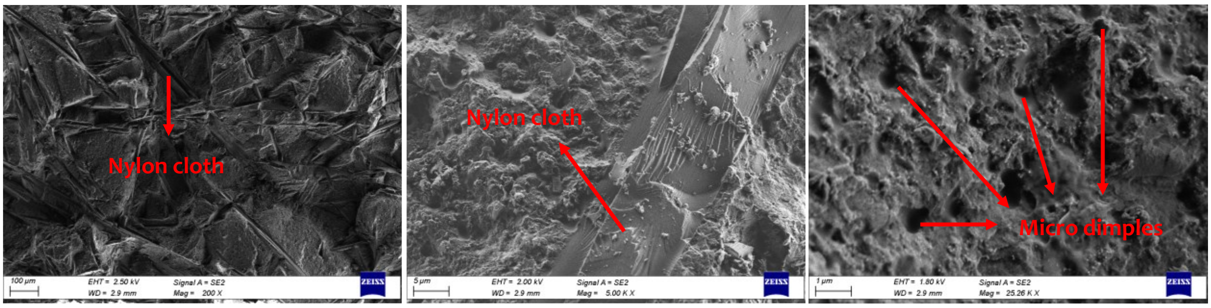

(a) (b) (c)

Figure 5-41 – SEM images of fracture surface of C0.5% - 3 at different magnification: 500X (a), 5000X (b) and 25260X (c)

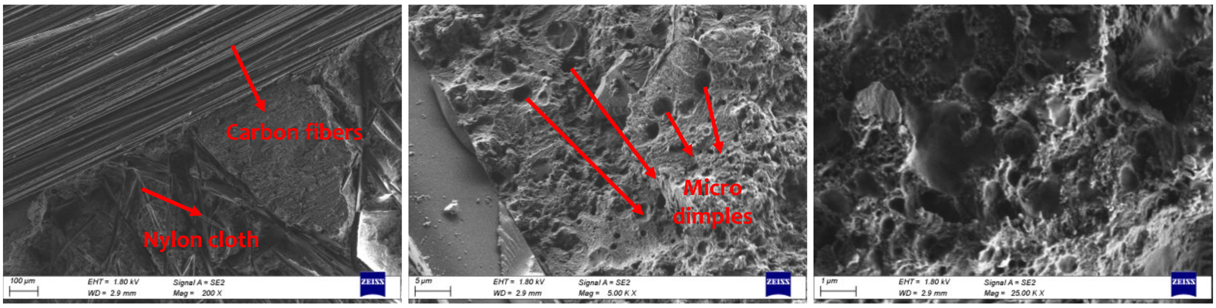

(a) (b) (c)

Figure 5-42 – SEM images of fracture surface of C0.25% - 2 at different magnification: 500X (a), 5000X (b) and 25000X (c)

5.1.3.4 *Resistance measure*

In this paragraph, the resistance variation is compared to the crack length, calculated during the test.

The test aims to verify if the joint resistance varies during the test, and therefore evaluate the potential application of nanomodified adhesive as a sensor for structural health monitoring tool.

The average initial resistance (R_0) of the system is measured for 10 seconds before starting the test. The results are reported in *Table* 5.4. R0 is strictly dependent on CNTs content, so samples C1% have lower resistance.

Table 5.4 – R_0 average values of MWCNTs modifies samples

Sample	Average R_0 (kΩ)
1S	29300.00
C1%	0.25
C0.5%	0.47
C0.25%	10.30

The electrical resistance (R) was measured during the mechanical test. Figure 5-43 and Figure 5-44 report the R/R_0 and load curves of representative samples, as a function of time, during DCB test. The peak of R/R_0 curves corresponds to the load peak, but the average R/R_0 values do not change during the test although crack propagation. Only the samples C0.25% - 4 present a resistance variation after the maximum load peak, but it is a unique case and it can be attributed to an error in measurements since the following crack propagation is not detected. Figure 5-46, Figure 5-47, and Figure 5-48 report the curves that correlate the resistance variation to crack length. No significant resistance variation related to crack propagation is noticed. The method used in this experimental campaign does not allow crack detection during its propagation, however the nanomodified adhesive present higher conductivity compared to virgin ones. For this reason, further refinements and improvements can be used to better control the variation of the electrical resistance of the adhesive layer.

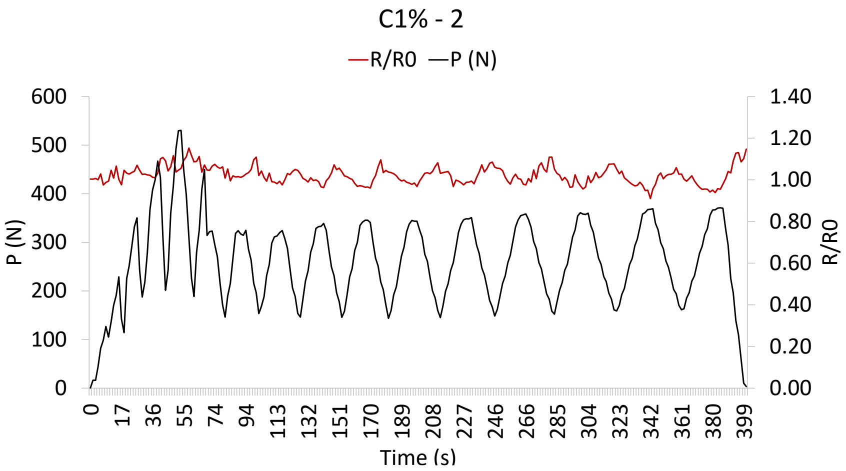

Figure 5-43 – R/R₀ and P curves of C1% - 2 samples as a function of time.

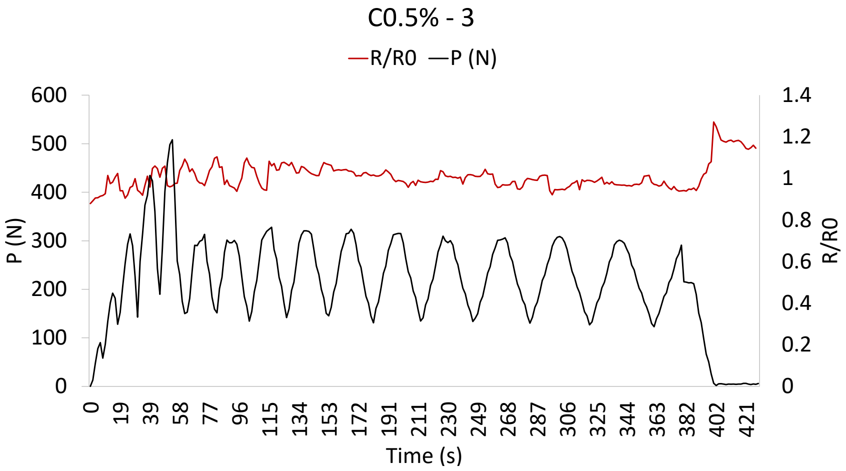

Figure 5-44 – R/R₀ and P curves of C0.5% - 3 samples as a function of time.

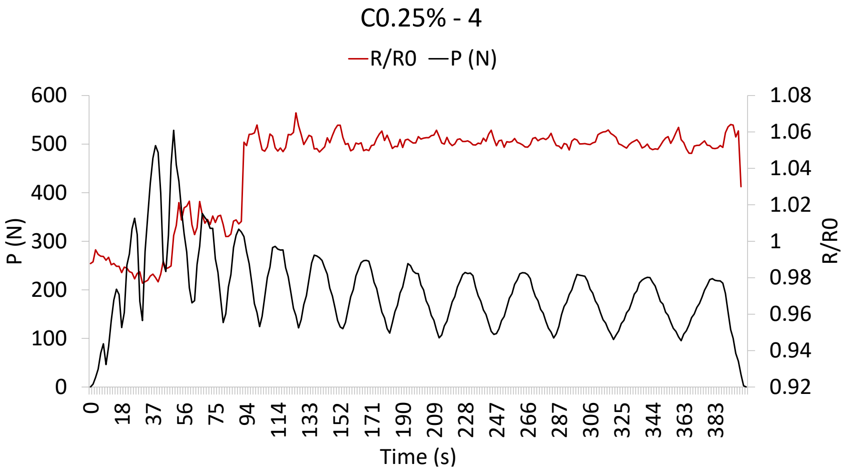

Figure 5-45 – R/R₀ and P curves of C0.25% - 4 samples as a function of time.

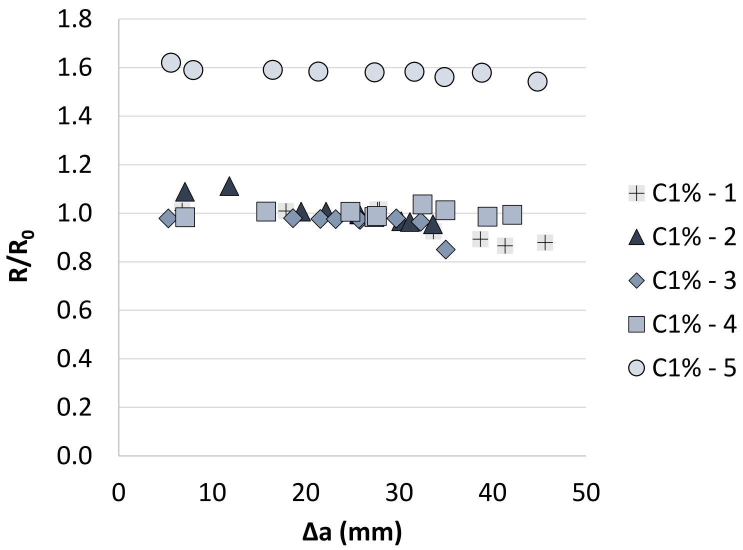

Figure 5-46 – R/R₀ variation as a function of crack propagation for samples C1%

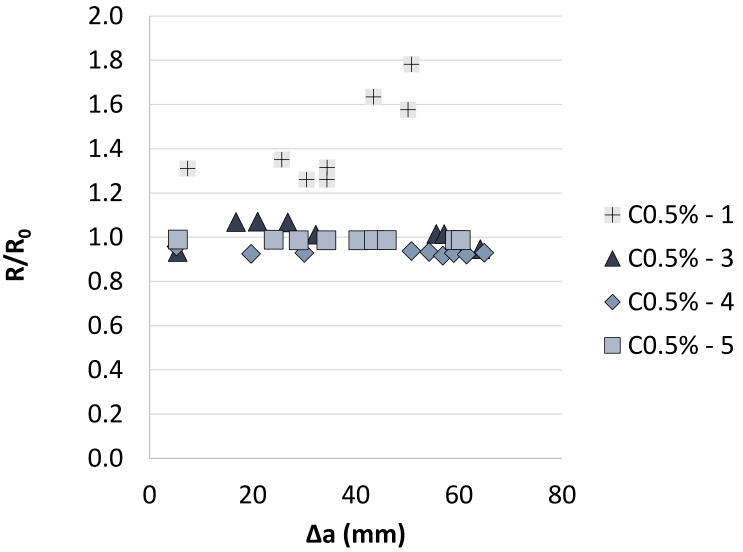

Figure 5-47 – R/R₀ variation as a function of crack propagation for samples C0.5%

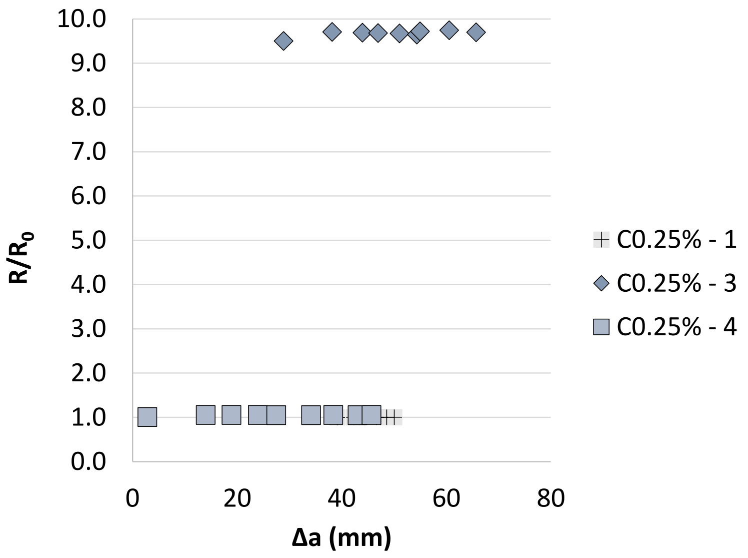

Figure 5-48 – R/R_0 variation as a function of crack propagation for samples C0.25%

5.1.4 Graphene Nanoplatelets

This section reports the mechanical and morphological characterization of the bonded joints modified with GNPs to investigate the effect of the nanofiller on the fracture toughness of the system. The resistance variation of the system is evaluated during the DCB test to evaluate these material as a candidate for SHM of bonded joints. Two bonding configurations are analyzed, named G1% and G0.5%. The samples differ in GNPs content which is 1% and 0.5% of the weight of epoxy fraction.

5.1.4.1 Mechanical Characterization

The test campaign focused on DCB joints is aimed to evaluate the influence of the GNPs embedded in the adhesive layer. The mechanical response of the DCBs is analyzed and later compared with the resulting fracture surface. The results of nanomodified and virgin samples are compared.

Figure 5-51 reports the load against CMOD of samples 1S – 1, G1% - 5, and G0.5% - 3, taken as representatives for each joint family. The load peak of nanomodified samples is around 500 N for G1%. Sample 1S and G1% withstand comparable loads until δ' values of 2mm, while G0.5% - 3 after the first peak exhibits a load values reduction that tends to be constant during the whole test.

Figure 5-52 and Figure 5-53 report the R-Curve of G1% and G0.5%, respectively.

The average fracture toughness values are reported inTable 5.5. The average fracture toughness of G1% is 0.44 ± 0.05 N/mm is comparable to sample 1S, considering the similar standard deviation. The R-Curves of G1% appear flat, and with constant values during crack propagation.

The samples G0.5% present constant G_{IC}, but the average value is lower (0.28 ± 0.07 N/mm) than samples with high GNPs concentration. Samples G0.5% present higher G_{IC} at the first point of R-Curves. This value, which corresponds to the maximum load peak, is comparable with the average fracture toughness of G1% samples.

Figure 5-54 reports the R-Curve of the representative samples of 1S, G1%, and G0.5%.

The fracture toughness of joint G1% is comparable to sample 1S, samples G0.5% have an average fracture toughness reduction of 33%.

Figure 5-55 reports the variation of G_{IC} values as a function of GNPs content. The presence of GNPs reduces joint performance at a concentration of 0.5%. At higher GNPs concentrations, the graphene nanoplatelets exhibit the same mechanical performance as virgin composite joints.

Figure 1-1 –Schematic representation of the equilibrium condition of interfacial forces, described by Young's equation.

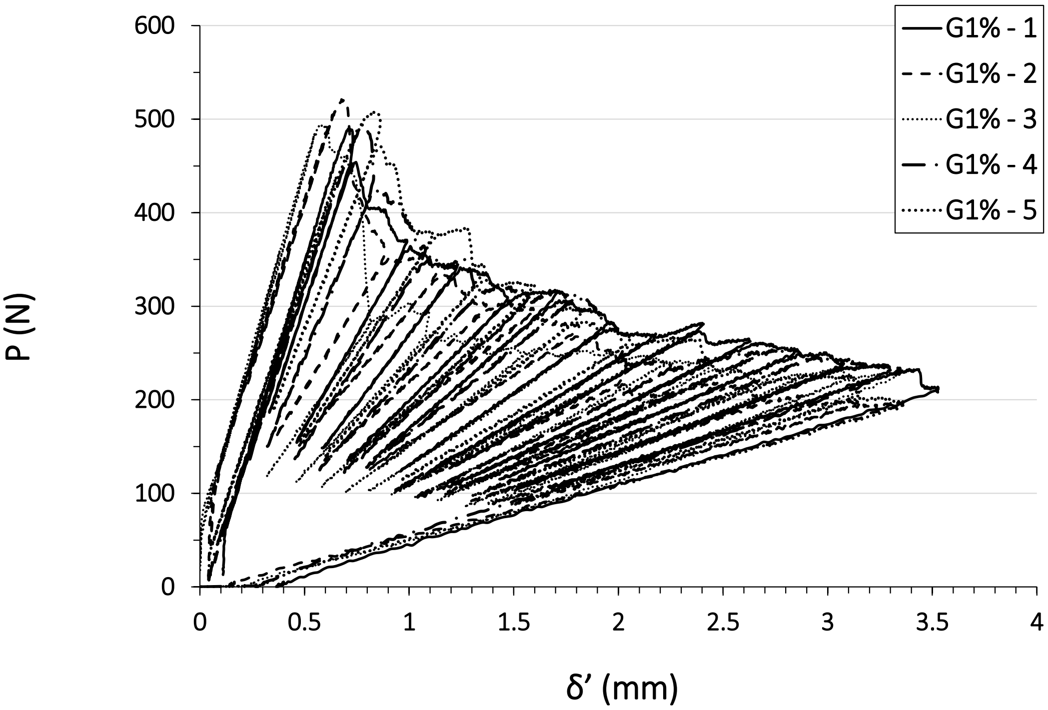

Figure 5-49 – Load against CMOD (δ') for G1% samples

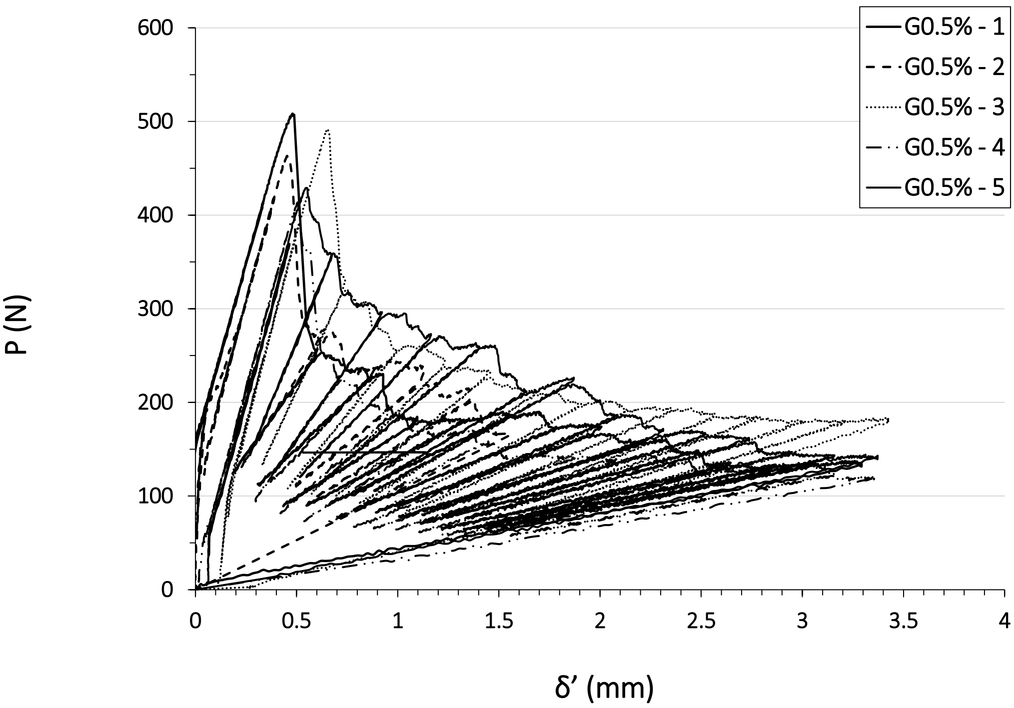

Figure 5-50 – Load against CMOD (δ') for G0.5% samples

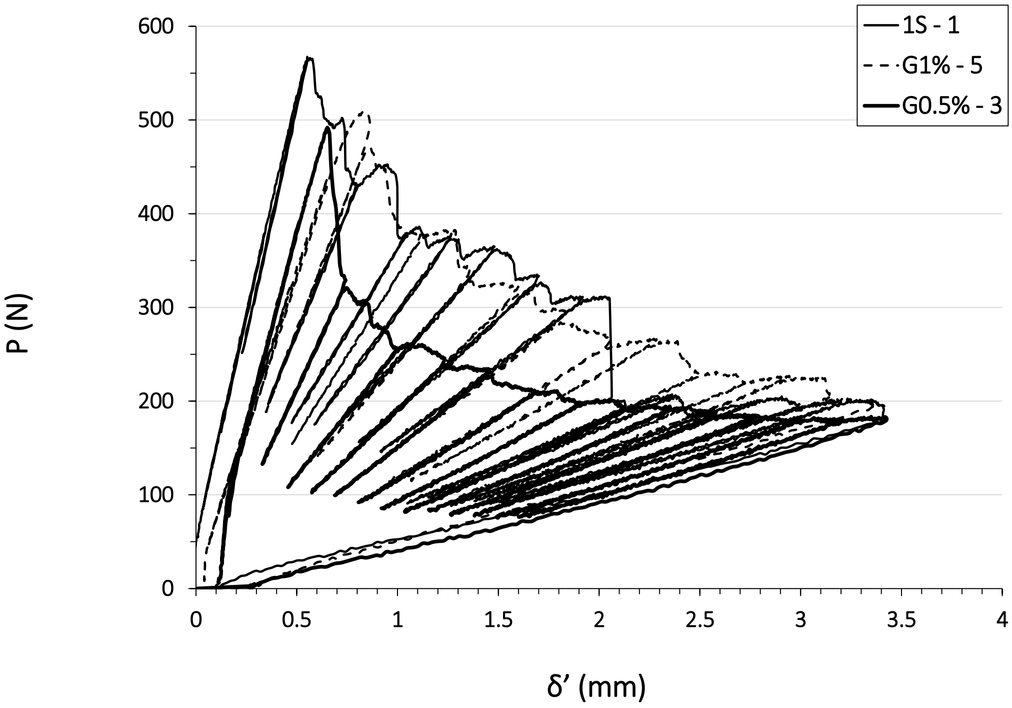

Figure 5-51 – Load against CMOD (δ') for both a virgin (1S 1 - 1) and GNPs nanomodified specimens (G1% - 5, G0.5% - 3) taken as representative

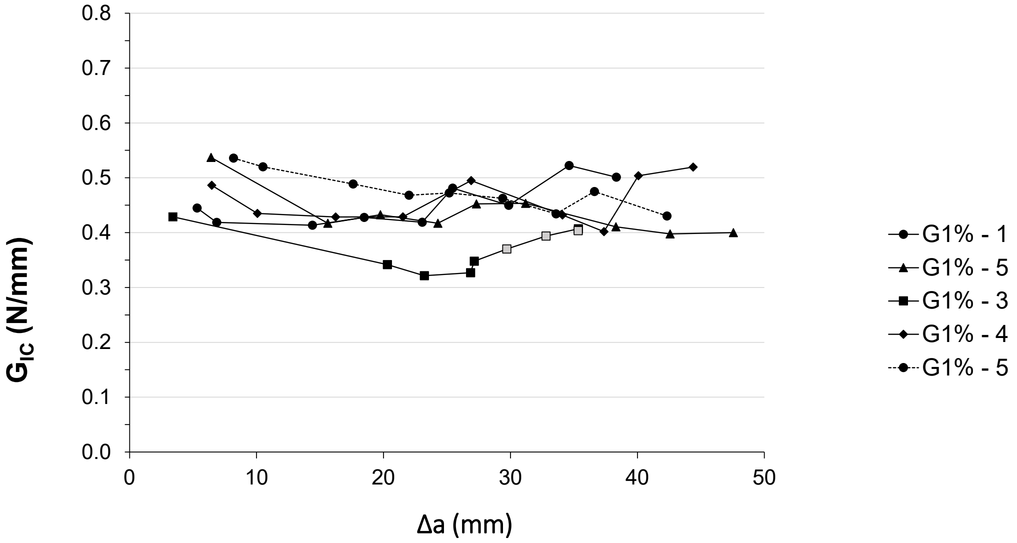

Figure 5-52 – R-Curves for nanomodified samples G1%.

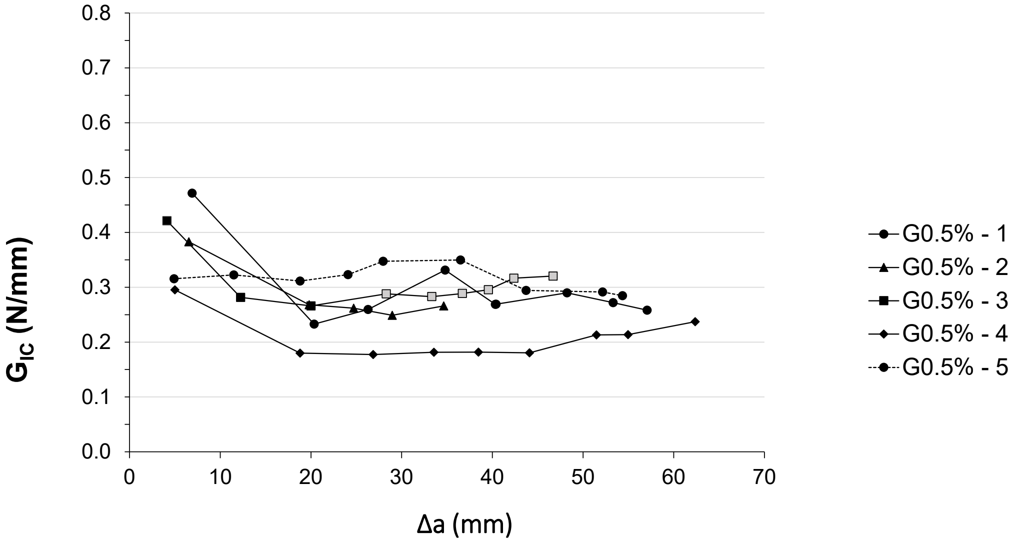

Figure 5-53 – R-Curves for nanomodified samples G0.5%.

Table 5.5 – Statistics of samples 1S, G1%, and G0.5%

Sample ID	G_{IC} Mean (N/mm)	Standard Deviation (N/mm)
1S	0.42	0.07
G1%	0.44	0.05
G0.5%	0.28	0.07

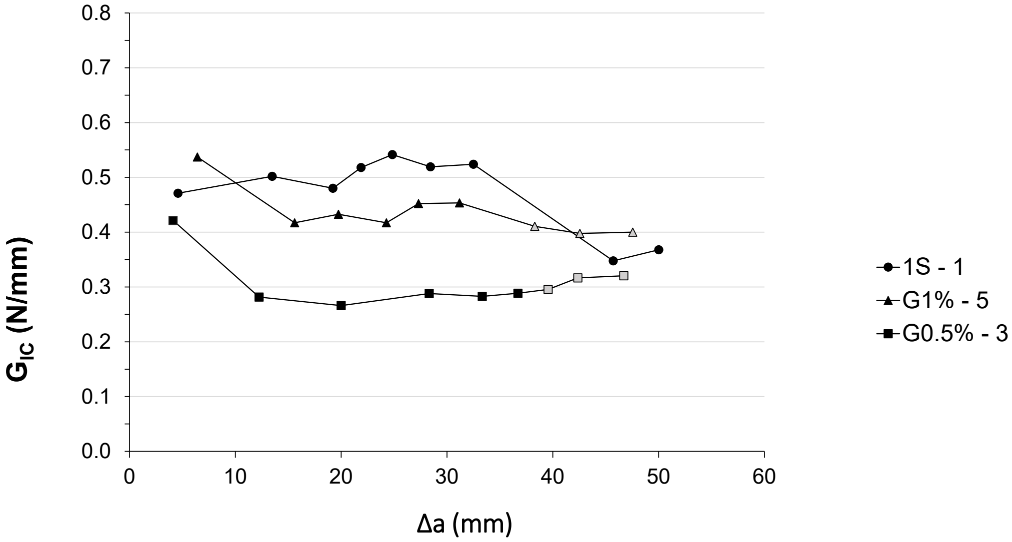

Figure 5-54 – Comparison of R-Curves of virgin (1S) and nanomodified (G1% and G0.5%) specimens.

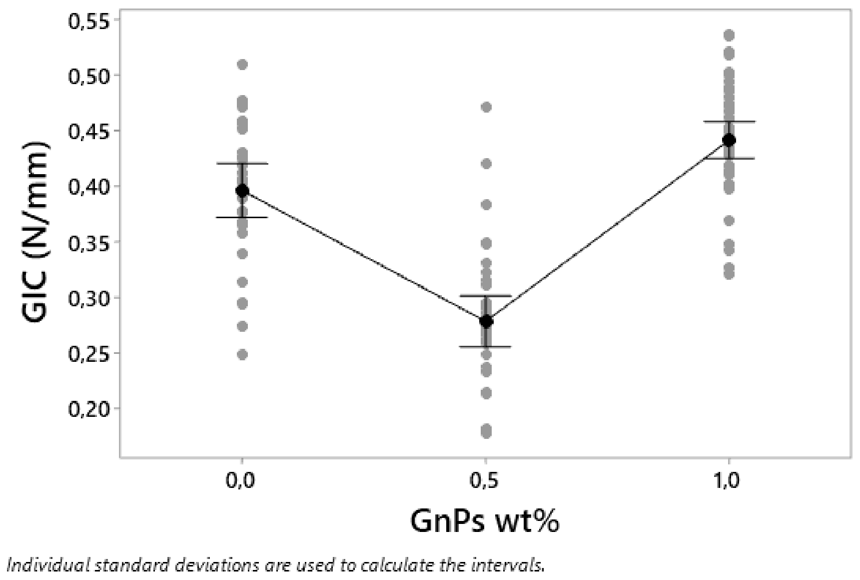

Figure 5-55 – Average G_{IC} variation as a function of GNPs content

5.1.4.2 *Fracture Surface Analysis*

This paragraph reports the morphological analysis of joints modified with different graphene nanoplatelets. The analysis of the fracture surfaces is related to the results of the mechanical characterization presented in the previous paragraph. The nanomodified samples are compared with virgin ones to understand the phenomena that act in the modified adhesive layers.

Figure 5-56 and Figure 5-57 show the fracture surfaces of the samples G1% and G0.5%, respectively.

Samples G1% exhibit cohesive fracture in the areas interested in crack propagation during the test. Samples G0.5% exhibit both cohesive and adhesive fracture surfaces. In particular, samples G0.5% - 1, G0.5% - 2, and G0.5% - 4 present adhesive failure that explains the lower fracture toughness values.

Adhesive failures could indicate problems with the surface treatment, although it is the same as that used with CNTs.

Samples G1% present cohesive failure in the Δa range monitored during DCB tests. Cohesive failure zones are characterised by the presence of adhesive (blue) on both bonded surfaces.The fracture surface is comparable for all joints and the behavior is similar for all samples which have flat R-Curves with constant G_{IC} values. The sample G1% - 3 shows lower values compared to the other samples, but it can be related to the crack path that appears to deviate to one adhesive/adherend interface, even if the adhesive is present on both adherend surfaces.

The fracture surfaces at Δa range of 30-40 mm of the representative samples are analyzed with SEM. In Figure 5-58 reports the fracture surface of sample G1% - 5 that appears rough. The crack propagates in the center of the adhesive layer, as the nylon fibers are visible in Figure 5-58 (a). Micro dimples are also present, as for samples 1S. The fracture surface of sample G0.5% - 3, shown in Figure 5-59, presents distributed flat zones, meaning that the fracture surface is not perfectly cohesive. Microdimple are still present but the adhesive is not very deformed as for G1% and virgin samples.

The different effect of GNP concentration is appreciated, samples modified by adding 0.5 wt% of GNPs show the worst interfacial adhesion compared to virgin samples. On the contrary, the 1 wt% of GNPs helps to obtain cohesive failure and more reproducible results, without affecting the mechanical performance of the adhesive. At concentrations of 0.5%, GNP caused a sharp decrease in fracture toughness, likely due to the reduced ability of the adhesive to plastically deform and absorb energy. However, at higher concentrations (1 % of GNP), crack deviation and bridging mechanisms may positively contribute to the fracture toughness of the joints, resulting in G_{IC} values similar to those of virgin joints.

Again, the trends found here deviate from the results of other work on GNPs, which suggest that polymer properties improve with increasing nanofiller concentrations up to a certain threshold, after which the trend reverses [197], [198]

G1%- 1 *G1%- 2* *G1%- 3* *G1%- 4* *G1%- 5*

Figure 5-56 – Fracture surface of G1% samples

Figure 5-57 – Fracture surface of G0.5% samples

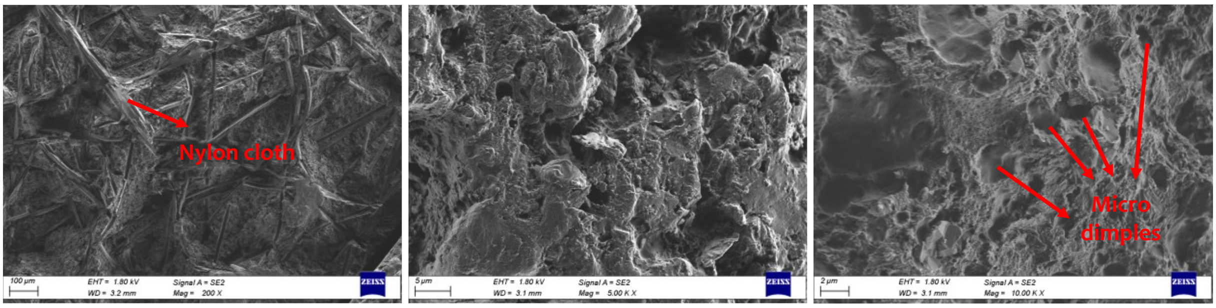

(a) (b) (c)

Figure 5-58 – SEM images of fracture surface of G1% - 5 at different magnification: 200X (a), 5000X (b) and 10000X (c)

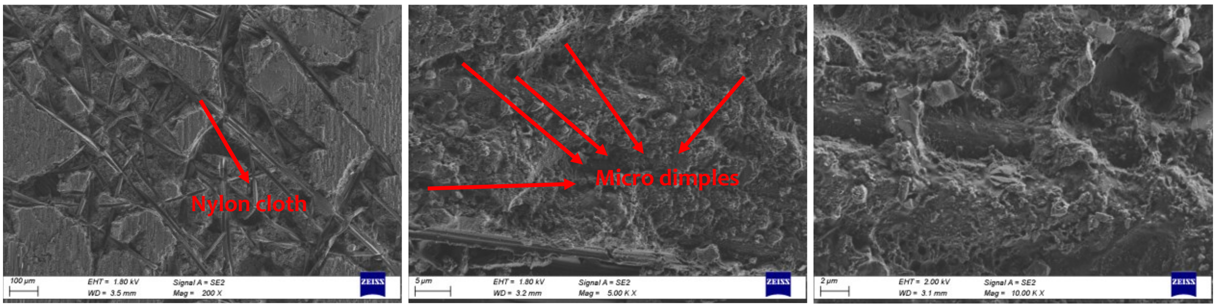

(a) (b) (c)

Figure 5-59 – SEM images of fracture surface of G0.5% - 3 at different magnification: 500X (a), 5000X (b) and 10000X (c)

5.1.4.3 Resistance Measures

The average initial resistance (R_0) of the system is measured for 10 seconds before starting the test. The results are reported in Table 5.6. R_0 is dependent on GNPs content, however, the G0.5% samples have lower resistance compared to G1%.

Table 5.6 – Statistics of samples 1S, G1% and G0.5%

Sample	Average R0 (kΩ)
1S	29300.00
G1%	1.36
G0.5%	0.28

The electrical resistance (R) was measured during the mechanical test. Figure 5-60, Figure 5-61 show the R/R0 and load curves as a function of the time of representative samples. The slope of the R/R_0 curve can be considered flat, and no significant resistance variation is detected. Sample G1% - 5 presents negative peaks. The resistance reduction is not expected since during the test there is the breakage of electrical paths due to crack propagation along the bondline that leads to resistance increment. For this reason, a negative peak can be considered meaningless. Sample G0.5% exhibits only one peak some seconds before the main load peak. After that, no resistance variations are detected.

Figure 5-62, and Figure 5-63 reports the curves that correlate the resistance variation to crack length during DCB tests. No significant resistance variation is detected that can be related to crack propagation. Samples G0.5% - 2 and G0.5% - 5 exhibit a signal variation due to the reduction of the bonded and conductive zone, but it is not sufficient to assess the effectiveness of the measurement method. The method used in this experimental campaign does not allow crack detection during its propagation, however, the nanomodified adhesive present higher conductivity compared to virgin ones. For this reason, further refinements and improvements can be used to better control the variation of the electrical resistance of the adhesive layer.

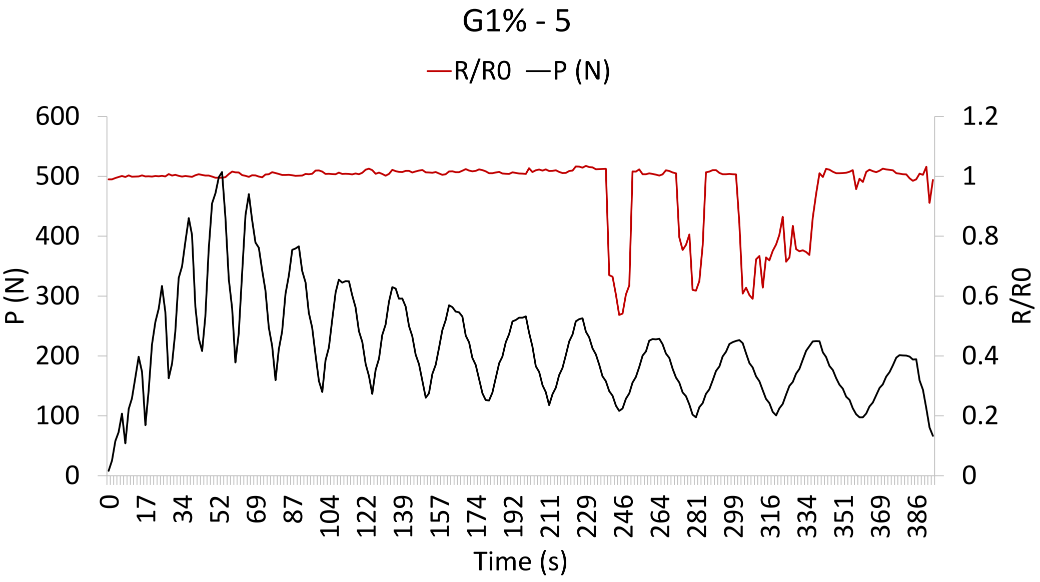

Figure 5-60 – R/R$_0$ and P curves of G1% - 5 samples as a function of time. The data are recorded during DCB test

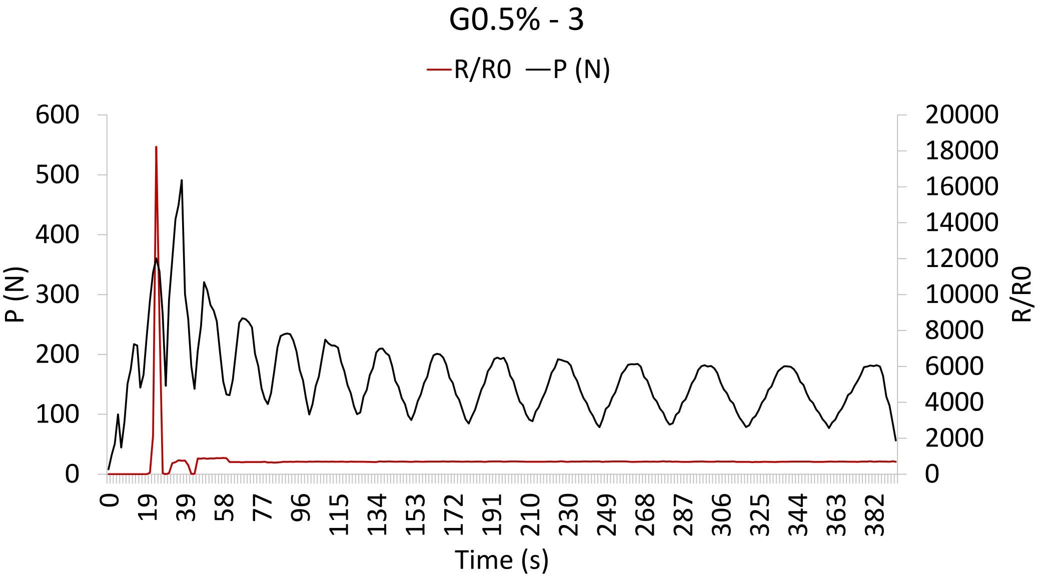

Figure 5-61 – R/R$_0$ and P curves of G0.5% - 3 samples as a function of time. The data are recorded during DCB test

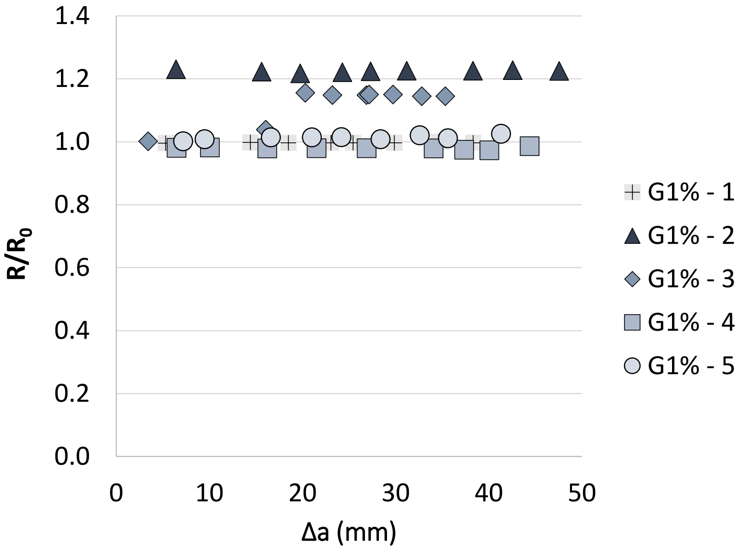

Figure 5-62 – R/R_0 variation as a function of crack propagation for samples G1%

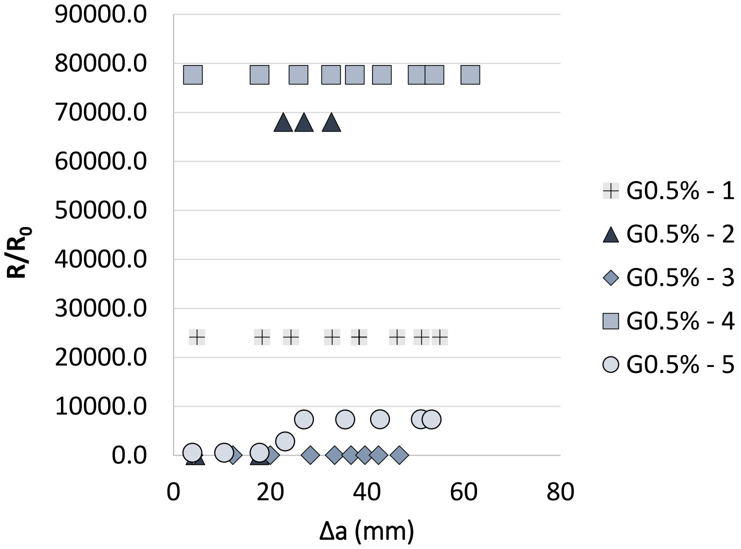

Figure 5-63 – R/R_0 variation as a function of crack propagation for samples G0.5%

5.1.5 Results Comparison

In this chapter, three different nanostructures were investigated to evaluate their effect on the fracture surface of the composite joint. The application of commercial XD10 PA nanofibers (XanturLayr) at the adhesive/adherend interface improves the mechanical performance of composite joints that exhibits higher fracture toughness compared to virgin samples. SEM images confirm the contribution of nanofibers that appear stretched and pulled out from the matrix. The same nanomat applied at the center of the adhesive layer does not contribute to the fracture toughness of the joints since the nanomodified joints exhibit the same G_{IC} values and standard deviation of neat samples.

Carbon-based nanofillers sprayed on the surfaces of adherends were also analyzed. Lower CNT concentration does not improve fracture toughness, even if samples containing 0.5% of CNT promote cohesive failure and reliable mechanical behavior. Higher CNT concentrations improve fracture toughness. The addition of graphene nanoplatelets shows similar behavior: lower concentrations of GNPs cause nonreliable adhesive failure and low fracture toughness; higher GNPs concentration exhibits practically the same results as virgin samples.

The trends found in this study diverge from the findings in the literature, which suggest that the properties of polymers improve with increasing nanofiller concentrations up to a certain threshold, after which the trend is reversed. This discrepancy can be attributed to the method used to distribute the nanofillers at the adhesive/support interface, as well as to the type of adhesive itself.

The presence of carbon-based filler makes the adhesive layer conductive, introducing the possibility of using this material as a tool for the structural health monitoring of bonded joints. The initial electrical resistance of the joints was measured: the presence of nanofillers improves the electrical conductivity. The resistance values can be affected by different factors, such as composite resistance and the quality and stability of the electrodes. Further refinements and improvements can be used to strictly control the variation of the electrical resistance of the adhesive layer.

CONCLUSIONS

The objective of this work is to investigate the effects of nanostructures on the fracture toughness of bonded joints and to evaluate their applicability at an industrial level. The fracture toughness of the joints was estimated by calculating the critical strain energy release rate, based on Mode I DCB test data. Three types of nanostructures were studied: electrospun nanofibres, multiwalled carbon nanotubes, and graphene nanoplatelets.

The effects of Nylon and NBR/PCL nanofibres, developed and produced at the University of Bologna, on metal joint fracture toughens was studied. The nanofibres were impregnated with a structural epoxy resin to produce the prepreg employed to bond S235 steel joints. The surface treatment before an adhesive deposition can determine the success or failure of the bonding application. Therefore, the optimization of the sandblasting parameters was carried out by evaluating the shear strength and fracture surfaces on steel SLJ. The optimized treatment is used for adherends preparation before DCB bonding.

The fracture toughness of joints bonded with both Nylon and NBR/PCL prepregs was lower than that of virgin samples. However, rubbery nanofibers exhibited improved performance compared to Nylon ones, as evidenced by the mean G_{IC} value of 0.58 N/mm for NBR/PCL modified adhesive and 0.38 N/mm for Nylon 6.6 nanomodified adhesive. Anyway, the behavior of nano modified joint is less scattered compared virgin sample. The SEM analyses of fracture surfaces of Nylon nanomodified specimens revealed no presence of microdimples, which are typically observed in virgin samples, and no evidence of fiber bridging or pull-out mechanisms. The rubber modified specimens show no fiber bridging and pull-out phenomena, similar to that seen in nylon specimens. The increased G_{IC} values for the rubber modified specimens can be attributed to the presence of a rubbery phase, which absorbs more energy than nylon nanofibers. The addition of nanofibers to an adhesive matrix does not increase adhesive fracture toughness, but it does provide a preferential pathway for crack propagation that exfoliates the nanomat embedded in the epoxy matrix. Furthermore, adhesives modified with nanofibers lead to more reproducible results, cohesive fracture, and constant G_{IC} values. The NBR/PCL nanomodified joint exhibits a guaranteed minimum G_{IC} fracture toughness value, regardless of the curing cycle adopted.

The effect of commercial XD10 PA (XantuLayr) nanofibres within composite joints bonded with the epoxy film was also studied. Materials and bonding techniques commonly employed in the automotive and aerospace sector were used for joint manufacturing. Since the adhesive is in the film form, the nylon nanofiber integration can be approached in two ways. The first is to apply the nanofiber at the adherends/adhesive interface. The second is to interleave the nanomat between two layers of adhesive.

The application of XanturLayr nanofibers at the adhesive/adherend interface of composite joints significantly improves their fracture toughness, as evidenced by SEM images showing nanofibers stretched and pulled out from the matrix. However, when the same nanomat is applied at the center of the adhesive layer, it does not contribute to the fracture toughness of the joints, therefore the nanomodified DCB exhibit comparable G_{IC} values and standard deviation to those of neat samples.

The toughening effects of MWCNT and GNP, at various concentrations, were examined when embedded into the adhesive layer of composite joints. The nanofillers were first dispersed in acetone and then sprayed on the composite bonding surface with an airbrush. After the solvent evaporation, the two substrates were bonded with the epoxy film and cured in autoclave. At low MWCNT concentrations, meaning 0.25 wt.%, the crack propagates into the adherend, indicating that the surface preparation is adequate and that the use of solvent did not generate a weak layer at the interface. Increasing the fraction of MWCNTs to 0.5 wt.% promotes crack propagation in the adhesive, but the it is less prone to plastic deformation mechanisms. Further addition of CNTs with concentrations of 1% promotes crack deflection mechanisms, mainly in the vicinity of CNT-rich zones near the interface.

The addition of graphene nanoplatelets shows similar behavior: at concentrations of 0.5%, GNP caused a sharp decrease in fracture toughness, likely due to the reduced ability of the adhesive to plastically deform and absorb energy. However, at higher concentrations, 1wt% of GNP, crack deviation and bridging mechanisms may positively contribute to the fracture toughness of the joints, resulting in G_{IC} values similar to those of virgin joints.

The trends found in this study diverge from the findings in the literature, which suggest that the properties of adhesives improve with increasing nanofiller concentrations up to a certain threshold, after which the trend is reversed. This discrepancy can be attributed to the method used to distribute the nanofillers at the adhesive/support interface, as well as to the type of adhesive itself.

The use of carbon-based nanofillers in the adhesive layer of bonded joints improves their electrical conductivity. The initial electrical resistance of the joints was measured and was found to be affected by a variety of factors, such as composite resistance and the quality and stability of the electrodes. Further optimization of the adhesive layer and of the test set up may allow for precise control over the electrical resistance of the joints.

REFERENCES

[1] A. Zucchelli, M. L. Focarete, C. Gualandi, and S. Ramakrishna, “Electrospun nanofibers for enhancing structural performance of composite materials,” *Polymers for Advanced Technologies*, vol. 22, no. 3, pp. 339–349, 2011, doi: 10.1002/pat.1837.

[2] R. Palazzetti and A. Zucchelli, “Electrospun nanofibers as reinforcement for composite laminates materials – A review,” *Composite Structures*, vol. 182, pp. 711–727, Dec. 2017, doi: 10.1016/j.compstruct.2017.09.021.

[3] S. Hamer, H. Leibovich, R. Intrater, E. Zussman, A. Siegmann, and D. Sherman, “Mode I Interlaminar Fracture Toughness of Nylon 66 Nanofibrilmat Interleaved Carbon/Epoxy Laminates,” *Polymer Composites*, vol. 32, pp. 1781–1789, Nov. 2011, doi: 10.1002/pc.21210.

[4] R. Palazzetti, A. Zucchelli, and I. Trendafilova, “The self-reinforcing effect of Nylon 6,6 nano-fibres on CFRP laminates subjected to low velocity impact,” *Composite Structures*, vol. 106, pp. 661–671, Dec. 2013, doi: 10.1016/j.compstruct.2013.07.021.

[5] F. Moroni, R. Palazzetti, A. Zucchelli, and A. Pirondi, “A numerical investigation on the interlaminar strength of nanomodified composite interfaces,” *Composites Part B: Engineering*, vol. 55, pp. 635–641, Dec. 2013, doi: 10.1016/j.compositesb.2013.07.004.

[6] G. Giuliese, R. Palazzetti, F. Moroni, A. Zucchelli, and A. Pirondi, “Cohesive zone modelling of delamination response of a composite laminate with interleaved nylon 6,6 nanofibres,” *Composites Part B: Engineering*, vol. 78, pp. 384–392, Sep. 2015, doi: 10.1016/j.compositesb.2015.03.087.

[7] G. W. Beckermann and K. L. Pickering, “Mode I and Mode II interlaminar fracture toughness of composite laminates interleaved with electrospun nanofibre veils,” *Composites Part A: Applied Science and Manufacturing*, vol. 72, pp. 11–21, May 2015, doi: 10.1016/j.compositesa.2015.01.028.

[8] H. Saghafi, R. Palazzetti, A. Zucchelli, and G. Minak, “Influence of electrospun nanofibers on the interlaminar properties of unidirectional epoxy resin/glass fiber composite laminates:,” *Journal of Reinforced Plastics and Composites*, May 2015, doi: 10.1177/0731684415584635.

[9] H. Zhang, A. Bharti, Z. Li, S. Du, E. Bilotti, and T. Peijs, “Localized toughening of carbon/epoxy laminates using dissolvable thermoplastic interleaves and electrospun fibres,” *Composites Part A: Applied Science and Manufacturing*, vol. 79, pp. 116–126, Dec. 2015, doi: 10.1016/j.compositesa.2015.09.024.

[10] L. Daelemans, S. van der Heijden, I. De Baere, H. Rahier, W. Van Paepegem, and K. De Clerck, “Using aligned nanofibres for identifying the toughening micromechanisms in nanofibre interleaved laminates,” *Composites Science and Technology*, vol. 124, pp. 17–26, Mar. 2016, doi: 10.1016/j.compscitech.2015.11.021.

[11] L. Daelemans, S. van der Heijden, I. De Baere, H. Rahier, W. Van Paepegem, and K. De Clerck, “Improved fatigue delamination behaviour of composite laminates with electrospun thermoplastic nanofibrous interleaves using the Central Cut-Ply method,” *Composites Part A: Applied Science and Manufacturing*, vol. 94, pp. 10–20, Mar. 2017, doi: 10.1016/j.compositesa.2016.12.004.

[12] H. J. Oh, H. Y. Kim, and S. S. Kim, “Effect of the Core/Shell-Structured Meta-Aramid/Epoxy Nanofiber on the Mechanical and Thermal Properties in Epoxy Adhesive Composites by Electrospinning,” *The Journal of Adhesion*, vol. 90, no. 9, pp. 787–801, Sep. 2014, doi: 10.1080/00218464.2013.843458.

[13] S. Y. On, M. S. Kim, and S. S. Kim, “Effects of post-treatment of meta-aramid nanofiber mats on the adhesion strength of epoxy adhesive joints,” *Composite Structures*, vol. 159, pp. 636–645, Jan. 2017, doi: 10.1016/j.compstruct.2016.10.016.

[14] S. M. J. Razavi, R. E. Neisiany, M. R. Ayatollahi, S. Ramakrishna, S. N. Khorasani, and F. Berto, “Fracture assessment of polyacrylonitrile nanofiber-reinforced epoxy adhesive,” *Theoretical*

and Applied Fracture Mechanics, vol. 97, pp. 448–453, Oct. 2018, doi: 10.1016/j.tafmec.2017.07.023.

[15] M. Ekrem and A. Avcı, “Effects of polyvinyl alcohol nanofiber mats on the adhesion strength and fracture toughness of epoxy adhesive joints,” *Composites Part B: Engineering*, vol. 138, pp. 256–264, Apr. 2018, doi: 10.1016/j.compositesb.2017.11.049.

[16] T. Takeda and F. Narita, “Fracture behavior and crack sensing capability of bonded carbon fiber composite joints with carbon nanotube-based polymer adhesive layer under Mode I loading,” *Composites Science and Technology*, vol. 146, pp. 26–33, Jul. 2017, doi: 10.1016/j.compscitech.2017.04.014.

[17] X. F. Sánchez-Romate, C. García, J. Rams, M. Sánchez, and A. Ureña, “Structural health monitoring of a CFRP structural bonded repair by using a carbon nanotube modified adhesive film,” *Composite Structures*, vol. 270, p. 114091, Aug. 2021, doi: 10.1016/j.compstruct.2021.114091.

[18] X. F. Sánchez-Romate *et al.*, “Monitoring crack propagation in skin-stringer elements using carbon nanotube doped adhesive films: Influence of defects and manufacturing process,” *Composites Science and Technology*, vol. 193, p. 108147, Jun. 2020, doi: 10.1016/j.compscitech.2020.108147.

[19] A. J. Kinloch, *Adhesion and Adhesives*. Dordrecht: Springer Netherlands, 1987. doi: 10.1007/978-94-015-7764-9.

[20] R. D. Adams, *Adhesive Bonding: Science, Technology and Applications*. Elsevier, 2005.

[21] L. F. M. da Silva, A. Öchsner, and R. D. Adams, Eds., *Handbook of adhesion technology*. in Springer reference. Heidelberg: Springer, 2011.

[22] S. Ebnesajjad and A. H. Landrock, *Adhesives Technology Handbook*. William Andrew, 2008.

[23] I. E. Klein, J. Sharon, A. E. Yaniv, H. Dodiuk, and D. Katz, “Chemical interactions in the system anodized aluminum—primer—adhesive,” *International Journal of Adhesion and Adhesives*, vol. 3, no. 3, pp. 159–162, Jul. 1983, doi: 10.1016/0143-7496(83)90122-7.

[24] T. Sugama, L. E. Kukacka, and N. Carciello, “Nature of interfacial interaction mechanisms between polyacrylic acid macromolecules and oxide metal surfaces,” *J Mater Sci*, vol. 19, no. 12, pp. 4045–4056, Dec. 1984, doi: 10.1007/BF00980770.

[25] S. Crisp, H. J. Prosser, and A. D. Wilson, “An infra-red spectroscopic study of cement formation between metal oxides and aqueous solutions of poly(acrylic acid),” *J Mater Sci*, vol. 11, no. 1, pp. 36–48, Jan. 1976, doi: 10.1007/BF00541072.

[26] S. R. Leadley and J. F. Watts, “The use of XPS to examine the interaction of poly(acrylic acid) with oxidised metal substrates,” *Journal of Electron Spectroscopy and Related Phenomena*, vol. 85, no. 1, pp. 107–121, Jul. 1997, doi: 10.1016/S0368-2048(97)00028-5.

[27] J. P. Bell and W. T. McCarvill, “Surface interaction between aluminum and epoxy resin,” *Journal of Applied Polymer Science*, vol. 18, no. 8, pp. 2243–2247, 1974, doi: 10.1002/app.1974.070180803.

[28] A. E. Yaniv, I. E. Klein, J. Sharon, and H. Dodiuk, “Bonding of adhesive primers to aluminium substrates,” *Surface and Interface Analysis*, vol. 5, no. 3, pp. 93–97, 1983, doi: 10.1002/sia.740050303.

[29] I. Kusaka and W. Suëtaka, “Infrared spectrum of α-cyanoacrylate adhesive in the first monolayer on a bulk aluminum surface,” *Spectrochimica Acta Part A: Molecular Spectroscopy*, vol. 36, no. 7, pp. 647–648, Jan. 1980, doi: 10.1016/0584-8539(80)80022-5.

[30] J. R. Huntsberger, “Interfacial energies, contact angles, and adhesion,” *Adhesives Age*, vol. 21, no. 12, pp. 23–27, 1978.

[31] F. M. Fowkes, “Treatise on adhesion and adhesives,” *New York*, vol. 1, p. 18, 1967.

[32] E. M. Petrie, *Handbook of adhesives and sealants*, Third edition. New York: McGraw-Hill, 2021.

[33] C. W. Jennings, “Surface Roughness and Bond Strength of Adhesives,” *The Journal of Adhesion*, vol. 4, no. 1, pp. 25–38, May 1972, doi: 10.1080/00218467208072208.

[34] J. R. G. Evans and D. E. Packham, “Adhesion of Polyethylene to Metals: The Role of Surface Topography,” *The Journal of Adhesion*, vol. 10, no. 3, pp. 177–191, Jan. 1979, doi: 10.1080/00218467908544624.

[35] J. P. Sargent, “Adherend surface morphology and its influence on the peel strength of adhesive joints bonded with modified phenolic and epoxy structural adhesives,” *International Journal of Adhesion and Adhesives*, vol. 14, no. 1, pp. 21–30, Jan. 1994, doi: 10.1016/0143-7496(94)90017-5.

[36] M. Shahid and S. A. Hashim, “Effect of surface roughness on the strength of cleavage joints,” *International Journal of Adhesion and Adhesives*, vol. 22, no. 3, pp. 235–244, Jan. 2002, doi: 10.1016/S0143-7496(01)00059-8.

[37] G. W. Critchlow and D. M. Brewis, “Influence of surface macroroughness on the durability of epoxide-aluminium joints,” *International Journal of Adhesion and Adhesives*, vol. 15, no. 3, pp. 173–176, Jul. 1995, doi: 10.1016/0143-7496(95)91628-J.

[38] Thery S, Legros A, Balladon P., “Study of parameters influencing the mechanical behaviour of and damage to steel-polymer interfaces,” vol. Mechanics and mechanisms of damage in composites and multi-materials.

[39] *Fundamentals of Adhesion and Interfaces*. De Gruyter, 2020. doi: 10.1515/9783112318515.

[40] P. Weiss, “The science of adhesive joints. 2nd Ed. J. J. Bikerman. Academic Press, New York, 1968. xi + 349 pp. $16.00.,” *Journal of Applied Polymer Science*, vol. 12, no. 12, pp. 2743–2744, 1968, doi: 10.1002/app.1968.070121219.

[41] S. G. Prolongo, M. R. Gude, and A. Ureña, “Nanoreinforced Adhesives,” *Nanofibers*, Feb. 2010, doi: 10.5772/8147.

[42] N. E. Dowling, *Mechanical Behavior of Materials: Engineering Methods for Deformation, Fracture, and Fatigue*. Pearson, 2013.

[43] ASTM D3433 - 99, “Standard Test Method for Fracture Strength in Cleavage of Adhesives in Bonded Metal Joints.” 1999.

[44] S. Krenk, “Energy release rate of symmetric adhesive joints,” *Engineering Fracture Mechanics*, vol. 43, no. 4, pp. 549–559, Nov. 1992, doi: 10.1016/0013-7944(92)90198-N.

[45] A. N. Giv, M. R. Ayatollahi, S. H. Ghaffari, and L. F. M. da Silva, “Effect of reinforcements at different scales on mechanical properties of epoxy adhesives and adhesive joints: a review,” *The Journal of Adhesion*, vol. 94, no. 13, pp. 1082–1121, Nov. 2018, doi: 10.1080/00218464.2018.1452736.

[46] İ. Saraç, H. Adin, and Ş. Temiz, “Experimental determination of the static and fatigue strength of the adhesive joints bonded by epoxy adhesive including different particles,” *Composites Part B: Engineering*, vol. 155, pp. 92–103, Dec. 2018, doi: 10.1016/j.compositesb.2018.08.006.

[47] M. D. Banea, L. F. M. da Silva, R. J. C. Carbas, and R. D. S. G. Campilho, “Mechanical and thermal characterization of a structural polyurethane adhesive modified with thermally expandable particles,” *International Journal of Adhesion and Adhesives*, vol. 54, pp. 191–199, Oct. 2014, doi: 10.1016/j.ijadhadh.2014.06.008.

[48] E. B. Caldona, A. C. C. De Leon, B. B. Pajarito, and R. C. Advincula, “A Review on Rubber-Enhanced Polymeric Materials,” *Polymer Reviews*, vol. 57, no. 2, pp. 311–338, Apr. 2017, doi: 10.1080/15583724.2016.1247102.

[49] C. K. Riew, A. R. Siebert, R. W. Smith, M. Fernando, and A. J. Kinloch, “Toughened Epoxy Resins: Preformed Particles as Tougheners for Adhesives and Matrices,” in *Toughened Plastics II*, C. K. Riew and A. J. Kinloch, Eds., in Advances in Chemistry, vol. 252. Washington, DC: American Chemical Society, 1996, pp. 33–44. doi: 10.1021/ba-1996-0252.ch003.

[50] R. J. J. Williams, B. A. Rozenberg, and J.-P. Pascault, “Reaction-induced phase separation in modified thermosetting polymers,” in *Polymer Analysis Polymer Physics*, in Advances in Polymer Science. Berlin, Heidelberg: Springer, 1997, pp. 95–156. doi: 10.1007/3-540-61218-1_7.

[51] W. L. Tsang and A. C. Taylor, "Fracture and toughening mechanisms of silica- and core–shell rubber-toughened epoxy at ambient and low temperature," *J Mater Sci*, vol. 54, no. 22, pp. 13938–13958, Nov. 2019, doi: 10.1007/s10853-019-03893-y.

[52] C. W. Wise, W. D. Cook, and A. A. Goodwin, "CTBN rubber phase precipitation in model epoxy resins," *Polymer*, vol. 41, no. 12, pp. 4625–4633, Jun. 2000, doi: 10.1016/S0032-3861(99)00686-2.

[53] R. Bagheri, B. T. Marouf, and R. A. Pearson, "Rubber-Toughened Epoxies: A Critical Review," *Polymer Reviews*, vol. 49, no. 3, pp. 201–225, Aug. 2009, doi: 10.1080/15583720903048227.

[54] A. J. Kinloch, "Toughening Epoxy Adhesives to Meet Today's Challenges," *MRS Bull.*, vol. 28, no. 6, pp. 445–448, Jun. 2003, doi: 10.1557/mrs2003.126.

[55] A. Avci, H. Arikan, and A. Akdemir, "Fracture behavior of glass fiber reinforced polymer composite," *Cement and Concrete Research*, vol. 34, no. 3, pp. 429–434, Mar. 2004, doi: 10.1016/j.cemconres.2003.08.027.

[56] L. W. H. Leonard, K. J. Wong, K. O. Low, and B. F. Yousif, "Fracture behaviour of glass fibre-reinforced polyester composite," *Proceedings of the Institution of Mechanical Engineers, Part L: Journal of Materials: Design and Applications*, vol. 223, no. 2, pp. 83–89, Apr. 2009, doi: 10.1243/14644207JMDA224.

[57] S. K. Gupta, D. K. Shukla, and D. K. Ravindra, "Effect of nanoalumina in epoxy adhesive on lap shear strength and fracture toughness of aluminium joints," *The Journal of Adhesion*, vol. 0, no. 0, pp. 1–23, Jul. 2019, doi: 10.1080/00218464.2019.1641088.

[58] Z.-M. Huang, Y.-Z. Zhang, M. Kotaki, and S. Ramakrishna, "A review on polymer nanofibers by electrospinning and their applications in nanocomposites," *Composites Science and Technology*, vol. 63, no. 15, pp. 2223–2253, Nov. 2003, doi: 10.1016/S0266-3538(03)00178-7.

[59] G. L. Burkholder, Y. W. Kwon, and R. D. Pollak, "Effect of carbon nanotube reinforcement on fracture strength of composite adhesive joints," *J Mater Sci*, vol. 46, no. 10, pp. 3370–3377, May 2011, doi: 10.1007/s10853-010-5225-6.

[60] M. B. Jakubinek *et al.*, "Single-walled carbon nanotube–epoxy composites for structural and conductive aerospace adhesives," *Composites Part B: Engineering*, vol. 69, pp. 87–93, Feb. 2015, doi: 10.1016/j.compositesb.2014.09.022.

[61] M. R. Gude, S. G. Prolongo, and A. Ureña, "Toughening effect of carbon nanotubes and carbon nanofibres in epoxy adhesives for joining carbon fibre laminates," *International Journal of Adhesion and Adhesives*, vol. 62, pp. 139–145, Oct. 2015, doi: 10.1016/j.ijadhadh.2015.07.011.

[62] A. H. Korayem, S. J. Chen, Q. H. Zhang, C. Y. Li, X. L. Zhao, and W. H. Duan, "Failure of CFRP-to-steel double strap joint bonded using carbon nanotubes modified epoxy adhesive at moderately elevated temperatures," *Composites Part B: Engineering*, vol. 94, pp. 95–101, Jun. 2016, doi: 10.1016/j.compositesb.2016.03.042.

[63] H. Khoramishad and M. Khakzad, "Toughening epoxy adhesives with multi-walled carbon nanotubes," *The Journal of Adhesion*, vol. 94, no. 1, pp. 15–29, Jan. 2018, doi: 10.1080/00218464.2016.1224184.

[64] I. A. Akpinar, A. Gürses, S. Akpinar, K. Gültekin, H. Akbulut, and A. Ozel, "Investigation of mechanical and thermal properties of nanostructure-doped bulk nanocomposite adhesives," *The Journal of Adhesion*, vol. 94, no. 11, pp. 847–866, Sep. 2018, doi: 10.1080/00218464.2017.1415809.

[65] W. Zielecki, A. Kubit, T. Trzepieciński, U. Narkiewicz, and Z. Czech, "Impact of multiwall carbon nanotubes on the fatigue strength of adhesive joints," *International Journal of Adhesion and Adhesives*, vol. 73, pp. 16–21, Mar. 2017, doi: 10.1016/j.ijadhadh.2016.11.005.

[66] P. Jojibabu, Y. X. Zhang, A. N. Rider, J. Wang, and B. Gangadhara Prusty, "Synergetic effects of carbon nanotubes and triblock copolymer on the lap shear strength of epoxy adhesive joints," *Composites Part B: Engineering*, vol. 178, p. 107457, Dec. 2019, doi: 10.1016/j.compositesb.2019.107457.

[67] J. Cha, J. Kim, S. Ryu, and S. H. Hong, “Comparison to mechanical properties of epoxy nanocomposites reinforced by functionalized carbon nanotubes and graphene nanoplatelets,” *Composites Part B: Engineering*, vol. 162, pp. 283–288, Apr. 2019, doi: 10.1016/j.compositesb.2018.11.011.

[68] P. K. Panda and S. Ramakrishna, “Electrospinning of alumina nanofibers using different precursors,” *J Mater Sci*, vol. 42, no. 6, pp. 2189–2193, Mar. 2007, doi: 10.1007/s10853-007-1581-2.

[69] E. N. Gilbert, B. S. Hayes, and J. C. Seferis, “Nano-alumina modified epoxy based film adhesives,” *Polymer Engineering & Science*, vol. 43, no. 5, pp. 1096–1104, 2003, doi: 10.1002/pen.10093.

[70] L. R. Xu, L. Li, C. Lukehart, and H. Kuai, “Mechanical Characterization of Nanofiber-Reinforced Composite Adhesives,” *Journal of nanoscience and nanotechnology*, vol. 7, pp. 2546–8, Aug. 2007, doi: 10.1166/jnn.2007.433.

[71] F. Musiari *et al.*, “Feasibility study of adhesive bonding reinforcement by electrospun nanofibers,” *Procedia Structural Integrity*, vol. 2, pp. 112–119, Jan. 2016, doi: 10.1016/j.prostr.2016.06.015.

[72] F. Musiari *et al.*, “Experimental investigation on the enhancement of Mode I fracture toughness of adhesive bonded joints by electrospun nanofibers,” *The Journal of Adhesion*, vol. 94, no. 11, pp. 974–990, Sep. 2018, doi: 10.1080/00218464.2017.1402301.

[73] T. Brugo, F. Musiari, A. Pirondi, A. Zucchelli, D. Cocchi, and D. Menozzi, “Development and fracture toughness characterization of a nylon nanomat epoxy adhesive reinforcement,” *Proceedings of the IMechE*, p. 146442071880773, Oct. 2018, doi: 10.1177/1464420718807733.

[74] D. Cocchi *et al.*, “Characterization of aluminum alloy-epoxy bonded joints with nanofibers obtained by electrospinning,” *The Journal of Adhesion*, vol. 96, no. 1–4, pp. 384–401, Mar. 2020, doi: 10.1080/00218464.2019.1666716.

[75] T. Ondarçuhu and C. Joachim, “Drawing a single nanofibre over hundreds of microns,” *EPL*, vol. 42, no. 2, p. 215, Apr. 1998, doi: 10.1209/epl/i1998-00233-9.

[76] K. Koenig, K. Beukenberg, F. Langensiepen, and G. Seide, “A new prototype melt-electrospinning device for the production of biobased thermoplastic sub-microfibers and nanofibers,” *Biomaterials Research*, vol. 23, no. 1, p. 10, Mar. 2019, doi: 10.1186/s40824-019-0159-9.

[77] B. Meyer and F. Croce, “MATERIALS | Nanofibers,” in *Encyclopedia of Electrochemical Power Sources*, J. Garche, Ed., Amsterdam: Elsevier, 2009, pp. 607–612. doi: 10.1016/B978-044452745-5.00058-7.

[78] J. V. Patil, S. S. Mali, A. S. Kamble, C. K. Hong, J. H. Kim, and P. S. Patil, “Electrospinning: A versatile technique for making of 1D growth of nanostructured nanofibers and its applications: An experimental approach,” *Applied Surface Science*, vol. 423, pp. 641–674, Nov. 2017, doi: 10.1016/j.apsusc.2017.06.116.

[79] T. Garg, G. Rath, and A. Goyal, “Biomaterials-based nanofiber scaffold: Targeted and controlled carrier for cell and drug delivery,” *Journal of drug targeting*, vol. 23, pp. 1–20, Dec. 2014, doi: 10.3109/1061186X.2014.992899.

[80] C. He, W. Nie, and W. Feng, “Engineering of biomimetic nanofibrous matrices of drug delivery and tissue engineering,” *J. Mater. Chem. B*, vol. 2, Sep. 2014, doi: 10.1039/C4TB01464B.

[81] J. D. Hartgerink, E. Beniash, and S. I. Stupp, “Self-Assembly and Mineralization of Peptide-Amphiphile Nanofibers,” *Science*, vol. 294, no. 5547, pp. 1684–1688, Nov. 2001, doi: 10.1126/science.1063187.

[82] J. Stanger, N. Tucker, and M. Staiger, *Electrospinning*. in Rapra review reports, no. 190 = Vol. 16, 2005,10. Shawbury: Rapra Technology, 2006.

[83] G. Mitchell, Ed., *Electrospinning: principles, practice and possibilities*. in RSC polymer chemistry series, no. 14. Cambridge, UK: Royal Society of Chemistry, 2015.

[84] H. Fong, I. Chun, and D. H. Reneker, “Beaded nanofibers formed during electrospinning,” *Polymer*, vol. 40, no. 16, pp. 4585–4592, Jul. 1999, doi: 10.1016/S0032-3861(99)00068-3.

[85] H. Khoramishad and D. Zarifpour, “Fracture response of adhesive joints reinforced with aligned multi-walled carbon nanotubes using an external electric field,” *Theoretical and Applied Fracture Mechanics*, vol. 98, pp. 220–229, Dec. 2018, doi: 10.1016/j.tafmec.2018.10.007.

[86] J. M. Wernik and S. A. Meguid, “On the mechanical characterization of carbon nanotube reinforced epoxy adhesives,” *Materials & Design*, vol. 59, pp. 19–32, Jul. 2014, doi: 10.1016/j.matdes.2014.02.034.

[87] G. Han, B. Tan, F. Cheng, B. Wang, Y.-K. Leong, and X. Hu, “CNT toughened aluminium and CFRP interface for strong adhesive bonding,” *Nano Materials Science*, vol. 4, no. 3, pp. 266–275, Sep. 2022, doi: 10.1016/j.nanoms.2021.09.003.

[88] V. K. Srivastava, T. Gries, T. Quadflieg, B. Mohr, M. Kolloch, and P. Kumar, “Fracture behavior of adhesively bonded carbon fabric composite plates with nano materials filled polymer matrix under DCB, ENF and SLS tests,” *Engineering Fracture Mechanics*, vol. 202, pp. 275–287, Oct. 2018, doi: 10.1016/j.engfracmech.2018.09.030.

[89] X. X. Fernández Sánchez-Romate, J. Molinero, A. Jiménez-Suárez, M. Sánchez, A. Güemes, and A. Ureña, “Carbon Nanotube-Doped Adhesive Films for Detecting Crack Propagation on Bonded Joints: A Deeper Understanding of Anomalous Behaviors,” *ACS Appl. Mater. Interfaces*, vol. 9, no. 49, pp. 43267–43274, Dec. 2017, doi: 10.1021/acsami.7b16036.

[90] X. F. Sánchez-Romate, A. Jiménez-Suárez, J. Molinero, M. Sánchez, A. Güemes, and A. Ureña, “Development of bonded joints using novel CNT doped adhesive films: Mechanical and electrical properties,” *International Journal of Adhesion and Adhesives*, vol. 86, pp. 98–104, Nov. 2018, doi: 10.1016/j.ijadhadh.2018.09.001.

[91] X. F. Sánchez-Romate, R. Moriche, A. Jiménez-Suárez, M. Sánchez, A. Güemes, and A. Ureña, “An approach using highly sensitive carbon nanotube adhesive films for crack growth detection under flexural load in composite structures,” *Composite Structures*, vol. 224, p. 111087, Sep. 2019, doi: 10.1016/j.compstruct.2019.111087.

[92] X. F. Sánchez-Romate *et al.*, “Fatigue crack growth identification in bonded joints by using carbon nanotube doped adhesive films,” *Smart Mater. Struct.*, vol. 29, no. 3, p. 035032, Mar. 2020, doi: 10.1088/1361-665X/ab7109.

[93] W. Y. W. Hanif, M. S. Risby, and M. Mohd. Noor, “Influence of Carbon Nanotube Inclusion on the Fracture Toughness and Ballistic Resistance of Twaron/Epoxy Composite Panels,” *Procedia Engineering*, vol. 114, pp. 118–123, Jan. 2015, doi: 10.1016/j.proeng.2015.08.049.

[94] J. Cha, G. H. Jun, J. K. Park, J. C. Kim, H. J. Ryu, and S. H. Hong, “Improvement of modulus, strength and fracture toughness of CNT/Epoxy nanocomposites through the functionalization of carbon nanotubes,” *Composites Part B: Engineering*, vol. C, no. 129, pp. 169–179, 2017, doi: 10.1016/j.compositesb.2017.07.070.

[95] J. Robertson, “Realistic applications of CNTs,” *Materials Today*, vol. 7, no. 10, pp. 46–52, Oct. 2004, doi: 10.1016/S1369-7021(04)00448-1.

[96] E. Dervishi *et al.*, “Carbon Nanotubes: Synthesis, Properties, and Applications,” *Particulate Science and Technology*, vol. 27, no. 2, pp. 107–125, Apr. 2009, doi: 10.1080/02726350902775962.

[97] O. Zaytseva and G. Neumann, “Carbon nanomaterials: Production, impact on plant development, agricultural and environmental applications,” *Chemical and Biological Technologies in Agriculture*, vol. 3, Jul. 2016, doi: 10.1186/s40538-016-0070-8.

[98] B. K. Billing and N. S. and P. K. Agnihotri, “The Growth of Carbon Nanotubes via Chemical Vapor Deposition Method; its Purification and Functionalization,” *INDJST*, vol. 10, no. 31, pp. 1–12, Aug. 2017, doi: 10.17485/ijst/2017/v10i31/113861.

[99] V. N. Popov, “Carbon nanotubes: properties and application,” *Materials Science and Engineering: R: Reports*, vol. 43, no. 3, pp. 61–102, Jan. 2004, doi: 10.1016/j.mser.2003.10.001.

[100] K. Lönnecke, O. Eberhardt, and T. Wallmersperger, “Electrostatic charge distribution in armchair and zigzag carbon nanotubes: a numerical comparison of CNT charge models,” *Acta Mech*, Nov. 2021, doi: 10.1007/s00707-021-03085-3.

[101] R. Rafiee and R. Pourazizi, “Evaluating the influence of defects on the young’s modulus of carbon nanotubes using stochastic modeling,” *Mat. Res.*, vol. 17, pp. 758–766, Jun. 2014, doi: 10.1590/S1516-14392014005000071.

[102] A. Gorkina, “Transparent and conductive hybrid graphene/carbon nanotube films,” 2015, doi: 10.13140/RG.2.1.3910.4244.

[103] A. K. Geim, “Graphene: Status and Prospects,” *Science*, vol. 324, no. 5934, pp. 1530–1534, Jun. 2009, doi: 10.1126/science.1158877.

[104] A. Gupta, T. Sakthivel, and S. Seal, “Recent development in 2D materials beyond graphene,” *Progress in Materials Science*, vol. 73, pp. 44–126, Aug. 2015, doi: 10.1016/j.pmatsci.2015.02.002.

[105] H. Khoramishad, M. Ebrahimijamal, and M. Fasihi, “The effect of graphene oxide nano-platelets on fracture behavior of adhesively bonded joints: GOPs on Fracture Behavior of Adhesively Bonded Joints,” *Fatigue Fract Engng Mater Struct*, vol. 40, no. 11, pp. 1905–1916, Nov. 2017, doi: 10.1111/ffe.12612.

[106] Z. Wang, Z. Jia, X. Feng, and Y. Zou, “Graphene nanoplatelets/epoxy composites with excellent shear properties for construction adhesives,” *Composites Part B: Engineering*, vol. 152, pp. 311–315, Nov. 2018, doi: 10.1016/j.compositesb.2018.08.113.

[107] P. Jojibabu, M. Jagannatham, P. Haridoss, G. D. Janaki Ram, A. P. Deshpande, and S. R. Bakshi, “Effect of different carbon nano-fillers on rheological properties and lap shear strength of epoxy adhesive joints,” *Composites Part A: Applied Science and Manufacturing*, vol. 82, pp. 53–64, Mar. 2016, doi: 10.1016/j.compositesa.2015.12.003.

[108] Z. Jia, X. Feng, and Y. Zou, “Graphene Reinforced Epoxy Adhesive For Fracture Resistance,” *Composites Part B: Engineering*, vol. 155, pp. 457–462, Dec. 2018, doi: 10.1016/j.compositesb.2018.09.093.

[109] R. Aradhana, S. Mohanty, and S. K. Nayak, “Comparison of mechanical, electrical and thermal properties in graphene oxide and reduced graphene oxide filled epoxy nanocomposite adhesives,” *Polymer*, vol. 141, pp. 109–123, Apr. 2018, doi: 10.1016/j.polymer.2018.03.005.

[110] B. Lokasani, P. Sampath, and S. Varghese, “Experimental investigation on graphene oxides coated carbon fibre/epoxy hybrid composites: Mechanical and electrical properties,” *Composites Science and Technology*, vol. 179, May 2019, doi: 10.1016/j.compscitech.2019.04.034.

[111] D. R. Bortz, E. G. Heras, and I. Martin-Gullon, “Impressive Fatigue Life and Fracture Toughness Improvements in Graphene Oxide/Epoxy Composites,” *Macromolecules*, vol. 45, no. 1, pp. 238–245, Jan. 2012, doi: 10.1021/ma201563k.

[112] M. Bhasin, S. Wu, R. B. Ladani, A. J. Kinloch, C. H. Wang, and A. P. Mouritz, “Increasing the fatigue resistance of epoxy nanocomposites by aligning graphene nanoplatelets,” *International Journal of Fatigue*, vol. 113, pp. 88–97, Aug. 2018, doi: 10.1016/j.ijfatigue.2018.04.001.

[113] D. Galpaya, M. Wang, G. George, N. Motta, E. Waclawik, and C. Yan, “Preparation of graphene oxide/epoxy nanocomposites with significantly improved mechanical properties,” *Journal of Applied Physics*, vol. 116, no. 5, p. 053518, Aug. 2014, doi: 10.1063/1.4892089.

[114] N. Domun *et al.*, “Improving the fracture toughness properties of epoxy using graphene nanoplatelets at low filler content,” *Nanocomposites*, vol. 3, no. 3, pp. 85–96, Jul. 2017, doi: 10.1080/20550324.2017.1365414.

[115] M. Cai, D. Thorpe, D. H. Adamson, and H. C. Schniepp, “Methods of graphite exfoliation,” *J. Mater. Chem.*, vol. 22, no. 48, pp. 24992–25002, Nov. 2012, doi: 10.1039/C2JM34517J.

[116] A. J. Pollard and C. A. Clifford, “Terminology: the first step towards international standardisation of graphene and related 2D materials,” *J Mater Sci*, vol. 52, no. 24, pp. 13685–13688, Dec. 2017, doi: 10.1007/s10853-017-1567-7.

[117] K. Parvez, S. Yang, X. Feng, and K. Müllen, "Exfoliation of graphene via wet chemical routes," *Synthetic Metals*, vol. 210, pp. 123–132, Aug. 2015, doi: 10.1016/j.synthmet.2015.07.014.

[118] W.-W. Liu, B.-Y. Xia, X.-X. Wang, and J.-N. Wang, "Exfoliation and dispersion of graphene in ethanol-water mixtures," *Frontiers of Materials Science*, vol. 6, pp. 176–182, Jun. 2012, doi: 10.1007/s11706-012-0166-4.

[119] G. Bepete *et al.*, "Surfactant-free single-layer graphene in water," *Nat Chem*, vol. 9, no. 4, pp. 347–352, Apr. 2017, doi: 10.1038/nchem.2669.

[120] Z. Y. Xia *et al.*, "The Exfoliation of Graphene in Liquids by Electrochemical, Chemical, and Sonication-Assisted Techniques: A Nanoscale Study," *Advanced Functional Materials*, vol. 23, no. 37, pp. 4684–4693, 2013, doi: 10.1002/adfm.201203686.

[121] T. Nakajima and Y. Matsuo, "Formation process and structure of graphite oxide," *Carbon*, vol. 32, no. 3, pp. 469–475, Jan. 1994, doi: 10.1016/0008-6223(94)90168-6.

[122] A. Singh, N. Sharma, M. Arif, and R. Katiyar, "Electrically reduce graphene oxide for photovolatic applications," *Journal of Materials Research*, Jan. 2019, doi: 10.1557/jmr.2019.32.

[123] Y. Zhu *et al.*, "Graphene and Graphene Oxide: Synthesis, Properties, and Applications," *Advanced Materials*, vol. 22, no. 35, pp. 3906–3924, 2010, doi: 10.1002/adma.201001068.

[124] D. G. Papageorgiou, I. A. Kinloch, and R. J. Young, "Mechanical properties of graphene and graphene-based nanocomposites," *Progress in Materials Science*, vol. 90, pp. 75–127, Oct. 2017, doi: 10.1016/j.pmatsci.2017.07.004.

[125] P. K. Mallick, *Fiber-reinforced composites: materials, manufacturing, and design*, 3rd ed., [Expanded and rev. Ed.]. Boca Raton, FL: CRC Press, 2008.

[126] I. M. Daniel and O. Ishai, *Engineering Mechanics of Composite Materials*. New York: Oxford University Press, 1994.

[127] S. K. Mazumdar, *Composites manufacturing: materials, product, and process engineering / Sanjay K. Mazumdar*. Boca Raton, Fla: CRC Press, 2002.

[128] K. Turan and G. Örçen, "Failure analysis of adhesive-patch-repaired edge-notched composite plates," *The Journal of Adhesion*, vol. 93, no. 4, pp. 328–341, Mar. 2017, doi: 10.1080/00218464.2015.1116984.

[129] S. O. Olajide, E. Kandare, and A. A. Khatibi, "Fatigue life uncertainty of adhesively bonded composite scarf joints – an airworthiness perspective," *The Journal of Adhesion*, vol. 93, no. 7, pp. 515–530, Jun. 2017, doi: 10.1080/00218464.2015.1112796.

[130] A. R. Rasane, P. Kumar, and M. P. Khond, "Optimizing the size of a CFRP patch to repair a crack in a thin sheet," *The Journal of Adhesion*, vol. 93, no. 13, pp. 1064–1080, Nov. 2017, doi: 10.1080/00218464.2016.1204236.

[131] J. A. B. P. Neto, R. D. S. G. Campilho, and L. F. M. da Silva, "Parametric study of adhesive joints with composites," *International Journal of Adhesion and Adhesives*, vol. 37, pp. 96–101, Sep. 2012, doi: 10.1016/j.ijadhadh.2012.01.019.

[132] "A strategy to reduce delamination of adhesive joints with composite substrates - X Shang, EAS Marques, JJM Machado, RJC Carbas, D Jiang, LFM da Silva, 2019." https://journals.sagepub.com/doi/10.1177/1464420718805712 (accessed Dec. 21, 2022).

[133] L. F. M. da Silva, T. N. S. S. Rodrigues, M. A. V. Figueiredo, M. F. S. F. de Moura, and J. A. G. Chousal, "Effect of Adhesive Type and Thickness on the Lap Shear Strength," *The Journal of Adhesion*, vol. 82, no. 11, pp. 1091–1115, Nov. 2006, doi: 10.1080/00218460600948511.

[134] J. Cai *et al.*, *Structural Health Monitoring for Composite Materials*. IntechOpen, 2012. doi: 10.5772/48215.

[135] J.-B. Ihn and F.-K. Chang, "Pitch-catch Active Sensing Methods in Structural Health Monitoring for Aircraft Structures," *Structural Health Monitoring*, vol. 7, no. 1, pp. 5–19, Mar. 2008, doi: 10.1177/1475921707081979.

[136] A. Güemes, A. Fernandez-Lopez, A. R. Pozo, and J. Sierra-Pérez, "Structural Health Monitoring for Advanced Composite Structures: A Review," *Journal of Composites Science*, vol. 4, no. 1, Art. no. 1, Mar. 2020, doi: 10.3390/jcs4010013.

[137] D. Montalvão, N. M. M. Maia, and A. M. R. Ribeiro, “A review of vibration-based structural health monitoring with special emphasis on composite materials,” *Shock and Vibration Digest*, vol. 38, no. 4, Art. no. 4, Jul. 2006.

[138] W. Fan and P. Qiao, “Vibration-based Damage Identification Methods: A Review and Comparative Study,” *Structural Health Monitoring*, vol. 10, no. 1, pp. 83–111, Jan. 2011, doi: 10.1177/1475921710365419.

[139] G. Luyckx, E. Voet, N. Lammens, and J. Degrieck, “Strain Measurements of Composite Laminates with Embedded Fibre Bragg Gratings: Criticism and Opportunities for Research,” *Sensors*, vol. 11, no. 1, Art. no. 1, Jan. 2011, doi: 10.3390/s110100384.

[140] J. Sierra-Perez, A. Guemes, and L. Mujica, “Damage detection by using FBGs and strain field pattern recognition techniques,” *Smart Materials and Structures*, vol. 22, p. 025011, Dec. 2012, doi: 10.1088/0964-1726/22/2/025011.

[141] H. W. Park, H. Sohn, K. H. Law, and C. R. Farrar, “Time reversal active sensing for health monitoring of a composite plate,” *Journal of Sound and Vibration*, vol. 302, no. 1, pp. 50–66, Apr. 2007, doi: 10.1016/j.jsv.2006.10.044.

[142] V. Giurgiutiu and C. Soutis, “Enhanced Composites Integrity Through Structural Health Monitoring,” *Appl Compos Mater*, vol. 19, no. 5, pp. 813–829, Oct. 2012, doi: 10.1007/s10443-011-9247-2.

[143] F. Ciampa and M. Meo, “A new algorithm for acoustic emission localization and flexural group velocity determination in anisotropic structures,” *Composites Part A: Applied Science and Manufacturing*, vol. 41, no. 12, pp. 1777–1786, Dec. 2010, doi: 10.1016/j.compositesa.2010.08.013.

[144] V. Giurgiutiu and J. Bao, “Embedded-ultrasonics Structural Radar for In Situ Structural Health Monitoring of Thin-wall Structures,” *Structural Health Monitoring*, vol. 3, no. 2, pp. 121–140, Jun. 2004, doi: 10.1177/1475921704042697.

[145] B. Yoo, A. S. Purekar, Y. Zhang, and D. J. Pines, “Piezoelectric-paint-based two-dimensional phased sensor arrays for structural health monitoring of thin panels,” *Smart Mater. Struct.*, vol. 19, no. 7, p. 075017, Jun. 2010, doi: 10.1088/0964-1726/19/7/075017.

[146] D. Roach, “Real time crack detection using mountable comparative vacuum monitoring sensors,” *1*, vol. 5, no. 4, Art. no. 4, Jul. 2009.

[147] S. Bhalla, A. Gupta, S. Bansal, and T. Garg, “Ultra Low-cost Adaptations of Electro-mechanical Impedance Technique for Structural Health Monitoring,” *Journal of Intelligent Material Systems and Structures*, vol. 20, no. 8, pp. 991–999, May 2009, doi: 10.1177/1045389X08100384.

[148] V. Giurgiutiu and C. A. Rogers, “Recent advancements in the electromechanical (E/M) impedance method for structural health monitoring and NDE,” in *Smart Structures and Materials 1998: Smart Structures and Integrated Systems*, SPIE, Jul. 1998, pp. 536–547. doi: 10.1117/12.316923.

[149] K. J. Loh, T.-C. Hou, J. P. Lynch, and N. A. Kotov, “Carbon Nanotube Sensing Skins for Spatial Strain and Impact Damage Identification,” *J Nondestruct Eval*, vol. 28, no. 1, pp. 9–25, Mar. 2009, doi: 10.1007/s10921-009-0043-y.

[150] I. Kang, M. J. Schulz, J. H. Kim, V. Shanov, and D. Shi, “A carbon nanotube strain sensor for structural health monitoring,” *Smart Mater. Struct.*, vol. 15, no. 3, p. 737, Apr. 2006, doi: 10.1088/0964-1726/15/3/009.

[151] N. GOLDFINE, V. ZILBERSTEIN, A. WASHABAUGH, D. SCHLICKER, I. SHAY, and D. GRUNDY, “Eddy current sensor networks for aircraft fatigue monitoring,” *Mater. eval*, vol. 61, no. 7, pp. 852–859, 2003.

[152] H. Speckmann and R. Henrich, “STRUCTURAL HEALTH MONITORING (SHM) – OVERVIEW ON TECHNOLOGIES UNDER DEVELOPMENT”.

[153] C. Tuloup, W. Harizi, Z. Aboura, Y. Meyer, K. Khellil, and R. Lachat, “On the use of in-situ piezoelectric sensors for the manufacturing and structural health monitoring of polymer-

matrix composites: A literature review," *Composite Structures*, vol. 215, pp. 127–149, May 2019, doi: 10.1016/j.compstruct.2019.02.046.

[154] B. Xiao *et al.*, "In-Situ Monitoring of a Filament Wound Pressure Vessel by the MWCNT Sensor under Hydraulic Fatigue Cycling and Pressurization," *Sensors*, vol. 19, no. 6, Art. no. 6, Jan. 2019, doi: 10.3390/s19061396.

[155] S. Luo and T. Liu, "Graphite Nanoplatelet Enabled Embeddable Fiber Sensor for in Situ Curing Monitoring and Structural Health Monitoring of Polymeric Composites," *ACS Appl. Mater. Interfaces*, vol. 6, no. 12, pp. 9314–9320, Jun. 2014, doi: 10.1021/am5017039.

[156] A. Naghashpour and S. Van Hoa, "A technique for real-time detection, location and quantification of damage in large polymer composite structures made of electrically non-conductive fibers and carbon nanotube networks," *Nanotechnology*, vol. 24, no. 45, p. 455502, Nov. 2013, doi: 10.1088/0957-4484/24/45/455502.

[157] K. Hamdi, Z. Aboura, W. Harizi, and K. Khellil, "Improvement of the electrical conductivity of carbon fiber reinforced polymer by incorporation of nanofillers and the resulting thermal and mechanical behavior," *Journal of Composite Materials*, vol. 52, no. 11, pp. 1495–1503, May 2018, doi: 10.1177/0021998317726588.

[158] B. Hao, Q. Ma, S. Yang, E. Mäder, and P.-C. Ma, "Comparative study on monitoring structural damage in fiber-reinforced polymers using glass fibers with carbon nanotubes and graphene coating," *Composites Science and Technology*, vol. 129, pp. 38–45, Jun. 2016, doi: 10.1016/j.compscitech.2016.04.012.

[159] N. D. Alexopoulos, C. Bartholome, P. Poulin, and Z. Marioli-Riga, "Structural health monitoring of glass fiber reinforced composites using embedded carbon nanotube (CNT) fibers," *Composites Science and Technology*, vol. 70, no. 2, pp. 260–271, Feb. 2010, doi: 10.1016/j.compscitech.2009.10.017.

[160] S. Boztepe, H. Liu, D. Heider, and E. T. Thostenson, "Novel carbon nanotube interlaminar film sensors for carbon fiber composites under uniaxial fatigue loading," *Composite Structures*, vol. 189, pp. 340–348, Apr. 2018, doi: 10.1016/j.compstruct.2018.01.033.

[161] A. Sanli, A. Benchirouf, C. Müller, and O. Kanoun, "Piezoresistive performance characterization of strain sensitive multi-walled carbon nanotube-epoxy nanocomposites," *Sensors and Actuators A: Physical*, vol. 254, pp. 61–68, Feb. 2017, doi: 10.1016/j.sna.2016.12.011.

[162] S. Ebnesajjad and C. F. Ebnesajjad, *Surface treatment of materials for adhesive bonding*, Second edition. Amsterdam: William Andrew, an imprint of Elsevier, 2014.

[163] L. Kozma and I. Olefjord, "Surface treatment of steel for structural adhesive bonding," *Materials Science and Technology*, vol. 3, no. 11, pp. 954–962, Nov. 1987, doi: 10.1179/mst.1987.3.11.954.

[164] Lucas. F. M. da Silva, R. J. C. Carbas, G. W. Critchlow, M. A. V. Figueiredo, and K. Brown, "Effect of material, geometry, surface treatment and environment on the shear strength of single lap joints," *International Journal of Adhesion and Adhesives*, vol. 29, no. 6, pp. 621–632, Sep. 2009, doi: 10.1016/j.ijadhadh.2009.02.012.

[165] R. F. Wegman, *Surface preparation techniques for adhesive bonding*. Park Ridge, N.J., U.S.A: Noyes Publications, 1989.

[166] J. P. B. van Dam, S. T. Abrahami, A. Yilmaz, Y. Gonzalez-Garcia, H. Terryn, and J. M. C. Mol, "Effect of surface roughness and chemistry on the adhesion and durability of a steel-epoxy adhesive interface," *International Journal of Adhesion and Adhesives*, vol. 96, p. 102450, Jan. 2020, doi: 10.1016/j.ijadhadh.2019.102450.

[167] K. Poorna Chander, M. Vashista, K. Sabiruddin, S. Paul, and P. P. Bandyopadhyay, "Effects of grit blasting on surface properties of steel substrates," *Materials & Design*, vol. 30, no. 8, pp. 2895–2902, Sep. 2009, doi: 10.1016/j.matdes.2009.01.014.

[168] S. Amada and A. Satoh, "Fractal analysis of surfaces roughened by grit blasting," *Journal of Adhesion Science and Technology*, vol. 14, no. 1, pp. 27–41, Jan. 2000, doi: 10.1163/156856100742096.

[169] D. Fernando, J. G. Teng, T. Yu, and X. L. Zhao, “Preparation and Characterization of Steel Surfaces for Adhesive Bonding,” *J. Compos. Constr.*, vol. 17, no. 6, p. 04013012, Dec. 2013, doi: 10.1061/(ASCE)CC.1943-5614.0000387.

[170] ISO 25178-2:2012, “Geometrical product specifications (GPS) - Surface texture: Areal. Part 2: Terms, definitions and surface texture parameters.” 2012.

[171] ASTM D1002-10(2019), “Standard Test Method for Apparent Shear Strength of Single-Lap-Joint Adhesively Bonded Metal Specimens by Tension Loading (Metal-to-Metal).” 2019.

[172] “Lap Shear and Impact Testing of Ochre and Beeswax in Experimental Middle Stone Age Compound Adhesives,” *PLOS ONE*, vol. 11, no. 3, p. e0150436, Mar. 2016, doi: 10.1371/journal.pone.0150436.

[173] E. Maccaferri, L. Mazzocchetti, T. Benelli, T. M. Brugo, A. Zucchelli, and L. Giorgini, “Rubbery nanofibers by co-electrospinning of almost immiscible NBR and PCL blends,” *Materials & Design*, vol. 186, p. 108210, Jan. 2020, doi: 10.1016/j.matdes.2019.108210.

[174] F. Musiari *et al.*, “Experimental investigation on the enhancement of Mode I fracture toughness of adhesive bonded joints by electrospun nanofibers,” *The Journal of Adhesion*, vol. 94, no. 11, pp. 974–990, Sep. 2018, doi: 10.1080/00218464.2017.1402301.

[175] T. Brugo, F. Musiari, A. Pirondi, A. Zucchelli, D. Cocchi, and D. Menozzi, “Development and fracture toughness characterization of a nylon nanomat epoxy adhesive reinforcement,” *Proceedings of the Institution of Mechanical Engineers, Part L: Journal of Materials: Design and Applications*, vol. 233, no. 3, pp. 465–474, Oct. 2019, doi: 10.1177/1464420718807733.

[176] D. Cocchi *et al.*, “Characterization of aluminum alloy-epoxy bonded joints with nanofibers obtained by electrospinning,” *The Journal of Adhesion*, vol. 96, no. 1–4, pp. 384–401, Mar. 2020, doi: 10.1080/00218464.2019.1666716.

[177] E. Maccaferri, L. Mazzocchetti, T. Benelli, A. Zucchelli, and L. Giorgini, “Morphology, thermal, mechanical properties and ageing of nylon 6,6/graphene nanofibers as Nano2 materials,” *Composites Part B: Engineering*, vol. 166, pp. 120–129, Jun. 2019, doi: 10.1016/j.compositesb.2018.11.096.

[178] S. Minosi, D. Cocchi, A. Pirondi, A. Zucchelli, and F. Campanini, “Integration of nylon electrospun nanofibers into structural epoxy adhesive joints,” *IOP Conf. Ser.: Mater. Sci. Eng.*, vol. 1038, no. 1, p. 012048, Feb. 2021, doi: 10.1088/1757-899X/1038/1/012048.

[179] S. Minosi *et al.*, “Exploitation of rubbery electrospun nanofibrous mat for fracture toughness improvement of structural epoxy adhesive bonded joints,” *Journal of Advanced Joining Processes*, vol. 3, p. 100050, Jun. 2021, doi: 10.1016/j.jajp.2021.100050.

[180] “ASTM D3039/D3039M-08 - Standard Test Method for Tensile Properties of Polymer Matrix Composite Materials,” ASTM International, 2014. doi: 10.1520/D3039_D3039M-08.

[181] A. J. Gunnion and I. Herszberg, “Parametric study of scarf joints in composite structures,” *Composite Structures*, vol. 75, no. 1, pp. 364–376, Sep. 2006, doi: 10.1016/j.compstruct.2006.04.053.

[182] Xu Yi, He Qiang, Yang Wenfeng, Sun Ting, and Tang Qingru, “Study on relationships between curing pressures and mechanical properties for epoxy adhesive films,” *Chemical Engineering Transactions*, vol. 66, pp. 43–48, 2018, doi: 10.3303/CET1866008.

[183] Z. Xie, S. Wang, and X. Li, “Composite tapered scarf joint repair: analytical model and experimental validation,” presented at the 2016 5th International Conference on Energy and Environmental Protection (ICEEP 2016), Atlantis Press, Nov. 2016, pp. 720–726. doi: 10.2991/iceep-16.2016.124.

[184] M. L. Arias, P. M. Frontini, and R. J. J. Williams, “Analysis of the damage zone around the crack tip for two rubber-modified epoxy matrices exhibiting different toughenability,” *Polymer*, vol. 44, no. 5, pp. 1537–1546, Mar. 2003, doi: 10.1016/S0032-3861(02)00829-7.

[185] S. R. Ranade, Y. Guan, R. B. Moore, J. G. Dillard, R. C. Batra, and D. A. Dillard, “Characterizing fracture performance and the interaction of propagating cracks with locally weakened interfaces in adhesive joints,” *International Journal of Adhesion and Adhesives*, vol. 82, pp. 196–205, Apr. 2018, doi: 10.1016/j.ijadhadh.2017.12.006.

[186] G. W. Beckermann, “Nanofiber interleaving veils for improving the performance of composite laminates,” *Reinforced Plastics*, vol. 61, no. 5, pp. 289–293, Sep. 2017, doi: 10.1016/j.repl.2017.03.006.

[187] M. Quaresimin, K. Schulte, M. Zappalorto, and S. Chandrasekaran, “Toughening mechanisms in polymer nanocomposites: From experiments to modelling,” *Composites Science and Technology*, vol. 123, pp. 187–204, Feb. 2016, doi: 10.1016/j.compscitech.2015.11.027.

[188] “The effect of carbon nanotubes on the fracture toughness and fatigue performance of a thermosetting epoxy polymer | SpringerLink.” https://link.springer.com/article/10.1007/s10853-011-5724-0 (accessed Dec. 22, 2022).

[189] A. Parashar and P. Mertiny, “Multiscale Model to Study of Fracture Toughening in Graphene/Polymer Nanocomposite,” *Int J Fract*, vol. 179, no. 1, pp. 221–228, Jan. 2013, doi: 10.1007/s10704-012-9779-y.

[190] Alamusi, N. Hu, H. Fukunaga, S. Atobe, Y. Liu, and J. Li, “Piezoresistive Strain Sensors Made from Carbon Nanotubes Based Polymer Nanocomposites,” *Sensors*, vol. 11, no. 11, Art. no. 11, Nov. 2011, doi: 10.3390/s111110691.

[191] S. K. Reddy, S. Kumar, K. M. Varadarajan, P. R. Marpu, T. K. Gupta, and M. Choosri, “Strain and damage-sensing performance of biocompatible smart CNT/UHMWPE nanocomposites,” *Materials Science and Engineering: C*, vol. 92, pp. 957–968, Nov. 2018, doi: 10.1016/j.msec.2018.07.029.

[192] X. F. Sánchez-Romate, J. Artigas, A. Jiménez-Suárez, M. Sánchez, A. Güemes, and A. Ureña, “Critical parameters of carbon nanotube reinforced composites for structural health monitoring applications: Empirical results versus theoretical predictions,” *Composites Science and Technology*, vol. 171, pp. 44–53, Feb. 2019, doi: 10.1016/j.compscitech.2018.12.010.

[193] S. Aziz and S.-H. Chang, “Smart-fabric sensor composed of single-walled carbon nanotubes containing binary polymer composites for health monitoring,” *Composites Science and Technology*, vol. 163, pp. 1–9, Jul. 2018, doi: 10.1016/j.compscitech.2018.05.012.

[194] S. Polat, A. Avcı, and M. Ekrem, “Fatigue behavior of composite to aluminum single lap joints reinforced with graphene doped nylon 66 nanofibers,” *Composite Structures*, vol. 194, pp. 624–632, Jun. 2018, doi: 10.1016/j.compstruct.2018.04.043.

[195] S. Yu, M. N. Tong, and G. Critchlow, “Use of carbon nanotubes reinforced epoxy as adhesives to join aluminum plates,” *Materials & Design*, vol. 31, pp. S126–S129, Jun. 2010, doi: 10.1016/j.matdes.2009.11.045.

[196] H. S. Hedia, L. Allie, S. Ganguli, and H. Aglan, “The influence of nanoadhesives on the tensile properties and Mode-I fracture toughness of bonded joints,” *Engineering Fracture Mechanics*, vol. 73, no. 13, pp. 1826–1832, Sep. 2006, doi: 10.1016/j.engfracmech.2006.02.013.

[197] D. Quan, D. Carolan, C. Rouge, N. Murphy, and A. Ivankovic, “Mechanical and fracture properties of epoxy adhesives modified with graphene nanoplatelets and rubber particles,” *International Journal of Adhesion and Adhesives*, vol. 81, pp. 21–29, Mar. 2018, doi: 10.1016/j.ijadhadh.2017.09.003.

[198] S.-S. Yao, C.-L. Ma, F.-L. Jin, and S.-J. Park, “Fracture toughness enhancement of epoxy resin reinforced with graphene nanoplatelets and carbon nanotubes,” *Korean J. Chem. Eng.*, vol. 37, no. 11, pp. 2075–2083, Nov. 2020, doi: 10.1007/s11814-020-0620-4.

ACKNOWLEDGEMENTS

In conclusion of this thesis work, I would like to express my deep gratitude to my tutor, Professor Fabrizio Moroni, who with great patience, attention and professionalism guided me throughout the entire PhD course. I would also like to express my gratitude to Professor Alessandro Pirondi, who first believed in me and gave me the opportunity to become part of his research group. I thank Professor Andrea Zucchelli and colleagues from the University of Bologna, Davide Cocchi and Emanuele Maccaferri, for their valuable contribution to my thesis work. I thank my colleagues and friends from the University of Parma who encouraged and supported me throughout these 3 years. In particular I thank Andrea Rossi for his constant availability in the realization of the tests, Francesco Musiari for his precious technical and moral support, Michele Gulino for his kindness and availability in helping me face the last year of my PhD, and Daniele Ambrosini, with whom I shared the challenges and joys of this journey.

I warmly thank my colleagues at Leonardo for supporting and motivating me during these last two years, in particular I thank Zahid, Samia, Eva, Sara and Nicola for their invaluable advice.

I am grateful to my family and friends for their faith in my abilities and for encouraging my pursuit of this goal. Finally, I thank Matteo who with love, perseverance and patience has been by my side, motivating and helping me every day to face the challenges, big or small, that this journey inevitably brings with it.